Improving the Calibration of Supernova Distances for Cosmology

DISSERTATION

zur Erlangung des akademischen Grades
doctor rerum naturalium
(Dr. rer. nat.)
im Fach: Physik
Spezialisierung: Experimentalphysik

eingereicht an der
Mathematisch-Naturwissenschaftlichen Fakultät
der Humboldt-Universität zu Berlin

von

M.Sc. Daniel Küsters

Präsidentin der Humboldt-Universität zu Berlin:
Prof. Dr.-Ing. Dr. Sabine Kunst

Dekan der Mathematisch-Naturwissenschaftlichen Fakultät:
Prof. Dr. Elmar Kulke

Gutachter: 1. Prof. Dr. Marek Kowalski
2. Prof. Dr. Thomas Lohse
3. Prof. Dr. Martin M. Roth

Tag der mündlichen Prüfung: 28.11.2018

Selbständigkeitserklärung

Ich erkläre, dass ich die Dissertation selbständig und nur unter Verwendung der von mir gemäß §7 Abs. 3 der Promotionsordnung der Mathematisch-Naturwissenschaftlichen Fakultät, veröffentlicht im Amtlichen Mitteilungsblatt der Humboldt-Universität zu Berlin Nr. 126/2014 am 18.11.2014 angegebenen Hilfsmittel angefertigt habe.

Daniel Küsters
Berlin, Juli 2018

Abstract

SCALA is a calibration system for the SuperNova Integral Field Spectrograph (SNIFS), which is mounted to the University Hawaii 2.2 m telescope. The aim of SCALA is to reduce the uncertainties on the flux calibration for luminosity distance measures. It therefore allows the reduction of the uncertainties on the time variability of the Dark Energy.

SCALA enables us to calibrate SNIFS relative to a laboratory standard, which is realized by a photodiode, that is itself calibrated against a primary standard at NIST[1]. To transfer the calibration, we illuminate both the photodiode and SNIFS with a wavelength-tunable, monochromatic light source. This calibration allows us to compare the laboratory system to the astronomical CALSPEC system.

The first results were presented in [Lombardo, 2017]. We have now identified several sources of systematic uncertainty that were affecting our measurements. After correcting for these effects, the wavelength-dependency of the calibration by SCALA agrees with the CALSPEC system in the wavelength range 4500 Å to 9000 Å (within our uncertainties of $\pm 1.5\,\%$).

In the future, the identified sources of systematic uncertainty could be reduced through improvements to the setup. This would allow comparisons to the CALSPEC system with uncertainties $< 1\,\%$ and a wavelength range extension down to 3500 Å.

[1] National Institute of Standards and Technology

Zusammenfassung

SCALA ist eine Kalibrationseinheit für den SuperNova Integral Feld Spektrographen (SNIFS) der am 2,2 m Teleskop der Universität Hawaii montiert ist. SCALA wurde gebaut um die Unsicherheiten in der Flusskalibration von Leuchtkraftentfernungen zu reduzieren. Dadurch erlaubt SCALA die mögliche zeitliche Veränderung der Dunklen Energie besser zu vermessen.

SCALA ermöglicht die Kalibration von SNIFS relativ zu einem Laborstandard, der durch eine Photodiode realisiert ist, die relative zu einem Primärstandard am NIST[1] kalibriert ist. Zur Übertragung der Kalibration werden SNIFS und die Photodiode gleichzeitig von einer monochromatischen, wellenlängen einstellbaren Lichtquelle beleuchtet. Dadurch wird ein Vergleich zwischen dem astronomischen CALSPEC System und dem Laborsystem möglich.

Erste Ergebnisse von SCALA wurden in [Lombardo, 2017] vorgestellt. Wir haben nun mehrere Quellen von systematischen Effekten identifiziert, die unsere Messungen beeinflussen. Nach der Korrektur dieser Effekte stimmt die Wellenlängenabhängigkeit der Kalibration an Hand von SCALA und CALSPEC im Wellenlängenbereich 4500 Å bis 9000 Å im Fehlerbereich von $\pm 1,5\,\%$ überein.

In der Zukunft könnten die Quellen von systematischen Effekte durch Veränderungen am Messaufbau unterdrückt werden. Dies ermöglicht Vergleiche zwischen CALSPEC und SCALA im Fehlerbereich $< 1\,\%$, außerdem könnte der Wellenlängenbereich bis zu 3500 Å erweitert werden.

[1] National Institute of Standards and Technology

Contents

Chapter 1

Introduction

Since the measurements of Hubble, it has been known that there are many galaxies in the universe and that most of them are receding form us - the universe is expanding.

As space is expanding, light which propagates through it, will be redshifted. The degree of redshift, is a measure of the total expansion of the universe, accumulated between emission and observation of the light. Cosmological models relate measured redshift and other measures of distance to the energy content of the universe (see sec. 2.1). Obtaining distance and redshift measurements of cosmological objects therefore allows to measure the energy composition of the universe.

Combining redshift measurements and luminosity distances, one obtains a so-called "Hubble Relation", which can be compared to the theoretical "Hubble Relation" derived from cosmological models. In 1999, the measurements of the Supernova Cosmology Project ([Perlmutter et al., 1999]) and the High-Z supernova search team ([Riess et al., 1998]) contradicted the current standard model of a universe only containing dark and "normal" matter. They found that high-redshifted supernovae appear dimmer than in such a universe. The expansion of the universe was found to be not decelerating as expected, but accelerating. This can be explained by an additional energy contribution from so-called "Dark Energy", which is mathematically the same as a cosmological constant, first introduced by Einstein ([Einstein, 1917]). The best fit cosmological model today, is a universe composed of 70 % Dark Energy (DE), 27 % Dark Matter (DM) and 3 % "normal" matter ([Ade et al., 2016]). The Nobel prize in 2011 was awarded to the discovery of the accelerated expansion of the universe ([Botner et al., 2011]).

To improve the knowledge of dark energy, the precision of flux measured for the individual sources, needs to be improved. However, the measurement uncertainty is not given by the statistics of the observed objects but by their calibration, see sec. 2.3.

Obtaining a measurement always includes a comparison to a stable reference point. As a field astronomy predates modern electronics, there is a long history of developing systems of reference. Sec. 3 gives an overview and a description of these reference systems.

Stars have historically been used as reference points for the apparent brightness of an object. As these objects are distant, their properties can not be directly tested. They can only be modeled. Modeling uncertainties must therefore be incorporated into the calibration. With the SNIFS CALibration Aparatus (SCALA), we provide a flux reference for the SuperNova Integral Field Spectrograph (SNIFS), which is mounted to the University Hawaii 2.2 m telescope (UH88)

and described in chapter 4.

Our flux reference is realized by a photodiode which is calibrated relative to a primary standard at NIST. The properties of the photodiode setup are described in chapter 5.

The initial concept of SCALA was presented by Amir Moqanaki in a Report in February 2012. He suggested the use of a lamp and monochromator setup to illuminate both the University Hawaii 2.2 m telescope (UH88) and a photodiode, in parallel. To reduce losses, the light of the monochromator setup should be collimated by a radio dish prior to illuminating the telescope. The initial tests using a mirror of 43 cm from a solar cooker, were performed by Moqanaki.

In a diploma thesis Eymen Alyaz concluded, that the suggested parabolic radio dish does not meet the surface quality which is needed for the optical illumination of the telescope.

The work was continued by Simona Lombardo and myself. My master's thesis explained the main optical elements of SCALA. Simona showed the first calibration results in her Phd-thesis and the data reduction software [Lombardo, 2017].

The results shown at that time, were limited by systematic effects which have now been identified and quantified for correction. These systematics are described in chapter 6. Section 6.5 applies the necessary corrections to the measurements. In chapter 7, we take into account the uncertainties on the observation of stars from the CALSPEC system. In chapter 8 we estimate the influence of aging on the corrections, as the systematics were found as much as three years after the calibration of SNIFS by SCALA.

Chapter 9 summarizes our results, and lists possible improvements to the SCALA system, which could improve the future performance of SCALA.

Chapter 2

Cosmology, Observables and Calibration

The field of cosmology describes the universe as a whole, at distances where gravitation is the dominant force. A theory of gravity is therefore needed: Einstein's general relativity. Based on this, I will explain the concepts of redshift and luminosity distance, and then motivate the need for precise calibration.

2.1 Cosmology based on General Relativity

Starting with the Einstein Field equation:

$$G_{\mu\nu} = \frac{8\pi}{c^4} G T_{\mu\nu} + \Lambda g_{\mu\nu} \tag{2.1}$$

where $G_{\mu\nu}$ is the Einstein tensor describing the geometry of space time, G is Newtons gravitational constant, $T_{\mu\nu}$ is the energy-momentum tensor describing the source of the gravitational field, Λ is the cosmological constant and $g_{\mu\nu}$ is the metric tensor, providing a measure for distances and angles. Following e.g. [Bergström and Goobar, 2006], one can relate $G_{\mu\nu}$ to the

metric tensor $g_{\mu\nu}$ via:

$$
\begin{aligned}
g_{\rho\mu}g^{\mu\nu} &= \delta^{\nu}_{\rho} \\
G_{\mu\nu} &= R_{\mu\nu} - \frac{1}{2}g_{\mu\nu}R && \text{Einstein tensor} \\
R_{\mu\nu} &= g^{\alpha\gamma}R_{\alpha\mu\gamma\nu} && \text{Ricci tensor} \\
R &= g^{\mu\nu}R_{\mu\nu} && \text{Ricci scalar} \\
R_{\alpha\beta\gamma\delta} &= g_{\alpha\rho}R^{\rho}_{\beta\gamma\delta} \\
R^{\mu}_{\sigma\beta\alpha} &= \frac{\partial\Gamma^{\mu}_{\sigma\alpha}}{\partial x^{\beta}} - \frac{\partial\Gamma^{\mu}_{\sigma\beta}}{\partial x^{\alpha}} + \Gamma^{\mu}_{\rho\beta}\Gamma^{\rho}_{\sigma\alpha} - \Gamma^{\mu}_{\rho\alpha}\Gamma^{\rho}_{\sigma\beta} && \text{Riemann curvature tensor} \\
\Gamma^{\sigma}_{\mu\nu} &= \frac{g^{\rho\sigma}}{2}\left(\frac{\partial g_{\nu\rho}}{\partial x^{\mu}} + \frac{\partial g_{\mu\rho}}{\partial x^{\nu}} - \frac{\partial g_{\nu\mu}}{\partial x^{\rho}}\right) && \text{Metric connections / Christoffel symbols}
\end{aligned}
\tag{2.2}
$$

The Einstein equation is therefore completely-defined by the metric tensor and the energy momentum tensor via the above equations.

From observations of the universe, it is known that the universe is homogeneous on large scales. As there is no reason to think that our position should be special in the universe, it should also be isotropic. The Friedman Lemaitre Robertson Walker metric tensor provides a measure of distance in such a universe:

$$
g_{\mu\nu} = \begin{pmatrix} 1 & 0 & 0 & 0 \\ 0 & -a^2(t)/(1-kr^2) & 0 & 0 \\ 0 & 0 & -a^2r^2 & 0 \\ 0 & 0 & 0 & -a^2r^2sin^2\theta \end{pmatrix} \tag{2.3}
$$

with spherical coordinates (r, θ, ϕ), scale factor a and the curvature $k = -1, 0, 1$ and $c = 1$. We find the line element to be $\mathrm{d}s^2 \equiv g_{\mu\nu}\,\mathrm{d}x^{\mu}\,\mathrm{d}x^{\nu}$:

$$
\mathrm{d}s^2 = \mathrm{d}t^2 - a^2(t)\left(\frac{\mathrm{d}r^2}{1-kr^2} + r^2\,\mathrm{d}\theta^2 + r^2sin^2\theta\,\mathrm{d}\phi^2\right) \tag{2.4}
$$

Under the assumption of a perfectly homogeneous and isotropic universe, the energy within it can be described by a perfect fluid with an energy-momentum tensor of the form:

$$
T_{\mu\nu} = (p+\rho)u_{\mu}u_{\nu} - pg_{\mu\nu} \tag{2.5}
$$

where p is the pressure and ρ is the density of the fluid and u is the four velocity.

Using the above equations (eqs. 2.1 & 2.3 & 2.5), one can relate the scale factor and its derivatives to the density and pressure of the ideal fluid, which provides two equations. The first Friedman equation is:

$$
\left(\frac{\dot{a}}{a}\right)^2 + \frac{k}{a^2} = \frac{8\pi G}{3}\rho \tag{2.6}
$$

with the Hubble parameter $H(t)$, and the second Friedman equation:

$$\frac{2\ddot{a}}{a} + \left(\frac{\dot{a}}{a}\right)^2 + \frac{k}{a^2} = -8\pi G p \tag{2.7}$$

Using the conservation equation $\nabla_\beta T^{\alpha\beta} = 0$[1] leads to the following differential equation:

$$\frac{\mathrm{d}}{\mathrm{d}t}(\rho a^3) = -p\frac{\mathrm{d}}{\mathrm{d}t}a^3 \tag{2.8}$$

with the thermodynamic equation of state $p = \omega\rho$, one finds the solution:

$$\rho = a^{-3(1+\omega)} \tag{2.9}$$

The content of the universe can be well-described by non-relativistic matter, radiation and a dark energy-like component in the form of a cosmological constant. Therefore we obtain:

$$\rho = \rho_{\mathrm{Matter}} + \rho_{\mathrm{rad.}} + \rho_\Lambda \tag{2.10}$$

For non-relativistic matter, where the velocity of the particles is small compared to the speed of light, we find that the pressure is zero and $\omega = 0$. For radiation, one finds $p = \rho/3$ and thus $\omega = 1/3$. For a cosmological constant, ρ should be constant, therefore one finds $\omega = -1$.

From the solution to eq. 2.8, we find the evolution of the different components of the energy densities of the universe with the scale factor. Therefore we can write:

$$\begin{aligned} \rho_{\mathrm{M}} &= \rho^0_{\mathrm{M}} \cdot a^{-3} \\ \rho_{\mathrm{rad.}} &= \rho^0_{\mathrm{rad.}} \cdot a^{-4} \\ \rho_\Lambda &= const. \end{aligned} \tag{2.11}$$

where the 0 index indicates its value today. Based on the critical energy density $\rho^0_{\mathrm{crit.}} = \frac{3H_0^2}{8\pi G}$, we can define the energy density fractions relative to the critical energy density for each component to $\Omega_i = \rho^0_i/\rho^0_{\mathrm{crit.}}$. Therefore eq. 2.6 reads:

$$H^2 = \left(\frac{\dot{a}}{a}\right)^2 = H_0^2\left(\Omega^0_{\mathrm{M}}a^{-3} + \Omega^0_{\mathrm{rad.}}a^{-4} + \Omega_\Lambda\right) - \frac{k}{a^2} \tag{2.12}$$

As we defined in 2.10 that the universe should be filled with these three energy densities. Finally we can define:

$$\Omega_K = \frac{-k}{a_0^2 H_0^2} \tag{2.13}$$

With this the Friedman equation takes the form:

$$H^2 = \left(\frac{\dot{a}}{a}\right)^2 = H_0^2\left(\Omega_{\mathrm{rad.}}a^{-4} + \Omega_{\mathrm{M}}a^{-3} + \Omega_{\mathrm{K}}a^{-2} + \Omega_\Lambda\right) \tag{2.14}$$

[1] In classical physics the continuity equation and energy conservation.

In the case of an additional contribution to the energy density, not defined in eq. 2.10, such as Ω_X with equation of state parameter $\omega_X = \omega_X(a)$, the above equation would take the form:

$$H^2 = \left(\frac{\dot{a}}{a}\right)^2 = H_0^2 \left(\Omega_{\text{rad.}} a^{-4} + \Omega_{\text{M}} a^{-3} + \Omega_{\text{K}} a^{-2} + \Omega_X \cdot f(a)\right) \tag{2.15}$$

where $f(a)$ includes the dependence of Ω_X on the scale factor a and is given by:

$$f(a) = \exp\left(\int_a^1 (1 + \omega_x(a'))a' \, \mathrm{d}a'\right) \tag{2.16}$$

For estimates of the necessary precision of the luminosity distance measurements we will use two different parameterizations of the dark energy: Ω_Λ =const. and Ω_X with $\omega_x = \omega_0 + \omega_a(1-a)$ so that $f(a) = \exp\left(1/2(1+\omega_0+\omega_a)(1-a^2) + 1/3\omega_a(a^3-1)\right)$. This kind of parameterization is shown in [Linder, 2003] to be well suited to differentiate between physical models for dark energy.

2.2 Observables

2.2.1 Redshift

Observations show that the light of distant objects is shifted in wavelength, and that the shift is larger for more distant sources. Using the metric equation, we can explain the observed shift in the spectra of distant sources. The following argumentation can be found e.g. in [1]: A source located at $r = 0$ emits two photons, one at $t = t_e$ and another at $t = t_e + \Delta t_e$. We use spherical coordinates and let the photon propagate along the r vector so $\mathrm{d}\theta = \mathrm{d}\phi = 0$. A photon propagates along a light-like geodesics, therefore $\mathrm{d}s^2 = 0$. Thus eq. 2.4 becomes:

$$\mathrm{d}t^2 = a^2(t)\frac{\mathrm{d}r^2}{1-kr^2} \tag{2.17}$$

An observer at $r = r_1$ detects the first photon at $t = t_0$ and the second at $t = t_0 + \Delta t_0$. We can now integrate eq. 2.17 over the path from the emission to the observation:

$$\int_{t_e}^{t_0} \frac{\mathrm{d}t}{a(t)} = \int_0^{r_1} \frac{\mathrm{d}r}{\sqrt{1-kr^2}} = r_{\text{CM}} = \int_{t_e+\Delta t_e}^{t_0+\Delta t_0} \frac{\mathrm{d}t}{a(t)} \tag{2.18}$$

We note r_{CM} is time-independent, as it does not change while the universe is expanding, and define this as the "co-moving distance" between emitter and observer.

The integral on the right side can be rewritten:

$$\int_{t_e+\Delta t_e}^{t_0+\Delta t_0} = \int_{t_e}^{t_0} + \int_{t_0}^{t_0+\Delta t_0} - \int_{t_e}^{t_e+\Delta t_e} \tag{2.19}$$

[1] http://icc.dur.ac.uk/~tt/Lectures/UA/L4/cosmology.pdf, last checked 19.02.2018

Combining eq. 2.18 and eq. 2.19 one obtains:

$$\int_{t_0}^{t_0+\Delta t_0} \frac{\mathrm{d}t}{a(t)} = \int_{t_e}^{t_e+\Delta t_e} \frac{\mathrm{d}t}{a(t)} \tag{2.20}$$

The time interval between the emission of the first and second photon is small therefore the change of $a(t)$ is negligible.

$$\frac{\Delta t_0}{a_0} = \frac{\Delta t_e}{a_e} \tag{2.21}$$

Setting Δt_0 as the period of the photon yields $\lambda_0 = c \cdot \Delta t_0$ and $\lambda_e = c \cdot \Delta t_e$. Using the definition of the observed redshift:

$$z \equiv \frac{\lambda_0 - \lambda_e}{\lambda_e} = \frac{\Delta t_0 - \Delta t_e}{\Delta t_e} = \frac{a_0}{a_e} - 1 \tag{2.22}$$

The observed redshift is therefore a measure of the change of the scale factor between emission and observation.

2.2.2 Luminosity Distances

We want to perform a distance measurement in the universe. We know that we can obtain the distance to a source of known luminosity by measuring the flux reaching us - such sources are called "Standard Candles". In euclidean space, we find that the flux is decreasing as a function of $(1/\text{distance})^2$. In cosmology, space-time is expanding, therefore we have to take into account several processes.

The following calculation can be found in e.g. [Bergström and Goobar, 2006]. Imagine a source emits N_γ photons isotropically at $t = t_e$ and a co-moving distance[1] r_{CM} from us.

If the Universe were static, we would observe $N_0 = N_\gamma \cdot A / \left(4\pi \left[a(t_e) r_{\mathrm{CM}}\right]^2\right)$ photons at a telescope with collecting area A at $t = t_0$. As the universe is expanding the area of the sphere instead increased to $4\pi \left[a(t_0) r_{\mathrm{CM}}\right]^2$.

There are two additional effects that need to be accounted for. We measure a flux (which is the power per unit area entering the telescope). However, power will decrease as the propagating photons are redshifted to longer wavelengths, as the energy of a photon is $E_\gamma = hc/\lambda$. Additionally the time interval of the arrival of the photons is increased due to the redshift, by a factor $(1 + z)$. The flux will therefore be reduced by $(1 + z)^2$:

$$F = \frac{L}{4\pi a^2(t_0) r_{\mathrm{CM}}^2 (1+z)^2} \equiv \frac{L}{4\pi d_L^2} \tag{2.23}$$

with the Luminosity (total emitted power) L, and the luminosity distance d_L defined as :

$$d_L \equiv \sqrt{\frac{L}{4\pi F}} = a(t_0) r_{\mathrm{CM}} (1+z) \tag{2.24}$$

[1] The co-moving distance r_{CM} is the distance between objects independent of the scale factor of the universe. The proper distance r, changing with the scale factor is therefore $r = a(t) \cdot r_{\mathrm{CM}}$.

We can now relate the luminosity distance d_L with the energy densities in the universe. For light propagating along a light-like geodesic ($\mathrm{d}s^2 = 0$) eq. 2.4 takes the following form:

$$\mathrm{d}t^2 = a^2(t)\frac{\mathrm{d}r^2}{1-kr^2} \tag{2.25}$$

Multiplying both sides by $a(t_0)$, using $(1+z) = a(t_0)/a(t_e)$ and taking the square root:

$$\frac{a(t_0)}{\sqrt{1-kr^2}}\,\mathrm{d}r = (1+z)\,\mathrm{d}t \tag{2.26}$$

Using:

$$H = \frac{\dot{a}}{a} = \frac{\mathrm{d}}{\mathrm{d}t}\ln\left(\frac{a(t)}{a(t_0)}\right) = \frac{\mathrm{d}}{\mathrm{d}t}\ln\frac{1}{1+z} = -(1+z)^{-1}\frac{\mathrm{d}z}{\mathrm{d}t} \tag{2.27}$$

Incorporating this result into eq. 2.26:

$$\frac{a(t_0)}{\sqrt{1-kr^2}}\,\mathrm{d}r = -H^{-1}\,\mathrm{d}z \tag{2.28}$$

We now integrate from the observer to the source. The source is placed at $r = r_1$, and the redshift of the light there is equal to zero. The detector is placed at $r = 0$, and the light is then shifted to $z = z_1$. Therefore we obtain:

$$\int_0^{r_1}\frac{a(t_0)}{\sqrt{1-kr^2}}\,\mathrm{d}r = \int_{z_1}^{0} -H^{-1}\,\mathrm{d}z \tag{2.29}$$

After exchanging the integration limits, and neglecting $\Omega_{\mathrm{rad.}}$, which is small compared to Ω_{M} and Ω_Λ, we obtain:

$$\int_0^{z_1}\frac{\mathrm{d}z}{H_0[\Omega_{\mathrm{M}}(1+z)^3+\Omega_K(1+z)^2+\Omega_\Lambda]^{1/2}} = a(t_0)\begin{cases}\arcsin(r_1\sqrt{k}), & \text{for } k>0\\ r_1, & \text{for } k=0\\ \operatorname{arcsinh}(r_1\sqrt{-k}), & \text{for } k<0\end{cases} \tag{2.30}$$

Using the observations of the Cosmic Microwave Background by the Planck satellite one finds that $\Omega_K = 0 \pm 0.005$ ([Ade et al., 2016] p. 39) which implies that the universe is spatially flat on large scales, $k = 0$. Eq. 2.30 simplifies to:

$$r_1 = \int_0^{z_1}\frac{\mathrm{d}z}{H_0[\Omega_{\mathrm{M}}(1+z)^3+\Omega_K(1+z)^2+\Omega_\Lambda]^{1/2}} \tag{2.31}$$

Inserting c again, and defining $a(t_0) = 1$, one finds:

$$d_L = \frac{c(1+z)}{H_0}\int_0^{z_1}\frac{\mathrm{d}z}{[\Omega_{\mathrm{M}}(1+z)^3+\Omega_\Lambda]^{1/2}} \tag{2.32}$$

Measuring the luminosity distance to multiple sources at different redshifts therefore allows us

to constrain the energy composition of the universe.

Standard Candle
An ideal standardized candle has perfectly-known luminosity, the temporal evolution of the luminosity is also perfectly-known, so its luminosity distance can be measured. Supernovae type Ia (SNeIa) can be approximated as standard candles, see. A.1. Deviations from this idealization will not be discussed further, but can be found e.g. in [Goobar and Leibundgut, 2011].

2.3 Motivation for Precision Calibration

In the previous section we derived the dependence of the luminosity distance on the cosmological model. This section will motivate, the need for a sub-percent measurement uncertainty in order to improve constraints on Dark Energy. We therefore estimate the maximal uncertainty allowed in the observables, by varying the composition of the universe around a best-fit model.

The observable astronomical quantity is the distance modulus, which is defined in the following way:

$$m_{\mathrm{dm.}} = m_{\mathrm{app.}} - M = 5\log\left(d_L\right) + 25 \tag{2.33}$$

with the apparent magnitude of the source $m_{\mathrm{app.}}$, the absolute magnitude[1] of the used standard candle M, and the luminosity distance d_L. As astronomers measure magnitudes rather than brightness, one can convert a change in distance modulus to a flux ratio by using the magnitude definition, for more details see chapter 3. For two different objects one finds:

$$m_1 - m_2 = -2.5\log\left(\frac{F_1}{F_2}\right) \tag{2.34}$$

with the observed magnitudes $m_1 \,\&\, m_2$ and the the corresponding fluxes $F_1 \,\&\, F_2$. Therefore, we can convert a change in the distance modulus to a change of flux via:

$$\frac{F_1}{F_2} = 10^{-\Delta m_{\mathrm{dm.}}/2.5} \tag{2.35}$$

In case of a small $\Delta m_{\mathrm{dm.}}$, we can perform a Taylor expansion to first order and obtain:

$$\frac{F_1}{F_2} = 1 - \frac{\ln(10)}{2.5}\Delta m_{\mathrm{dm.}} = 1 - 0.921\Delta m_{\mathrm{dm.}} \tag{2.36}$$

where this Taylor expansion is precise to 0.4 % for $|\Delta m_{\mathrm{dm.}}| < 0.1$. An uncertainty in magnitude of 10 mmag thus corresponds to a flux uncertainty of 1 %. One can now constrain the precision of the flux calibration which is needed to constrain the energy composition of the universe.

Fig. 2.1 plots the measured distance modulus of SNIa combined in the Joint Lightcurve Analysis (JLA) ([Betoule et al., 2014]) dataset against the measured redshift, the so-called

[1] The absolute Magnitude is the apparent magnitude of the object, if the object is seen in a distance of 10 pc ≈ 32.6 ly

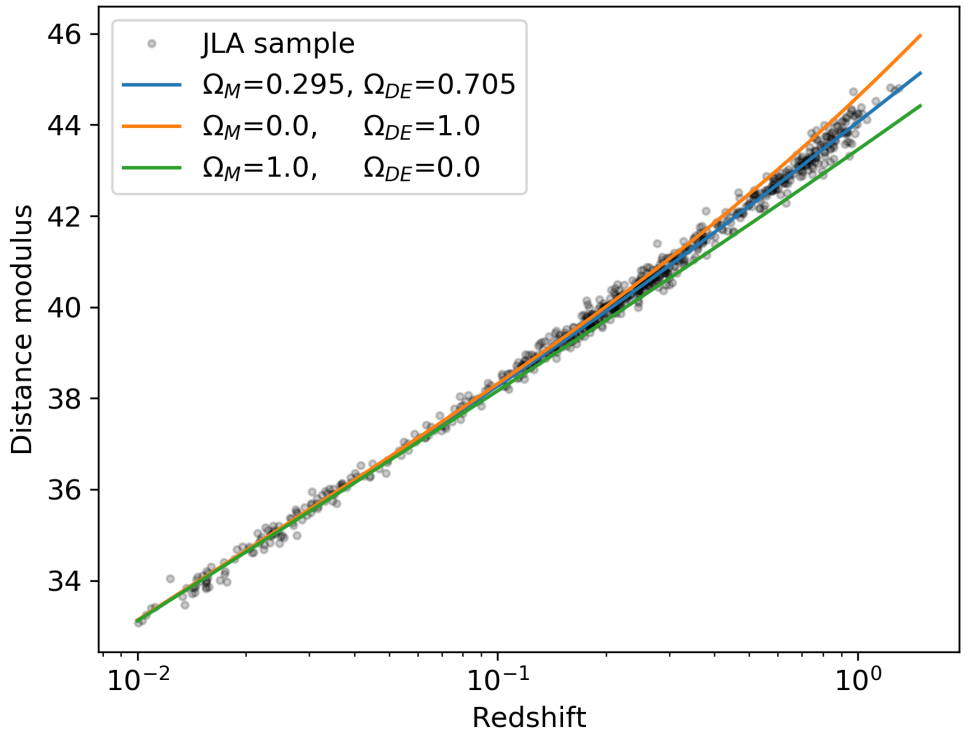

Figure 2.1: The distance moduli are plotted for various SNIa at different redshift (Hubble Diagram), based on the JLA dataset. The solid lines show the distance modulus based on the luminosity distance and three different cosmological models. The best-fit cosmology, as obtained from the JLA dataset, is shown in blue. Two extreme cases are also shown, one without dark energy in green and one with only dark energy in orange.

"Hubble Relation". The theoretical Hubble relations based on different energy compositions of the Universe are shown. The two extreme cases shown are, no DE ($\Omega_m = 1.0$ & $\Omega_{\mathrm{DE}} = 0.0$) and only DE ($\Omega_m = 0.0$ & $\Omega_{\mathrm{DE}} = 1.0$). The third model is $\Omega_m = 0.295$ & $\Omega_{\mathrm{DE}} = 0.705$ the best fit cosmology based on the JLA sample ([Betoule et al., 2014],Tab. 10). For all calculations we assume a flat universe, therefore $\Omega_m + \Omega_{\mathrm{DE}} = 1.0$.

The upper panel of the fig. 2.2 describes DE as a cosmological constant. Varying the amount of DE in the uncertainty range quoted in [Betoule et al., 2014] (tab. 10.) $\Omega_m = 0.295 \pm 0.034$ would result in the blue band around zero, shown in fig. 2.2 upper panel. The width of the band is $\approx 4\,\%$ at $z = 1$. In a universe with less DE the distance modulus would decrease, therefore the supernovae would be brighter, as their flux on Earth is increased.

The middle and lower panels show effects from a possible change of ω with scale factor, as $\omega(a) = \omega_0 + \omega_a(1-a)$. The middle panel shows the resulting flux change based on the uncertainty on $\omega_0 = -0.957 \pm 0.124$ ([Betoule et al., 2014] tab. 15) and a fixed $\omega_a = 0$. The lower panel illustrates the influence on the flux, based on the uncertainties on $\omega_a = -0.336 \pm 0.552$ ([Betoule et al., 2014] tab. 15) and a fixed $\omega_0 = -0.957$.

These panels can be interpreted as showing that a $\approx 4\,\%$ accuracy at $z \approx 1$ would be sufficient to improve on current constrains. However the difference in shape introduced by changing ω_0 can be partially covered by changing ω_a, as these two quantities are correlated. This effect is shown in fig. 2.3. Here we fix two redshifts, typical for intermediate- and high-redshifts, and show how lines of constant luminosity distance are oriented. The band is obtained by requiring the flux uncertainties to be $\leq 2\,\%$. To improve the constraints we need to reduce the overlap of the bands, where the width of them is determined by the flux uncertainty. To increase the constraints on ω_0, ω_a a sub-percent flux calibration would be required.

The redshifts used here have been chosen to contain only distant supernovae, as the supernovae with lower redshifts will be used for the absolute scaling of the Hubble relation (H_0). At even higher redshifts the statistics would be reduced, so here we use two bins centered at 0.4 and 0.7 in redshift.

To obtain the above constraints, one compares supernovae at different distances from us. As the universe is expanding, this means one compares objects at different redshifts. Fig. 2.4 illustrates the issue. The spectrum of SNIa 2011fe, which exploded at a redshift of 0.0008, is shown in blue. In orange and green, the same spectrum is shown, but it is shifted in wavelength as result of redshift and scaled in flux as result of the different luminosity distance.

Ideally one would obtain spectra of all supernovae used for the measurements, however obtaining a spectrum is time-consuming and difficult for distant objects, as the low flux is spread in wavelength.

Therefore measurements in filter bands are preferred, where flux is integrated across a wavelength band. An example filter band is shown by the blue shaded region in fig. 2.4, it indicates the transmission range of the Johnson blue band filter ([Bessell, 1990]). Comparing the flux of a supernova at $z = 0.008$ with one at $z = 0.3$ requires calibration between the instrumental sensitivity at different wavelength, as indicated by the blue and green band in fig. 2.4. As it is the relative brightness of standard candles at different redshifts that constrains cosmological parameters, a sub-percent relative flux calibration in the instrumental sensitivity across wavelengths is needed

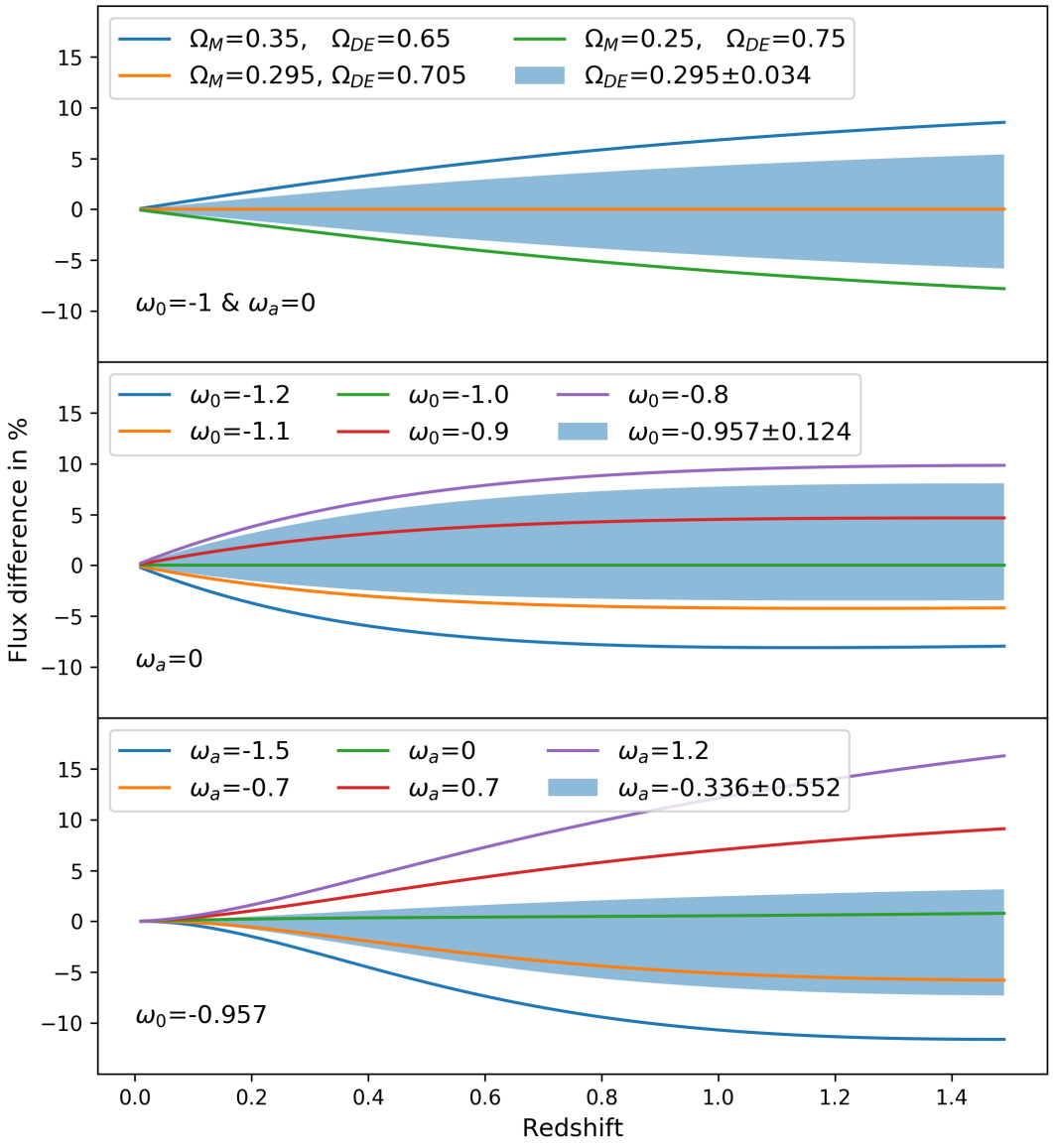

Figure 2.2: The change of the measured flux of a supernova at redshift z in an alternative cosmology is shown relative to the best-fit cosmology. The blue band in each panel shows the uncertainty on the best fit cosmology. In the upper panel the contribution of Dark Energy is varied. In the middle panel, the equation of state parameter is varied around the best fit value. The lower panel shows the effect of an equation of state parameter changing with scale factor like: $\omega(a) = \omega_0 + \omega_a(1-a)$, where we change the amplitude of ω_a.

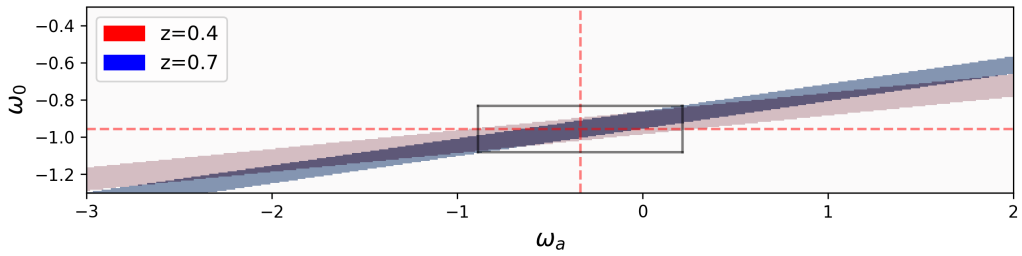

Figure 2.3: For two fixed redshift (0.4, 0.7) we calculate the distance modulus in the ω_0 - ω_a plane, based on the cosmological models. The two bands are obtained by requesting the value of the distance modulus to be within $\pm$**2 %** of the JLA best fit cosmology ([Betoule et al., 2014] tab. 14.). The best fit parameter range for ω_0 & ω_a according to ([Betoule et al., 2014]) is shown by the gray box. The uncertainty on the parameters ω_0 & ω_a is represented by the overlap of the two bands. To improve the uncertainty on ω_0 & ω_a one would need to reduce the width of the bands, this requires a sub-percent flux uncertainty.

Additionally these sources span a wide range of fluxes. It is therefore necessary to observe them with different telescopes / instruments of different sensitivities. The JLA sample above combines data from the Sloan Digital Sky Survey (SDSS 2.5 m), the SuperNova Legacy Survey (SNLS 3.6 m) and Hubble Space Telescope (HST 2.4 m). The higher sensitivity of Hubble relative to SNLS is due to longer exposure times and the lack of an atmosphere disturbing the measurement. The SDSS data samples a redshift range up to 0.4, while the SNLS data samples the range $0.3 < z < 1.0$ and the HST data $0.8 < z < 1.3$.

As the time evolution of the Dark Energy is correlated with the amount of Dark Energy, it is necessary to know the wavelength dependent sensitivity at the sub-percent scale, for each contributing instrument.

With SCALA we can calibrate the University of Hawaii 2.2 m telescope and SNIFS. With the calibrated instrument we can observe standard stars and can then transfer our flux calibration based on a laboratory standard to these objects. These stars will then be available to other observers / instruments for their calibration. In this thesis we show that the wavelength dependence of a calibration with SCALA agrees to the existing CALSPEC system within our uncertainties (1.5 %) in the wavelength range 4500 Å to 9000 Å. This immediately means that the wavelength dependence of the flux calibration of the standard stars agrees to the laboratory system within 1.5 %.

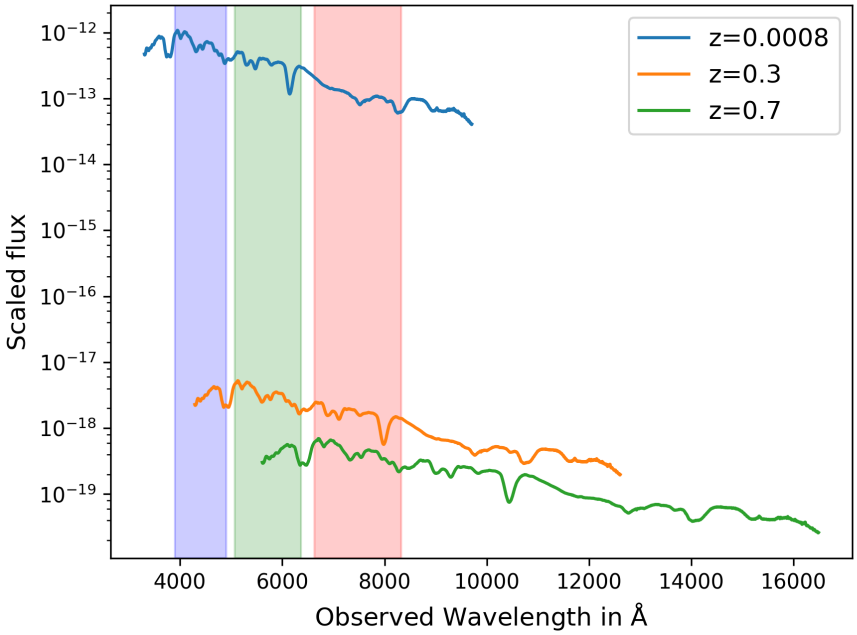

Figure 2.4: Spectrum of SN2011fe as it was observed at redshift 0.0008 (from [Pereira et al., 2013]), and scaled to the expected values using a flat universe with $\Omega_m = 0.295$ & $\Omega_{\mathrm{DE}} = 0.705$ and redshifts of $z = 0.3$ and $z = 0.7$. The region of sensitivity of the Johnson blue filter is shown in blue. The regions in green and red indicate the wavelength region, in which measurements would need to be obtained to compare same regions in the emission spectra.

Chapter 3

Photometry: System, Units, History, Standards

Photometry measures object brightness on the sky and historically the human eye was used as detector.

Pogson Magnitude System
The mathematical definition [Pogson, 1856] of the visible magnitude m_1 of an object with flux f_1, relative to an other object with magnitude m_2 and flux f_2 is:

$$m_1 - m_2 = -2.5 \log \left(\frac{f_1}{f_2} \right) \tag{3.1}$$

Magnitudes correlate with the impression of brightness in the human eye, which responds to flux logarithmically. Early catalogs assign a magnitude of 1 to the brightest objects and a magnitude of 6 to the dimmest visible objects (Ptolemey's Almagenst). A star with brightness m_1 and physical flux f_1 will have a smaller magnitude than a dimmer star of magnitude m_2 and flux f_2 (magnitudes and flux ratios are anti-correlated).

The proportionality constant was set to 2.5 by Norman Pogson in 1856 [Pogson, 1856]. In this way a magnitude difference of 5 corresponds to a flux ratio of 100. This selection is arbitrary but convenient, for more detail see sec. B.1.

As the above relation is based on flux ratios, we need a reference object or a set of objects to normalize the system and assign magnitudes to objects. In the history of astronomy these reference objects have changed, but the systems were designed in such a way that the magnitude of known objects do not or only minimally change. A summary of historic reference systems can be found in sec. B.2.

Photoelectric Magnitudes
Modern photometry relies on measurements of the stellar brightness using PhotoMultiplier Tubes (PMTs). As these do not provide spacial resolution, aperture stops in the field of view of the telescope are used to select single stars. These are then observed through broadband color filters. For more details see B.2.

In the following I will show that broadband photometric systems require spectral information of the sources, which can not be obtained from the broadband measurements themselves. Therefore we start from the observed PMT current, I, which can be written as:

$$I = e \int_{\lambda_0}^{\lambda_1} f_\gamma(\lambda)\, \tau_{\text{atm.}}(\lambda)\, \tau_{\text{tel.}}(\lambda)\, \tau_{\text{fil.}}(\lambda)\, S_{\text{det.}}(\lambda)\, \mathrm{d}\lambda \tag{3.2}$$

where e is the electron charge, f_γ is the photon number entering the atmosphere and collected by the telescope per unit time, and S_{det} denotes the number of electrons produced per incident photon. The different τ denotes throughputs of the atmosphere, telescope and filters. All quantities are wavelength-dependent.

If the observations are performed with a different setup, the different τ_i and S_{det} will change. These changes can be illustrated with the following example.

The incoming photon number flux is $n_\gamma = m_1(\lambda - \lambda_0) + k$, (number of photons per time within a wavelength band $\Delta\lambda$, centered at a wavelength λ). The throughput of atmosphere and telescope is assumed to be constant 100 % ($\tau_{\text{atm.}}(\lambda) = \tau_{\text{tel.}}(\lambda) = 1$) and the detector is assumed to be perfectly detecting all photons ($S_{\text{det.}} = 1$). The filter is transmitting in the range $\lambda_0 \pm \Delta$, but has a slope, so that its throughput can be written as:

$$\tau_{\text{fil.}} = \begin{cases} m_2(\lambda - \lambda_0) + c & \text{for } \mid \lambda - \lambda_0 \mid < \Delta \\ 0 & \text{else} \end{cases} \tag{3.3}$$

The current produced is therefore:

$$I = \int_{\lambda_0 - \Delta}^{\lambda_0 + \Delta} n_\gamma \cdot \tau_{\text{fil.}}\, \mathrm{d}\lambda = \frac{2}{3} m_1 m_2 \Delta^3 + 2kc\Delta \tag{3.4}$$

As we see here, the observed current depends on both the instrument throughput (product of τ_i and S_{det}) and the shape of the spectrum of the object being observed, rather than just the mean throughput c. The above calculation begins with a known spectrum, and parameterizes it to be changing linearly in wavelength. However, the measured PMT current is the integrated number of electrons produced in the PMT, therefore the spectrum of the source is not known. But this additional information would be needed to construct a measurement system in which fluxes measured at different instruments can be accurately compared. This effect was noted by Arlo Landolt in [Landolt, 1983], when he compared measurements taken with two different PMTs and needed more then a scaling for different mean throughputs.

Of course astronomical objects generally have a far more complex shape than a linear spectrum e.g. see fig. C.2.

From these considerations, we see that every measurement setup defines its own photometric system. Every comparison to measurements obtained with other instruments requires a transformation.

All later photometric systems are therefore based on precisely-measured spectra, to enable the calculation of these transformations. The calibration of a broadband detector is achieved starting from the known source spectrum, assuming the sensitivity of the device to also be

known. The product of spectra and sensitivity is integrated in wavelength to infer the detected number of photons. Starting with spectra and integrating them for filter curves and sensitivities is called spectrophotometry, i.e. photometry obtained from calibrated spectra.

The CALSPEC System

The Hubble Space Telescope (HST) was calibrated based on spectrophotometry obtained by John B. Oke in 1990 [Oke, 1990]. Between 1970 and 1985 several groups ([Oke and Schild, 1970], [Hayes, 1970] and others) observed Vega in comparison to a laboratory standard. An overview can be found in [Hayes, 1985]) In this case the reference was a gold point blackbody light source mounted several hundred meters from the telescope. Gold was used to stabilize the temperature of the blackbody around it's melting point. After correcting for the different atmosphere (see a discussion of the results in [Hayes and Latham, 1975]) between star and telescope and standard and telescope, they provided flux-calibrated spectra for Vega. As the two measurements [Oke and Schild, 1970] and [Hayes, 1970] showed tension, they measured their standards relative to each other (see [Hayes et al., 1970]). A critical summary of the measurements was performed by [Mégessier, 1995] and he provides a flux of 3.4610^{-11}W m^{-2}nm^{-1}, with 0.7 % uncertainty for a wavelength of 5556 Å. John B. Oke and James E. Gunn used their calibrated spectra of Vega to calibrate further objects such as the cool subdwarfs HD 19445, HD 84937, BD +26°2606 and BD +17°4708 [Oke and Gunn, 1983]. These were then used as references to spectrophotometrically calibrate 25 further stars [Oke, 1990], which then were used to calibrate the HST. In 1990, the ground-based photometric measurements by Arlo Landolt still had smaller uncertainties than the spectrophotometry described above ([Colina and Bohlin, 1994], p. 1). Combining the Landolt photometry with the Oke spectra for the white dwarf G191B2B, Colina and Bohlin [Colina and Bohlin, 1994] found, that the calibrated spectra agree within 0.3-0.7 % with the modeled spectrum of this object ([Finley et al., 1990], [Rauch et al., 2013]). The comparison of the modeled spectra with the original spectrophotometric spectrum agrees to just 1 % ([Colina and Bohlin, 1994], sec. 5.1).

Therefore the modeled spectra of white dwarfs were used in [Bohlin, 2000] as the basis for calibrations of HST. Following the above description, the presently used flux scale depends on the model of white dwarfs and indirectly on a long series of calibrations. The absolute flux scale is not based on the model, but defined relative to measurements of Vega [Mégessier, 1995]. Landolt did not observe Vega, but he provided a transformation from the Johnson system to his system [Landolt, 1983]. The Vega magnitude observed by Johnson and Morgan [Johnson and Morgan, 1953] can therefore be transformed to the Landolt System being 0.029 mag in V band and the (B-V)=0.000 color. Using eq. B.1, one can obtain the flux ratio of Vega to the individual white dwarfs using the magnitude difference, and thus normalize the modeled spectra of the white dwarfs relative to Vega.

To remove the uncertainties in the absolute flux scale, introduced by the transformation of the magnitude of Vega from one system to the other, Bohlin observed Vega directly with the HST (for more details see [Bohlin and Gilliland, 2004]). This observation now provides the base scaling between Vega and the white dwarfs.

Based on the modeled spectra of the white dwarfs GD71, GD153, and G191B2B, the CALSPEC system is defined. Using the HST, further stars (so far ≈100) have been calibrated

relative to this system http://www.stsci.edu/hst/observatory/crds/calspec.html, checked on 14.09.2017.

Modern Laboratory Flux Standards

In the SCALA project we want to relate the flux of stars, which are calibrated relative to the CALSPEC System to a laboratory standard which can be tested.

Today's laboratory standard for light measurements is no longer a light source but a detector. This detector is a light trap operated at cryogenic temperatures ([Larason and Houston, 2008]). The trap absorbs all incident light and converts it into heat, which can then be measured as a temperature increase of the trap. The light source, a stabilized wavelength tunable laser [Brown et al., 2006][Brown et al., 2004], is blocked and afterwards the trap is electrically heated to the same temperature. In this way the optical power can be related to the electrical power which is needed to produce the same temperature increase (0.01-0.02 % uncertainty [Larason and Houston, 2008]). Standards like this have been developed by several countries, however our photodiode is calibrated relative to the primary standard at the National Institute for Standards and Technologies (NIST, USA). Now that the power of the stabilized laser source is known, it illuminates further detectors to transfer the calibration. In several steps the calibration is transfered to lower optical power and applied to a so-called Transfer Standard (TS). This is a light trap made from photodiodes, without entrance windows (see. fig. 5.5 p. 33 [Larason and Houston, 2008]). The TS are calibrated by the laser light source and then inserted into a setup with a monochromator (MC) light source. The monochromator light source is then used to transfer the calibration from the TS to the Working Standard (WS).

Why is this done? "The working standards are calibrated on a 12 to 18 month schedule" see. sec. 7.2.4 Long-term stability p. 56 [Larason and Houston, 2008]. Therefore the WS needs to be stable on scale of years, requiring the photodiode being protected by a window. The laser calibration requires a photodiode without window, because of the coherence of the source and issues caused by interference. The TS can therefore not be protected by a window and is thus not stable on year scales. It is thus used to calibrate the WS. Afterwards the TS can be replaced by the customer photodiode and the calibration can be transfered from the WS to it.

Fig. 3.1 shows a reproduction of the uncertainties plot in [Larason and Houston, 2008]. It can be seen that the final uncertainty on the photodiode which can be purchased is limited by systematic uncertainties in their setup.

This laboratory standard can be tested against other standards like the spectral emission from a blackbody of known temperature or synchrotron radiation of electrons of known kinetic energy orbiting in a known magnetic field, see e.g. [Fox et al., 1986]. They find an agreement to better then 0.1 %.

There are several proposals to use such a customer photodiode as flux reference for telescopes and their instruments. Justin Albert proposed building a light source which could be monitored by a photodiode, and placing this light source into an earth orbit [Albert, 2011]. The advantage of such a source would be that different observatories could observe it, and thus calibrate relative to the same system. Mary E. Kaiser proposed a sub-orbital mission using a calibrated telescope and spectrograph to recalibrate standard stars above the earth atmosphere [Kaiser et al., 2010]. The telescope is equipped with an internal calibration system so that changes

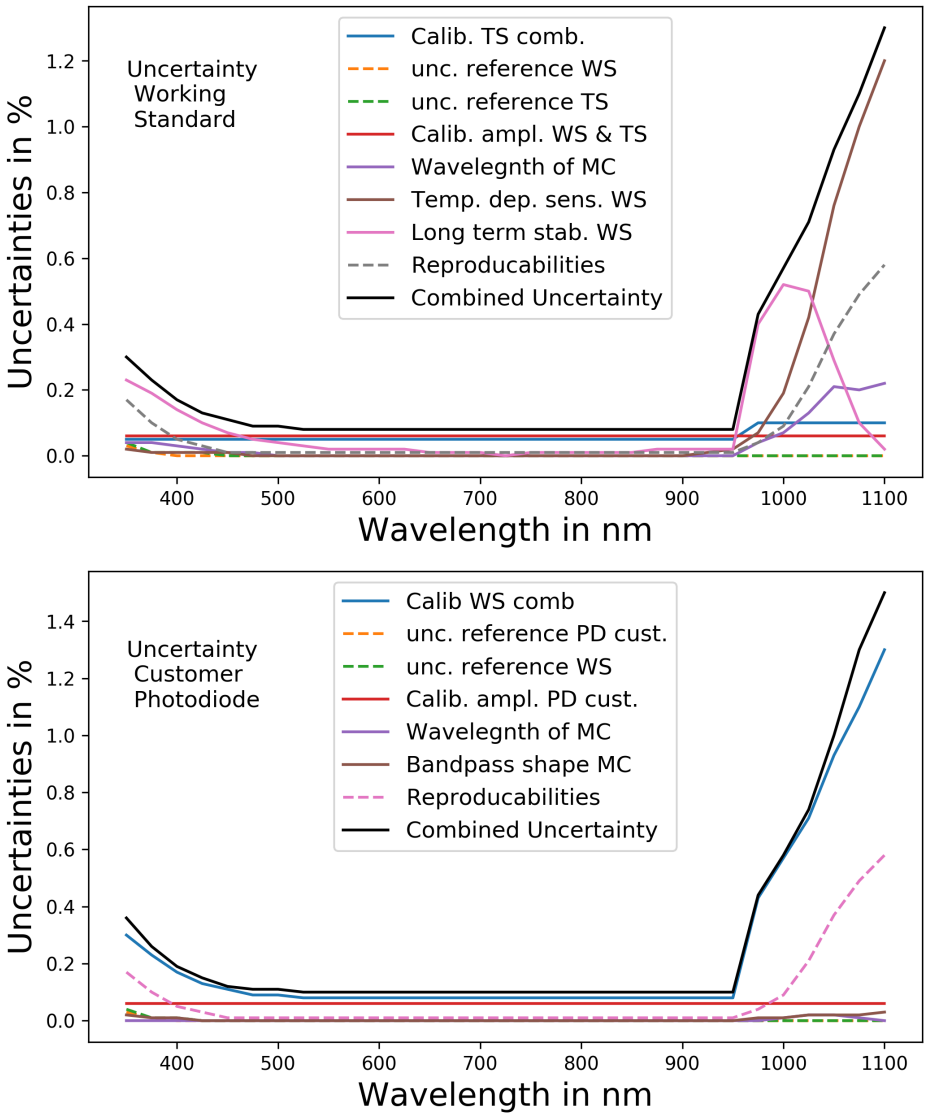

Figure 3.1: A reproduction of the uncertainty figures from [Larason and Houston, 2008]. Solid lines show systematic uncertainties, while dashed lines indicate statistical uncertainties. The upper figure shows the uncertainties incorporated in the calibration of the working standard. The main contributions are from the calibration of the amplifier (red), the long-term stability of the working standard (purple), the calibration of the transfer standard (blue) and the temperature dependence of the sensitivity of the working standard for infrared wavelength (brown).
The lower figure shows the additional contributions in the transfer to the customer photodiode. This calibration transfer is essentially limited by the calibration of the Working standard (blue) and the calibration of the amplifier (red).

during the flight can be monitored. Christoffer Stubbs and John Tonry proposed splitting of the issue in two parts, one device which calibrates the instrument and modeling the throughput of the atmosphere [Stubbs and Tonry, 2006]. With SCALA we followed their suggestion, but we used a monochromator light source setup and collimated the light prior to illuminating the telescope + instrument. A description how to measure the atmospheric transmission can be found in C.2.2

The standard for our setup is the so-called "Cooled Large Area Photodiode" (CLAP). This device was build by the Paris Supernova Cosmology Group for the SNDICE project [Juramy et al., 2008]. They have purchased a customer photodiode from NIST, and calibrated the CLAP relative to this photodiode. The uncertainty introduced by their transfer of calibration is quoted to be 0.15 % in the range 3500 Å to 9500 Å. The final uncertainties of the CLAP device are presented in chapter 5.

Chapter 4

SNIFS CALibration Apparatus: SCALA

Christoffer Stubbs and John Tonry [Stubbs and Tonry, 2006] concluded in their paper that the calibration of an astronomical device should be split in two segments, the instrumental and the atmospheric part. They suggest to model the atmospheric transmission via the components affecting the throughput (Rayleigh-, aerosol- and molecule scattering) and using the airmass[1] dependence to measure the amplitude of the effects (for more detail see. C.2).

For the instrumental part they propose to use a broadband detector as flux reference. They recommend a NIST-calibrated photodiode, for which the wavelength dependence of the sensitivity is known. This calibration should then be transfered via a monochromatic light source, tunable in wavelength, from the photodiode to the instrument. They propose to use an optical parametric oscillator (OPO) as light source. To illuminate the telescope, they suggested a screen with a diffuse surface which is illuminated through an optical fiber.

SCALA partly follows their ideas, but differs in the light source and illumination properties. We use a monochromator as wavelength-tunable bandpass filter, to select monochromatic light from a continuous lamp spectrum. This setup is less complicate and more robust than the (OPO), which requires a laser light source. It can therefore be mounted to the dome and move with the setup[2]. To reduce stray light, as the screen would illuminate a 2π solid angle, we use mirrors to collimate the light provided from a homogeneously illuminated surface. To produce such a surface we use integrating spheres. A concept similar to SCALA was presented by Amali L. Vaz in his bachelor thesis [Vaz, 2011].

All these components will be explained in the following. But as SCALA is built to calibrate the SuperNova Integral Field Spectrograph SNIFS, I will first explain its working principles and the requirements resulting thereof.

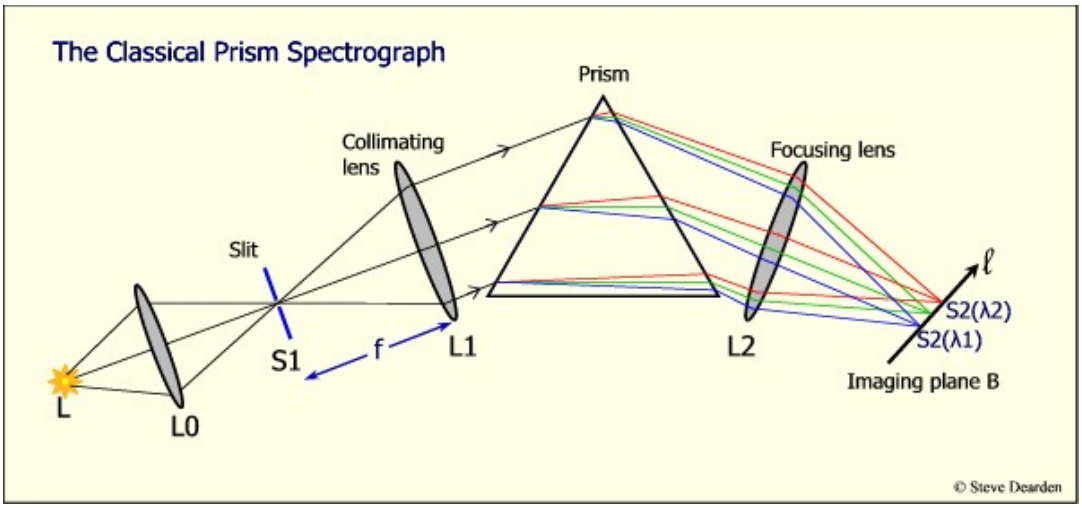

Figure 4.1: Schematic sketch of the working principle of a spectrograph. The light from a star (L) is collected by a telescope (L0). The telescope forms an image of the source on the entrance slit (S1). The collimator represented here by lens (L1) creates parallel light bundles, for each point in the slit, which then pass through the dispersing element, here a prism, which splits the incoming parallel rays for their wavelength. Lens (L2) represents the objective, which creates images of the slit on the image plane. Due to the splitting of the rays by the prism, the images are shifted relative to each other. Therefore we see in the image plain a spectrum of the light source illuminating the entrance slit. http://www.physast.uga.edu/~jss/oldcourses/3010/Kaler/k1/classicprismspec.jpg, last checked 03.01.2018

4.1 Spectrograph

To analyze the SED of astronomical objects in detail, spectrographs are used. A simple spectrograph consists of an entrance slit, a collimator, a dispersing element, an objective and a detector with spatial resolution (see fig. 4.1). The astronomical source is imaged onto the entrance slit using the telescope (L0). The entrance slit selects a region in the image plane of L0. The light beam passing through the slit is collimated by the collimator (L1), an inverse telescope, providing a parallel beam for each point in the entrance slit. Afterwards the light passes through the dispersing element (here a prism). The dispersing element will split a white light ray into a bundle of rays with different wavelengths. The angle between incident ray and outgoing ray becomes wavelength dependent, and the objective (focusing lens L2) can be used to separate the different wavelength in the "Imaging plane B". This intensity distribution can then be record by a detector with spatial resolution, like a photographic plate or CCD.

Let us assume that the entrance slit is illuminated with light of wavelength λ_0. The collimator (L1) and the objective (L2) will project the illumination of the slit on the detector creating an image of the slit. If the wavelength of illumination is changed, the image of the slit on the detector will move relative to the initial image due to the dispersing element. The spectrum on the detector can therefore be understood as the superposition of monochromatic slit images, which are shifted relative to each other due to their different wavelength.

The resolution is increased if the slit width is reduced, but will always be limited by the resolving power of the dispersing element.

A spectrograph, as described above, will produce a spectrum for all points along the length of the slit. Therefore it will provide spectral information for all objects on a line (a 1D slice of sky).

4.2 SNIFS

SCALA was primarily built to calibrate the SuperNova Integral Field Spectrograph (SNIFS), used by the Nearby Supernova Factory. SNIFS is mounted to the bent Cassegrain port of the University of Hawaii 2.2 m telescope (UH88) and consists of an imaging channel and two spectroscopic channels. In usual operation, all three of its channels are used in parallel.

Imaging Channel

The imaging channel is meant for broadband photometry, has a Field-of-View (FoV) of 9' x 9', and can be equipped with various filters via a filter wheel. These filters are:

- SDSS-like filters: u, g, r, i, z [Pereira, 2008]
- A Blue filter with a pinhole grid
- Multi-Filter Array (MFA)

The MFA is created by mounting several filters of different passbands next to each other, so that simultaneous observations in different bands and positions on the sky are possible. An image

[1] Optical path length through atmosphere relative to zenith optical path length, see sec. A.3.

[2] The OPO used by Stubbs and Tonry is mounted to the basement and connected to the setup by a long optical fiber.

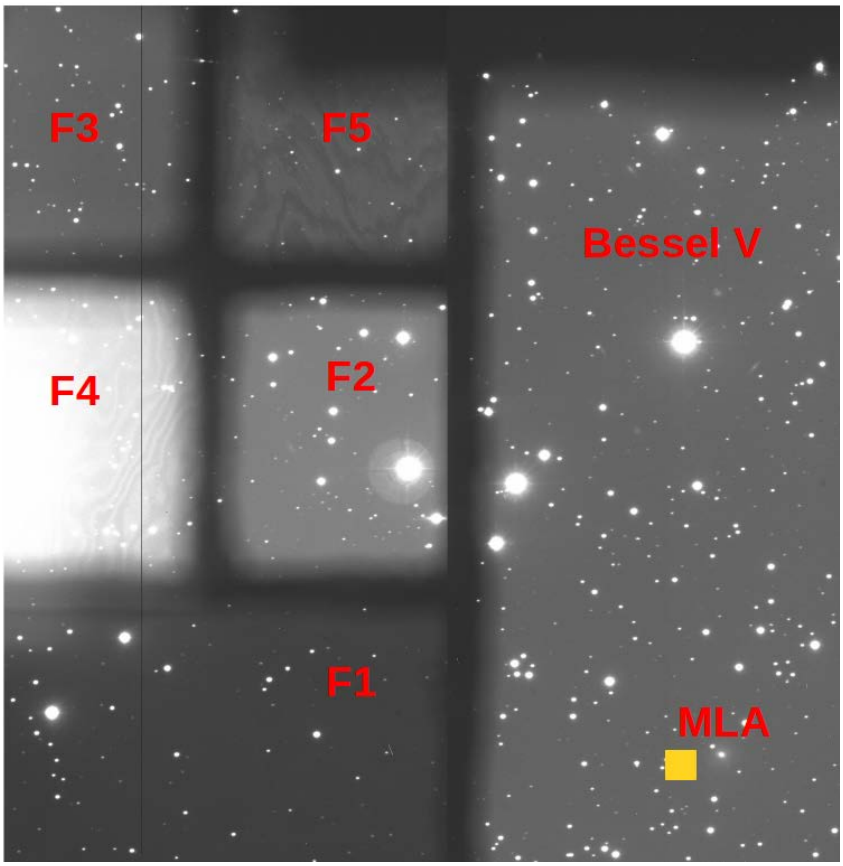

Figure 4.2: Observation with the imaging channel of SNIFS. The multi filter array was selected, and the six filters of different passband placed next to each other are visible. The filter names are given in red. The yellow square (labeled MLA) indicates the location where the field of view of the spectroscopic channels can be placed.

taken through the combined filters is shown in fig.4.2, the throughput curves of the individual filters are shown in fig. 4.3. There are two main reasons for the imaging channel and the MFA. The right side of the MFA (see fig. 4.2) is equipped with a Bessel V filter. This part of the CCD is used to point and guide the telescope. The telescope follows the movement of the stars on the sky. Due to mechanical limitations, small corrections are needed. These are obtained by measuring shifts of the star position on the CCD and using these to create move commands for the telescope. The second reason is to monitor the sky properties, therefore the filter passbands on the left side of the MFA (see fig. 4.2) are used. Their passbands align with the main sources for the absorption in the atmosphere. Rayleigh scattering is strong at short wavelength (filter F1), Ozone shows a absorption feature in the filter F2, filters F3 and F4 are used for aerosols and F5 for the water vapor absorption.

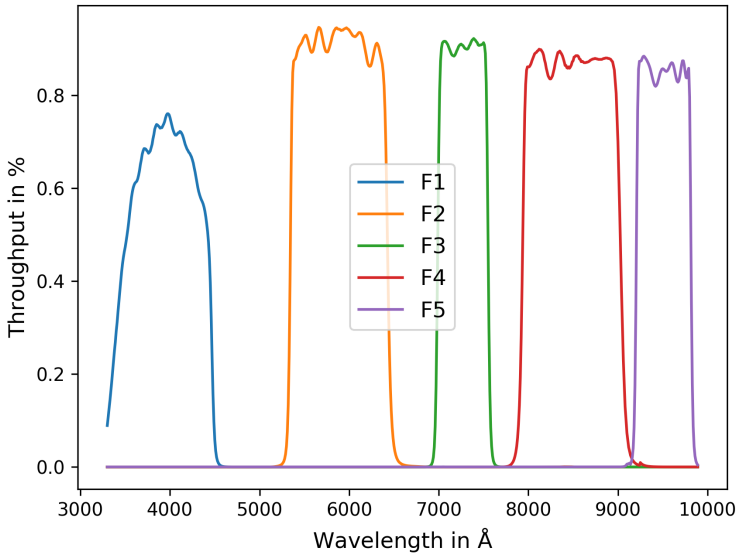

Figure 4.3: Transmission curves for the filters of the multi filter array used in front of the imaging channel CCD.

Spectroscopic Channels

The light for the spectroscopic channels is taken from the beam provided by the telescope before passing through the filter wheel of the imaging channel. A small prism is therefore moved into the beam, which redirects the light via reflection towards the spectroscopic channels. The placement of the resulting FoV is indicated in fig. 4.2, and has an angular dimension of 6.4 " x 6.4 ". At the telescope focal length this correspond to spacial scale of 0.7 x 0.7 mm, which is too small to fit a 15 MicroLenses Array (MLA). The image is therefore enlarged (by a factor e_f) to fit to a array of lenses with a side length of ≈ 20 mm.

The array of microlenses is then placed in this enlarged image. Each of these lenses focuses the light falling on it and creates a small image of the entrance pupil of the telescope. Each small image of the entrance pupil contains therefore all the light which passed the corresponding microlens. The spatial resolution of this setup is then limited to the extend of the single lens of the microlens array, which we call a "spaxel". The image of the entrance pupil created by each microlens is far smaller than the pitch between microlenses in the array[1]. Each of these images is

[1]The UH88 telescope is a Cassegrain type telescope (see sec. C.13). The entrance pupil looks like an annulus limited at the outer edge by the outer diameter of the primary mirror and in the inner by the outer diameter of the secondary mirror housing. For the micro lenses, the entrance pupil is placed at a distance equal to 720 m - Focal length of the telescope (22 m, diameter 2.2m) multiplied by the enlarging factor e_f =32. The focal length of the microlenses is ≈7 mm. Each of the microlenses will create an image of the entrance pupil. The diameter of the pupil image d_i is approximately given by geometric optics to $d_i = 2.2\,\text{m}/720\,\text{m} \cdot 7\,\text{mm} = 21\mu\text{m}$. As the spacing of the lenses is ≈1.3 mm we obtain a grid of 15 x 15 pupil images, which are well-separated from each other.

then used as an entrance slit for the following spectrograph. As the images are far smaller than the lens pitch, the images do not overlap and we obtain separated spectra on the spectrograph. As there are 15 x 15 lenses there will be 225 spectra placed on the detector. Each spectrum belongs to one of the microlenses. The data-reduction pipeline uses an optical model to arrange these spectra in a datacube with the two spatial directions and the wavelength direction. Each of the spectroscopic channels has a FoV of 6.4 " x 6.4 " subdivided into 15 x 15 spatial elements. The blue channel is sensitive between 3200-5200 Å with a resolution $R = \lambda/\Delta\lambda$ of 1000 at 4300 Å. The red channel is sensitive from 5100 Å to 10,000 Å with $R = 1300$ at 7600 Å (see [Lantz et al., 2003]).

The signal in the data cube can be understood as a addition of the source Point Spread Function (PSF), formed by the atmosphere (C.2) and the telescope (C.3), and the background. The background is itself composed of the sky emission (C.2), and in case of a SN observation, the host galaxy. As we here work on the calibration we only observe standard stars, which are well separated from other sources. Thus our background is entirely composed of sky emission.

Now the advantages of the more complicated optical setup of SNIFS compared to a slit spectrograph can be seen. Due to Atmospheric Differential Refraction (ADR C.2.3), the star position in the image plane of the telescope is wavelength-dependent. In the datacube, this distortion can be measured and taken into account in the extraction of the star spectrum. For a slit spectrograph, the star is centered in the slit at some wavelength. At other wavelengths, the star light will be partially obscured by the slit.

Similarly, the extent of the star image is wavelength-dependent because of the wavelength-dependence of seeing and diffraction in the telescope. In case of the slit spectrograph, a slice of the star image would be taken and light would again be lost as the aperture/slit-size is not wavelength-dependent. As SNIFS samples the star image in two spatial directions, the wavelength-dependent width of the star image can be taken into account in the extraction of the star spectrum from the data cube.

The sky background emission can be estimated because the stellar intensity in each wavelength image will form a PSF, while the sky background is uniform across the field of view of the spectroscopic channels.

As described in section C.2, the absorption losses in the atmosphere are proportional to the amount of atmosphere along the optical path. Through observing the spectra of multiple stars S_{obs} of known spectra S_{tab} at different airmasses, we can measure both the atmospheric and the instrumental throughput (see Eq. C.6). These observations yield the measured attenuation, $\log\left(\frac{S_{\text{obs}}}{S_{\text{tab}}}\right)$, at all instrument wavelengths and at each airmass. As described in [Buton et al., 2013], taking into account the wavelength-dependence of Rayleigh and aerosol scattering and Ozone absorption reduces the measurement uncertainties. A correction for the absorption by O_2 and H_2O vapor is obtained in a second step.

Parameterizing the measured attenuation as a function of the physical scattering processes therefore provides us with the throughput of the instrument $\tau_{\text{SNIFS,CALSPEC}}$ (intercept at zero airmass), so that we can calculate the percentage of photons producing a signal. The throughput can also be converted into the flux solution, F_{Sol}, which is the wavelength-dependent scaling factor between counts on the detector and spectral flux density entering the telescope. The throughput of SNIFS ($\tau_{\text{SNIFS,CALSPEC}}$) measured with CALSPEC standard stars and the flux

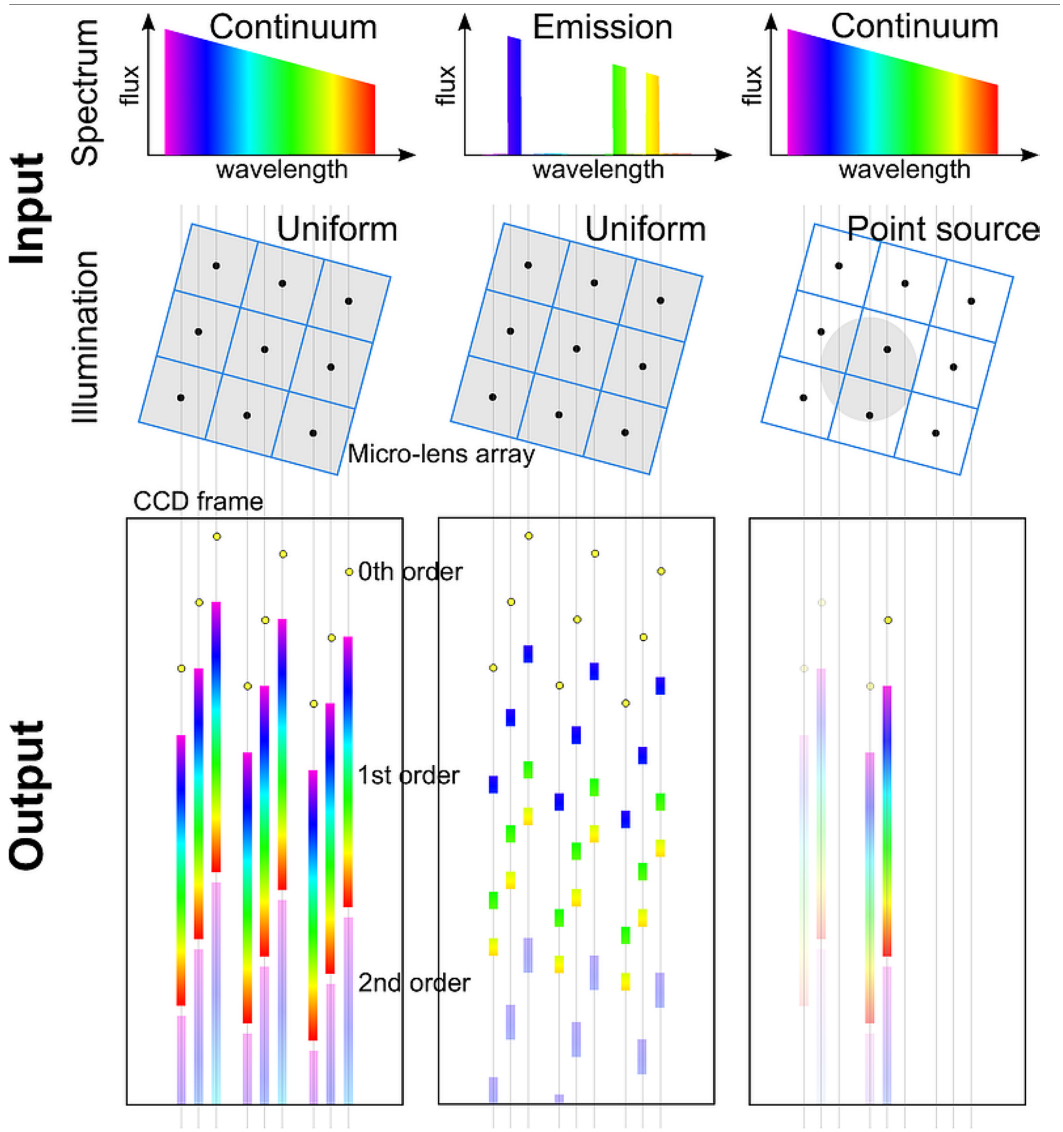

Figure 4.4: Working principle of SNIFS spectroscopic channels explained for three different sources (columns), from [Copin, 2013], fig. 2.4.
The first row shows the spectrum of the sources, and the second, its spatial extent. The third row then shows the spectra, lined up, on the detector of the spectrograph.
The signal on the detector belonging to one spatial element is given by a vertical trace. As SNIFS uses a combination of a prism and a grating, we see several orders of diffraction on the detector. At the top of the third row we see the non-dispersed 0th order in the same arrangement as the spatial elements in the second row. Below it we see the first order. For the first source the traces are completely illuminated as the source is continuous. Below that we find the second order, which can partially overlap with the end of the first order. As the spectrum of the second source shows emission lines, the vertical traces of 1st and 2nd order on the detector are no longer continuously illuminated (3rd row, 2nd column). The spectrum of the third source is again continuous, but illuminates only a subset of the spatial elements, so only a few traces are visible.
Note that one can also see that the spectra next to each other on the CCD (lower left panel) are shifted relative to each other in wavelength, this is used in sec. 6.4.2)

.

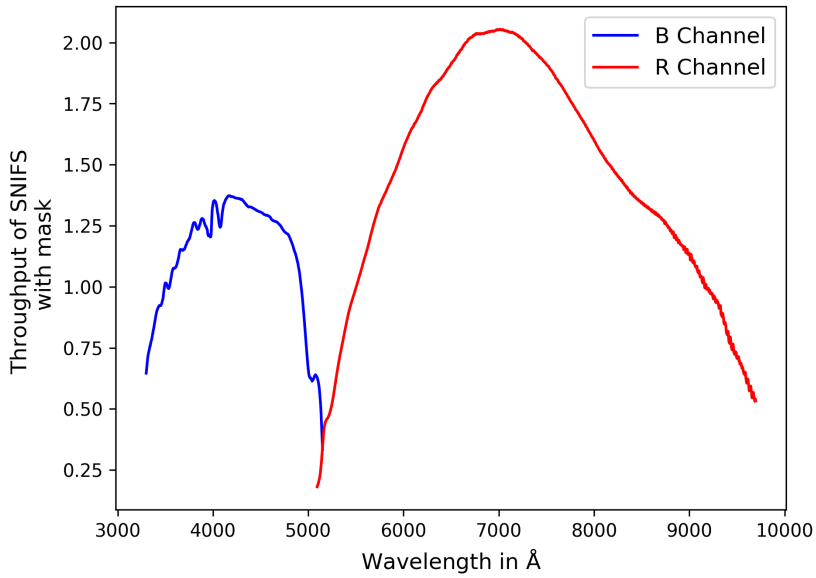

Figure 4.5: Instrumental throughput measured via the two dimensional fit of the ratio of observed to tabulated spectrum in wavelength and airmass. We show here the throughput of the UH88 equipped with a entrance pupil mask. The collecting area is therefore reduced by 90 % and the measured throughput is a factor ten smaller than usual.

solution (F_{Sol}) are therefore linked via:

$$F_{\mathrm{Sol}} \approx \frac{h \cdot \nu}{\tau_{\mathrm{SNIFS,CALSPEC}}} \tag{4.1}$$

where λ is the wavelength of the photons, c is the speed of light and h is the Planck constant.

We obtain flux-calibrated spectra for the observed sources. As shown in sec. 3, such spectrophotometry is necessary to define proper photometric systems (like CALSPEC), and therefore enables the comparison of sources at different redshift.

4.3 SCALA Device

Concept

SCALA provides a monochromatic, wavelength-tunable light source of variable exposure time to illuminate a large area within the telescope entrance pupil, and to transfer the flux calibration from the photodiode to the instrument attached to the telescope.

The wavelengths used for calibration lie in the range 3000 Å to 10,000 Å, as the instrument to calibrate (SNIFS) is sensitive in this range. The bandwidth must be $\approx$ 30 Å, as signals with smaller bandwidth could result in issues in the data-reduction pipeline [1] of SNIFS while those with a broader wavelength band would result in a bad spectral resolution. The outer diameter of the telescope entrance pupil is 2.2 m, with a central obscuration of 85 cm. The ratio of illuminated area to total entrance pupil area should be maximized. So that faint objects can be observed with the calibrated but smaller entrance pupil. The faint primary standards which should be observed are GD153, GD71 and G191B2B (the main calibrators of the CALSPEC system), with visual magnitudes 13.349, 13.032 and 11.69 respectively (for spectra see sec. C.1, fig. C.3).

By illumination of both, SNIFS and our photodiode, with SCALA at the same time, we can measure the throughput of SNIFS. The data-reduction pipeline of SNIFS is used to extract the signal from the CCD image and to produce a datacube. As we illuminate all the spaxels of SNIFS homogeneously, we do not need to extract a spectrum of the cube but can average over all spaxels. Comparing the number of electrons produced on the CCD to the number of photons emitted by SCALA, we obtain the throughput of SNIFS.

If standard stars are observed close in time to SCALA calibrations, we can immediately compare the standard SNIFS throughput and flux solution to the one of SCALA and therefore relate the flux of the observed stars to the laboratory standard.

Construction

SCALA was designed in 2012/13 and verified via simulations in 2013. The mechanical workshop of the University Bonn was responsible for the manufacturing and the assembled device was tested in the optical lab in Bonn until 2014. In May - June 2014, SCALA was mounted to the ladder within the UH88 dome. The first calibrations of SNIFS were performed, but no stars were

[1] The signal could be miss-interpreted as the signal of a cosmic ray interacting with the detector and thus would be removed from the data cube

observed. In 2014/15, we constructed an entrance pupil mask for the UH88 telescope in Berlin. This mask was applied to the telescope in May - June 2015 for standard star observations.

Implementation

SCALA uses six Integrating Spheres (ISs), from which light is fed to 18 collimating mirrors, that illuminate the telescope. These elements are grouped in six modules, arranged in a hexagonal grid. Each module therefore contains three mirrors and an integrating sphere. The setup is shown in fig. 4.6.

The 18 parallel beams illuminate 17 % of the total collecting area of the UH88 telescope. To reject starlight, which would also illuminate the uncalibrated areas, an entrance pupil mask can be mounted to the UH88 telescope. The apertures in the mask are aligned like the mirrors of SCALA. The diameter of the apertures is selected to be smaller than the SCALA beam diameter. Using the mask guarantees that the stars and SCALA have identical telescope paths, but at the cost of a significantly smaller collecting area. The collecting area of the telescope is thus reduced to 10 % of its original size (2.5 mag).

The ISs are illuminated by one of two different lamps via a monochromator. The monochromatic light, with selectable wavelength and ≈ 35 Å bandwidth, is transported to the IS via a six-armed fiber bundle. Each IS will then illuminate 3 exit ports homogeneously. The light from the exit port is collected by the corresponding collimating mirrors and sent into the telescope.

The SCALA device itself is permanently mounted to the maintenance ladder in the UH 88 dome. The whole device can thsu be moved with the dome, and aligned in front of the telescope. Fine adjustments are performed by the telescope mount and through adjustments to the individual mirrors, see chpt. 8.1 of [Lombardo, 2017].

The illuminated area in the focal plane of the telescope is completely defined by the geometry of the setup. The port diameter of the IS is 14 mm, together with the focal length of the collimating mirrors of 80 cm, this correspondents to an angular diameter of 1°. The use of the IS guarantees that the FoV of SNIFS is homogeneously illuminated. For the telescope the SCALA setup thus looks like a planet (disk) of 1° diameter and constant surface brightness (no variations across the disk). The solid angle illuminated by SCALA is thus 0.24 msr or 0.79 sq.deg.

Components

- **Light Source:**
  We use a 150 W Xenon Lamp for wavelengths between 3000 Å and 7000 Å. The high effective temperature of the electric arc results in a higher flux at lower wavelengths. We switch to a tungsten halogen lamp (20 W) for wavelengths longer than 7000 Å, to avoid the strong emission lines of the Xenon lamp in the IR. The lamps are equipped with a filter wheel with order sorting filters from SCHOTT, which can be inserted to the light beam to remove light that would otherwise pass the monochromator as second order light. The spectra of the different configurations (grating: 1,2; order sorting filter: none, 3090 Å, 4950 Å; lamps: Xenon, Tungsten) are shown in fig. 4.7.

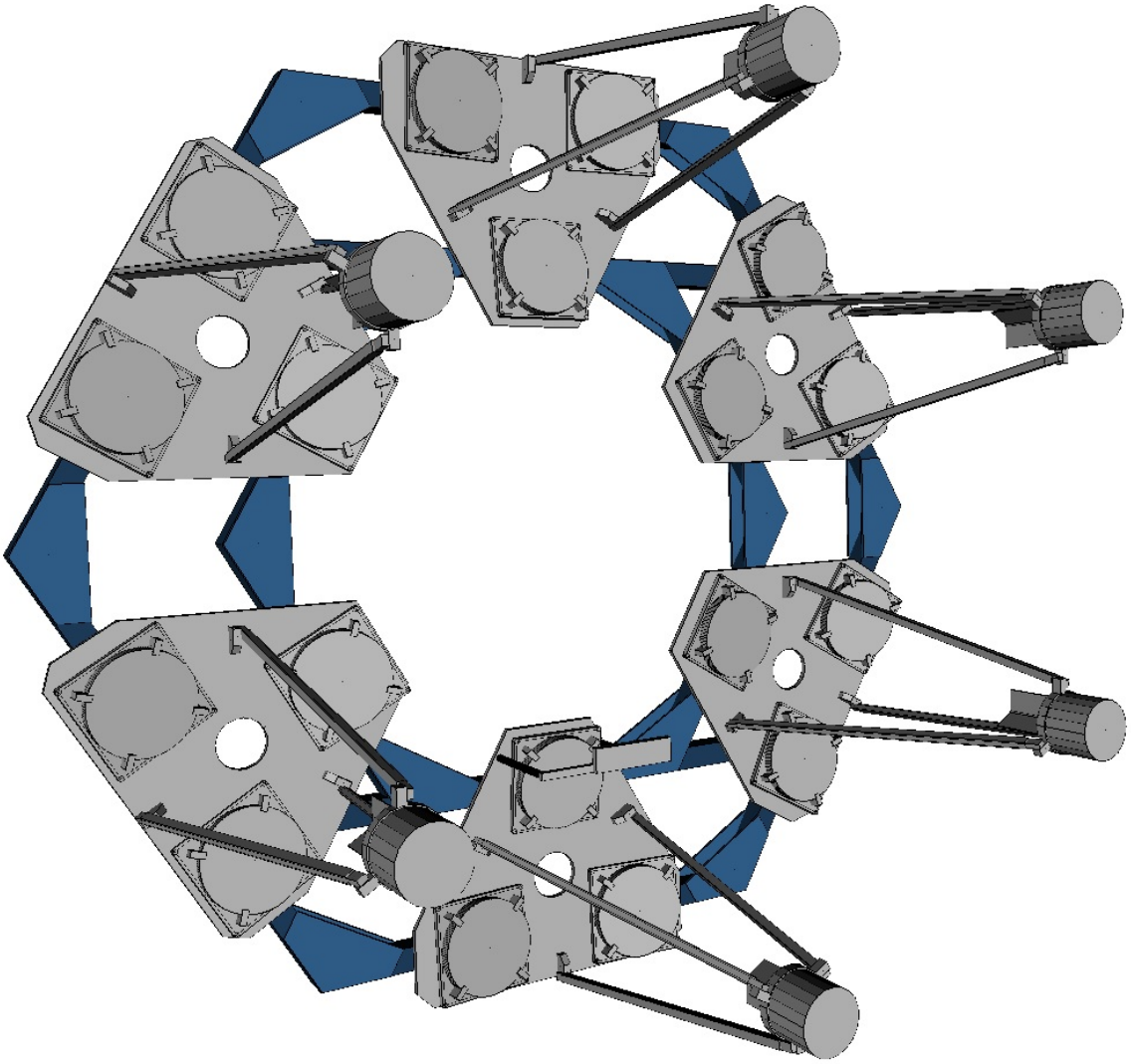

Figure 4.6: Technical drawing of SCALA, with six submodules forming a hexagon. Each is equipped with a integrating sphere and three mirrors

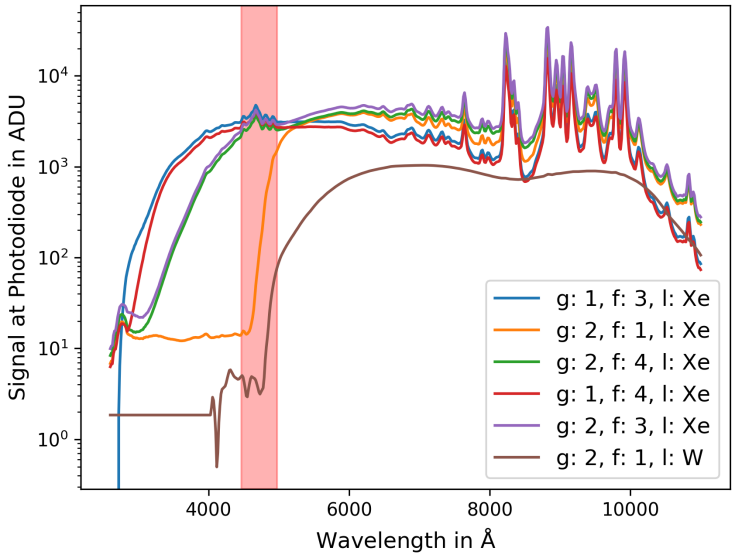

Figure 4.7: Spectra observed by one of our photodiodes for the different configurations of the light source / monochromator. We use two gratings (g: 1,2), three filters (f: 1,3,4 corresponding to GG495, none , WG305) and two lamps (l: Xenon, Tungsten). The red region indicates where the bandpass of the SCALA system is defined by emission lines in the Xenon spectrum rather than by the bandpass of the monochromator.

- **Monochromator:**
  We use a Cornerstone 260 monochromator from Oriel as a tunable bandpass. It is equipped with two 1200 l/mm gratings, one with a blaze wavelength of 3500 Å and the other with 7500 Å. The slit width of 1 mm corresponds to a bandwidth of ≈ 35 Å. As we avoid the emission lines in the spectra of our light source, the bandpass shape is defined by the monochromator. For a detailed description of the bandpass shape see sec. 6.4. The exit of the monochromator is mounted to the entrance of the fiber bundle without additional optical elements to increase throughput.

- **Fiber Bundle:**
  The fiber bundle entrance is arranged in a rectangular way. To increase the area illuminated by SCALA, the fiber bundle is divided into six different arms. Fibers belonging to each arm are distributed in the exit slit of the monochromator in a semi-random way, see figure 4.8. Due to small deviations from symmetry in the distribution and the subdivision of the fibers in the exit slit, the resulting bandpasses of the six arms are slightly shifted relative to each other in wavelength (for more details see [Küsters, 2014] chpt. 3.3).

- **Integrating Sphere**

Figure 4.8: Image taken of the fiber bundle entrance, with the exit of the fiber bundle arms illuminated by light of different color to show the distribution of the individual fiber bundle arms in the bundle entrance / monochromator exit

An IS is a hollow sphere coated at the inside with a highly reflecting, diffuse material. In this way light entering an IS is scattered several times before leaving it. If the port area is small compared to the surface of the sphere, the output illumination pattern is independent of the input distribution. This means that the opening of the sphere is homogeneously illuminated, and provides a Lambertian emitting surface.
Our IS are made from PolyTetraFluorEtylen (PTFE) cylinders. In these cylinders half spheres are milled, and the resulting spherical surfaces are salt-blasted. The two PTFE cylinders, each containing a semi sphere, are mounted in a black anodized Aluminum housing.
In [Lombardo et al., 2014] we presented a test which confirmed the homogeneous illumination. As this test used a CCD camera, the result can only be as good as the reference flat field used to correct for pixel-to-pixel variations and differences in the optics used. In a second approach we tiled a fiber as a small light probe through the opening, (chpt. 4.4 [Küsters, 2014]). This measurement independently confirmed the homogeneity. Variations across the 14 mm opening are smaller then 0.03 %. At the openings of the IS there are shutters to block light leaving the sphere for special tests with only a subset of the SCALA beams.
The throughput of the IS was measured to be $\approx 45\,\%$ for the three holes together (see. [Lombardo et al., 2014] fig. 3).

- **Collimating Mirror:**
  We use parabolic mirrors with diameters of 20 cm and focal length of 80 cm to collimate the light sent from the exit ports of the IS. Together with the telescope optics the exit port of the IS is imaged onto the image plane of the telescope. In this way we illuminate all spatial elements in the image plane homogeneously.

- **Photodiode:**
  The reference flux standard used here is a S3477-04 photodiode from Hamamatsu integrated with a two-stage Peltier cooler. The so-called "Cooled Large Area Photodiode" (CLAP) is the integration of such a photodiode with a low noise amplifier and a digitizing unit. The photodiode monitors the light reflected off the mirrors, and therefore the

amount of light emitted from SCALA. For more details see chapter 5 with a description of the device and possible systematics.

- **Entrance pupil mask**
  The entrance pupil mask is split into four sheets of Alucore 6 mm. The plates are coverd with a black mat finish to reduce stray light. The holes are milled into the plate to ensure precise positioning and clean edges. The plates are equipped with strong magnets to simplify mounting, and are secured by C-clamps when attached to the UH88 telescope. For more details, see [Küsters et al., 2016].

4.4 Comparison of SCALA and CALSPEC Flux Calibration

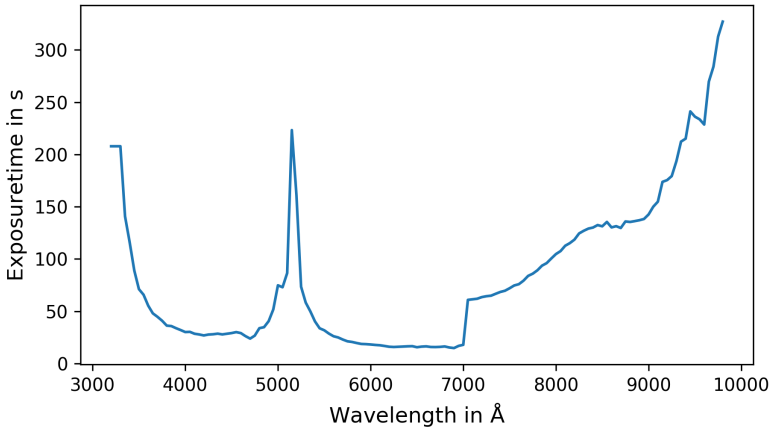

Figure 4.9: Exposure times of SCALA required to produce more than 10^4 signal electrons per spaxel of SNIFS. The exposure times are long due to the low throughput of SNIFS at the endpoints of the two channels, for comparison see fig. 4.5.

Through illuminating both the spectrograph (SNIFS) and the photodiode at the same time with a wavelength-adjustable, monochromatic light source, we obtain the wavelength-dependent throughput of SNIFS via SCALA. We can then compare this to the throughput obtained by the observation of standard stars with SNIFS in a close-by night.

Flux incident to photodiode
As the central wavelength (λ_c) and bandpass are known, the measured photodiode current can be converted to a physical flux by the use of the known response (R_1 see sec. 5.2) and gain (g_1) of the photodiode.

The light reaching our photodiode directly from the IS port is also seen by SNIFS - the desired signal. However light from the IS can also reach the photodiode via unwanted reflections, for

which the photodiode current needs to be corrected. See fig. 4.11 for further discussions. For the moment we assume there are no such reflections.

After correction for external backgrounds, we assume that the light level detected by the photodiode is independent of the position within the beam, i.e. that the beam is homogeneously illuminated. Based on this assumption, we scale the flux measured by the photodiode with the ratio of the beam area (A_{Beam}) to the area of the photodiode ($A_{\text{PD}} = 33.6\,\text{mm}^2$). $A_{\text{Beam}} = 314.2\,\text{cm}^2$ without the entrance pupil mask applied to the telescope and $A_{\text{Beam}} = 201.1\,\text{cm}^2$ with the mask.

If all optical components were identical, we would obtain the total emitted flux from SCALA by scaling the above flux by a factor of 18 (as SCALA has 18 beams). However the elements are not the same. They slightly deviate from each other due to minor material property differences, so we define an effective number of beams, $N_{\text{eff.}}$.

Effective number of beams

$N_{\text{eff.}}$ gives us the number of reference beams, which would be needed to reproduce the total emission from the SCALA system. We use two photodiodes, one is fixed to one of our SCALA beams and is our reference photodiode (CLAP1). The other photodiode (CLAP0) is placed in the other beams, one at a time, and the ratios to the reference beam are calculated. $N_{\text{eff.}}$ is the sum over these ratios plus one for the reference beam itself.

$$N_{\text{eff.}} = 1 + \sum_{i=1}^{17} \frac{(I_{\text{PD0,i}} - B_{0,i}) \cdot \text{corr}_{0,i}}{(I_{\text{PD1,i}} - B_{1,i}) \cdot \text{corr}_{1,i}} \tag{4.2}$$

where $I_{\text{PD0,i}}, I_{\text{PD1,i}}$ are the photodiode currents, $\text{corr}_{0,i}, \text{corr}_{1,i}$ accounts for corrections like gain and responsivities of the photodiodes, while $B_{0,i}$, $B_{1,i}$ accounts for the backgrounds at each exposure. In the ideal case, $\frac{(I_{\text{PD0,i}} - B_{0,i}) \cdot \text{corr}_{0,i}}{(I_{\text{PD1,i}} - B_{1,i}) \cdot \text{corr}_{1,i}} = 1.0$ and therefore $N_{\text{eff.}} = 18$. In sec. 6.3, we see that $18 < N_{\text{eff.}} < 21$ and show the incorporated uncertainties.

$N_{\text{eff.}}$ was also obtained from independent laboratory measurements, which are described in detail in [Lombardo, 2017]. Both measurements agree with each other within the uncertainties.

Amount of light emitted by SCALA

The total flux emitted by SCALA can now be written as:

$$F_{\text{SCALA}} = (I_{\text{PD1}} - B_{1,i}) \frac{1}{g \cdot R} \cdot \frac{A_{\text{Beam}}}{A_{\text{PD}}} \cdot N_{\text{eff.}} \tag{4.3}$$

with $B_{1,i}$ the background for the CLAP1 measurement I_{PD1}, g, the photodiode gain (42), and R, the photodiode responsivity (conversion between CLAP counts and incident power). However this quantity is not yet comparable to the measurement of SNIFS. SNIFS detectors see the time-integrated signal of SCALA. As SNIFS is mounted behind the telescope it can only see a subsection of the artificial planet of SCALA. We therefore integrate the signals of the photodiodes in time (obtaining the energy emitted by SCALA) and scale for the solid angle

of the artificial planet[1], as we know from tests that the surface brightness is constant.

$$(\mathrm{E}/\Omega)_{\mathrm{Pd}} = \frac{1}{\Omega_{\mathrm{SCALA}}} \int_{t=0}^{t=t_{\mathrm{exp.}}} F_{\mathrm{SCALA}}\, \mathrm{d}t \tag{4.4}$$

Amount of light detected by SNIFS

We observed standard stars and obtain the instrumental and atmospheric throughput based on the standard star system (CALSPEC). With the throughputs, we are able to convert a signal at the detectors of SNIFS to a physical flux and obtain therefore a second measurement of the flux emitted by SCALA. We perform this step as we want to compare SCALA and CALSPEC calibration. In future, when the systematic uncertainties of SCALA are understood, we could obtain the instrumental throughput from SCALA. To measure the atmospheric throughput, we still need to observe stars, but the required number of observations is smaller and therefore we save time for science objects.

As SNIFS provides spectral resolution, we have to integrate its signal (flux calibrated spectrum F_{SNIFS}) in wavelength and multiply by the telescope collecting Area A_{tel} and the exposure time t_{exp} to obtain the energy detected. The energy emitted by SCALA can now be measured by SNIFS but using a calibration relative to the CALSPEC-system. To obtain comparable quantities, we have to scale for the solid angle of a spatial element of SNIFS (spaxel)[2]. We then obtain

$$(\mathrm{E}/\Omega)_{\mathrm{SNIFS}} = \frac{A_{\mathrm{tel}} t_{\mathrm{exp}}}{\Omega_{\mathrm{spaxel}}} \int_{\lambda_c-\Delta\lambda}^{\lambda_c+\Delta\lambda} F_{\mathrm{SNIFS}}\, \mathrm{d}\lambda \tag{4.5}$$

To not be limited by the statistics on the number of photons detected, the SCALA exposure time for calibrations of SNIFS is adjusted to result in at least 10^5 electrons on the detectors of SNIFS per spaxel. As the throughput of SNIFS is low at the limiting wavelengths of each spectroscopic channel, the exposure time is longer there (see fig. 4.9).

Comparison of calibrations

In 2015, we observed standard stars for four consecutive nights and calibrated SNIFS using SCALA. As SNIFS does not change in its sensitivity over time scales of days[3], comparing the calibrations of SNIFS via SCALA and standard stars is justified.

The energy-per-solid-angle observed by SNIFS, determined through the flux solution (standard stars / CALSPEC), can be compared with the energy-per-solid-angle measured by the photodiode (laboratory standard). If the calibration by SCALA and standard stars delivers the same solution, the following equation should be true:

$$(\mathrm{E}/\Omega)_{\mathrm{SNIFS}} = (\mathrm{E}/\Omega)_{\mathrm{Pd}} \tag{4.6}$$

[1]The photodiode can see the whole angular extent of the IS port of 1° which results in a solid angle of $\Omega_{\mathrm{SCALA}} \simeq 0.25\pi$ sq.deg.

[2]The solid angle of the spaxel is defined by the size of the rectangular microlens and the effective focal length of the UH88 telescope + enlarger. The angular extent of it is 0.4251 ± 0.0003 " (Table 2.2 p.13 [Copin, 2013]), which corresponds to a solid angle of $\Omega_{\mathrm{spaxel}} = (0.4251/3600)^2$ sq.deg. $= (1.3963 \pm 0.002) \cdot 10^{-8}$ sq.deg..

[3]Checked by comparing the flux solutions of the last 10 years.

However, with the above assumptions we find that eq. 4.6 is not true, therefore we define the Ratio of Calibrations, RoC:

$$\mathrm{RoC} = \frac{(\mathrm{E}/\Omega)_{\mathrm{SNIFS}}}{(\mathrm{E}/\Omega)_{\mathrm{Pd}}} \overset{(\mathrm{D.1})}{=} \frac{\tau_{\mathrm{SCALA}}}{\tau_{\mathrm{CALSPEC}}} \tag{4.7}$$

RoC gives the deviation between the two calibrations and is shown in fig. 4.10. It can also be obtained from the ratio of instrumental throughput measured with SCALA to that with standard stars (CALSPEC), for the equations see, sec. D.1. We show three independent calibrations performed within the same night (run 1-3). The consistency between them can be used as an estimate of the statistical uncertainties and the changes of SNIFS in time. The lower panel shows the same measurements but this time sorted by observation time rather than monochromator bandpass wavelength. We see gaps of several hours length between the runs. The standard star observations have been performed in these gaps. The deviation between the two calibrations (SCALA and CALSPEC) grows linearly with wavelength, with an amplitude of up to 25 %.

This comparison can be seen as a preliminary result for SCALA, as we included several assumptions in the calculation. Our goal was to find differences between the calibration based on standard stars and laboratory standards. Such a large discrepancy would have strong consequences for cosmology. If this trend were true, the fraction of dark energy would be changed from $\approx 70\,\%$ to $\approx 50\,\%$. But before we should think about something so drastic, we should check the assumptions which were made.

The main aim for this thesis, coupled with the original goal of developing an error model, is to find the explanation for this trend. A long list of assumptions were made, we assumed that

- the light emitted from SCALA is centered at λ_{c} with a width of 35 Å
- there is no emission outside the selected monochromator wavelength band
- the illumination of the beams is homogeneous
- no light is scattered within the telescope optics
- no reflections occurs within SCALA
- the responses of photodiodes are known
- the backgrounds can be removed without biases
- the shutter of the SCALA monochromator is light tight
- the geometry of the setup is known, as are the solid angles
- $N_{\mathrm{eff.}}$ can be measured precisely

In the following I will give an overview of the next chapters, which will test the above assumptions and provide corrections if necessary.

4.5 Overview: Sources of Systematic Uncertainties

The following chapters will focus on the sources of systematic uncertainties in the measurements of SCALA. A graphical overview is given in fig. 4.11. It shows how light is generated, propagated and potentially scattered within SCALA. We can subdivide the main sources of systematics in SCALA into two groups, with three subgroups for the second category:

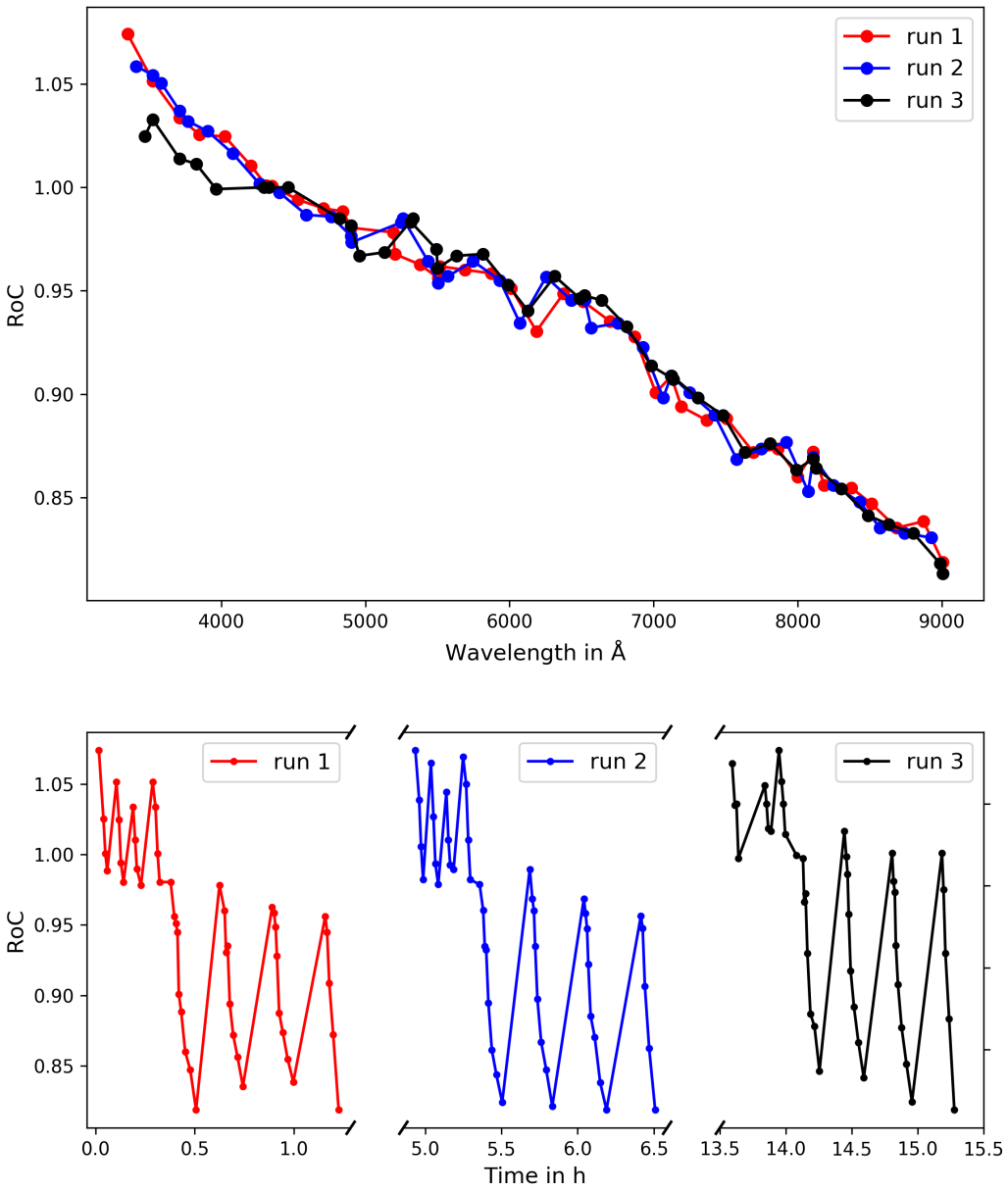

Figure 4.10: Upper panel: Ratio of calibrations (RoC) obtained with stars and with SCALA sorted for monochromator wavelength. We see three different runs taken in the same night, the same datapoints sorted by measurement time are shown in the lower panel. The gaps in between the calibrations are used for the standard star observations. An agreement between the two calibrations (CALSPEC & SCALA) would result in a constant value of 1.0. We see a trend in wavelength growing linearly, with an amplitude of up to 25 %.

- Limitations of the flux reference (photodiode calibration)
- Background light detected by the photodiode from:
  - External light
  - Internal reflections
  - Light emission outside the desired monochromator wavelength band (out-of-band emission).

The uncertainties in the flux reference are caused by limitations in the transfer of calibration at NIST and the Paris Supernova Cosmology Group, as well as aging since the calibration (see chapter 5).

In the ideal case, we would see light leaving the IS port, being reflected off the collimating mirror and detected by the photodiode. There are three different mechanisms which can provide additional signals. First, ambient light and a dark current in the photodiode can generate a signal. Both sources are *independent* of the SCALA light source, so we call them *external* background (see sec. 6.1). Second, the ISs are illuminating far more than just the collimating mirror area, so light can reach the photodiode via unwanted reflections and scattering. These signals are *related* to the desired signals, as they share the same light source, we call them *internal* backgrounds. As there are different surfaces on which the reflections occur, these backgrounds are subdivided into the following groups:

Crosstalk
: Light leaving one IS can be reflected off the SCALA structure twice or more, before reaching the photodiode of another beam, see sec. 6.2.1.

Reflection off the IS light shield
: Light leaving the IS port can be reflected off the light shield which prevents one mirror seeing multiple IS ports, and then reach the photodiode, see sec. 6.2.2.

Reflection off the IS port walls
: Light leaving the IS under small angles can be reflected off the wall of the port drilling and reach the photodiode see sec. D.8.

Reflection off the photodiode housing
: Light, which would miss the photodiode can be reflected off the metal housing of the packaging and reach the sensitive area, see sec. D.7.

The third sub-group is caused by emission of the SCALA monochromator outside the desired wavelength band. Therefore we discuss the monochomator in sec. 6.4.

How can emission outside of the desired wavelength band cause biases? In sec. 4.4 we assumed monochromatic light being emitted from SCALA, deviations from monochromaticity will cause systematic biases as the photodiode is integrating the spectrum over its hole sensitivity range, while in SNIFS we apply wavelength cuts.

As shown in sec. 4.4 we compare the instrumental throughput of SNIFS measured with SCALA to the one measured with CALSPEC standard stars. As our night of star observation (night 159 in 2015) is different from usual nights (entrance pupil mask, see sec. F), we need to account for possible systematic offsets for our night, see chapter 7.

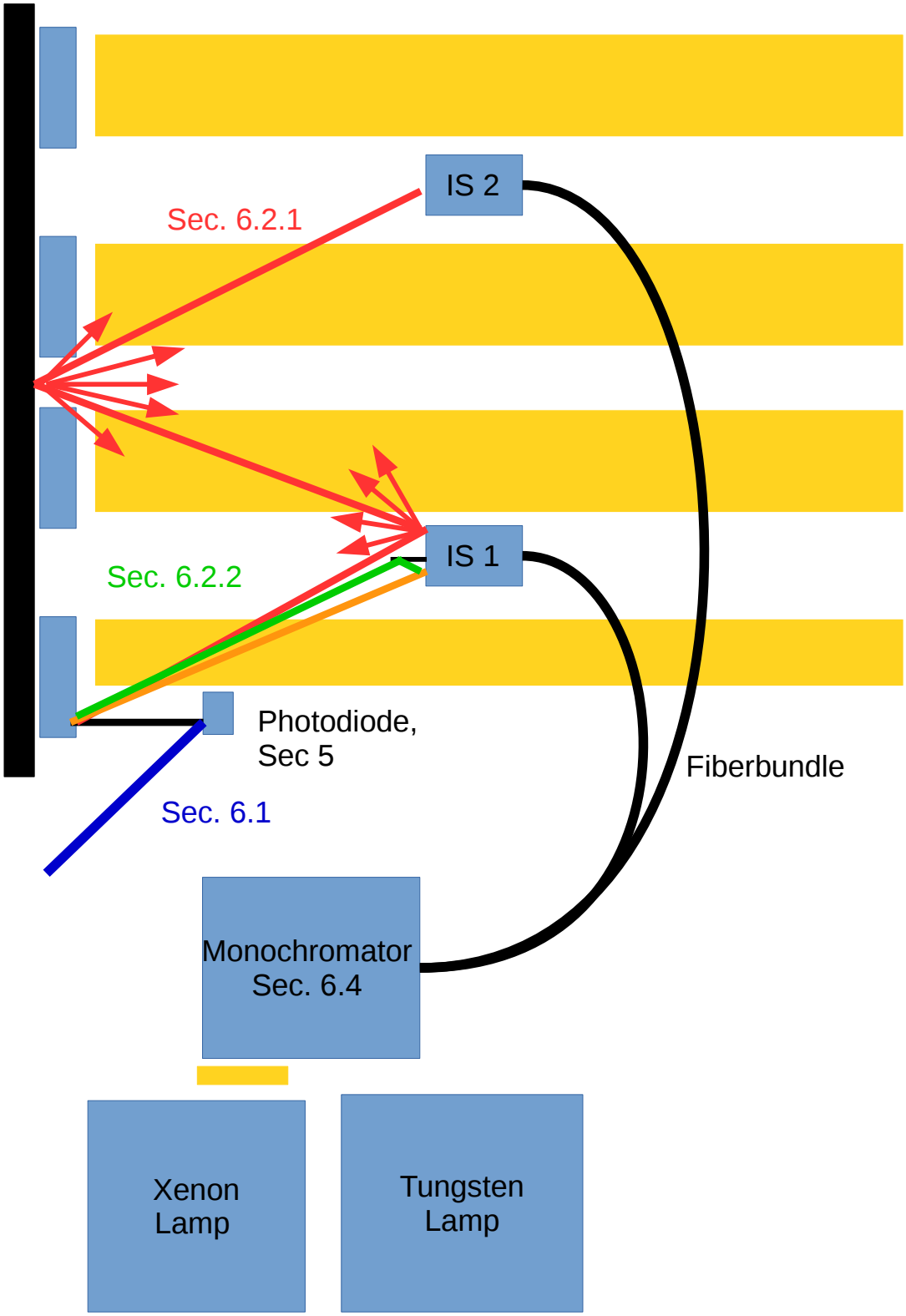
IS 2
Sec. 6.2.1
IS 1
Sec. 6.2.2
Photodiode,
Sec 5
Fiberbundle
Sec. 6.1
Monochromator
Sec. 6.4
Xenon
Lamp
Tungsten
Lamp

Figure 4.11

These backgrounds have been characterized up to 30 months after the calibration of SNIFS with SCALA and CALSPEC. As we know that the effects are evolving in time, we need to estimate the influence of the aging on our corrections. These corrections for aging lead to our final results, see chapter 8.

Chapter 5

The SCALA Flux Standard: the Photodiode

We want to calibrate the flux of standard stars, therefore we need to know the instrumental throughput of our observing system. To measure its wavelength dependent throughput we need a flux standard to compare to. This standard is realized in SCALA by a photodiode, which itself has been calibrated via other detectors relative to a primary standard. In the following section, I will describe the photodiode system and its properties.

5.1 Photodiode Readout System

The Hamamatsu S3477 photodiode we use is integrated in a front-end, containing a low noise amplifier, and a back-end box, containing the analog digital conversion, data storage and communication elements. The whole setup is called CLAP, and we purchased two devices from the Paris Supernova Cosmology Group (PSCG): CLAP0 and CLAP1. CLAP1 is mounted in the *reference beam* of SCALA. To protect it from ambient light, a light shield is mounted in front of the photodiode, which is covered on the inside with black velvet. The light shield is open to one side (U-shape) which allows light from the IS-port to illuminate the collimating mirror and via reflection the photodiode. The position of CLAP1 was chosen such that the open side of the U-shaped light shield is facing downwards. This orientation reduces the sensitivity to ambient light, entering through the dome above the device, and also reduces the collection of dust. The second photodiode is used to measure the efficiency of the individual beams relative to the reference beam, the so called effective number of beams (sec. 4.4).

Uncertainties due to Electronics
The signal of the photodiode, which is a pn-junction, is created by illumination via the internal photo effect. The incoming photon provides enough energy to create an electron-hole pair. This pair is split due to the internal electric field, provided by the different doping of the two semiconductors forming the pn-junction. As the energy of the optical photons is only slightly larger than the gap-energy, only one electron-hole pair is created for each detected photon, so the produced current is proportional to the illuminating photon current. The probability

of a photon to be detected is called Quantum Efficiency (*QE*) and is discussed in sec. 5.2. The photodiode provides a current I_{photo}, which is proportional to the incident photon flux, with the quantum-efficiency as proportionality constant. As the light flux and collecting area are small we have to measure a small current. In the CLAP devices an ASIC (Application-Specific Integrated Circuit) double gain amplifier with gains of 1 and 40 is used. To describe the basic properties we will replace it by a transimpedance amplifier as described in [Larason and Houston, 2008] and summarized in sec. D.2. The transimpedance amplifier is converting an input current I_{photo} to a proportional voltage U_{meas} according to $U_{\text{meas}} = R \cdot I_{\text{photo}}$, without applying a ohmic load R to the photodiode[1]. The CLAP1 unit uses a 1 GΩ resistor, while the CLAP0 unit uses a 100 MΩ resistor. Because of this properties the raw readings of the CLAPs are different by a factor ten, for this thesis the readings from CLAP0 have been scaled by ten. To display both of them the absolute value of the CLAP0 device was also shifted by 10,000 for visualization. For both devices a second amplification by ≈40 is available. Measurements of the PSCG showed that for CLAP0 this gain is 41.05 and for CLAP1 it is 43.5. The photodiode current can be maximally sampled with a rate f_r of 500 kHz. Maximally $8 \cdot 10^6$ sampling points can be stored in the internal buffer.

We assumed a linear conversion between photocurrent I_{photo} and measured digital signal in ADU[2] (including amplifier and ADC). The linearity of the ASIC amplifier and ADC was tested by the PSCG in an output voltage range of -2 V to 2 V. The deviations are centered around 0 with an RMS of 0.709 ADU, corresponding to an RMS voltage of 58 μV or 31 ADU at gain 40. A full uncertainty estimate of the amplifier as a function of voltage is still needed from the PSCG, as we do not have access to the individual measurements.

As the SCALA system is powered by the power grid, there is the possibility of pickup noise from the grid. Fig. 5.1 shows the noise spectrum of the CLAP device. We recognize harmonics of the power grid frequency at Hawaii at 60 Hz, 120 Hz and 180 Hz. Applying a filter to them reduces the standard deviation of the sample from 67 ADU to 66 ADU. We conclude, that the pickup from the power grid is not a significant contribution to the measured noise.

One external background to our signal is dark current. In the following we will estimate its amplitude using manufacturer specifications. The data sheet quotes a dark current of 25 pA at 25 °C. At Hawaii the two photodiodes are operated at a temperature of ≈-10 °C, using the internal two stage thermoelectric cooler. The dark current rises exponentially with temperature, the data sheet quotes an increase by a factor of 1.15 per increase of device temperature of 1 °C, we therefore obtain a current of 0.188 pA at -10 °C. This corresponds to a voltage of 0.188 pA·1 GΩ =0.188 mV. Using the measured gain of the Analog-to-Digital Converter (ADC) of 81.2 μV per ADU we obtain a dark current signal of 2.32 ADU at gain 1 or 101 ADU at gain 40 level for CLAP 1. A change of temperature by one degree, would then correspond to a change of background signal by 15.1 ADU.

This has to be compared with the expected signal. Fig. 5.2 shows the measured signal in ADUs. The signal, after removal of external backgrounds, is smallest at a wavelength of

[1] With an ohmic load at the output of the diode, the photo-current will result in a potential across the diode, and therefore change the geometry and efficiency of the device. The photo-current is not anymore proportional to the incident photon current

[2] Analog Digital Units, the amplitude of the signal after analog-to-digital conversion.

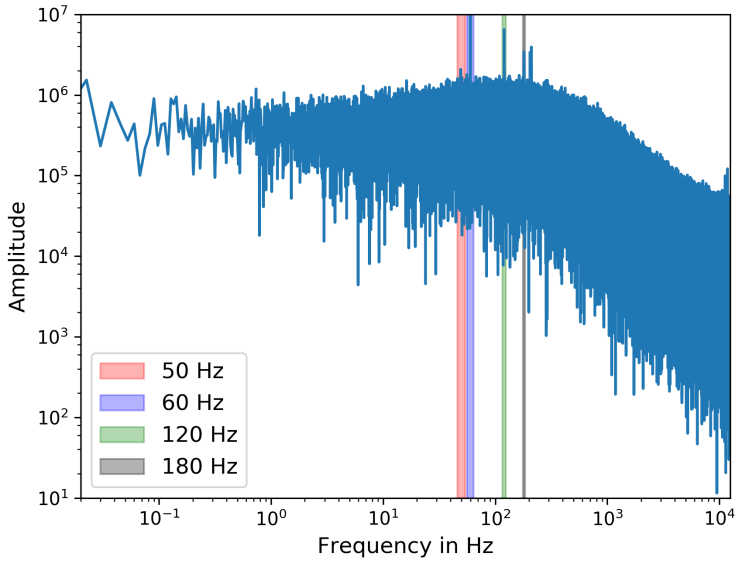

Figure 5.1: Fast Fourier transform of a CLAP measurement at a sampling frequency of 25 kHz (Noise spectrum). We see artifacts from the power grid at 60 Hz, 120 Hz and 180 Hz.

≈8500 Å and reaches a value of 800 ADU. The maximum amplitude of the signal is reached at ≈6000 Å with an amplitude of 4500 ADU. As the temperature of the photodiode is stabilized, the dark current background is slowly changing in time. It can then be removed by the measurement of a pre-signal and post-signal background. Even in a worst case approximation a temperature change of 0.1°C would result in an change of background by 0.2 % of our weakest signal. Therefore dark current is no concern.

Based on the measurements and the above properties of the readout system we can now estimate, whether we are within the tested linearity range. In fig. 6.2 we will see background measurements performed continuously over two days. The change of background amplitude is caused by daylight leaking into the dome and is up to 4000 ADU. The maximum signal provided by our light source is 4500 ADU and the estimate of the dark current is 100 ADU. All in all we have less then 10 kADU (at gain 40), which correspond to a voltage of less then 20 mV, which is small compared to the tested range of ± 2 V.

Based on the basic properties of the amplifier and ADC we conclude that dark current and non-linearity are no significant contribution to the systematic uncertainty.

Photodiode Data taking

The photodiode reading starts 2.34 s before the opening of the shutter and reads another 3.06 s after the closing of the shutter. In this way the photodiode data consists of a pre-signal background, a signal and an post-signal background data region. The background measurements can be used to remove backgrounds constant in time.

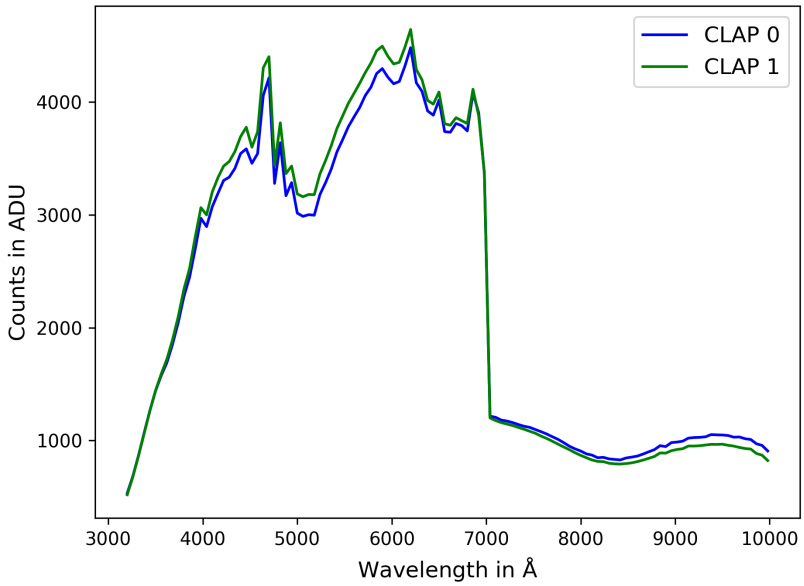

Figure 5.2: Average count level detected by the two photodiodes in our setup after background removal.

Due to the electronics constantly reading the photodiode current (1 kHz), we see the rising and falling of the light signal and can use this to measure the exposure time. As the shutter being placed at the entrance of the monochromator and the fibers sampling the monochromator exit in a semi random way (fig. 4.8), the shutter opening to one side of the entrance slit will result in the same exposure time for all integrating spheres.

Based on the pre-signal and post-signal-background we calculate a linearly changing background, and can therefore also remove external backgrounds slowly changing in time.

As the photodiode provides time resolution, while the spectrograph integrates in time, we also integrate the photodiode data, when we compare to SNIFS measurements.

Coordinating Photodiodes and SNIFS Observations

As the readout of SNIFS CCDs takes ≈ 90 s we usually perform a multi-wavelength sequence, in which several monochromatic SCALA observations illuminate a single SNIFS exposure. When the shutter of SNIFS is opened the shutter of SCALA is still closed. The first wavelength is selected. Reading of the CLAPs starts and after 2.34 s the shutter of SCALA is opened. The shutter of SCALA is closed after the exposure time, which is adjusted to result in at least 10^4 electrons at the CCD of SNIFS per spaxel and wavelength band of SCALA (see fig. 4.9). The reading of the CLAPs ends 3.06 s after the closing of the shutter. The next wavelength is selected, far enough from the first SCALA band to ensure there is no spectral overlap in SNIFS. For a calibration of the blue channel this allows 4 wavelength samples and for the red channel 7 samples, before the shutter of SNIFS is closed and the detector read out. To not introduce systematics here we have to ensure that:

- the shutter of SCALA is light tight. This was confirmed by long exposures of SNIFS, observing SCALA with closed shutter. No signal was detected.
- there is no spectral overlap of the wavelength samples in the SNIFS spectra. This is connected to the question of out-of-band emission by the monochromator. See sec. 6.4.
- that the wavelength of the monochromator is properly calibrated: This is obtained as the wavelength of the calibration is extracted from the SNIFS spectrum. Here we use the resolution of SNIFS of 5.2-7.2 Å, depending on the measured wavelength (see [Lombardo, 2017]), to obtain a correction for the monochromator wavelength.

5.2 Photodiode Response

The wavelength dependent response of our photodiode has been calibrated relative to a NIST calibrated photodiode at the optical bench of the PSCG. They illuminated both photodiodes, one at a time, with light from a monochromator. The monochromator itself was fed by several stabilized monochromatic (250 Å) Light Emitting Diodes (LEDs). As the LEDs were stabilized, the efficiency of the photodiode to calibrate is the efficiency of the reference photodiode, scaled by the ratio of the measured photodiode currents (ratio at fixed wavelength).

Several photodiode sensitivities will be compared in the following. We will see that the variations between individual photodiodes of same type are small and therefore these devices are an useful standard. The Quantum Efficiency (QE) gives the probability for an incident photon to generate an electron-hole pair and therefore an electron in the signal current[1]. Fig. 5.3 shows the quantum efficiencies of the two CLAPs (S3477) and one photodiode of the same type as the CLAPs (S3477) but calibrated by Hamamatsu[2]. Additionally there are the quantum efficiencies of photodiodes of type (S1337), two calibrated by Hamamatsu and one calibrated by NIST. The difference between the two types of photodiodes is caused by the difference in the optical glass, which is used to close the package of the photodiode. The photodiodes of type

[1]For technical reasons data sheets provide the responsivity and not the quantum efficiency. The responsivity provides the conversion between incident optical power and generated current. For the conversion between QE and responsivity we need to consider the energy of a photon of given wavelength ($E = h \cdot c/\lambda$) and the elementary charge q_e of an electron. We find the following relation, see e.g. [Larason and Houston, 2008]:

$$QE(\lambda) = \frac{I_\gamma \cdot hc}{P_{opt} n q_e \lambda} \tag{5.1}$$

where I_γ is the photo current, P_{opt} is the incident radiant flux and n is the index of refraction of air. The spectral responsivity is given by $s(\lambda) = I_\gamma / P_{opt}$ in units [A/W]. With λ measured in [nm] it follows:

$$QE(\lambda) = 1239.48 \frac{s(\lambda)}{\lambda} \tag{5.2}$$

Based on fig. 5.3 we expect the responsivity to linearly increase in wavelength as, the quantum efficiency of silicon photodiodes is nearly constant between 4500 Å and 9500 Å. The energy per photon is decreasing with wavelength. So the number of photons needed to transport the same optical power increases linearly in wavelength, with a constant quantum efficiency this results in a linear increase of the produced number of electrons. The current is therefore growing for longer wavelengths as the number of photons grows.

[2]We are not reproducing the data sheet, which is available online, but showing a calibration performed on a real device by Hamamatsu. The reason is that the data-sheet shows an expected sensitivity of a silicon photodiode covered with a UV fused silica window, but the used photodiode is covered with a Sapphire window.

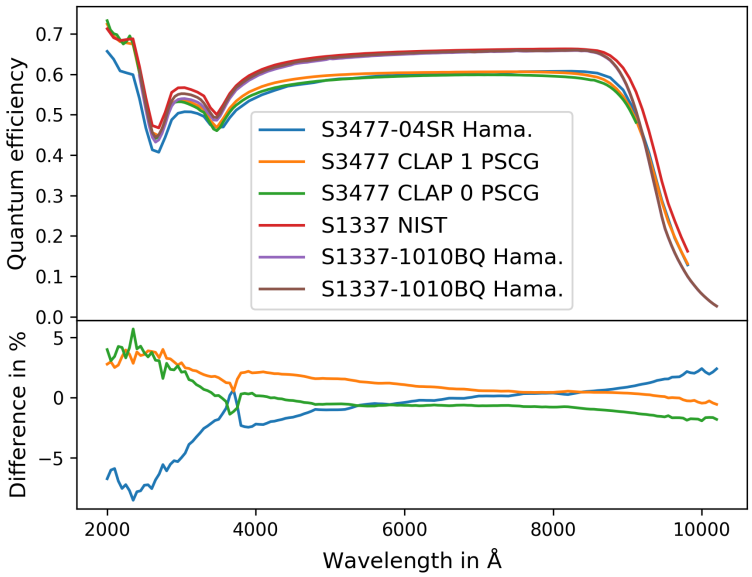

Figure 5.3: Quantum efficiency of six photodiodes. Listed is the type of photodiode (S3477 & S1337) and the calibrator, Hamamatsu (Hama.), NIST and Paris Supernova Cosmology Group (PSCG). The lower panel shows the deviation between the three photodiodes of type S3477 relative to their mean.

S1337 are covered by UV fused silica, while the others type S3477 are covered with sapphire glass. The window is necessary to reduce the effects of aging on the sensitivity of the device.

In the lower panel we show a comparison of the three photodiodes of type (S3477). This we can compare to fig. 5.4, which shows the typical variations between photodiodes of type S1336[1], and was provided by Hamamatsu Germany, (Dr. Christoph Seibel, sales engineer). Fig. 5.4 provides the statistics of all calibrations performed between April 2010 and October 2013. Included are the variations of their calibrating system and the variations caused by different batches of production. We see that the photodiode sensitivity is stable at the 3 % scale in the interesting wavelength range (indicated by vertical lines). Using an uncalibrated photodiode together with the appropriate data sheet results therefore in an uncertainty of $\approx 3\,\%$. These variations represent material properties of the photodiode, and are therefore specific to the individual device. As these variations are stable a calibration against a primary standard can be used to take these variations into account. The photodiode as flux reference can therefore be improved to a sub-percent level.

The internal variations might be stable but there is still the possibility for aging, for which we obtain an estimate in the following. The NIST reference photodiode used for the calibration of our photodiodes at PSCG was calibrated in January 2008. The final measurement, in which

[1]The photodiodes of type S1336 BQ, S1337 BQ and S3477 are differing in the used packaging and by the use of different cover glasses. The Si-photodiode inside is the same, therefore the reproducibility of the type S1336 is representative for the shown photodiodes

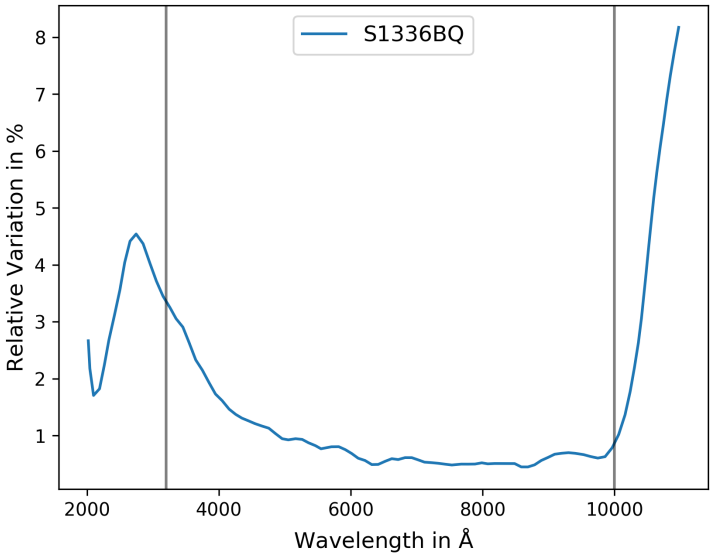

Figure 5.4: One sigma standard deviation of all calibrations performed between April 2010 and Oktober 2013 for photodiodes of type S1336 BQ, from Hamamatsu.

we calibrated SNIFS, was performed in June 2015. Therefore we need to account for an aging of ≈ 7 years.

To approximate the uncertainties, we use the aging uncertainty provided in [Larason and Houston, 2008] for a period of 12-18 month. NIST is recalibrating their working standards on a basis of 12-18 month, this uncertainty is therefore based on the measured aging of the working standard. To account for the long time between usage of the photodiode and the calibration of the NIST photodiode, we conservatively linearly scale the uncertainty up to 91 month.

The final uncertainty (fig. 5.5) is composed of the uncertainty in the transfer of calibration from the primary standard to the NIST photodiode used in Paris (composition already shown in fig. 3.1), the uncertainty of the transfer performed by the PSCG, estimated by them to be 0.2 %, and the uncertainty due to aging. For wavelength shorter than 5500 Å and longer than 9500 Å the uncertainty is dominated by aging, between these wavelengths the uncertainty is limited by the precision obtained in the transfer of calibration in Paris.

Alternative Flux Standard

We can now estimate the photon flux η incident to our photodiodes. From fig. 5.2 we know, that the signal S is between 800 ADU and 4500 ADU, for the calculation we take $S = 1000$ ADU. The amplifier gain G_{ampl} is 43.5, and the gain of the ADC G_{ADC} was specified to 81 μV/ADU. CLAP1 is equipped with a resistor R of 1 GΩ. Therefore the electron-current I_e produced by

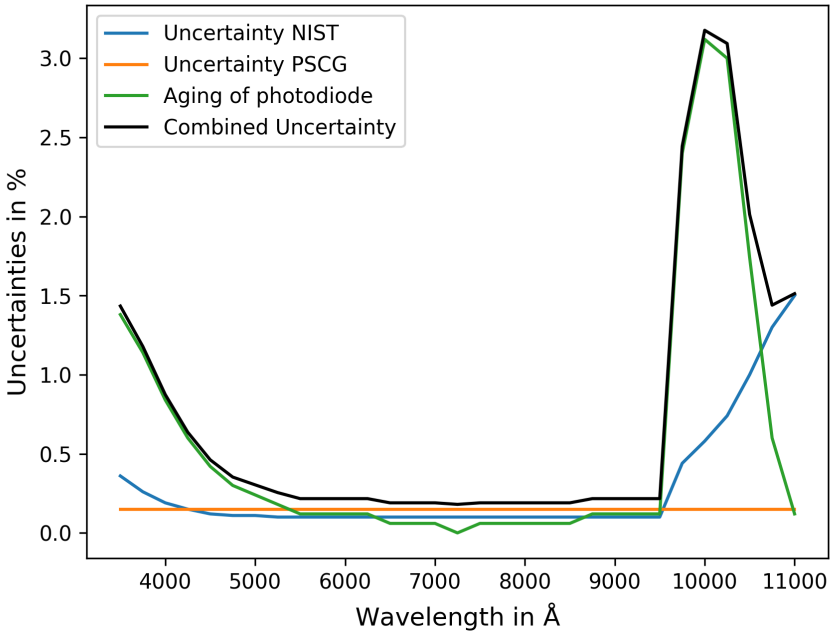

Figure 5.5: Combined uncertainty of the calibration of CLAP including the uncertainties of the NIST calibrated photodiode, the transfer to our photodiode and the aging of both of them between 2008 and 2015. Below 5500 Å and above 9500 Å the uncertainty on the photodiode calibration is dominated by aging.

the photodiode is:

$$I_e = \frac{SG_{\mathrm{ADC}}}{G_{\mathrm{ampl}} R q_e} = \frac{10^3 \cdot 81 \cdot 10^{-6}}{43.5 \cdot 10^9 \cdot 1.602 \cdot 10^{-19}} \mathrm{e}^-/\mathrm{s} = 1.16 \cdot 10^7 \mathrm{e}^-/\mathrm{s} \tag{5.3}$$

where q_e is the charge of the electron. The sensitive area of the photodiode is $A_{\mathrm{PD}} = 33.6\,\mathrm{mm}^2$. At a wavelength of 5500 Å we find a *QE* of $\approx 60\,\%$. So that the photon flux will be:

$$\eta = \frac{I_e}{QE A_{\mathrm{PD}}} = 5.77 \cdot 10^5 \frac{\gamma}{\mathrm{s\ mm}^2} = 0.577 \frac{\gamma}{\mathrm{s}\ \mu\mathrm{m}^2} \tag{5.4}$$

We calculate the flux per $\mu\mathrm{m}^2$, as there is the idea to use astronomical CMOS detectors instead of the photodiode and their typical pixel size is of the order μm. In the following we will estimate the signal generated within such a device and the uncertainties.

As an example we take a ASI183MMPro camera from ZWO[1]. The pixel area A_{pixel} is $\approx 5.76\,\mu\mathrm{m}^2$ and the *QE* at 5500 Å is 84 %. With a typical exposure time t_{exp} of 30 s we would collect N electrons within a pixel:

$$N = \eta \cdot A_{\mathrm{pixel}} \cdot QE \cdot t_{\mathrm{exp}} = 84\mathrm{e}^- \tag{5.5}$$

We would have 84 signal electrons from the SCALA illumination. Additionally, we would collect dark current, which is specified to $0.015\,\mathrm{e}^-/\mathrm{s}$ at 10 °C, so $0.5\,\mathrm{e}^-$ within our exposure time. The noise would then be composed of the statistics of the signal $\Delta_{\mathrm{sig.}} = \sqrt{84}$, the dark noise $\Delta_{\mathrm{dark}} = \sqrt{0.5}$ and the read noise $\Delta_{\mathrm{read}} = 3$, which is specified to $< 3\mathrm{e}^-$. The relative uncertainty on N is therefore:

$$\frac{\Delta N}{N} = \sqrt{\frac{\Delta^2_{\mathrm{sig.}} + \Delta^2_{\mathrm{dark}} + \Delta^2_{\mathrm{read}}}{N^2}} = 11.5\,\% \tag{5.6}$$

As we have $N_{\mathrm{pixel}} = 20 \cdot 10^6$ pixels to average, we obtain a final uncertainty of:

$$\frac{\Delta N}{N \cdot \sqrt{N_{\mathrm{pixel}}}} = 0.003\,\% \tag{5.7}$$

Here we assumed, that the read noise is uncorrelated. It is thus possible to obtain the flux measurements with a CMOS detector. As the room temperature at Hawaii is low, even a device without Peltier cooling might be feasible, this reduces the price to $\approx 840\,€$. Using such detectors, it would be possible to equip all beams with detectors. It would then be possible to measure the emitted flux at each beam at the same time as we illuminate/calibration SNIFS. A measurement of the effective number of beams would not be necessary and therefore all measurements could be performed while night time. The proposed camera can be controlled via Linux and Python and could therefore be easily integrated in the existing software. An example of the calibration of the *QE* of a CMOS sensor (Canon EOS 1000D) is shown in sec. E.2. Aging might be similar for a CMOS sensor and a photodiode, as both are packaged

[1] https://astronomy-imaging-camera.com/product/asi183mm-pro-mono, last checked 21.06.2018.

and sealed with an optical window, to protect the surface of the detector from the ambiance.

Chapter 6

Backgrounds

The removal of the external backgrounds will be discussed in sec. 6.1. We will find, that we can remove these backgrounds without introducing systematic offsets on average. Sec. 6.2 focuses on reflections internal to SCALA, causing background signals for our photodiode measurements. The strength of these reflections will be quantified, to allow a correction of the measured photodiode signal, which is performed in sec. 6.3. In sec. 6.4 the monochromator passband will be characterized, and we obtain an estimate for the amount of light emitted outside the desired passband. Based on the estimate of the out-of-band emission we can remove this background from the photodiode signal, but we also restrict the wavelength range to $\lambda > 4500\,\text{Å}$. In sec. 6.5 we summarize the backgrounds. Afterwards we obtain a preliminary comparison of the calibration by SCALA and the one obtained from CALSPEC standard stars.

6.1 External Background

The external photodiode background consists of the dark current of the photodiode and all light illuminating the photodiode, that did not originate from the SCALA monochromator. To quantify the precision of the background removal, we have taken continuous background measurements for two days. We split the dataset into day and night time and exclude regions, in which the photodiode was saturated or which were taken during twilight.

The daytime dataset was divided into subsets imitating the usual data length. The typical daytime CLAP reading is (2.34 s+5 s+3.06 s=10.4 s) long, including background measurements. For the nighttime dataset the exposure time is varied between 10 s and 300 s as we simulate SNIFS calibration, where the exposure time is adjusted to produce at least 10^4 electrons per spaxel and SCALA wavelength band.

To simulate the usual data shape (pre-signal background, signal, post-signal background) for the reduction code, a constant value was added to the signal region (see fig.6.1), so the individual measurement looks like a top-hat function. The width of the top-hat function represents the exposure time, in which we usually do not have a measurement of the background, while the height represents the simulated light signal, which is usually unknown.

Based on the pre-signal and post-signal background, the data analysis will calculate a background changing linearly in time (see fig. 6.1 solid black line) and remove this background

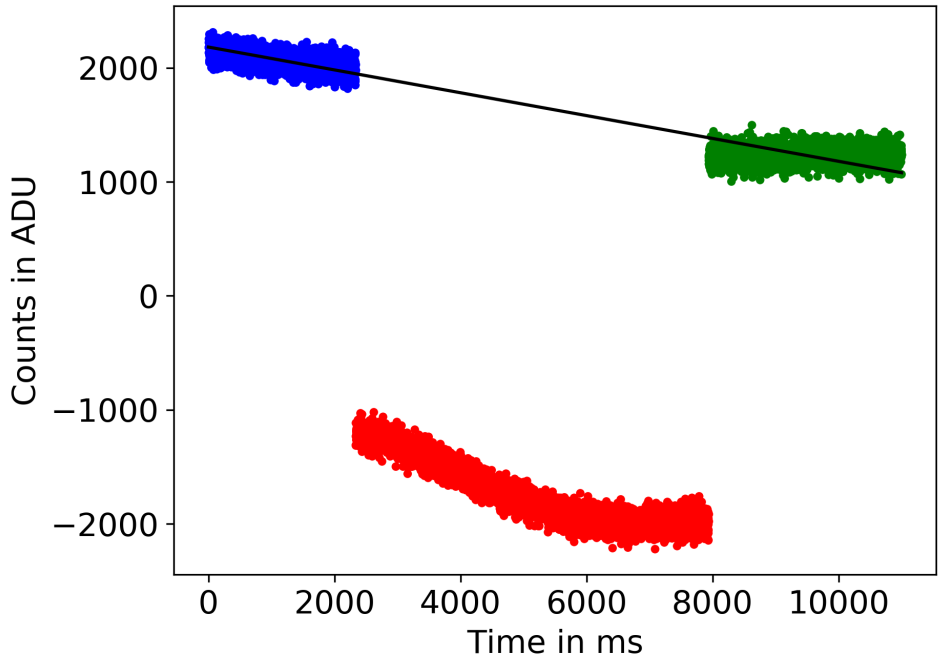

Figure 6.1: Subset of the dataset from fig. 6.2, subdivided into a exposure of 5 s length, with pre-signal background region in blue, signal region in red (5 s) and post-signal background region in green. The estimate of a linearly changing background is shown as solid black line. We show here raw data, evident since the brighter regions have lower count levels.

estimate from the data. The assumption here is, that the additive background is slowly changing in amplitude. The difference between measured signal and introduced top-hat height is then a direct measure of the error on the background removal.

I will first describe the results on the day time dataset, followed by the results on the night time dataset. For the initial tests the signal amplitude was large (3200 ADU). The question remains how large the signal needs to be, to be recognized by the code. To estimate this, the signal amplitude is reduced in the daytime dataset, as a varying background will increase the minimal required signal. This test is shown in appendix. E.1. We find that for signals larger than 600 ADU the code delivers stable results.

6.1.1 Daytime External Background Removal

Daytime SCALA measurements are used to calculate the effective number of beams, the uncertainties discussed here only apply to these measurements. The daytime dataset is shown in fig, 6.2. As described above we introduce a signal to the background measurements. We then use our data reduction code to measure this signal. The difference between extracted and inserted signal, our residuals, is a measure of the quality of the background removal. We obtain these residuals for both photodiodes, CLAP0 and CLAP1. A scatter plot of the residuals obtained

for both photodiodes is shown in fig. 6.3.

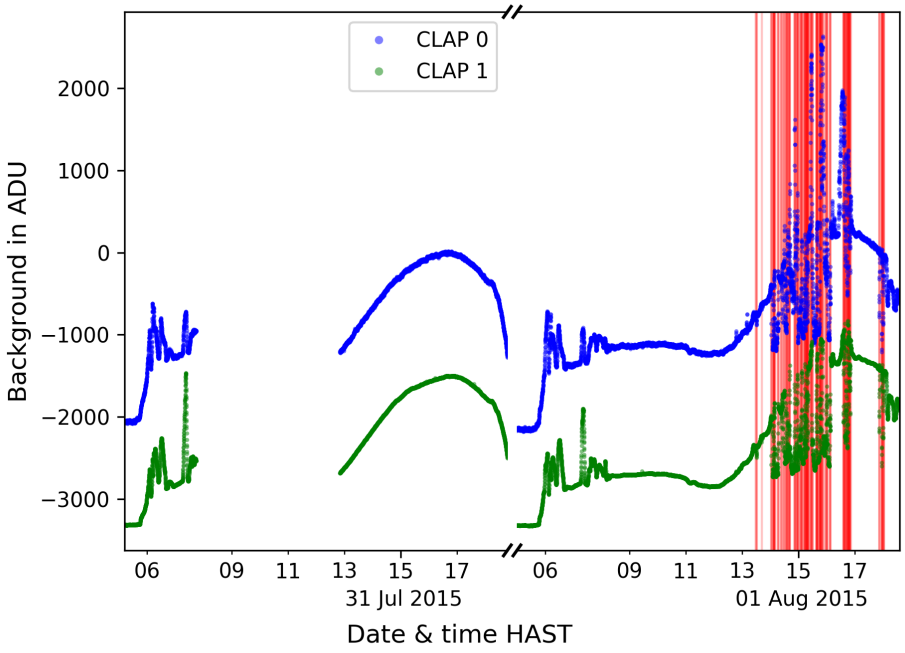

Figure 6.2: Shown are the raw background measurements of both photodiodes (CLAP 0,1), the red regions in time indicate the measurements which belong to the broad, correlated component. The weather cameras of Mauna Kea show quickly moving small clouds for that times. Note that the quick changes in the background are asymmetric between the two photodiodes. At the beginning of day two the additive peaks in CLAP1 are bigger than in CLAP0, while at the end of day two the peaks above the smooth background are nearly gone for CLAP1 (red region).

At a first look we see a correlation between the residuals for both photodiodes[1]. The correlation coefficient is 0.86. For each of the photodiodes a histogram of the residuals shows a narrow core distribution with broad wings. The residuals can be divided in two distributions, a narrow and a broad distribution (small and large residuals), which are colored in fig. 6.3 blue and red respectively. The histograms after splitting are shown on the right panels of fig. 6.3. Both distributions are centered at zero, which means that the background removal does not introduce systematic offsets into the dataset. The devision in two distributions is discussed in the following.

For each photodiode we obtain a histogram of the residuals between inserted and extracted signal. The measurement of the Full Width at Half Maximum (FWHM) of these histograms (one for each photodiode) delivers an estimate on the standard deviation of the narrow distribution. Assuming a Gaussian distribution, we obtain a standard deviation σ of $\sigma = \mathrm{FWHM}/2.355$.

[1]We will find that this correlation is caused by ambient light leaking into the dome. This light is then changing the background for both photodiodes.

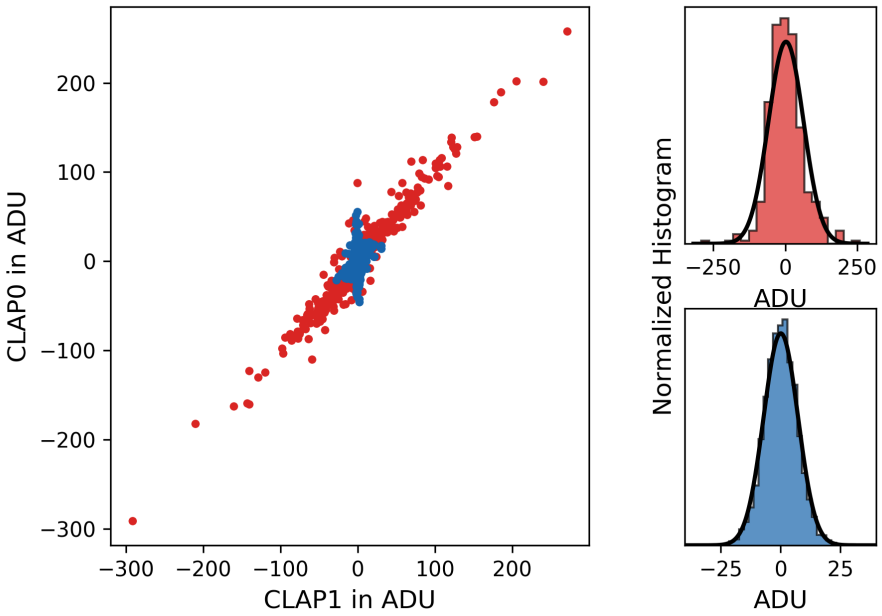

Figure 6.3: The left panel shows the residual between inserted and extracted signal. The residuals are divided into two distributions a narrow and a broad component, this splitting is described in the text. The narrow component is colored blue and the broad one in red. The histograms of CLAP0 after splitting into two components is shown on the right, with corresponding colors.

We divided the dataset into two modes assuming every residual with absolute value bigger than $3.5\sigma_{\text{narrow}}$ to belong to the broad component. We assume that the correlation is caused by a change of ambient light level visible for both photodiodes. One possibility would be clouds modulating the amount of daylight leaking into the dome. Often the modulation of the background due to changing ambient light will be smaller than the cut we use, therefore we can not use the $3.5\sigma_{\text{narrow}}$ cut to obtain the hole subset of measurements affected by modulation e.g. by clouds. The subset of large residuals would have a central hole of $7\sigma_{\text{narrow}}$ width. But if there is a residual bigger than $3.5\sigma_{\text{narrow}}$ the measurements next to it in time will also be affected by modulation, therefore we also attribute them to the subset of strong residuals (see fig. 6.3). We implement this by smoothing our mask to take into account the next neighbors. From fig. 6.3 we see, that there is a strong correlation for the large residuals, we therefore request, that the a strong residual ($> 3.5\sigma_{\text{narrow}}$) is detected in both photodiodes, CLAP0 and CLAP1.

For the subgroup of strong residuals (5 % of daytime dataset) the correlation coefficient is large and positive (0.98), meaning the effect is changing counts on both photodiodes in the same way, which could be caused by a changing background like a change of the ambient light in the dome. The correlation coefficient in this case should vanish, if the residuals of CLAP1

are compared to the residuals of CLAP0 at other times. We compared CLAP1 residuals to CLAP0 residuals next in time (10.4 s offset) and find that the correlation vanishes.

To understand the cause of the two components we plotted the background measurements and marked the times, in which the broad component showed up. In fig. 6.2 we can see, that the strong residuals are found in the second half of the second day. We checked the web cams and the weather forecasts of Mauna Kea, and we found small clouds from a storm passing by, which then quickly modulated the light leaking into the dome.

In fig. 6.2 we see, that there are also background variations different for the two photodiodes. At the beginning of day two the peaks are larger in CLAP1 than in CLAP0, while at the end of the day (red regions), the peaks are nearly gone for CLAP1 but strong in CLAP0. This effect could be caused by the movement of the sun relative to the holes in the dome, and the different locations of the photodiodes in SCALA and the dome. We can not make the dome light tight and some of the measurements need to be performed during the day, as they require work at the summit, so we can not avoid these times. In the following, we will therefore evaluate the induced uncertainties.

The above separation into two distributions (narrow and broad) and the measurement of the widths of their distributions depends on the binning of the used histograms. To avoid this effect we obtain the final uncertainty by calculating Probability Density Functions (PDF) instead of using histograms. Each residual background measurement is therefore described by a Gaussian distribution, with uncertainties calculated from the statistical properties of the individual measurements. The final PDF is then obtained by summing over all residuals. The summation to both axes (CLAP0 & CLAP1) of the PDFs are shown in fig. 6.4 for both modes.

The projected PDFs are afterwards approximated with Gaussian, both using the standard deviation (STD) and the FWHM of the probability distribution. The calculated STDs are listed in table 6.1.

Photodiode	distribution	STD in ADU	FWHM/2.355 in ADU
CLAP 0	narrow	8.9	8.5
	broad	61	44
CLAP 1	narrow	2.5	1.9
	broad	60	17

Table 6.1: STD and FWHM of the probability distributions show in figure 6.4, representing the uncertainty of the background removal while daytime (5s exposure time)

Looking at the distributions in fig. 6.4, we see that the narrow component is better represented by a Gaussian based on the FWHM. For the broad component the Gaussian distribution based on the STD of the PDF is a better estimate. Nevertheless we use for both cases the uncertainties based on the STD, as they are larger.

All distributions are centered around zero, so there is on average no residual background left, which could result in a systematic offset. For the error propagation we are conservative and use the larger uncertainties which are, CLAP0 8.9 ADU and 61 ADU for the narrow and broad component, respectively. For CLAP1 we use 2.5 ADU and 60 ADU respectively. The correlation

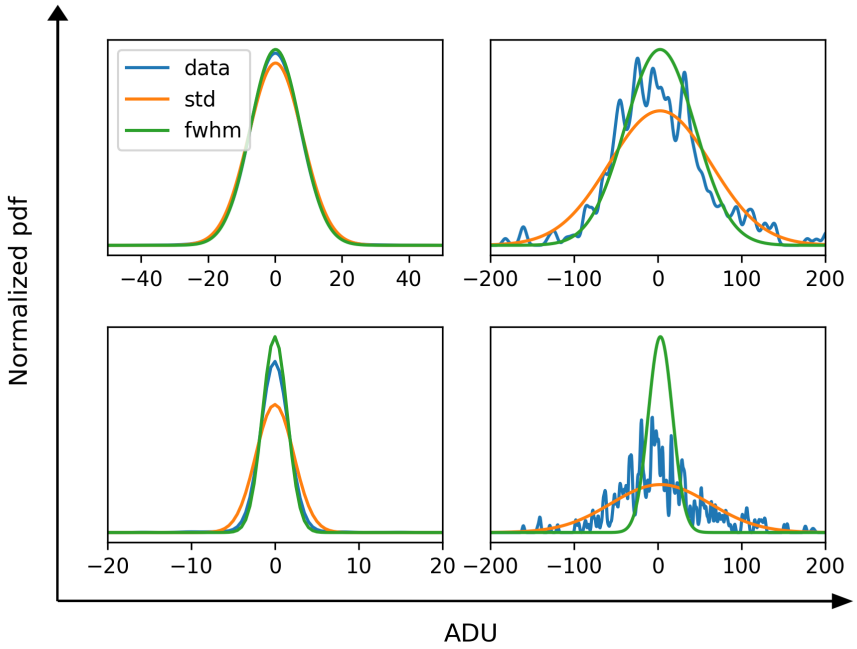

Figure 6.4: Shown are the PDFs of the residual using the individual Gaussian uncertainties and the described splitting of the two modes. The upper row corresponds to CLAP0 while the lower one to CLAP1. The left column shows the narrow component, while the right one shows the broad. The residual distribution is shown in blue, while Gaussian approximations to it are shown in green and orange. The orange one is based on the STD of the distribution, while the green one is based on the FWHM. We see that the distributions are centered on zero, thus no systematic background residual is introduced to the data. The Gaussian approximations are used to estimate the uncertainties conservatively.

coefficient between the CLAPs is 0.15 for the narrow and 0.98 for the broad component.

6.1.2 Nighttime External Background Removal

The background measurements obtained in night time are shown in fig. 6.5. The analysis of the uncertainties of the background removal is performed in the same way, as for the daytime data. We subdivide the dataset into individual exposures, and add a signal to the exposures. The artificial exposures are then analyzed, and the recovered signal is compared to the inserted signal.

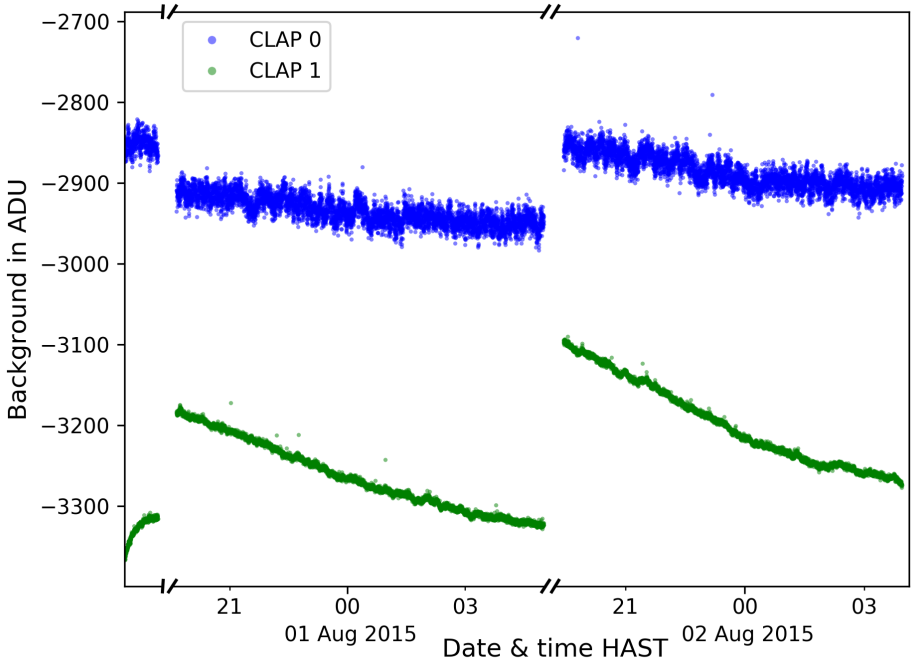

Figure 6.5: Background measured at both photodiodes CLAP 0 & 1 in the first and second night of August 2015. For visibility reasons the background level of CLAP0 has been shifted by 800 ADUs.

Differently from daytime, the residuals of recovered signal and inserted signal do not show multiple components, they can not be split into a narrow and broad component. Finding multiple components while night, would have been a sign, that the description for the daytime - daylight leakage - could not be true.

For CLAP1 we find a STD smaller than 1.8 ADU (see fig. 6.6) while for CLAP0 it is smaller then 8.2 ADU. The correlation coefficient is distributed randomly around zero. As the residuals are estimated on the same dataset, we obtain ≈ 6000 residual measurements for short exposures (5 s) and only 220 for long exposures (295 s)

For exposure time smaller then 20 s, we see a increase of the measured uncertainties, while for longer exposures the uncertainties are nearly constant. The reason for this shape can be

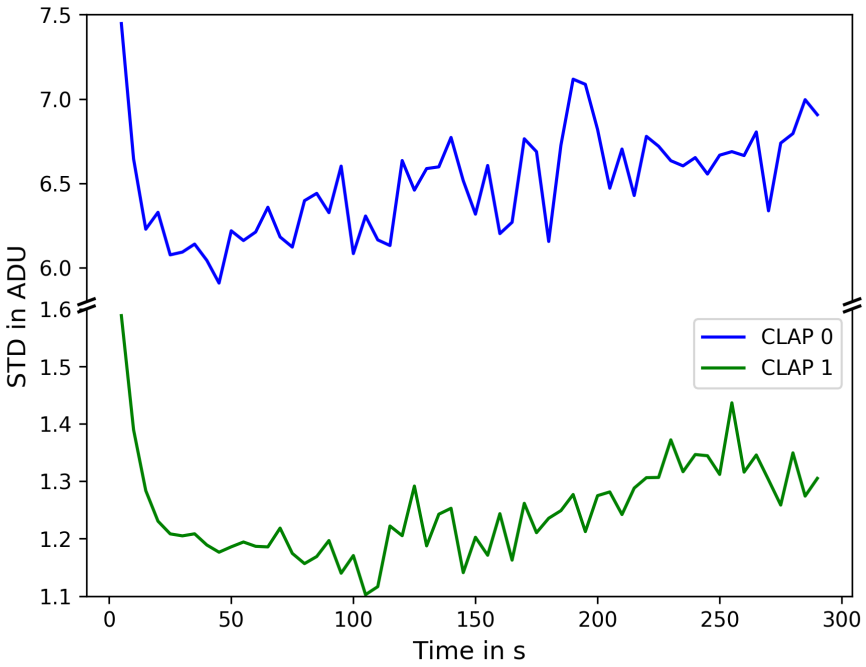

Figure 6.6: Uncertainty of the background removal while night time for CLAP0&1, depending on the exposure time. Shown is the standard deviation of the probability distribution of the residuals. For exposure times longer than 20 s the uncertainties in the background removal are nearly constant.

found in the measurement procedure. While increasing the measurement time for the signal, we do not increase the time, in which we measure the background. Long exposures are therefore limited by the statistical uncertainty of the background measurement.

In case we use a photodiode to sample the light emitted from SCALA continuously (rate $\approx$ 1kHz), an improvement would be obtained by replacing the shutter of the monochromator by a slowly rotating chopper (1-3 Hz). The shutter has been an issue throughout the whole time of SCALA on Hawaii due to mechanical failures. It also would allow one to measure alternately background and signal, and would therefore reduce uncertainties during day time, due to a changing background. The increase of total time by a factor two is not an issue as it could allow calibration during daytime, and therefore would save valuable night time. The chopper itself can be built and tested in the optical lab at the Humboldt University as a second monochromator of same type is used there. Building the device ourselves would also allow an integration in the monochromator and therefore no changes of the software are needed.

In case of CMOS detectors like proposed in sec. 5.2 we need long exposure times, therefore a chopper would not help. We then should improve the shielding of the system to ambient light by additional baffles.

6.2 Internal Backgrounds

The second kind of background contamination is due to light from SCALA, reaching the photodiode via undesired optical paths. We have identified several sources of such backgrounds. Our desired signal is generated by light rays leaving the IS port and reaching the photodiode via a reflection off the collimating mirror of SCALA. The backgrounds are generated by light leaving the IS port, being reflected off the SCALA structure (sometimes multiple times) and then reaching the photodiode via a reflection off the collimating mirror.

The following sections will summarize two main effects and their influence on our measurements. Further effects are discussed and quantified in sec. D.8 and sec. D.7.

6.2.1 Crosstalk between SCALA Beams

As the source of these backgrounds is SCALA, I will first describe the properties of the SCALA emitters. Our IS illuminates a solid angle of $2\pi\,\mathrm{sr}$. Only a small fraction of the emitted light reaches the collimating mirrors and is redirected towards the telescope. The IS is producing a Lambertian illumination, following Lambert's cosine law:

$$I \approx I_0 \cos(\theta) \tag{6.1}$$

where I_0 is the intensity of the emitted light, and θ is the viewing angle[1] onto the IS port. The mirror radius is 10 cm and its distance to the IS port is given by its focal length of 80 cm. The mirror therefore appears under an angle of $14.2\,^\circ$ as seen from the integrating sphere. The amount of light collected by the mirror (c_{eff}) follows from integration:

$$c_{\mathrm{eff}} = \frac{\int_0^{2\pi}\int_0^{0.1244} I_0 \cos(\theta)\sin(\theta)\,\mathrm{d}\theta\,\mathrm{d}\phi}{\int_0^{2\pi}\int_0^{\pi/2} I_0 \cos(\theta)\sin(\theta)\,\mathrm{d}\theta\,\mathrm{d}\phi} = 1.54\,\% \tag{6.2}$$

Only 1.54 % of the light emitted by SCALA will be sent towards the telescope (in a cone of 1° opening angle). The remaining 98.46 % will be reflected off SCALA (black anodized aluminum), and illuminate the dome. Because there is no shielding between the SCALA beams, except close to the IS, it can be expected, that some of the light leaving SCALA at one beam can be detected at the photodiode of another beam.

To reach the *telescope*, the light leaving the IS and not collected by the mirrors needs to be scattered at leased once in a diffuse way and will therefore be redistributed into a solid angle of $2\pi\,\mathrm{sr}$. The solid angle of a spaxel is $4.3 \cdot 10^{-12}\,\mathrm{sr}$. If the IS emits a flux F_0, a spaxel of SNIFS will collect a flux F_{stray} resulting from scattered light and the flux F_{sign} resulting from

[1] Angle between observed ray and symmetry axis of IS. The symmetry axis is given by the center of the port and the center of the IS

the desired illumination.

$$F_{\text{stray}} = F_0 \cdot 0.9844 \cdot \frac{4.3 \cdot 10^{-12}}{2\pi} = 6.74 \cdot 10^{-13}$$
$$F_{\text{sign}} = F_0 \cdot 0.0156 \cdot \frac{4.3 \cdot 10^{-12}}{(\pi/180)^2 \frac{\pi}{4}} = 2.80 \cdot 10^{-10}$$

The stray light Flux F_{stray}, is therefore smaller than 0.24 % of the flux generating the signal F_{sign}, and we can thus neglect it at the moment. Other optical paths reaching the telescope require multiple diffuse scatterings, and are therefore suppressed. SNIFS, mounted to the telescope, will thus not detect this light, but it might be detected by the CLAPs.

In December 2015 we directly measured the amplitude of optical crosstalk between SCALA beams and seen by the *photodiodes*. For this purpose we asked the telescope engineer to close the IS-shutter of the beam equipped with CLAP1 (our reference beam). We afterwards measured the light flux received at the closed beam. Any light detected by CLAP1 was then due to crosstalk (measurement performed while night time). At the same time CLAP0 was measuring the light at an open beam, so that changes in the lamp flux were monitored.

Because of the small amplitude of the crosstalk, several measurements were averaged. The measurements were repeated also with the shutter of CLAP0 closed, this time CLAP1 was used for reference. Due to the small amplitude of the crosstalk the usual method of finding start and end times of the signal region in the data cannot be used[1]. To circumvent this issue, we used an exposure time of 5 s, the same as for the measurement of the effective number of beams. For these kind of measurements we know the length of pre-signal background, signal and post-signal background region, and can therefore use predefined regions to retrieve the signal and the background

We now have three different measurements to take into account. The first measurement, here all IS-shutters except that in front of CLAP1 are open. After external background removal we obtain $C_1^{1,\text{off}}$ for CLAP1. This measurement contains the crosstalk generated from all beams except the reference beam. At the same time CLAP0 measures $C_0^{1,\text{on}}$ counts, this signal is the superposition of the desired signal and crosstalk.

During the second measurement, all IS-shutter except that belonging to CLAP0 are open. We obtain $C_1^{2,\text{on}}$ for CLAP1 and $C_0^{2,\text{off}}$ for CLAP0. Now CLAP0 measures pure crosstalk and CLAP1 measures the superposition of desired signal and crosstalk.

The third measurement needed, is one, where all IS-shutters are open. It provides the relative light level of CLAP0 to CLAP1, which are mounted on different beams (different fiber bundle arms, IS). Here we have $C_0^{3,\text{on}}$ and $C_1^{3,\text{on}}$, both count levels contain desired signal and crosstalk.

These measurements were taken within a few days so that aging of the system is not an issue. As the light source for the crosstalk is the IS, the same light source as for the desired signal, we can define the crosstalk level relative to the signal level. In this way we obtain a multiplicative correction to all our data.

[1] An estimate of the minimal signal amplitude can be found in sec. E.1.

The simplest, first order definition of the crosstalk could be:

$$CT_0' = \frac{C_0^{2,\mathrm{off}}}{C_0^{3,\mathrm{on}}} \cdot \frac{C_1^{3,\mathrm{on}}}{C_1^{2,\mathrm{on}}} \tag{6.3}$$

and

$$CT_1' = \frac{C_1^{1,\mathrm{off}}}{C_1^{3,\mathrm{on}}} \cdot \frac{C_0^{3,\mathrm{on}}}{C_0^{1,\mathrm{on}}} \tag{6.4}$$

for both, CT_0' & CT_1', the first ratio gives the amount of crosstalk relative to the usually measured signal, while the second ratio removes changes in the lamp brightness. This definition does not take into account, that the reference measurement three also contains crosstalk. The following definition also removes the crosstalk in measurement three:

$$CT_0 = \frac{C_0^{2,\mathrm{off}}}{C_0^{3,\mathrm{on}} \cdot (1 - CT_0) \cdot \frac{C_1^{2,\mathrm{on}}}{C_1^{3,\mathrm{on}}}} \tag{6.5}$$

Here we correct the counts of CLAP0 in measurement three for crosstalk of CLAP0, and use the ratio of the counts at CLAP1 in measurement two and three for normalization. We assume, that the crosstalk contribution to CLAP1 did not change, due to closing the shutter of CLAP0 in measurement two. The definition for CLAP1 looks similar. This time we use CLAP0 for normalization, and again assume the change of crosstalk due to the shutter of CLAP1 closed being small.

$$CT_1 = \frac{C_1^{1,\mathrm{off}}}{C_1^{3,\mathrm{on}} \cdot (1 - CT_1) \cdot \frac{C_0^{1,\mathrm{on}}}{C_0^{3,\mathrm{on}}}} \tag{6.6}$$

These quadratic equations can be solved for CT_0 and CT_1.

$$CT_0 = \frac{1}{2} \pm \sqrt{\frac{1}{4} - \frac{C_0^{2,\mathrm{off}}}{C_0^{3\mathrm{on}}} \frac{C_1^{3,\mathrm{on}}}{C_1^{2,\mathrm{on}}}} \tag{6.7}$$

and:

$$CT_1 = \frac{1}{2} \pm \sqrt{\frac{1}{4} - \frac{C_1^{1,\mathrm{off}}}{C_1^{3\mathrm{on}}} \frac{C_0^{3,\mathrm{on}}}{C_0^{1,\mathrm{on}}}} \tag{6.8}$$

Because of the quadratic equations (eq. 6.5 & 6.6) we obtain each time two solutions, where the larger can be rejected, as the crosstalk is small compared to the signal. This information is obtained from the first order approach. Based on the above equations, the fraction of signal detected by the photodiode but caused by crosstalk can be calculated together with the uncertainties. Fig. 6.7 shows the result using eq. 6.7 & 6.8 (quadratic) together with the first order expectation eq. 6.3 & 6.4.

For wavelengths shorter than 7000 Å crosstalk contributes 2.5 % of the usual CLAP1 signal amplitude. For CLAP0 we measured 3.4 % of the original signal being produced by crosstalk. For wavelength longer than 7000 Å the amplitude of crosstalk is linearly increasing, reaching

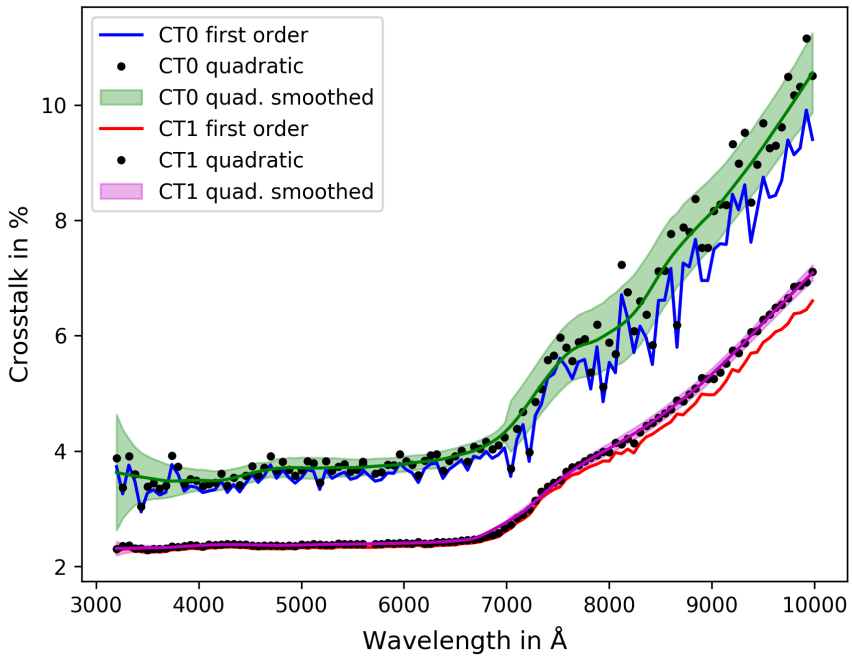

Figure 6.7: Fraction of signal detected by the photodiodes but caused by crosstalk between SCALA beams. Based on the measurement we can define a first order approximation for the crosstalk eqs. 6.3 & 6.4 blue and red respectively. The second order approximation eqs. 6.5 & 6.6 is shown in green and magenta. The black data points indicate the measurements before smoothing (green & magenta), The crosstalk for CLAP0 is larger than for CLAP1.

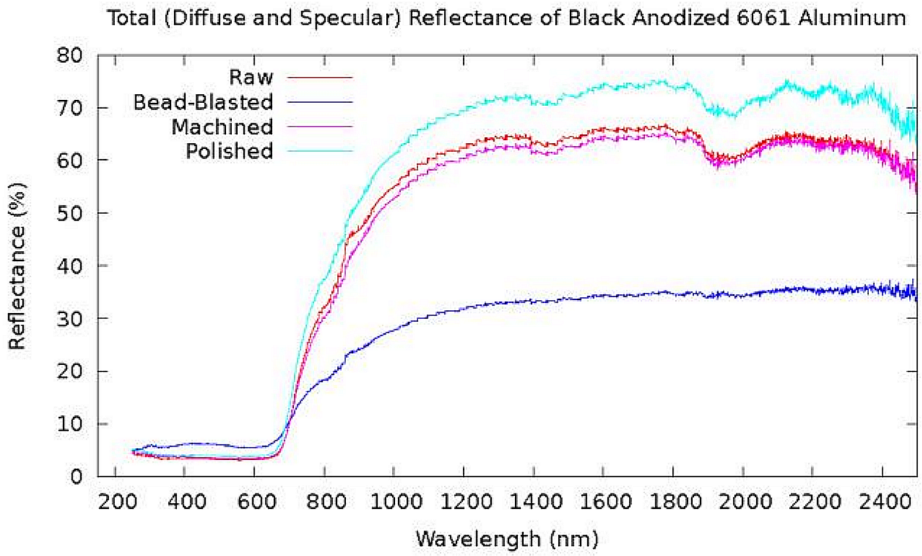

Figure 2. Total reflectance of aluminum samples.

Figure 6.8: Reflection of various kinds of black anodized Aluminium from [Marshall and et al., 2014]. The same wavelength behavior is visible as for the crosstalk comp. to fig. 6.7. Low reflectivity up to 7000 Å, afterwards quickly growing.

up to 11 % for CLAP0 and up to 7 % for CLAP1 at around 1μm. The increase of crosstalk in the infrared is enhanced by the second order definition compared to the first order expectation. As we now have quantified the amplitude of the crosstalk, we can correct the photodiode measurements.

The wavelength dependence of the crosstalk and the larger contribution for CLAP0, will be discussed in the following. The crosstalk shown in fig. 6.7 is proportional to the reflectivity of the object, which redirected the light towards the photodiode. Figure 6.8 shows the measured reflectivity of various sorts of black anodized aluminum, for wavelength longer than 7000 Å we see an increase in reflectivity. The reflectivity of black anodized aluminum shows the same behavior as the crosstalk, constant and low for visual wavelength and higher in the infrared. Based on these similarities we think the crosstalk is mostly caused by reflections off the SCALA structure and not e.g. off the dome insulation. A future improvement would then be obtained by painting SCALA with coatings with low reflectivity in all wavelength. The crosstalk can also be reduced by reducing the solid angle illuminated by the IS, e.g. by baffles.

The crosstalk is larger for CLAP0 than for CLAP1. This might reflect that CLAP1 is mounted to beam D3, while CLAP0 is mounted to beam B2 (see fig. 6.15). As the U-shaped light shield is opened downwards, we can see more SCALA beams from the higher CLAP0 position than from the lower CLAP1 position.

So far we have neglected crosstalk light seen by SNIFS. Using the entrance pupil mask, we

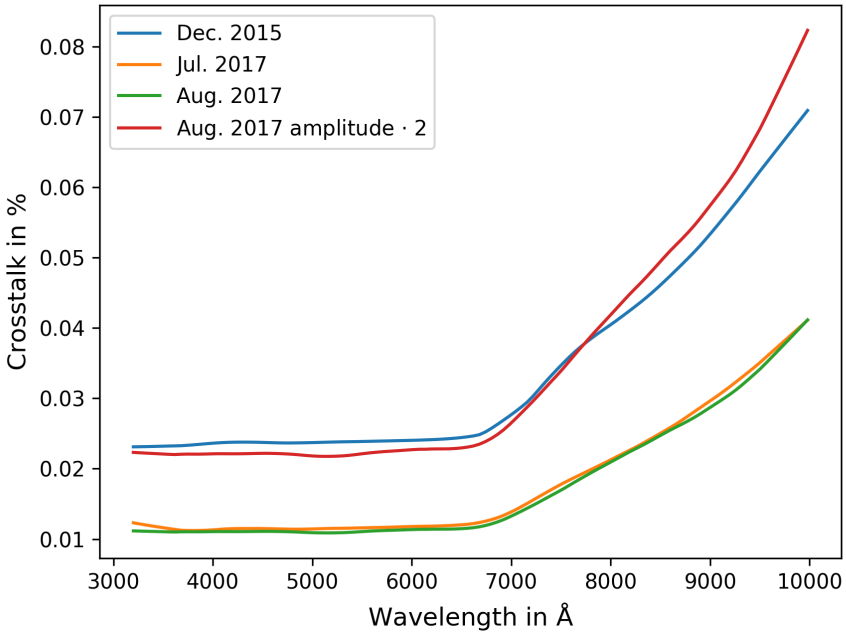

Figure 6.9: Crosstalk for CLAP1 measured in Dec. 2015 compared to two measurements in July and Aug. 2017. The amplitude of the crosstalk decreased by a factor two, for comparison the Aug. 2017 measurement is shown scaled by a factor two.

can test whether the telescope and SNIFS can see the crosstalk light. Therefore we compare the RoC (eq. 4.7) with and without mask. The mask would suppress the number of possible optical path in between SCALA and SNIFS and / or introduce at least one more scattering surface for the diffuse light, which causes the crosstalk. The signal amplitude of SNIFS should therefore decrease when introducing the mask. The signal detected by the photodiodes is unaffected by the mask, as the photodiode is placed earlier in the optical chain than the mask. We do not find a change of the RoC, which shows that light scattered before the entrance pupil of the telescope does not significantly affect the signal detected by SNIFS (see fig. 10.16 on p.127 of [Lombardo, 2017]).

At the end of August 2017 we repeated the measurement of the crosstalk and found, that the crosstalk level decreased by 50 % (see fig. 6.9). We attribute this change to dust accumulation on the SCALA structure, example pictures showing the amount of accumulated dust are shown in fig. D.2 & D.3.

Finally we have shown that crosstalk reaches the photodiode via a reflection off the SCALA mirror and the housing of the IS. We asked the telescope engineer to place a light blocker at the end of the U-shaped light shield. No light was therefore able to reach the mirror and being reflected towards the photodiode. The lower end of the U-shaped light shield was however open (close to the mirror). In case the crosstalk light would reach the photodiode via diffuse reflections

in the U-shaped light shield, we should still measure it. With the light blocker mounted, no crosstalk signal larger than the uncertainties (0.5 %) was detected. We therefore conclude, that the crosstalk light reaches the photodiode via a reflection off the mirror. Based on the geometry the crosstalk light needs to come from the direction of the IS. The shortest way from one beam to another, where it is detected, looks as followed. Light leaving the first IS misses the collimating mirror, is then diffusely scattered of the SCALA structure and illuminates the housing of another IS. Here the light is scattered again and hits via a reflection off the SCALA mirror the photodiode. Therefore at least two reflections off the SCALA structure are needed.

6.2.2 Reflection off the IS Light Shield

The second background discussed here is caused by a specular reflection close to the IS port. Our IS is equipped with three exit ports which illuminate the three collimating mirrors within one of the SCALA modules. In front of the IS a light shield is mounted. This is necessary, as one could otherwise see all three exit ports of the IS from each mirror. With the light shield SCALA looks like a single artificial planet with 1° diameter. Without a light shield the additional visible ports would create further artificial planets arranged around the desired planet. As these planets being more distant than 1° from the desired planet, their light would not reach the focal plane of the telescope (limited field of view) and would create stray light within it.

A picture of the IS with light shield is shown in fig. 6.10. It can be seen immediately, that light leaving the integrating sphere port under a big angle to the symmetry axis, would usually leave the system, but now illuminates the light shield. From there it is reflected towards the collimating mirror and then detected by the photodiode.

In the following the reflection will be quantified to correct the photodiode measurement. To understand the origin of background signals we have sent a Canon EOS 1000D camera to Hawaii. This camera is mounted in a position similar to the photodiode. To measure the direction from which the background light originates, the camera is equipped with a pinhole objective. The whole device is therefore working like a pinhole camera.

A daytime picture is shown in fig. 6.11. The camera is looking towards the collimating mirror, it will therefore partially see itself, but it also sees the IS and its support.

The original plan was to quantify the amount of light seen, therefore the quantum efficiency of the Canon EOS 1000D was measured. The results of this calibration are discussion and shown in sec. E.2.

The first measurements (fig. 6.11) showed, that the camera was mounted too close to the mirror, and the housing of the camera therefore obscured the light path from the IS port to the mirror. The obtained data could only be used to qualitatively understand the origin of the detected light. Fig. 6.12 therefore shows a superposition of the daytime image (fig. 6.11) with a map obtained from night time exposures with SCALA emitting light. The yellow patches show regions, where light is reflected. We see that light emitted from the IS can reach the photodiode via a reflection off the IS support rod, but also via a reflection off the light shield mounted in front of the IS. The reflection off the rod will be shielded away by the U-shaped light shield in font of the photodiode. The light reflected off the light shield in front of the IS can be detected and is the source of the background discussed here.

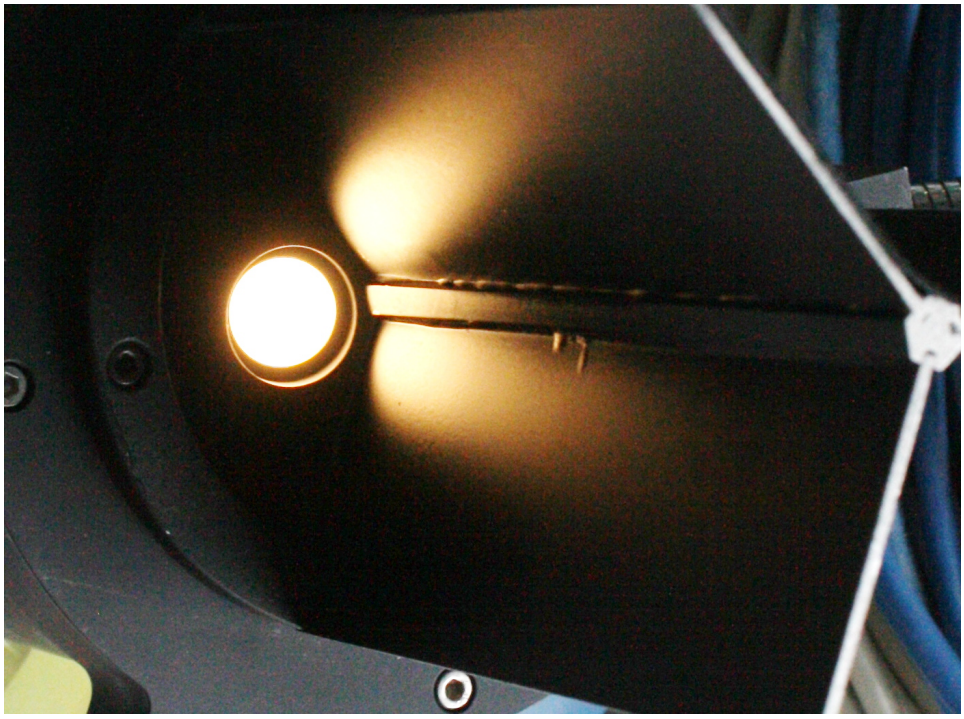

Figure 6.10: Image of the illuminated prototype IS, showing the reflection off the light shield, but also showing the reflections off the walls around the IS port.

The amount of light reflected off the light shield can be obtained by comparison of measurements with and without the light shield. To prevent the other ports of the IS to be seen by the photodiode, when there is no light shield, these are blocked. To block the light, we use Acktar Metal Velvet with a reflectivity $< 0.7\,\%$. The light, which would usually leave these ports is absorbed to $99.3\,\%$. The residual light is reflected ($r_{\mathrm{Acktar}} = 0.7\,\%$) backwards into the IS and will therefore increase the flux level at the third port, which was left open. Using the throughput τ_{IS} of the IS of $\tau_{\mathrm{IS}} = 15\,\%$ ([Lombardo et al., 2014]), we can estimate the increase at the third port to be $2 r_{\mathrm{Acktar}} \tau_{\mathrm{IS}} = 0.21\,\%$ of the flux level before closing the ports, and can be neglected.

We asked the telescope engineer to unmount the light shield in front of the IS and closed the two ports with Acktar Metal Velvet in January 2018. The amount of light reflected of the light shield was then measured against a measurement two days before, with the mounted light shield. While unmounting it was noticed, that the light shield was covered with dust, see fig. D.3. A second measurement was thus performed to investigate the influence of the dust on the amount of light reflected off the light shield. The light shield was therefore cleaned and mounted again. All measurements have been performed during Hawaiian night time, to suppress the influence of daylight leaking into the dome.

Fig. 6.13 shows the results of the measurements. Dust on the surface of the light shield results in a reduction of the measured photodiode current by $8\,\%$, compared to a clean light shield.

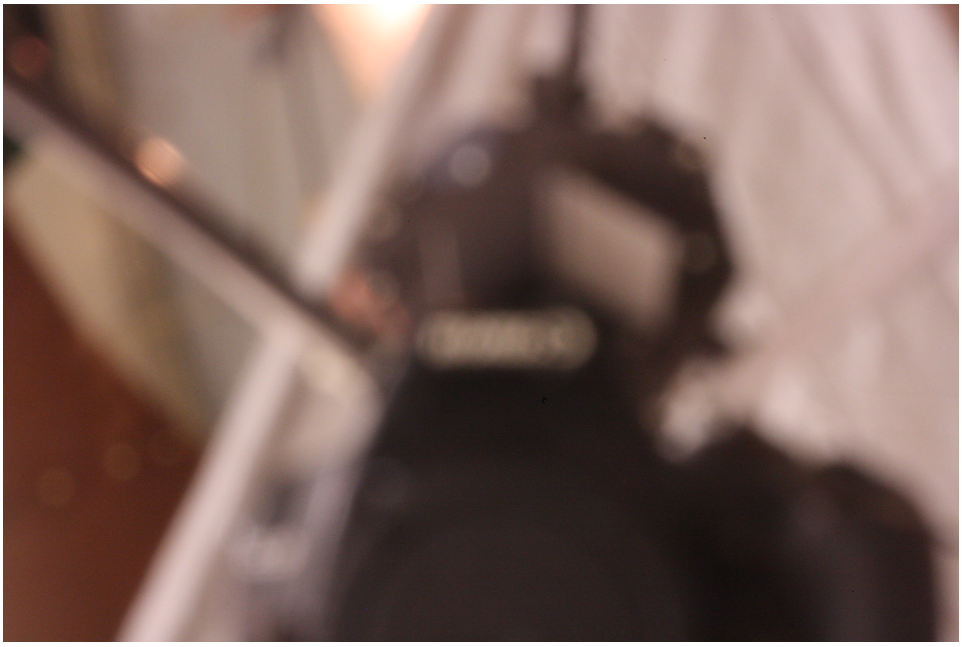

Figure 6.11: We see an image taken with the pinhole camera. As the camera is looking towards one of SCALAs collimating mirrors, the camera can see itself, black structure in the lower half of the image. Above it we see the IS with the light shield. Also visible are the rods holding the integrating sphere.

The removal of the light shield and closing the other two ports results in a reduction of 12 % for wavelength shorter than 7000 Å, compared to a clean light shield. For longer wavelength the effect linearly increases up to 20 % at 1 μm.

The wavelength dependence of this effect is similar to the one of the crosstalk, as also the light shield is made from black anodized aluminum.

From laboratory measurements we learned that the light is reflected on the light shield via a specular reflection and not via a diffuse reflection. This effect is also confirmed by the Hawaiian measurements as the measured photodiode current is decreased due to dust accumulation. A possible improvement could be obtained by structuring the surface of the light shield and application of a paint with low infrared reflectivity. Both ideas can be obtained by the application of a self adhesive film with a black velvet surface. Now that the amplitude of this background is measured, we can correct the photodiode measurements.

Two further processes for background signals have been identified. Light can be reflected off the walls of the drilling of the IS port (see fig. 6.10). The amplitude is only weakly depending on the wavelength and ≈ 2 % of the usual photodiode signal, for more details see sec. D.8. The second process is concerning the photodiode itself. Light can be reflected off the photodiode housing, which is made of metal, and reach the sensitive area. The amplitude of the effect is large 12 to 15 % but its wavelength dependence is small. Its measurement is discussed in sec. D.7.

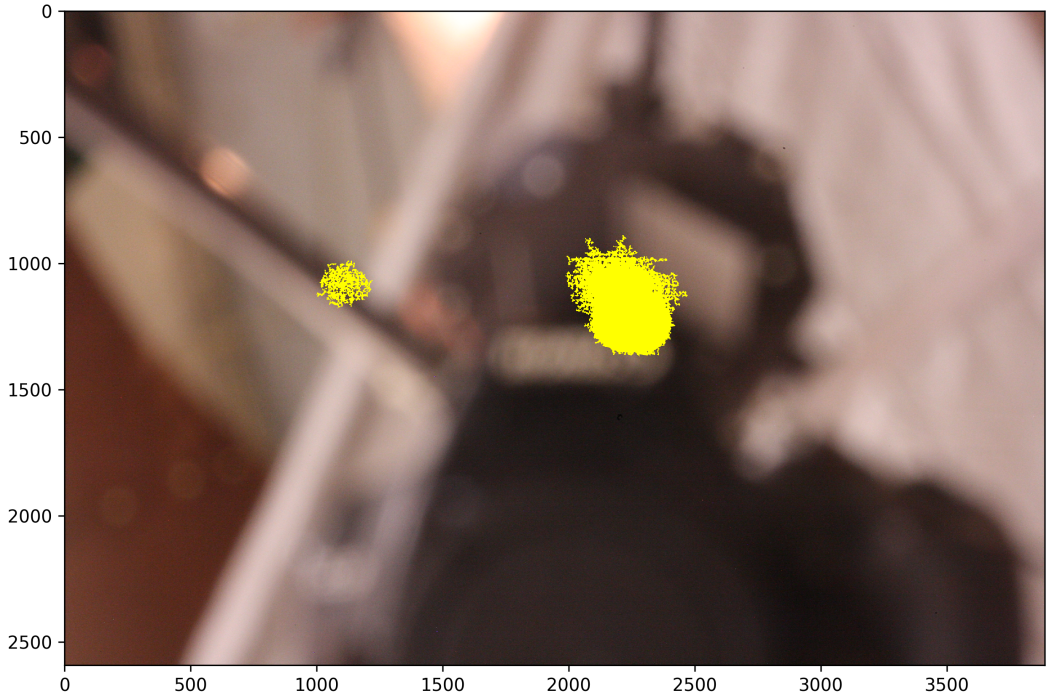

Figure 6.12: Same picture as in fig. 6.11, but now regions which are sources of light are shown in yellow. We therefore see that light is reflected off from one of the support rods of the IS, but also light is reflected off the light shield which is mounted in front of the IS.

6.3 Combining the External and Internal Backgrounds

In the previous sections we have identified backgrounds to the photodiode current, which can affect the transfer of the flux calibration from the photodiode to the spectrograph. These backgrounds can disturb the measurement of the flux emitted from SCALA in two places, which we can identify from eq. 4.3, repeated here:

$$F_{\mathrm{SCALA}} = (I_{\mathrm{CLAP1}} - B_i)\frac{1}{g \cdot R} \cdot \frac{A_{\mathrm{Beam}}}{A_{\mathrm{PD}}} \cdot N_{\mathrm{eff.}} \tag{6.9}$$

We need to account for these backgrounds in the measurement of our reference photodiode $(I_{\mathrm{CLAP1}} - B_i)$ and in the measurement of the effective number of beams $N_{\mathrm{eff.}}$ (eq. 4.2). I will first discuss the effect on the reference photodiode. Afterwards the results will be applied to the measurement of the effective number of beams.

Background removal from single measurement

In eq. 4.3 the photodiode signal I_{CLAP1} was affected by several backgrounds B_i. The above sections showed that we can split the backgrounds into two groups, the external and internal backgrounds. The light sources for the external backgrounds are *independent* of SCALA, like

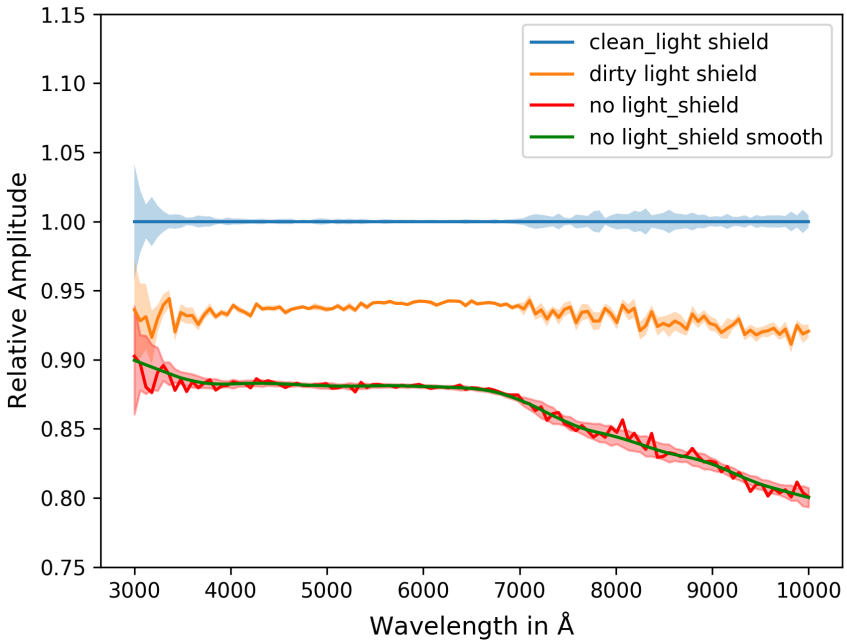

Figure 6.13: Flux ratios referenced to a clean light shield. The dust on the light shield reduces the flux seen by the photodiode by 8 %, due to its diffuse properties. Removing the light shield results in a reduction of the photodiode flux by 12 to 20 %.

light leaking into the dome or dark current. The internal backgrounds are caused by reflections within SCALA and are therefore *proportional* to the light emitted from SCALA, they are proportional to the desired signal. Therefore we first correct the data for the external background $B_{\text{Ext.}}$ and afterwards for the internal backgrounds, the corrected signal $I_{\text{Corr.}}$ is therefore obtained as:

$$I_{\text{Corr.}} = (I_{\text{PD}} - B_{\text{Ext.}}) \cdot (1 - CT - R_{\text{LS.}} - R_{\text{Port}} - R_{\text{PDH.}}) \tag{6.10}$$

where CT is the crosstalk between SCALA beams (sec. 6.2.1), $R_{\text{LS.}}$ is the reflection off the IS light shield (sec. 6.2.2), R_{Port} is the reflection off the IS port walls (sec. D.8) and $R_{\text{PDH.}}$ is the reflections off the metallic photodiode housing (sec. D.7). All internal backgrounds are shown in fig. 6.14 with their measurement uncertainties.

We see that $27\,\text{to}\,42 \pm 4\,\%$ of the signal detected by the photodiodes is caused by internal backgrounds. The uncertainty on the absolute scale is limited by the measurement of the amount of light reflected off the photodiode housing ($\pm 4\,\%$). The limitation here is given by the limited knowledge about the used aperture areas. The wavelength dependence of the backgrounds is limited by the uncertainty on the amount of light which is reflected off the light shield.

The internal reflections could be suppressed by improvements to the SCALA setup. The

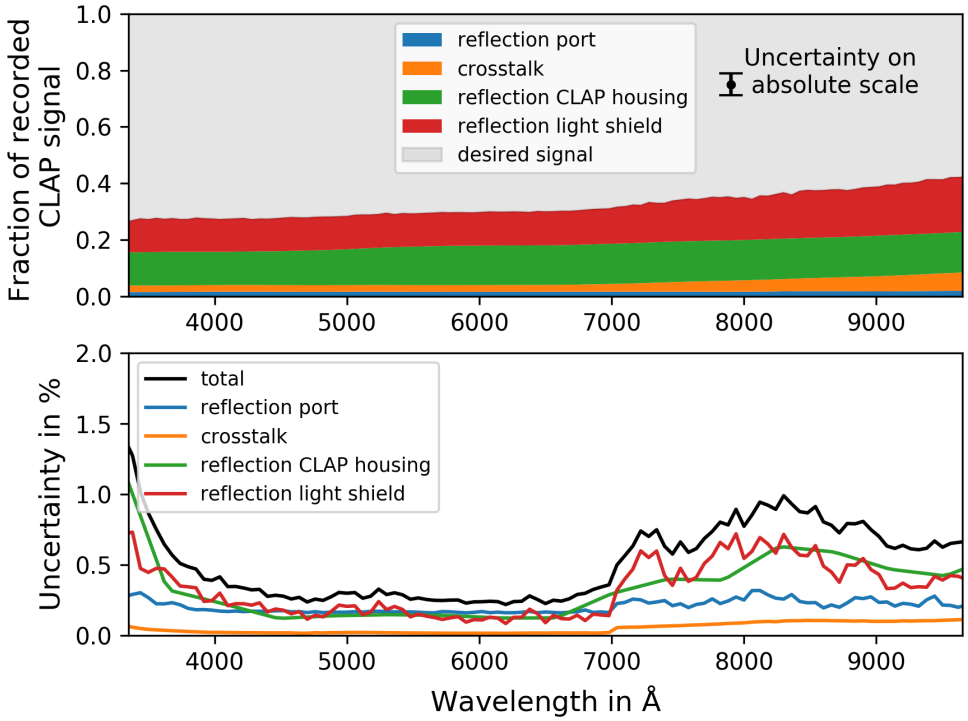

Figure 6.14: The upper panel shows the composition of the light reaching the photodiode. The individual backgrounds are shown with color shaded regions, the desired signal is therefore only 58-63 % of the registered photodiode current. The lower panel provides the measurement uncertainties (relative uncertainties) to the shaded regions in the top panel.

attachment of black velvet self adhesive film on the IS light shield could suppress reflections there. A baffle system attached to each of the IS ports, could reduce the solid angle illuminated by the IS to a region comparable to the extent of the collimating mirrors. This would completely remove the need of a light shield and could additionally reduce the amount of crosstalk between beams.

Uncertainty on effective number of SCALA beams

$N_{\text{eff.}}$ is needed since the different optical beams, although being constructed out of the same kind of optical components, have slightly different relative throughputs. We therefore use one beam (D3) as reference beam for our measurements. For our naming convention of the beams see fig. 6.15. N_{eff} gives the number of beams of kind D3, needed to reproduce the amount of light emitted by SCALA. To measure N_{eff} we have iteratively placed CLAP0 in all beams,

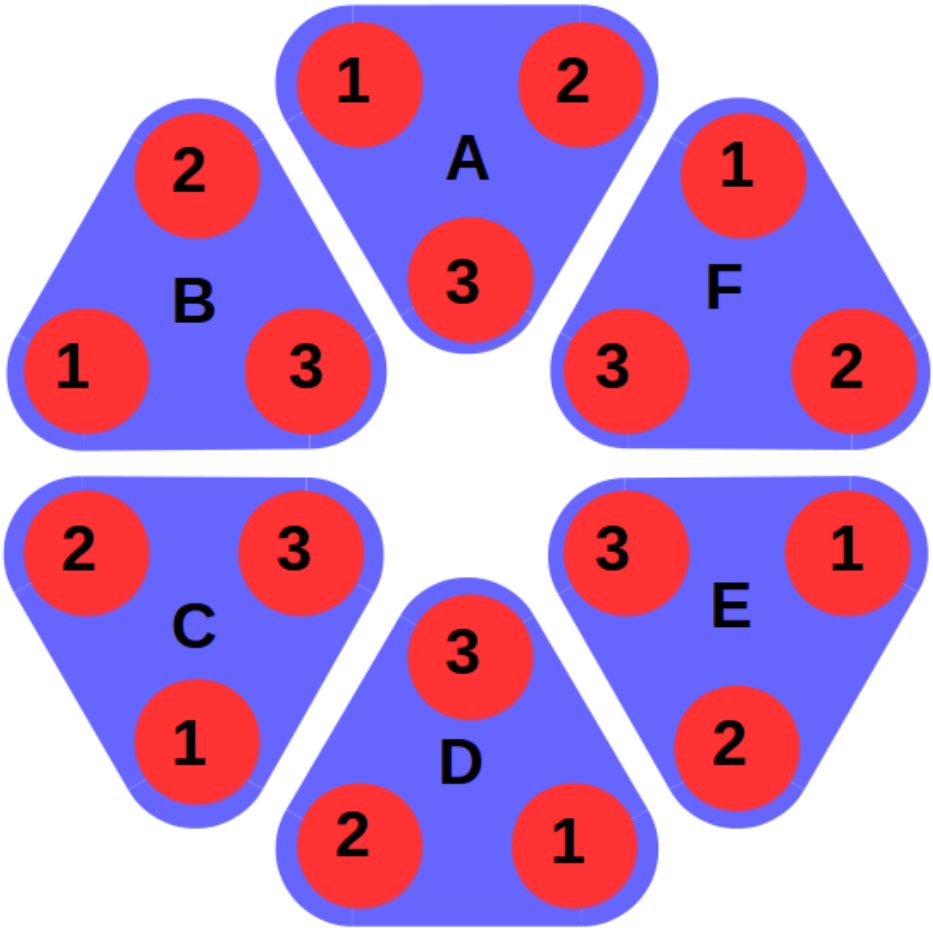

Figure 6.15: Shown is the SCALA module naming convention. The modules are named A to F and in each one the mirrors are counted from 1 to 3. D3 is the reference beam with CLAP1.

except the reference beam, which is equipped with CLAP1 permanently.

In sec. 4.4 the effective number of SCALA beams was defined by eq. 4.2 and is repeated here using the corrections for external and internal backgrounds obtained above:

$$N_{\text{eff}} = 1 + \sum_{i=1}^{17} \frac{I^i_{\text{Corr.},0}}{I^i_{\text{Corr.},1}} \cdot \frac{g_1 R^i_1}{g_0 R^i_0} = 1 + \sum_{i=1}^{17} H_i \tag{6.11}$$

where $I^i_{\text{Corr.},0}$ & $I^i_{\text{Corr.},1}$ are the for background corrected photodiode signals, g_0 & g_1 are the amplifier gains and R_0 & R_1 are the photodiode responsivities. Based on these corrections we obtain N_{eff} as shown in fig. 6.16 in blue. N_{eff} is larger than 18, which means that the

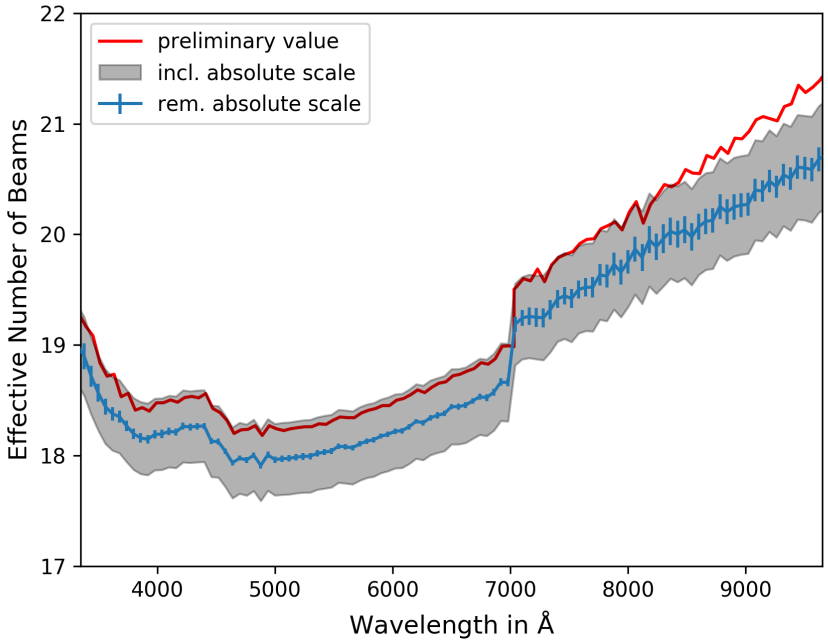

Figure 6.16: Effective number of reference beams required to reproduce the light output of SCALA together with its uncertainty (blue). Had all beams been equal, $N_{\text{eff.}}$ would be 18. That the measured values are larger, means that the reference beam is less transmitting than the average beam. The previously used value provided by Simona Lombardo only accounts for crosstalk and external background, and is shown in red. Taking into account the internal reflections reduced the overall amplitude of $N_{\text{eff.}}$ and reduced the slope for long wavelength. The gray band represents the uncertainty on the effective number of beams, the width is driven by the uncertainty on the reflection off the photodiode housing. The steps at 7000 Å is caused by the switch between Xenon and Tungsten Lamp.

throughput of the reference beam is smaller than the throughput of the average SCALA beam. The wavelength dependent shape is introduced by variations in the PTFE material used for the IS, as shown in [Lombardo, 2017], fig. 6.18. The discontinuity at 7000 Å is due to the exchange

of lamps, which illuminate the entrance slit of the monochromator differently and introduce therefore a weighting between the fiber bundle arms. The precision for N_{eff} is limited by several effects, which are discussed in the following and are shown in fig. 6.17.

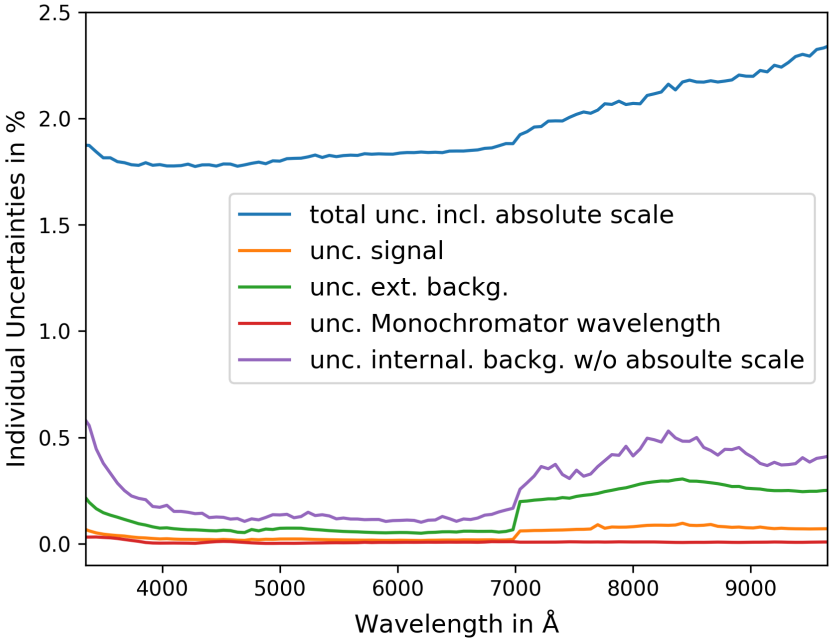

Figure 6.17: Relative uncertainties contributing to the effective number of beams shown in fig. 6.16. The individual uncertainties are discussed in the text.

The contributing uncertainties (sorted by size) are: uncertainty on the internal backgrounds, uncertainty on the external backgrounds, statistical uncertainty on the signal and the reproducibility of the wavelength selected by the monochromator[1].

The precision for the internal backgrounds is limited by the uncertainties on the reflection off the IS light shield and by the reflections off the photodiode housing (see fig. 6.14).

The measurement of N_{eff} is only possible during daytime, as it requires the manual movement of the CLAP0 photodiode and the UH88 is not staffed at night-time. We therefore need to take into account the potentially increased uncertainties during daytime. The first step of doing this is to determine which observations could be affected by rapidly changing backgrounds. The alternative of only performing one beam measurement each night would require continuous work at the mountain and would be limited by the system evolution instead. We therefore follow the first approach. To check for rapidly changing backgrounds we look at the external background level for the performed N_{eff} measurements which is shown in fig. 6.18, with labels

[1] In the measurement of N_{eff}, we can not use SNIFS to measure the wavelength of the monochromator as the exposure times are to short. We therefore need to rely on the reproducability of the monochromator.

for the measured beams. Looking at the background we see that there are two behaviors:

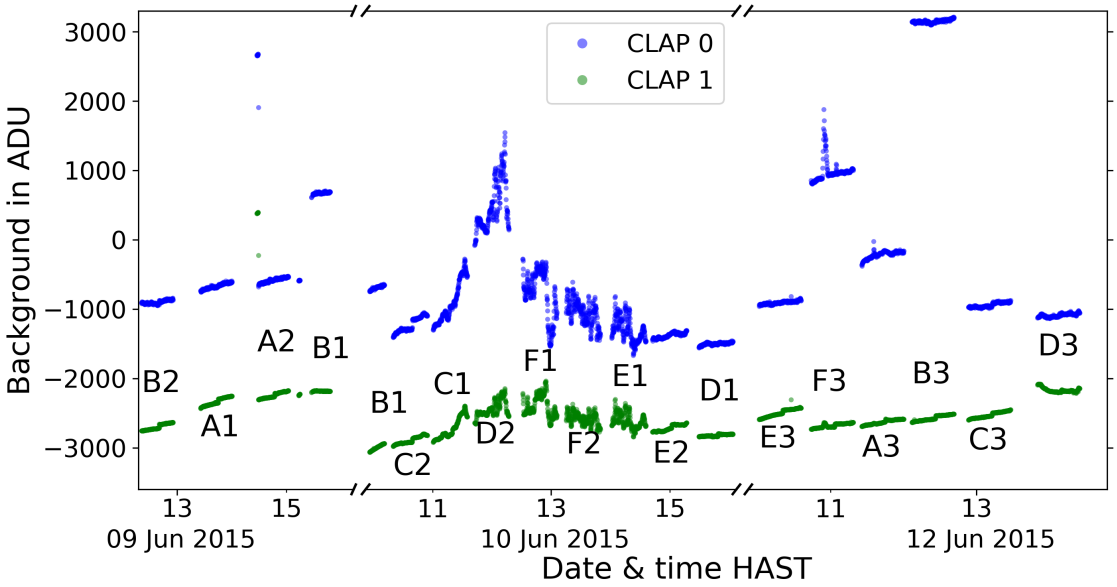

Figure 6.18: Background measurements of the two photodiodes while measuring the effective number of SCALA beams on Hawaii in 2015. The measurements are distributed over three days, the second and third day are affected by quickly changing backgrounds. The labels (A-F 1-3) indicate the name of the beam under investigation, following the naming convention of fig 6.15.

smoothly changing or rapidly varying background. We classify the measurements C1, D2, E1, F1, F2, F3 (6/17 measurements) to the rapidly changing backgrounds, for which we obtained the uncertainties and correlation coefficient in sec. 6.1.1. For measurements with rapidly changing backgrounds we obtained an uncertainty for the removal of the external background of 61 ADU (CLAP0) and 60 ADU (CLAP1) with a correlation coefficient of 0.98 (see sec. 6.1.1). Based on eq. D.18 we can then estimate the uncertainty on the individual H^i_{fast} (case of fast variations) to:

$$\Delta H^i_{\text{fast}} = \sqrt{\left(\frac{61}{800}\right)^2 - 2\left(\frac{61}{800}\right)\left(\frac{60}{800}\right)0.98 + \left(\frac{60}{800}\right)^2} = 1.52\,\% \tag{6.12}$$

Where the uncertainty on the photodiode current is given by the uncertainty on the background removal. The minimal measured photodiode current is 800 ADU (at a wavelength of 8500 Å). In case of slowly changing backgrounds we are also limited by the background removal, but the uncertainties are smaller like described in sec. 6.1.1. The uncertainty is 8.9 ADU (CLAP0) and 2.5 ADU (CLAP1) with a correlation coefficient of 0.15. Following eq. D.18 we find for times with slowly changing background an uncertainty of:

$$\Delta H^i_{\text{slow}} = \sqrt{\left(\frac{8.9}{800}\right)^2 - 2\left(\frac{8.9}{800}\right)\left(\frac{2.5}{800}\right)0.15 + \left(\frac{2.5}{800}\right)^2} = 1.11\,\% \tag{6.13}$$

We then obtain a preliminary approximation for the uncertainty of the external background removal, assuming all beams to be equal in throughput. The uncertainty of N_{eff} at 8500 Å is therefore

$$\frac{\Delta N_{\text{eff}}}{N_{\text{eff}}} = \frac{1}{18}\sqrt{11 \cdot (1.1\,\%)^2 + 6 \cdot (1.5\,\%)^2} = 0.29\,\% \tag{6.14}$$

With the individual H^i being uncorrelated as the CLAP measurements are taken at different times. In sec. 6.1.1 we showed that only measurements taken at the same time are correlated due to the external background changing in time.

This approximation is not including the different relative throughputs of the beams nor the statistical uncertainty of the background. The full calculation taking these details into account is straight forward but lengthy, so it is not reproduced here. The full result is given in fig. 6.17 green curve and is found to be $\approx 30\,\%$ larger than the approximation shown here.

In the measurement of N_{eff} the individual exposure times are short, so SNIFS can not be used to determine the true wavelength of the light emitted by SCALA[1]. We therefore need to rely on the wavelength reproducibility of the monochromator. To evaluate the resulting uncertainty we parameterize the wavelength as a nominal wavelength, which is the same for all measurements of N_{eff}, and a scatter in wavelength of 10 Å (Based on measurements with SNIFS at repeated wavelength). With this approach the responses $R_0^i \& R_1^i$ become independent of i. We can then take the gain and response ratios in front of the summation (eq. 6.11). The uncertainty due to the reproducibility is then the amplitude of the scatter (10 Å) multiplied with the slope of $I^i_{\text{Corr.},0}/I^i_{\text{Corr.},1}$. The result of this calculation is shown in fig. 6.17 red line, we see that the effect is negligible. We can further see that systematic uncertainties affecting the determination of the photodiode gain and response are strongly suppressed for the measurement of N_{eff} as the measured quantity is proportional to the ratio of these quantities.

The statistical uncertainty on the signal (I_{PD} in eq. 6.10) level of the CLAP measurement is small compared to the uncertainty of the external background. The later includes the statistical uncertainty and also the systematic uncertainty due to external background removal. However, the statistical uncertainties can be reduced by an increase of the read frequency of the photodiodes. The uncertainties on the internal backgrounds can be reduced by improvements to the SCALA setup. The external background can not be reduced by us, as this requires changes to the dome of the UH88 telescope. However, we could take care that these measurements are performed on days without clouds, so without rapid modulations of the light leaking into the dome. The possible improvement is evaluated and shown in fig. 6.19. Four different cases are shown, a day, where all measurements are affected by rapid modulations of the external background ("only rapid variations"). The conditions, which were present in the measurement of N_{eff} are shown for comparison with the label "our measurement". In case no rapid modulations are present we would obtain the uncertainties labeled with "no rapid variations". The smallest uncertainties would be obtained for measurements taken during night time. In this case we are limited by the statistical uncertainties of the background measurements, as explained in sec. 6.1.2. With a calibrated detector at each SCALA beam, there is no need for a measurement of the effective number of beams as the emission from all beams could always be monitored.

[1] Using SNIFS would also slow down the process due to long CCD reading times and overlapping spectra.

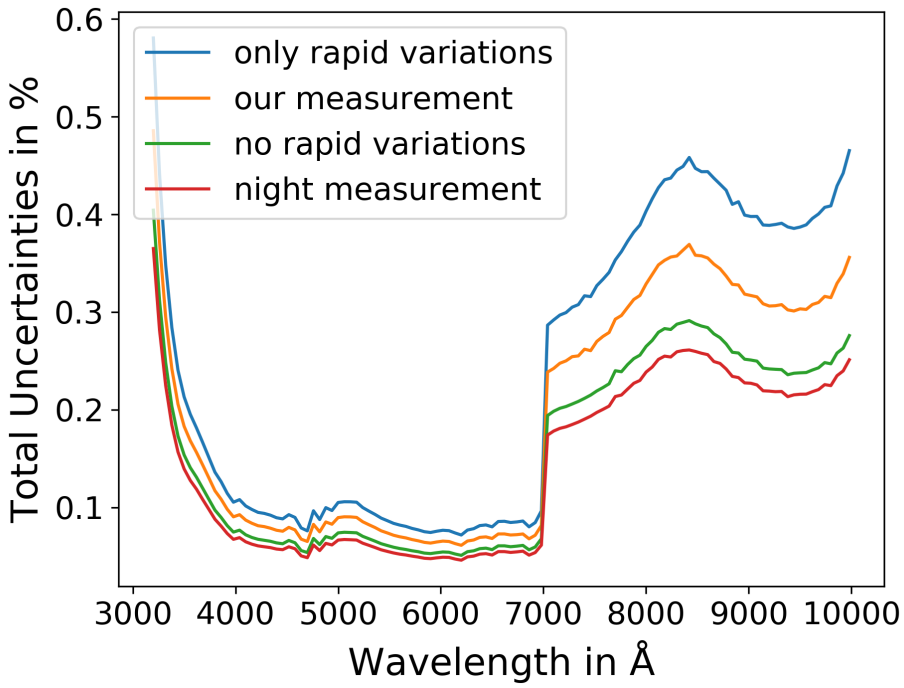

Figure 6.19: Comparison of the uncertainty on the removal of the external background in the measurement of N_{eff}. Four cases with different properties of the measured background are shown and discussed in the text.

6.4 Out-of-Band Emission

Light emitted from the monochromator outside of the desired SCALA passband is called out-of-band emission. To understand the importance of monochromatic light being emitted by SCALA one needs to remember the working idea. A continuous lamp spectrum is filtered to a single wavelength by the monochromator. This light is measured by the photodiode, for which the wavelength dependent sensitivity is known (see sec. 5.2). Therefore we know the number of photons which have left SCALA. This light is also detected by SNIFS and the throughput of the system is given by the number of photons detected, compared to the number of photons emitted. The influence of a finite out-of-band throughput of the monochromator is now illustrated for a broad band filter.

We assume the lamp spectrum $F_{\mathrm{Lamp}}(\lambda)$ as measured by the photodiode by stepping through wavelength with the monochromator (see fig. 4.7). We then divide the spectrum for the quantum efficiency of the CLAP device (τ_{CLAP}) (see. fig. 5.3) to convert to the number of photons per wavelength bin. We model the passband of the monochromator τ_{MC} with a rectangular bandpass of 35 Å width, centered at the selected wavelength λ_{c}, and a throughput of 1.0. Outside this band we attribute a wavelength independent throughput of $4 \cdot 10^{-5}$. The spectrum emitted by SCALA is therefore the product of lamp spectrum ($F_{\mathrm{Lamp}}(\lambda)$) multiplied with the throughput spectrum of the monochromator ($\tau_{\mathrm{MC}}(\lambda_{\mathrm{c}}, \lambda)$).

Lets imagine we calibrate the I-band filter of the imaging channel of SNIFS. The system to calibrate therefore only contains a few elements. There are three telescope mirrors, each with throughput τ_{mirror}, the entrance window of SNIFS with throughput τ_{window}, the bandpass filter for the I-band with throughput $\tau_{\text{I-band}}$, and finally the quantum efficiency of the detector CCD $\tau_{\text{QE-CCD}}$. We want to measure the system throughput τ_{system} which can be modeled as:

$$\tau^{\mathrm{model}}_{\mathrm{system}}(\lambda) = \tau^{3}_{\mathrm{mirror}}(\lambda)\tau_{\mathrm{window}}(\lambda)\tau_{\text{I-band}}(\lambda)\tau_{\text{QE-CCD}}(\lambda) \tag{6.15}$$

We use manufacturer specifications / measurements to model the system throughput. With SCALA we can only obtain the system throughput, not the individual throughputs.

The CCD signal is the wavelength integral over the sensitivity range of the CCD. The number of collected photons at λ_{c} will therefore be:

$$N_{\mathrm{SNIFS}}(\lambda_{\mathrm{c}}) = \int_{2000\text{Å}}^{11000\text{Å}} F_{\mathrm{Lamp}}(\lambda)\tau_{\mathrm{MC}}(\lambda_{\mathrm{c}}, (\lambda))\tau^{\mathrm{model}}_{\mathrm{system}}(\lambda)\,\mathrm{d}\lambda \tag{6.16}$$

The lower integration limit is determined by the lamp, not anymore emitting light, and the upper limit by the end of the sensitivity range of the CLAP and the CCD. If we assume that all photons are emitted at a wavelength λ_{c}, then we obtain the number of photons by scaling the wavelength integrated signal for the sensitivity of the photodiode at λ_{c}:

$$N_{\mathrm{CLAP}}(\lambda_{\mathrm{c}}) = \frac{1}{\tau_{\mathrm{CLAP}}(\lambda_{\mathrm{c}})} \int_{2000\text{Å}}^{11000\text{Å}} F_{\mathrm{Lamp}}(\lambda)\tau_{\mathrm{MC}}(\lambda_{\mathrm{c},\lambda})\tau_{\mathrm{CLAP}}(\lambda)\,\mathrm{d}\lambda \tag{6.17}$$

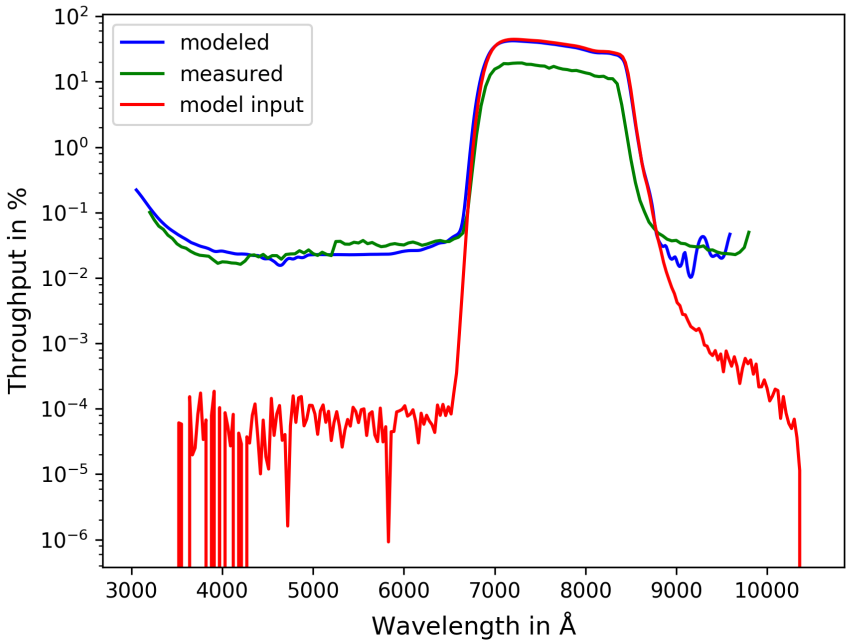

Figure 6.20: Shown is the theoretical system throughput of the imaging channel equipped with a I-band filter (red) and how it would be measured by SCALA with a monochromator which has an out-of-band throughput of $4 \cdot 10^{-5}$ (blue). Also shown is a true measurement performed with SCALA (green).

The measured system throughput $\tau_{\text{system}}^{\text{meas.}}$ will be:

$$\tau_{\text{system}}^{\text{meas.}}(\lambda_{\text{c}}) = \frac{N_{\text{SNIFS}}(\lambda_{\text{c}})}{N_{\text{CLAP}}(\lambda_{\text{c}})} \tag{6.18}$$

Fig. 6.20 shows the resulting systematic effect between inserted $\tau_{\text{system}}^{\text{model}}$ (red in figure) and the above calculation (blue in figure). Within the bandpass region of the I-band filter the measured throughput is close to the model input throughput. In the rejection region of the bandpass filter the throughput is overestimated in the measurement, as the modeled monochromator emits a dim floor of light outside the SCALA bandpass. This light emitted within the I-band filter passband is transmitted and collected by the CCD as a signal. The measured throughput is therefore larger than the true throughput.

Fig. 6.20 also shows the bandpass as measured with the true SCALA setup. Indeed we find a significant throughput in the rejection region of the I-band filter (i.e. $\leq 6500\,$Åand $\geq 9000\,$Å). We therefore conclude that the SCALA system is emitting light outside the desired bandpass. There is out-of-band emission from the monochromator.

In the same way as the calibration of the imaging channel is affected by the emission of light outside the SCALA bandpass, the transfer of calibration from the photodiode to the

spectrograph is affected. For the above example a rough model of the bandpass was enough, as details were smeared out by the wide sensitivity range of the I-band filter. To model the effect on the transfer of calibration a more detailed model is needed.

In the next section I will describe the theoretical monochromator. Afterwards we will use the SNIFS spectrograph to construct a model for the emission spectrum of SCALA. This can then be used to correct the photodiode current for the out-of-band emission which allows for a better estimate of the instrumental throughput. We could in principle obtain the proper instrumental throughput of the system, if we knew exactly the spectrum emitted by SCALA. However, in this way the measurement of the throughput at λ_c would not be independent of the throughputs of the system at other wavelength in the sensitivity range of both SNIFS and CLAP. This leads to correlations that would make the subsequent analysis very challenging. To fully break this wavelength correlation in the measurement of the throughputs we need monochromatic light. For this we would need to improve the SCALA bandpass - increase the out-of-band rejection.

6.4.1 Theoretical Bandpass of the Monochromator

The monochromator used in SCALA is a Cornerstone 260 monochromator from Newport, its optical configuration is shown in fig. 6.21. The light entering the monochromator through the entrance slit is collimated before illuminating one of the two reflective diffraction gratings. The difference between the two gratings will be described later. They have grove densities of 1200 lines per millimeter, and therefore a line spacing of 8333 Å. Constructive interference will occur if the path length difference Δs satisfies the following condition:

$$\Delta s = d \cdot (\sin(\alpha) - \sin(\beta)) = m\lambda \tag{6.19}$$

where m is the order of diffraction ($m = 0, \pm 1, \pm 2, ...$), λ is the desired wavelength, d is the distance between the groves (≈ 8333 Å), α is the incidence angle and β is the outgoing angle. In the configuration of our monochromator the sum of incidence and outgoing angle is fixed by the geometry of the system (see fig. 6.21) to $\gamma = \alpha + \beta \approx 24°$. Therefore eq. 6.19 reads:

$$\lambda = \frac{2d}{m} \cos\left(\frac{\gamma}{2}\right) \sin\left(\frac{\gamma}{2} - \beta\right) \tag{6.20}$$

For a given λ_c we can calculate the outgoing angle β_0 relative to the grating normal:

$$\beta_0 = \frac{\gamma}{2} - \arcsin\left(\frac{m\lambda_c}{2d\cos(\gamma/2)}\right) \tag{6.21}$$

The incidence angle on the grating follows from $\alpha_0 = \gamma - \beta_0$.[1]

The bandwidth of the monochromator at a given wavelength λ_c is determined by the slit width of both the exit and the entrance slit. The slit widths in our case are ≈ 1 mm. The focal length of the objective of the monochromator is ≈ 260 mm. Therefore we can estimate the

[1] From eq. 6.21 we see that $\lambda_c = 0$ is obtained for $\beta_0 = \alpha_0 = \gamma/2.$, which means that the grating acts like a mirror and images entrance slit to exit slit without dispersion. In this way we can let white light pass the monochromator via the zeros order of diffraction.

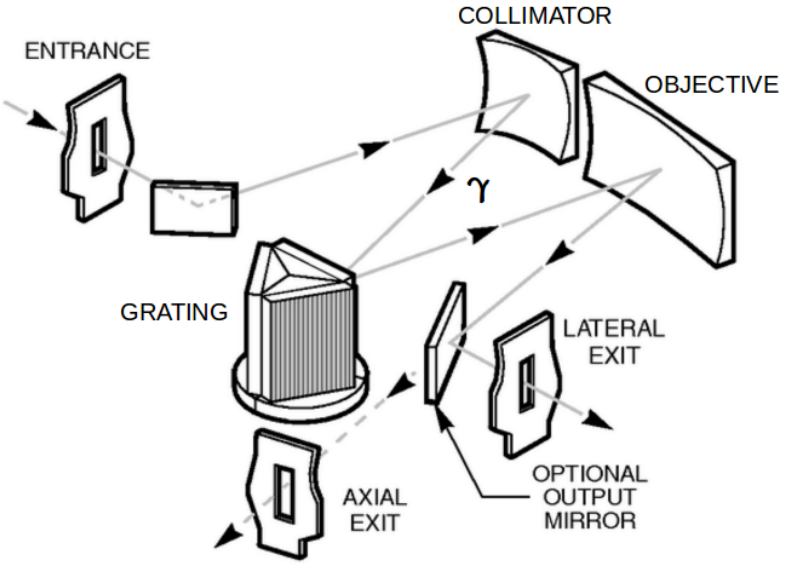

Figure 6.21: Optical configuration of the Cornerstone 260 monochromator used in the SCALA setup. The light entering through the entrance slit is redirected towards the collimator via a small flat mirror. The collimated light is illuminating the grating and the objective, which images the light onto the exit slit. The angle γ between the collimated beam going to the grating and away from it is fixed by the placement of the collimating and objective mirrors. The schematic is taken from https://www.newport.com/medias/sys_master/images/images/hae/h47/8797226926110/Oriel-Cornerstone-260-User-Manual-RevA.pdf, last checked 27.03.2018

opening angle of the outgoing light cone, leaving the grating and passing the slit in the focal plane of the objective (exit port of monochromator). With x being the position in the slit we can rewrite the outgoing angle to (using small angle approximation):

$$\beta = \beta_0 + \frac{x}{f} \tag{6.22}$$

The reciprocal linear dispersion R_d is then the change of wavelength with position in the slit plane:

$$R_d = \left| \frac{\mathrm{d}}{\mathrm{d}x} \left(\frac{d}{m} \Big(\sin(\alpha_0) - sin(\beta_0 - x/f) \Big) \right) \right|_{x=0} = \frac{d}{mf} \cos(\beta_0) \tag{6.23}$$

With the properties of the monochromator ($d = 8333\,\text{Å}$, $\beta_0 = -0.5\,^\circ$, $\alpha = 24.5\,^\circ$, $m = +1$ and $f = 260\,\text{mm}$) we find:

$$R_d = 32.0 \frac{\text{Å}}{\text{mm}} \tag{6.24}$$

at a wavelength of $\lambda_\text{c} = 3500\,\text{Å}$. Which is exactly the specification from the manufacturer. The wavelength dependence of the linear reciprocal dispersion will be evaluated in the following.

We use measurements of SNIFS from 2015 day 159 to evaluate the bandwidth of SCALA. The flux calibrated data cubes have been averaged over all spaxels to obtain a spectrum and increase the signal to noise ratio. The spectrum has been linearly interpolated to a wavelength scale of 0.01 Å, to measure the FWHM of the SCALA bandpass. The theoretical curve and the measured data points are shown in fig. 6.22. As the precise widths of the monochromator slits are not known, the absolute scale of the bandwidth is determined from the measurements. From the scaling we can estimate that the slit widths of SCALAs monochromator are $1.19 \pm 0.02\,\text{mm}$.

In the wavelength range from 4000 Å to 5000 Å we see an increase of scatter. The above calculation assumed that the lamp spectrum is continuous and flat over the bandwidth range ($\approx 100\,\text{Å}$), but the Xenon lamp shows narrow emission lines there, therefore the bandpass width is modified. Above 7000 Å the Xenon lamp spectrum is dominated by strong emission lines and we therefore switch to a tungsten halogen lamp. This switch of lamps causes a change in the illumination of the entrance slit, which then results in a change of the bandwidth, which is visible as a jump in the measured bandwidth at 7000 Å.

Above we obtained the width of the bandpass (fig. 6.22), but not its shape. To obtain the shape of the bandpass we imagine the entrance slit of a monochromator being illuminated homogeneously with monochromatic light. The intensity distribution in the entrance slit plane can therefore be approximated by a top hat function, as the light will either pass the slit or be occulted by it.

Due to the monochromatic illumination we can approximate the grating with a mirror[1], which images the entrance slit to the exit slit, when the selected wavelength is the same as the wavelength of the entering monochromatic light. Small inclinations of the mirror departing from this position result in shifts of the entrance slit image relative to the exit slit. The amplitude of the light passing through the slit is a function of the mirror inclination relative to the position

[1] The wavelength resolution of the monochromator is limited by the slit width and not by diffraction on the grating, shown later.

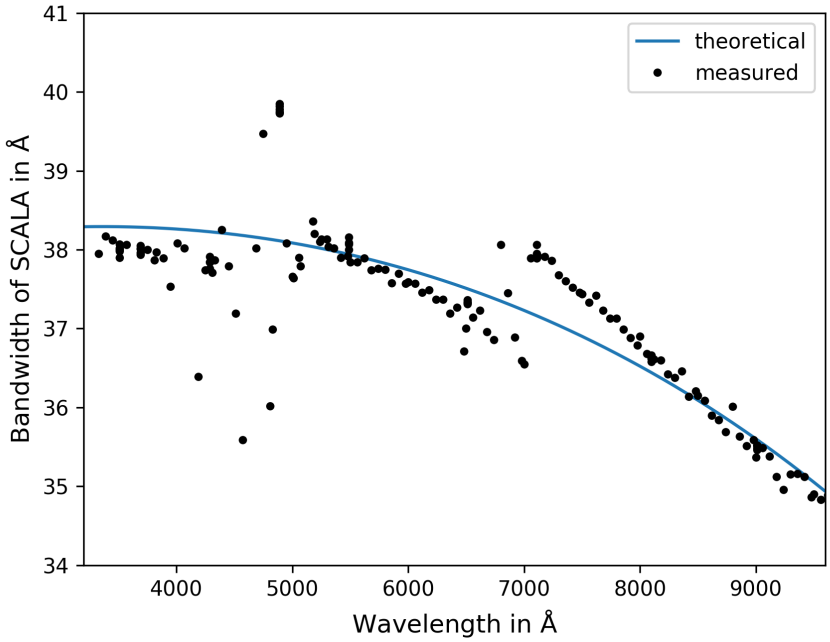

Figure 6.22: Shown is the measured FWHM bandwidth of SCALA together with the theoretical calculation based on eq. 6.23 and eq. 6.21

where the selected wavelength is passing without attenuation. The bandpass shape is triangular, as we sample a top-hat illumination with a top-hat response of same width[1]. The inclination of the mirror corresponds to a change in wavelength as shown above. We therefore obtain a bandpass triangular in wavelength, with the FWHM given by the above considerations.

In practice, the entrance illumination will not be perfectly transfered to the exit slit, as the collimator and objective have a finite angular resolution, resulting in an additional smearing of the image. We also use a fiber bundle, which samples the exit slit. Due to sub-sampling of the exit slit we further decrease the resolution and increase the bandwidth. We describe these two effects by a Gaussian convolution kernel, with a FWHM of 12 Å, see [Küsters, 2014]. The bandpass shape of the monochromator is therefore a smoothed triangle.

In the following I will describe the throughput of the monochromator based on wave optics. We can then obtain the interference pattern, which shows a finite throughput even at a wavelength far away from our "triangular" bandpass, and we will also see that the spectral resolution of the monochromator is limited by the slit width and not by the grating (assumed before). The calculation of the full interference pattern can be factorized into two parts, the single slit interference pattern and the periodic grating pattern.

The grating interference pattern (N slits) can be calculated assuming that there are N narrow groves, each producing a spherical wave, interfering at large distance[2]. The full calculation can be found e.g. in [Paus, 2002] and delivers:

$$I = \frac{\sin\left(N\frac{\pi}{\lambda}\Delta s\right)}{N \cdot \sin\left(\frac{\pi}{\lambda}\Delta s\right)} \tag{6.25}$$

The common calculation uses a transmitting grating with incidence angle $\alpha = 0$ and a varying outgoing angle β. In this case the path difference is $\Delta s = d\sin(\beta)$. In case of a reflective grating we find $\Delta s = d(\sin(\alpha) - \sin(\beta))$.

Using the above functional dependence we can determine the Rayleigh resolution of the grating as:

$$R = \frac{\Delta\lambda}{\lambda} = m \cdot N \tag{6.26}$$

For our monochromator we use the first order and a grating with a width of 50 mm and a line density of 1200 l/mm, therefore $R = N \approx 60,000$. This would result in a resolved wavelength scale of 0.2 Å at 1 μm wavelength, which is a larger resolution than obtained using a slit of $\approx$ 1 mm, which resulted in a bandwidth of $\approx$ 37 Å. The resolution of the monochromator is thus limited by the slit width.

The calculation of the single slit intensity pattern itself can also be factorized into two pieces. First we calculate the pattern for a transmission grating at an incidence angle of 0°, then we apply this result to a reflection grating, in which the single grove facets are inclined relative to the grating plane (see fig. 6.23). To obtain the pattern of a transmission grating we place N sources in the slit, emitting in phase spherical waves (Huygens Principle), and sum their

[1] Like a convolution of two top-hat functions with same width, or a moving average over a top-hat function with a window of same width as the top-hat function

[2] Distance large compared to the grove distance.

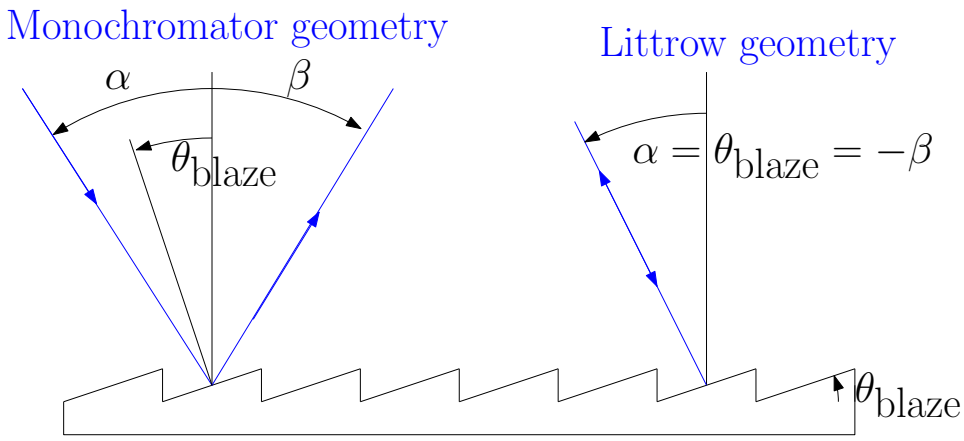

Figure 6.23: Drawing of the used angles at the grating together with the grating normal and the normal to the grove facets. Left side: Geometry within the monochromator, right side: Littrow configuration. Here the incident ray is reflected into itself.

contributions at a screen far away[1] from the slit. Afterwards we calculate the pattern for the case of N going to infinity. The detailed calculation can be found e.g. in [Paus, 2002] with the following result:

$$I = \mathrm{sinc}^2\left(\frac{\pi}{\lambda}\Delta s\right) \tag{6.27}$$

where λ is the wavelength of the light illuminating the grating. In case of a slit, we find that the maximal path length difference is $\Delta s = D\sin(\beta)$, where the plane wave is incident orthogonal to the slit plane and β is the outgoing angle and D the distance between the groves. We now apply the result to a reflective grating where the single grove acts like a single slit, but now in reflection, so that we need both the incidence and outgoing angle.

For a grating with grove facets parallel to the grating plane, the maximum of the single slit interference coincidences with the zeroth order of the grating interference pattern. The maximum intensity therefore will be in the non-dispersed order and the largest fraction of the light will therefore be unavailable for measurements. By inclining the facets of the groves relative to the grating plane, one can introduce a phase shift, which results in a shift of the maximum of the single-slit interference pattern to the first order of the grating interference pattern. The resulting single slit pattern for a grating with blaze angle θ_{blaze} is:

$$I = \mathrm{sinc}^2\left(\frac{\pi D}{\lambda}\left(\sin(\alpha - \theta_{\mathrm{blaze}}) - \sin(\beta + \theta_{\mathrm{blaze}})\right)\right) \tag{6.28}$$

where α and β are measured against the normal on the grating plane, see fig. 6.23 for the geometry.

[1] Distance to the screen large compared to the slit width

The full interference pattern is given by the product of single-slit and N-slit interference:

$$I = I_0 \cdot \mathrm{sinc}^2 \left(\frac{\pi D}{\lambda} \left(\sin(\alpha - \theta_{\mathrm{blaze}}) - sin(\beta + \theta_{\mathrm{blaze}}) \right) \right) \frac{\sin\left(N \frac{\pi}{\lambda} \Delta s\right)}{N \cdot \sin\left(\frac{\pi}{\lambda} \Delta s\right)} \tag{6.29}$$

To calculate the bandwidth shape of the monochromator we now need the blaze angle θ_{blaze}, so the inclination of the grove facets relative to the grating plane.

θ_{blaze} is defined in Littrow configuration (see fig. 6.23 for the used angles), were $\alpha = -\beta = \theta_{\mathrm{blaze}}$. The light illumination is therefore orthogonal onto the facets. The step between a facet and its adjacent is therefore equal to $\lambda_{\mathrm{blaze}}/2$, for constructive interference, as the path length is twice the step. From this geometry the blaze angle is: $\theta_{\mathrm{blaze}} = \lambda_{\mathrm{blaze}}/(2d)$. The first grating used in the monochromator has a blaze wavelength of 3500 Å which corresponds to an angle $\theta_{\mathrm{blaze}} = 12.1°$, the blaze wavelength for grating two is 7500 Å, which corresponds to $\theta_{\mathrm{blaze}} = 26.7°$.

Based on the above considerations, the final bandpass of the theoretical monochromator is the convolution of the interference bandpass with the triangular bandpass and a Gaussian kernel. The triangular passband accounts for the finite slit width, and the Gaussian kernel accounts for the sampling of the fiber bundle and the resolution of the optics within the monochromator. The combined theoretical result is shown for a wavelength of 8000 Å in fig. 6.24. The wavelength of 8000 Å was selected for the first order of diffraction, as then the higher orders of diffraction are visible at 4000 Å and 2666 Å. For the calculation the width of the single slit was assumed to be the same, as the distance between two groves ($D = d$).

To prevent light of higher order being transmitted, we use order sorting filters. They are long-pass colored glass filters from SCHOTT, with cut-on wavelength of 3090 Å and 4950 Å. Below the cut-on wavelength their throughput is specified to be smaller than 10^{-5}, and they are therefore effectively absorbing the light from the beam entering the monochromator.

We were informed by SCHOTT, that these filters show fluorescence, meaning the absorbed light results in excitation and reemission at longer wavelength. We were provided with measurements showing that the total efficiency of this effect can be as high as 23 % [Reichel et al., 2015]. As the filters are placed in front of the monochromator the fluorescence is contributing to the spectra of the lamps and is afterwards filtered by the monochromator. If these filters were mounted behind the monochromator, they could easily provide a wide-wavelength floor to the bandpass.

As will be seen the finite out-of-band emission of the theoretical monochromator is a factor 10 to 100 smaller than the out-of-band emission needed to explain the measurements (compare to initial example). As the out-of-band emission from the theoretical monochromator can not explain our measurements we will use SNIFS to obtain a measurement of the out-of-band emission of SCALA.

6.4.2 Bandpass of the Monochromator constrained by Measurements

In sec. 6.4 we concluded that there is out-of-band emission from the monochromator. We would now like to measure the spectral distribution of the SCALA emission using SNIFS. We then create a detailed model of the effect and estimate its influence on the calibration of SNIFS using

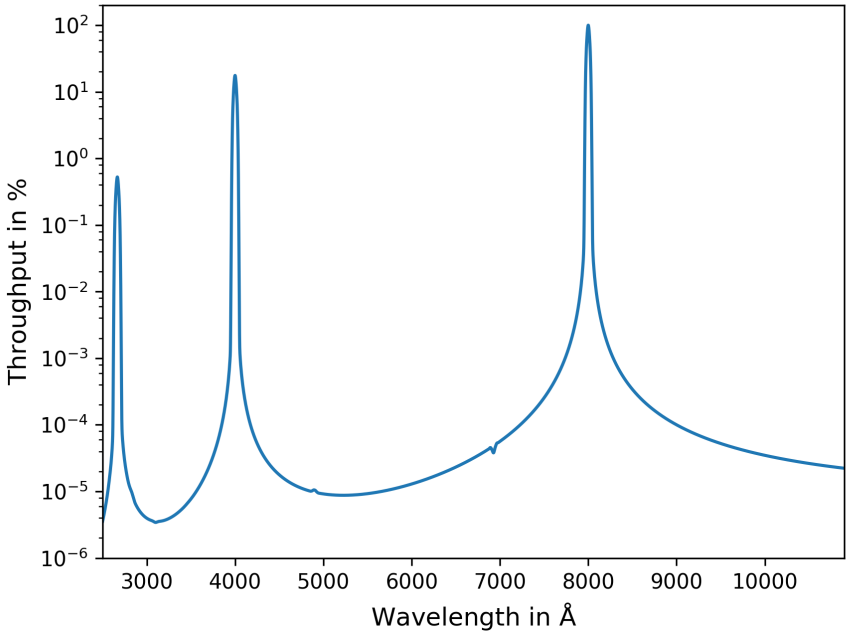

Figure 6.24: Relative monochromator throughput based on the above equations describing diffraction. The first order is selected to be at 8000 Å, therefore also second order (4000 Å) and third order (2666 Å) are visible. The amplitude of first order is set to 100 % and the expectation for second order is 11.7 % and 7.8 % for third order.

SCALA.

The amount of stray light within SNIFS will be evaluated in the following paragraph, afterwards the bandpass of SCALA is measured and modeled. In these explanations we will present further results which independently confirm the existence of out-of-band emission from SCALA. With the obtained bandpass model for the monochromator we successfully describe the throughput measured for the imaging channel equipped with an I-band filter. The application of the model to a U-band filter shows that the model fails to describe the details. In the following the obtained models will be used to estimate the influence of out-of-band emission on the spectroscopic calibration. The variations between the model predictions will be used as a uncertainty estimate. At the end of the section we will propose an improvement to the setup which allows for a significant reduction of out-of-band emission and therefore measurements without this systematic effect.

Straylight within SNIFS and out-of-band emission from SCALA

Fig. 6.25 shows in the upper panels a comparison of a measured truly monochromatic source and SCALA. To obtain the truly monochromatic illumination a narrow band filter was placed between the arc lamp[1], which is usually used for the wavelength calibration, and SNIFS. The passband of the filter was chosen to select one of the narrow emission lines of the arc lamp, and to suppress the others. The average of 20 such measurements is shown in the upper left[2].

As the lamp gas pressure is low the line width is smaller than the resolution of SNIFS, the pattern we see on the CCD is therefore only caused by instrumental effects. Each cross in the image represents a spaxel and is caused by diffraction on the rectangular lenses of the micro-lens array.

In case of a source with a continuous spectrum, we would see vertical tracks, aligned with the red box, which represent the spectral trace of the source. The intensity map is in log scale and the bright limit is set low, to see also a faint spectral track.

In the following we will perform a manual extraction of the spectrum. The full CCD image shows 225 spaxels, of which only a subset is shown in the figure. Around each of them a box like the red one is placed to extract the spectrum. Like indicated in the figure the wavelength direction is aligned with the long side of the box, over the short side we sum. The final spectrum shown in the lower panel of the figure (green) is obtained by averaging over all 225 extracted spectra. As the box passes by the next spaxel closely the diffraction wing of neighboring spaxel (above or below) will cross the box. We will therefore have a crosstalk between spaxels. This crosstalk results in the peaks in the extracted spectrum at $\pm 320\,\text{Å}$, see the lower panel of fig. 6.25.

In the upper right panel we see a spectrum obtained from SCALA. Here the crosses are smeared in vertical direction, as the SCALA light is not monochromatic but has a bandwidth of $\approx 37\,\text{Å}$ (as discussed in sec. 6.4.1). But, additionally, there are long faint tracks, reaching even further than the next spaxel. This is the out-of-band emission. The spectrum of the SCALA light source is extracted in the same way, as for the monochromatic illumination and is shown in the lower figure in orange.

[1] Arc lamp: Low pressure gas lamp

[2] Amplitude for monochromatic line: $26\,\text{ke}^-$, amplitude of SCALA line: $19\,\text{ke}^-$

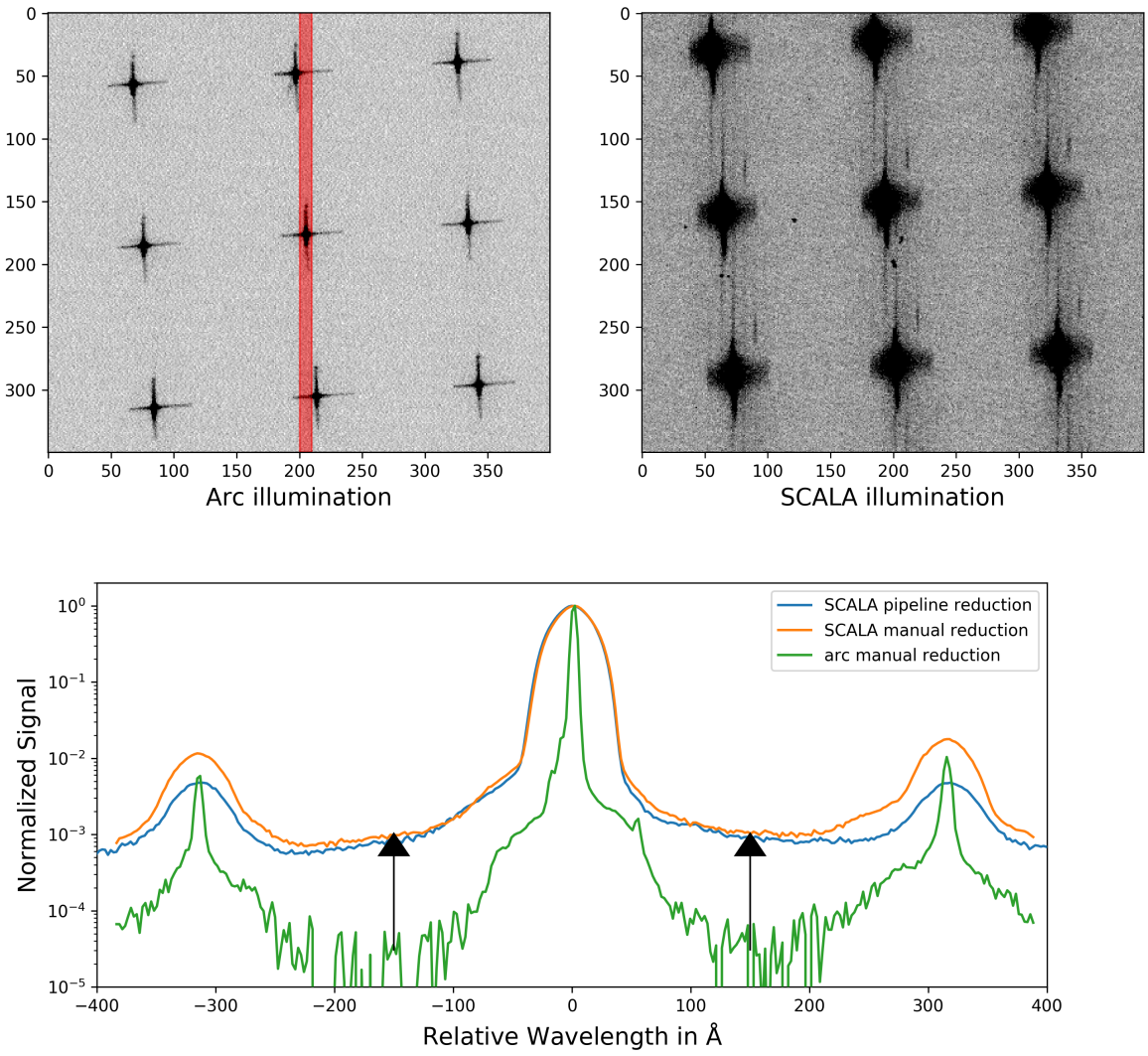

Figure 6.25: Upper left: CCD exposure of the SNIFS blue channel illuminated by monochromatic light. Each cross is formed by a spaxel. The red box indicates the region used to extract the spectrum of the central spaxel, the corresponding spectrum is shown in the lower part in green. Upper right: SCALA illuminating SNIFS. We see that the crosses are more extended in the vertical direction and also have narrow vertical tracks. The narrow tracks show that SCALA emits light outside the desired bandpass. Lower part: Comparison of the extracted spectrum of the monochromatic illumination (green) and the SCALA spectrum (blue and orange). The green and orange curves are obtained by the manual extraction. The blue curve shows for comparison the spectrum obtained from the summit data-reduction pipeline. The black arrows indicate the amount of out-of-band emission from the monochromator, as seen by SNIFS.

The approach of extracting the spectrum within a box works only locally on the CCD as the spectral tracks are curved on the detector. To account for this effect the data-reduction pipeline uses an optical model. It also takes into account the diffraction profile, and the crosstalk signal at ± 320 Å is therefore smaller.

The manual extraction was applied to the monochromatic observations, as the truly monochromatic observations were not reduced with the standard pipeline. For a consistency check of the described manual extraction the spectrum of the SCALA illumination was extracted manually and with the summit data-reduction pipeline.[1] In fig. 6.25 lower panel the comparison is shown, which confirms that the manual pipeline is able to reproduce the results of the standard SNIFS pipeline.

As the spectrum for the truly monochromatic light falls off more quickly than in the SCALA case, we can rule out that flux observed between lines (indicated by the black arrows in fig. 6.25) is caused by stray light within SNIFS. It must instead be due to out-of-band emission from the monochromator.

We now have a second independent confirmation of out-of-band emission from the monochromator (for a single wavelength). We thus conclude that stray light in SNIFS is insignificant, and that SNIFS can be used for testing of the SCALA bandpass. In the following we obtain a model for out-of-band emission which is valid in the whole wavelength range sampled by SCALA.

6.4.2.1 Analyzing the SCALA bandpass with SNIFS

Fig. 6.26 shows the extracted spectrum of a long SNIFS exposure with SCALAs bandpass centered at 5000 Å. The spectrum is wavelength calibrated but not flux calibrated, as this would reduce the wavelength range. The SCALA wavelength of 5000 Å was selected, because this wavelength can be observed in both channels of SNIFS(see sec.4.2). As SNIFS uses as dispersive element a grism[2], light of 5000 Å will also be visible at a wavelength of 10000 Å, as the interference condition is satisfied again (see eq. 6.19). We therefore see a peak at ≈ 10000 Å, with a width twice as wide as at 5000 Å.

To the left and right of the SCALA bandpass we see periodical lines. Some of them are the previously discussed crosstalk between spaxels, they are marked by black dashed lines in fig. 6.26. The crosstalk lines have a spacing of ≈ 320 Å in the blue channel and ≈ 380 Å in the red channel. The spectra of the individual spaxels are shown in the lower panels of the figure. We can see, that the crosstalk lines are not visible in the spectra of all spaxels. In the blue channel the upper spectra (see lower panel of fig. 6.26), do not show crosstalk lines bluer than 5000 Å, but redder ones. On the other end, the lower spectra show lines bluer than the SCALA bandpass, but not redder. This asymmetry is caused by the vertical alignment of spectral traces on the CCD (see fig. 6.25). The crosstalk is caused by the diffraction wings of the spaxels above and below the spaxel to evaluate. The wings cross the spectral trace of the spaxel we want to measure. When the extraction is approaching the first line of spaxels, there is no higher spaxel, there is therefore no further crosstalk. This also explains the reverse ordering approaching the last line of spaxels on the CCD and also the stepwise (line wise) increase of crosstalk peaks left

[1] Early version of the data-reduction pipeline, which is run immediately after data-taking on Mauna Kea.
[2] Combination of a prism with a grating

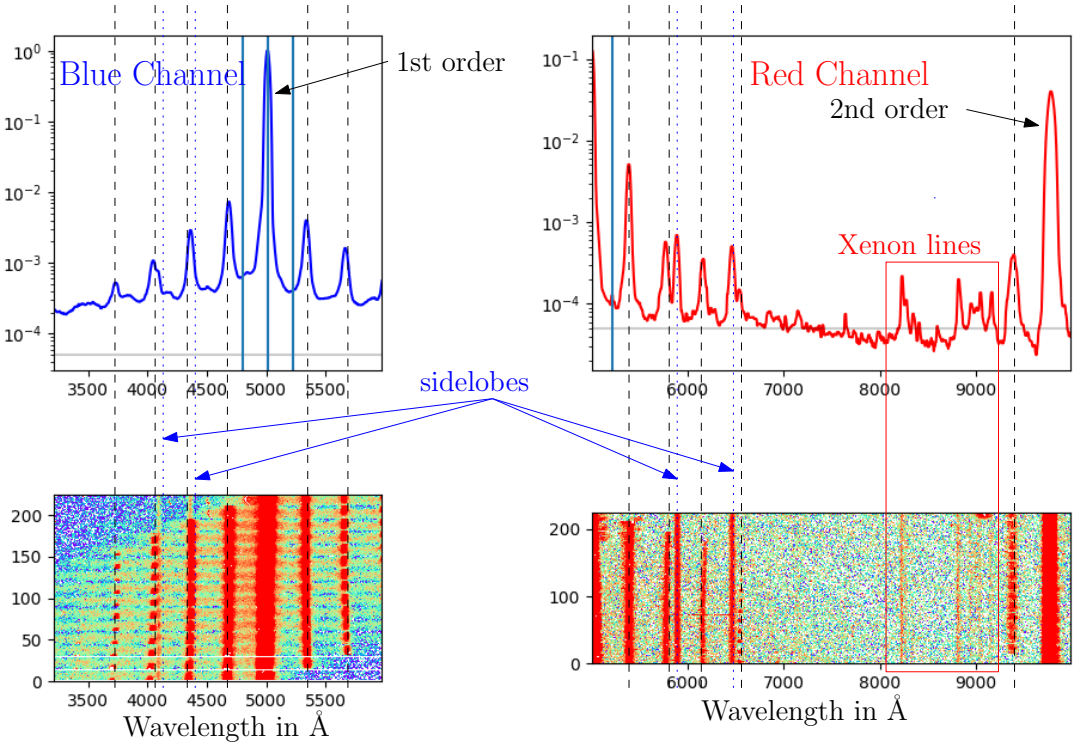

Figure 6.26: The upper panels show the SCALA passband in logarithmic scale. The lower panels show the corresponding 225 spectra obtained in each spectroscopic channel, layered in the y-direction. The SCALA main passband is set to 5000 Å. The second order of diffraction from SNIFS is visible at $\approx$ 10000 Å. The lines which are not visible in all spectra (lower panel) are caused by the crosstalk between SNIFS spaxels and are marked with dashed black lines, while the lines visible in all spectra are artifacts of SCALA. They are subdivided into side lobes of the SCALA bandpass (dotted blue) and out-of-band emission (red box), visible at the emission lines of the Xenon spectrum.

and right of the SCALA line. This effect is well known for SNIFS and can be found for example in fig. 3.14 & 3.15 in [Copin, 2013], where these lines are called ghosts.

However, we also find additional lines visible in the spectra of all spaxels (fig. 6.26). Observing them in all spaxels means that these lines are a property of the light illuminating SNIFS and not an artifact of SNIFS. They are *side lobes* of the SCALA bandpass, caused by imperfections in the ruling of the grating. Using the other SCALA grating and repeating the observation at 5000 Å, these lines disappear while others appear. However, these side lobes are still only individual lines with an amplitude relative to the main SCALA line smaller than $8 \cdot 10^{-4}$. They thus only contribute a sub-percent flux and can not be the cause of any significant out-of-band emission.

We now finally get to the set of lines indicated by the red box in fig. 6.26. These are different in that they do not depend on the spaxels or when switching the grating. They are also not caused by crosstalk in SNIFS. From the comparison to fig 4.7 we find that they are emission features of the Xenon lamp spectrum *outside of the target SCALA wavelength region*. This therefore shows again that there is light from the lamp propagating through the monochromator at undesired wavelengths. We remind the reader that this causes a systematic difference since all of this light will be measured by the integrative photodiode while it will not be included in the wavelength-restricted SNIFS reduction.

Modeling the bandpass at a specific wavelength

Above we used the emission lines of the Xenon spectrum to show the existence of out-of-band emission from SCALA also at large wavelength distance from the target SCALA passband. To quantify the impact of out-of-band emission on the calibrations performed with SCALA, we need the full wavelength dependent throughput model of the monochromator. The goal of this model is to explain all observations, without the need for further systematics.

We model the emission spectrum of SCALA as the product of lamp spectrum and wavelength dependent throughput of the monochromator and compare this to the SCALA emission observed with SNIFS. For the lamp spectrum we could observe the Xenon lamp with SNIFS by setting the target wavelength of the monochromator to 0 Å[1]. However, the throughput of the monochromator might be different for out-of-band light and light at zeroth order of diffraction. More similar in throughput should be the spectrum obtained from the photodiodes by stepping through the target wavelength range, but then we would face the problem of different spectral resolution. The spectral resolution of the photodiode measurement is lower (37 Å) than the spectral resolution of SNIFS (5.2-7.2 Å). Emission lines in the Xenon spectrum observed with the photodiode will appear dimmer and wider than in the SNIFS spectrum. To correct for both effects, the different throughput and resolution, we use a SNIFS spectrum of the Xenon lamp at 0 Å, and distort it according to the continuum spectrum in the CLAP measurements (take the ratio of the spectra and smooth it). The result is shown in fig. 6.27 red curve. For comparison also the CLAP spectrum is shown (blue).

To extend the wavelength range of the lamp spectrum to wavelengths longer than 1μm[2] we

[1]The undispersed zeroth order is placed as the output of the monochromator, thus we can observe the whole spectrum.

[2]Sensitivity limit of SNIFS but not of the photodiode.

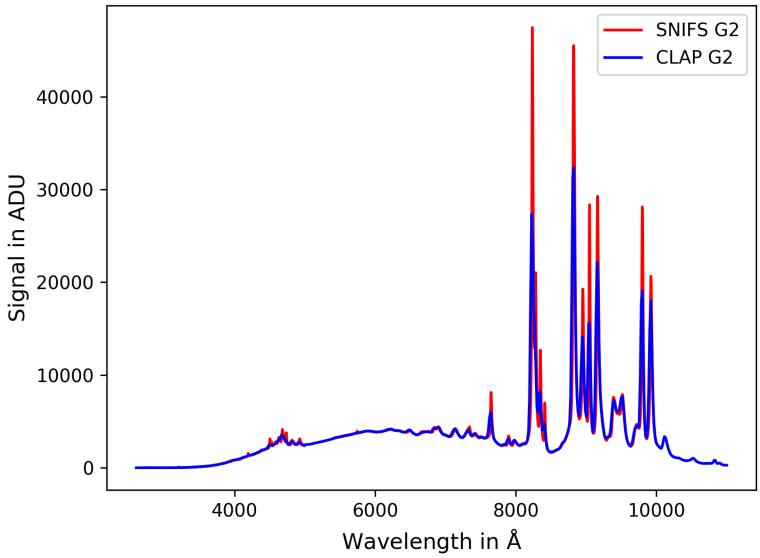

Figure 6.27: Shown is the SCALA lamp spectrum measured with CLAP by stepping through wavelength with the monochromator in (blue). In red we see the continuum adjusted spectrum measured with SNIFS. As the resolution of SNIFS is higher than the one of the monochromator the Xenon emission lines are narrower and higher. Shown is the spectrum obtained with grating 2 (7500 Å blaze wavelength).

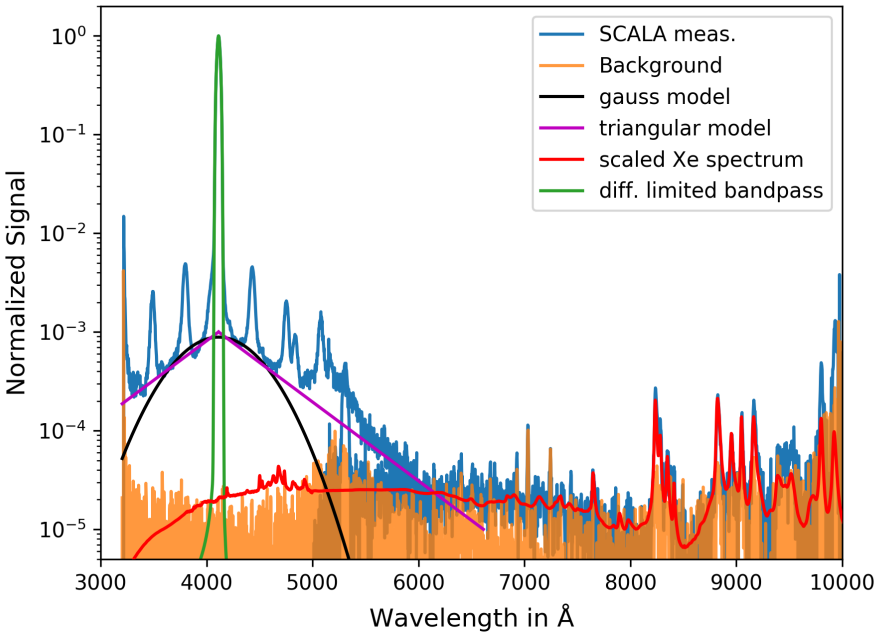

Figure 6.28: Spectrum obtained for the SCALA bandpass at 4113 Å within a 20 min exposure (blue) and averaging over all 225 spaxels. In orange we see a dark measurement of the same exposure time. The red curve shows a scaled version of the Xenon lamp model. A Gaussian approximation for the excess around the SCALA passband is shown in black. In magenta we see a triangular approximation for the excess. The green curve is showing the theoretical monochromator passband based on diffraction.

use the spectrum obtained with the photodiodes, without corrections. For the Halogen lamp, which we use for wavelengths longer than 7000 Å, no corrections are needed as the spectrum is continuous.

To account for the different throughputs of the gratings, we perform the distortion of the SNIFS spectra twice (like for fig. 6.27), once based on CLAP measurements with grating one and once with grating two. The result for grating two is the one shown in fig. 6.27. The effect of different gratings on the CLAP spectrum can be seen in fig. 4.7.

To account for the throughput of the order sorting filters on the lamp spectrum, we use the filter throughputs provided by SCHOTT (filters GG495 and WG305).

Now that we have a model for the lamp spectrum we can obtain a model for the throughput of the monochromator. We therefore use a spectrum obtained with SNIFS from SCALA. The wavelength of the monochromator was set to 4113 Å. To measure the low light level we chose a exposure time of 1200 s. The photon number spectrum normalized to one at peak is shown in fig. 6.28[1] in blue. Also shown is a dark measurement (SCALA shutters closed) of same exposure time in orange.

We see that the observed spectrum can be decomposed into three components, a core for the target SCALA passband, an excess around it and a constant throughput at even further distances form the target passband. The green curve shows the expected diffraction passband shape. We see that diffraction describes the passband for amplitudes larger than $7 \cdot 10^{-3}$. For smaller amplitudes we see deviations caused by the diffraction at the micro-lenses (i.e between 10^{-3} and $7 \cdot 10^{-3}$ compare to fig. 6.25). For even smaller amplitudes we observe an excess of light around the SCALA passband, which can be modeled in log scale through adding a triangular contribution (magenta curve). We can also describe the excess with a Gaussian contribution of 900 Å FWHM (black curve). The Xenon lamp model scaled to fit the amplitude of the emission line at 8823 Å is shown in red. We see that the out-of-band emission at large wavelength distance from the target SCALA passband can be obtained from the lamp model via a wavelength-independent scaling factor τ_{OOB}.

The models for the throughput of the monochromator are summarized here and the components are discussed in the following. We first show the functional relation and then give an example for the monochromator throughput at a specific target wavelength of the monochromator λ_{c}. The throughput of the monochromator τ_{MC} is parameterized with:

$$\tau_{\mathrm{MC}} = \left(D\left(\lambda_{\mathrm{c}}\right) + A\left(\lambda_{\mathrm{c}}\right) \begin{cases} G\left(\lambda_{\mathrm{c}}\right) \\ T\left(\lambda_{\mathrm{c}}\right) \\ F\left(\lambda_{\mathrm{c}}\right) \end{cases} + \tau_{\mathrm{OOB}} \right) \cdot \Theta(\lambda - 3200\text{Å}) \cdot \Theta(9900\text{Å} - \lambda) \tag{6.30}$$

with $D\left(\lambda_{\mathrm{c}}\right)$ the theoretical diffraction bandpass (sec. 6.4.1) and $A\left(\lambda_{\mathrm{c}}\right)$ the amplitude of the excess around the SCALA passband. The functions $G\left(\lambda_{\mathrm{c}}\right)$, $T\left(\lambda_{\mathrm{c}}\right)$ and $F\left(\lambda_{\mathrm{c}}\right)$ describe the

[1] This measurement was taken in March 2018 and as the telescope was refurbished before, no up-to-date throughput was available. The long-time throughput average (see appendix. D.5) was therefore used to convert from collected number of electrons to the number of photons incident to the telescope. As described in sec. D.5 there are several ways to normalize the average. As the measurement is normalized to one at 4113 Å, we use the average throughput with a absolute normalization at 4113 Å (see fig. D.4).

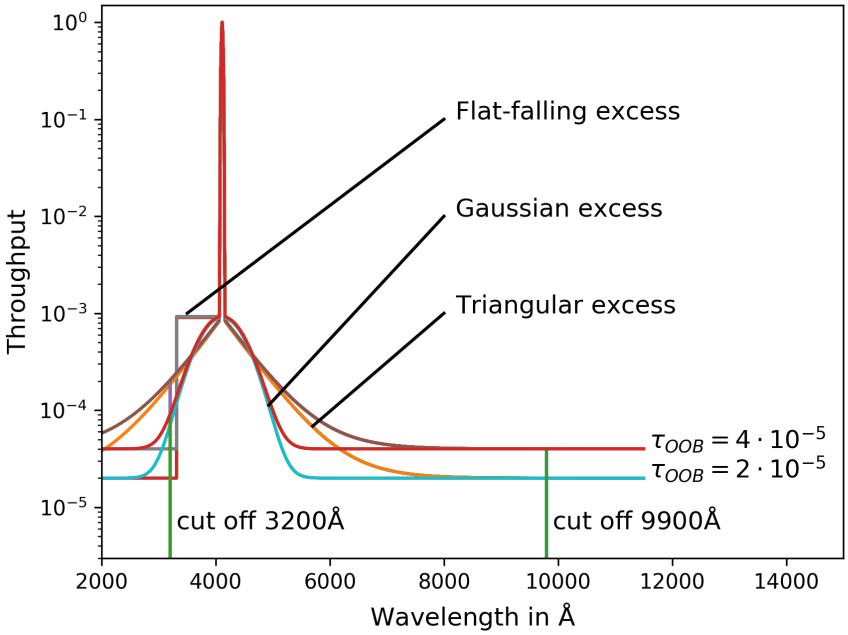

Figure 6.29: Models for the bandpass of the monochromator. The excess of light around the SCALA passband at 4113 Å is modeled using a Gaussian, a triangle or a flat-falling excess. Two different τ_{OOB} of $2 \cdot 10^{-5}$ and $4 \cdot 10^{-5}$ are used. Also visible are the optional cutoffs at 3200 Å and 9900 Å.

shape of the excess, where G represents a Gaussian, T a triangular and F a flat-falling excess. τ_{OOB} represents the constant monochromator throughput at large distances from the SCALA passband and the two last factors are optional cutoffs at 3200 Å and 9900 Å. The different throughput curves are shown in fig. 6.29 for $\lambda_{\mathrm{c}} = 4113$ Å.

In the following paragraph we will describe the excess around the SCALA passband at λ_{c} and afterwards show measurements on the value of τ_{OOB}. The obtained models will then be used to estimate the performance of SCALA in the calibration of the imaging channel. We will use the comparisons to real SCALA measurements to evaluate the models.

Excess around the SCALA passband

The best explanation for the excess emission around the target passband is internal reflections within the monochromator. Newport / Oriel the manufacturer of the monochromator gives the following hint:

> "Stray Light Considerations for Spectrographs
> In a spectrograph / detector array system, stray light can be a more significant problem than it is with scanning monochromators. The array is a much larger target for stray radiation; there is no exit slit to limit the field of view for the detector.

> Some signal is reflected back off the array where it is scattered as stray light, and the array itself typically has less dynamic range than single element detectors."
> https://www.newport.com/t/stray-light-in-monochromators-and-spectrographs, last checked 19.06.2017

The same explanation can be found in [Zong and et al., 2006], however they provide a quantitative explanation of the effect and describe how to correct the measurements. We now have an explanation for the effect but SCALA is not equipped with an array detector, but the exit slit is filled with a fiber bundle to transports the light towards the modules of SCALA. Due to the change of refractive index from air ($n_1 = 1$) to the optical fibers ($n_2 \approx 1.5$), $\approx 4\,\%$[1] of the incident light will be reflected back into the monochromator. There is an additional issue, which needs to be accounted. The fibers are glued into an aluminum holder, afterwards this piece including the fibers has been polished. The front side of the aluminum holder reaching into the monochromator is therefore highly reflecting. Light can then be reflected back into the monochromator and can reach the exit slit via reflections off the optical elements within the monochromator. The diameter of the fiber holder and its adapter is 22.3 mm. From sec. 6.4.1 we know that the linear reciprocal dispersion is of the order 32 Å/mm, we therefore obtain a wavelength scale of this reflector of 780 Å. This scale is comparable to the width of the Gaussian of 900 Å, used in fig. 6.28. To improve the out-of-band performance of the monochromator the aluminum holder should be painted black.

In case of usual exposure times used for the transfer of calibration (28 s at 4113 Å) the excess of light around the passband is hardly visible in the spectra due to low count levels. At the long exposure times, like shown in fig. 6.28 (1200 s), a triangular shape can be used as approximation of the excess around the passband. For medium exposure times (300 s) only the core of the excess can be seen and can be well modeled by a Gaussian component with a width of 900 Å. We use a Gaussian excess even if we know from long exposures that the excess has stronger wings than a Gaussian. For both models of the excess, the Gaussian and the triangular, we assume that they are centered and symmetric around the target SCALA passband.

In eq. 6.30 we allowed a wavelength dependent amplitude of the excess. In the following we will use medium exposure times to investigate a possible dependence of the width and amplitude of the excess with the target wavelength λ_c. From manual adjustments of the Gaussian model to the measurements, we find that the width of the Gaussian component is stable. However, the amplitude changes with the target wavelength λ_c. This change of amplitude is shown in fig. 6.30 by red points. The above result depends on the manual adaption of the Gaussian component to the data. For a second flux calibrated dataset from 2017 day 120 the amplitude of the Gaussian component was measured in the blue and red channel in the minimum between SCALA bandpass and first peak of the crosstalk between spaxels. We normalize the amplitude relative to the amplitude of the SCALA passband. As the distance from the SCALA bandpass to the minimum between SCALA bandpass and first crosstalk peak is different in the two channels (210 Å in the blue and 230 Å in the red channel), we need two different scalings to correct for the decrease in amplitude of the Gaussian. For a Gaussian with 900 Å FWHM we find a decrease of 14 % for the blue and 17 % for the red channel. The measured amplitudes

[1] Reflectivity based on the Fresnel equation: $r = (n_1 - n_2)^2/(n_1 + n_2)^2$

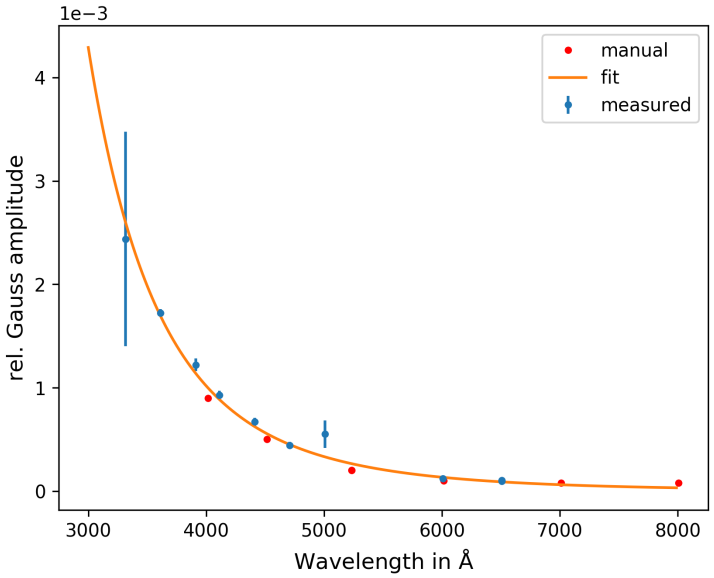

Figure 6.30: Shown is the amplitude of the Gaussian component introduced to the bandpass of the monochromator. The amplitude was measured by modeling the spectra (red dots) or by measuring the ratio between peak amplitude and amplitude at the minimum between the bandpass and the first crosstalk peak produced by SNIFS (blue dots). The curve shows a power law with a scaling exponent of -5

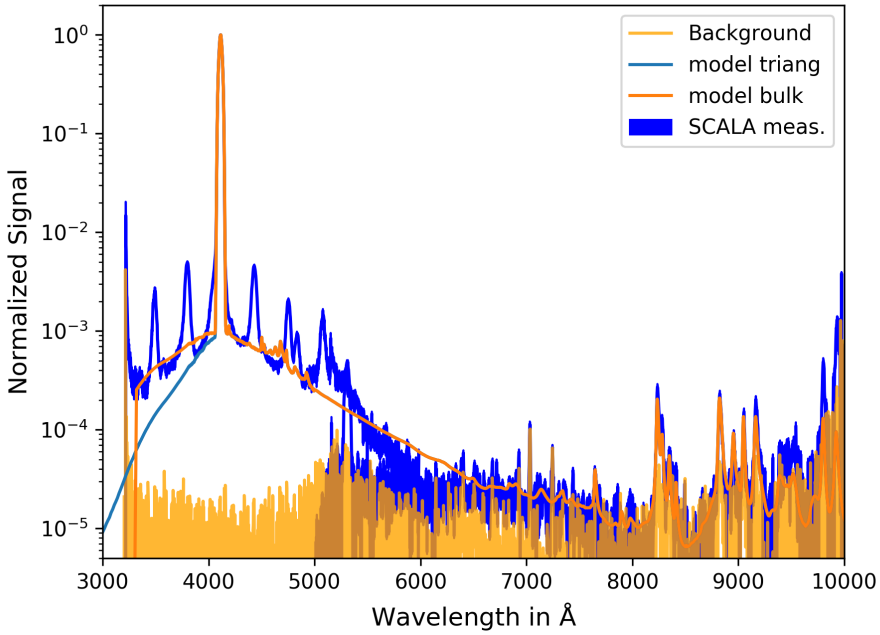

Figure 6.31: In blue we see again the emission from SCALA as measured by SNIFS, the same curve as in fig. 6.28 and in orange and light blue two different models trying to reproduce the observed spectrum. The light blue one is using a triangular model for the throughput while for the orange curve the throughput at wavelength shorter than the SCALA bandpass was set to a constant value. The spectrum is still decreasing as the source spectrum is decreasing for shorter wavelength.

are shown in fig. 6.30 and are scaled by these values to obtain the Gaussian amplitude at λ_c. The uncertainty on these measurements is obtained from the difference in amplitude in the minimum blue and red of the target wavelength. For the first data point at 3315 Å we can not obtain a measurement bluer than the SCALA bandpass, the error bar is therefore increased. We find that the decrease of the amplitude of the Gaussian component can be well described by a power law with a scaling exponent of -5 (see fig. 6.30).

In fig. 6.31 we show the final model (green) using a diffraction core, a triangular excess and a throughput at large distances of $\tau_{\mathrm{OOB}} = 2 \cdot 10^{-5}$. For wavelengths longer than the monochromator wavelength the model is able to describe the observed flux. For wavelengths shorter than the monochromator wavelength the model spectrum is decreasing faster than the observed spectrum. This is caused by the combined decrease of triangular bandpass and model lamp spectrum. To compensate for the decrease in the Xenon spectrum we set the throughput at wavelengths shorter than the monochromator wavelength to a constant amplitude, equal to the amplitude of the Gaussian component (this model differs from the other only at wavelengths shorter than the monochromator wavelength). The decrease, which is still visible in fig. 6.31 is then only caused by the decrease of the source spectrum. We call this excess model a flat-falling

excess. We restrict the region of constant throughput shorter than λ_c to a width of 800 Å.

Throughput at large wavelength distance from the target passband

In fig. 6.28 we saw that the emission spectrum far away from the SCALA passband can be obtained from the lamp model via a wavelength independent throughput τ_{OOB}. We now will constrain its value. From the Xenon emission lines visible in fig. 6.28 and 6.26 and the model for the lamp spectrum, we can estimate that the continuum level in the surrounding of the Xenon lines should be found at a level of 10^{-5} (8000 Å)[1]. The Xenon emission lines are brighter than the continuum and can therefore be detected. We can use them to estimate the continuum in the surrounding of the Xenon lines, even if the continuum itself is still hidden in the measurement noise[2]. To now obtain the value of τ_{OOB} we need to take into account the model spectrum. The model spectrum is 1.75 times brighter at 4113 Å than at 8000 Å, we therefore obtain $\tau_{OOB} = 1.75 \cdot 10^{-5}$.

To further constrain the amplitude of τ_{OOB} we use the model for the monochromator emission and estimate the performance of SCALA in the calibration of the imaging channel equipped with an I-band filter. We therefore use equations 6.15 to 6.18 of the initial example (beginning of sec. 6.4). We use the lamp model shown in fig. 6.27 and the models of the monochromator throughput shown in fig. 6.29. The spectrum emitted by SCALA is then described as the product of monochromator throughput and lamp spectrum.

Before we can constrain the value of τ_{OOB} I will recall the working principle of SCALA. SCALA is made to transfers the calibration from the calibrated photodiode to SNIFS, by stepping through wavelength using the discrete wavelength bands provided by the monochromator. As we step through wavelength we optimize the configuration of SCALA by switching filters, gratings and lamps.

We now need to think about the dependence of τ_{OOB} on switches in the SCALA setup. We do not expect a change of τ_{OOB} when changing the lamp or the order sorting filter (it is a property of the monochromator). We might see an effect when switching the grating. The following table (from [Lombardo, 2017]) gives the wavelengths where the SCALA setup is changed.

λ Range [Å]	Lamp	Grating [Å]	Filter[Å]
3200-4500	Xe lamp	3500	none
4500-5220	Xe lamp	3500	3090
5220-6240	Xe lamp	7500	3090
6240-7020	Xe lamp	7500	4950
7020-10000	W lamp	7500	4950

To optimize the throughput of the monochromator we exchange the gratings with different blaze wavelengths at a wavelength of 5220 Å. However, for our model we do *not* allow for a change of τ_{OOB} when switching the grating.

We can now estimate how the calibration of the imaging channel equipped with the I-band filter should look like. Fig. 6.32 shows the predictions based on the different models, superimposed is a true measurement of SCALA. We have obtained the performance estimate with different

[1] Spectrum at λ_c is normalized to one.

[2] To measure this count level with SNIFS directly at least 2 h of exposure time would be needed. As the detector would saturate after 40 min, several exposures would need to be stacked.

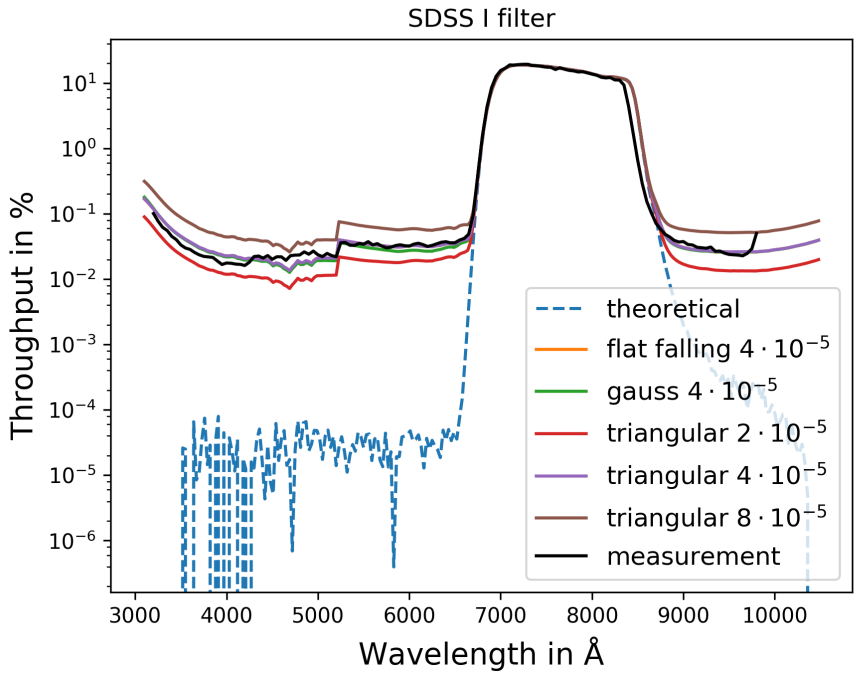

Figure 6.32: Calibrations of the imaging channel of SNIFS equipped with the I band filters. In blue dashed we see a model of the throughput using manufacturer specifications and scaled to the measured throughput within the filter band. The orange, green and red curves show the influence of using different models for the excess, while the red purple and brown curves show different values of τ_{OOB}. The differences between models and measurement are discussed in the text.

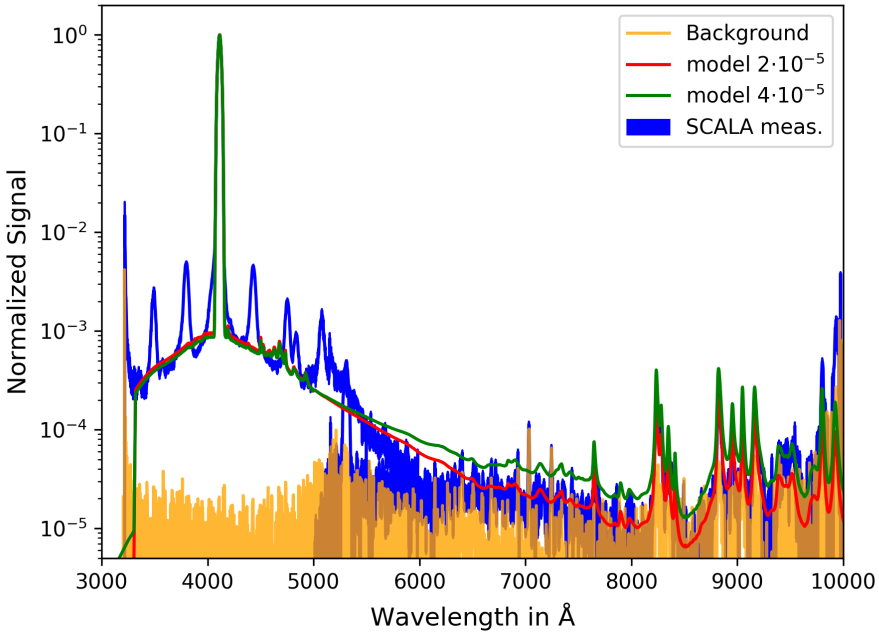

Figure 6.33: Measured spectrum with the same model as in fig. 6.31 with a throughput of $2 \cdot 10^{-5}$ and one with a throughput of $4 \cdot 10^{-5}$. The larger value was needed to explain the measured out-of-band rejection of the imaging channel equipped with a I-band filter.

levels of τ_{OOB}. We find that the model describes the observation best with $\tau_{\mathrm{OOB}} = 4 \cdot 10^{-5}$. The excess of light around the passband is not important for the calibration of the imaging channel with I-band filter, as the passband of the filter is wide and at red wavelength, where the amplitude of the excess is low. However, the measured bandwidth is smaller than in the manufacturer measurements, this deviation can not be explained by out-of-band emission, but needs to be a filter property. We also included cutoffs at 3200 Å and 9800 Å. They represent the limited sensitivity range of SNIFS, and take into account that we can not measure the out-of-band emission spectrum outside of SNIFS sensitivity range. Such cutoffs do not have an influence on the model estimate and are therefore not shown.

The above comparison of SCALA calibration and the model expectation agrees best for $\tau_{\mathrm{OOB}} = 4 \cdot 10^{-5}$. This value of τ_{OOB} is a factor two larger than in the previous estimate based on the Xenon emission lines. Fig. 6.33 shows two models for the emission spectrum from SCALA using a value for τ_{OOB} of $2 \cdot 10^{-5}$ and $4 \cdot 10^{-5}$ together with the observed spectrum to visualize the effect. The model with the stronger throughput explains the filter measurements nicely, but is predicting more flux than observed with SNIFS (i.e in the spectral range from 5800 Å to 8200 Å). Further tests of the SNIFS data-reduction pipeline would be needed here, as such low light levels are usually not used. Flux might have been removed from the data in a background removal step of the data-reduction pipeline.

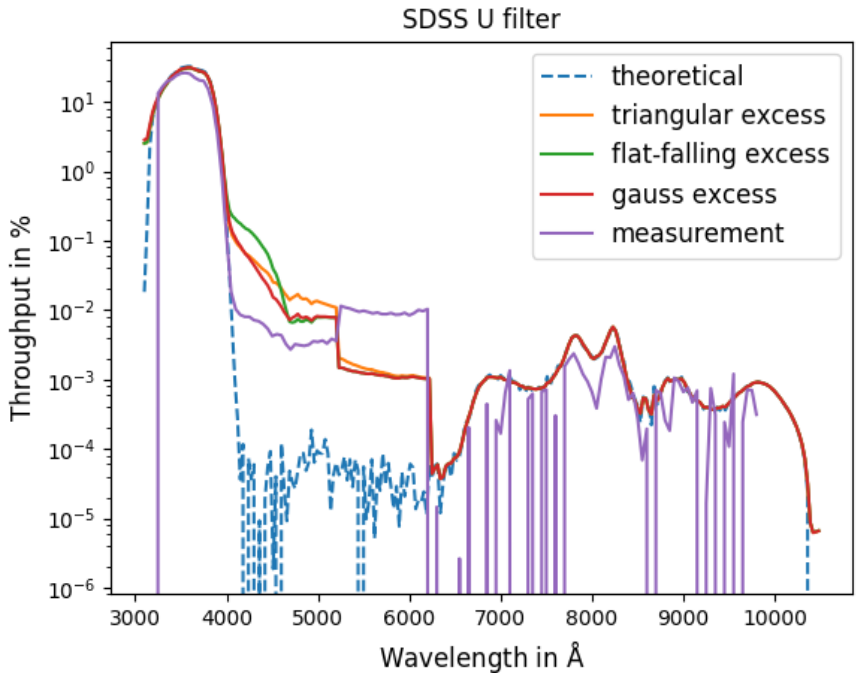

Figure 6.34: Calibration of the imaging channel of SNIFS equipped with the U band filters. In blue dashed we see a model of the throughput using manufacturer specifications and scaled to the measure throughput within the filter band. The orange, green and red curves shows how the measurement would look like using the models obtained for the out-of-band emission from the monochromator. The different models are shown in fig. 6.29. The differences between model and measurement (purple) are discussed in the text.

Comparison of the obtained Models with a Measurement of the U-band filter

We now use the model for the monochromator emission spectrum to estimate the performance of SCALA in the calibration of the imaging channel equipped with a U-band filter. From the models there are two expectations to this test. First we should be able to measure the high out-of-band rejection of the U-band filter for $\lambda_c > 6240\,\text{Å}$. At this wavelength we insert the GG495 order sorting filter between lamp and monochromator, the out-of-band emission from SCALA within the passband of the U-band filter is therefore strongly suppressed[1]. Second, for wavelength $\lambda_c < 6240\,\text{Å}$ we might be able to differentiate between the excess models, as the U-band filter passband is in a wavelength range where the amplitude of the excess is larger than for the I-band filter.

Fig. 6.34 shows now the expectation for the U-band filter together with a measurement by SCALA. We indeed are able to measure the expected filter curve for $\lambda_c > 6240\,\text{Å}$. For $\lambda_c < 6240\,\text{Å}$ the different excess models lead to different expectations for the true SCALA measurements. However, *none* of the models is able to describe the shape of the SCALA

[1]The throughput of the order sorting filter at wavelength shorter than the cut-on wavelength is $< 10^{-5}$.

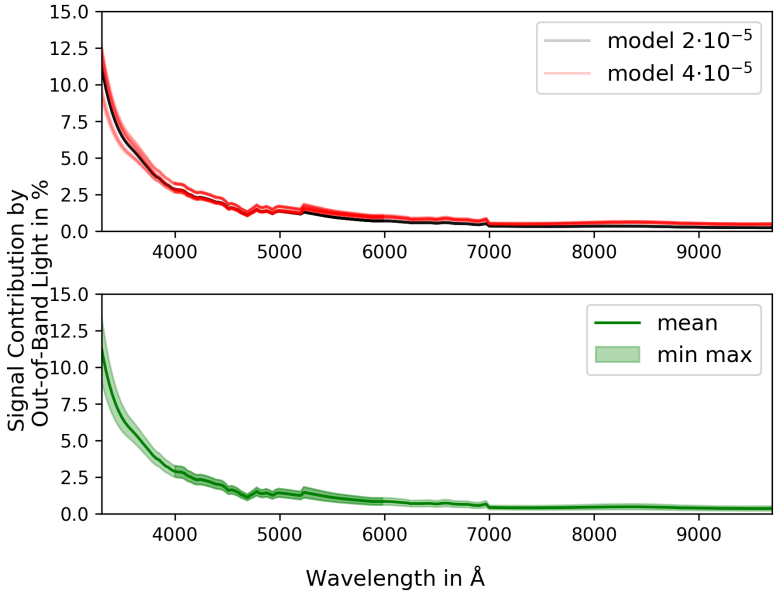

Figure 6.35: Fraction of light detected at the photodiode but generated by out-of-band emission. The upper figure shows in red the fraction obtained for models with high wavelength independent out-of-band throughput ($4 \cdot 10^{-5}$) and in gray with low throughput ($2 \cdot 10^{-5}$). The lower part shows the mean value and the maximal deviations from it.

measurement nor the amplitude and direction of the jump when switching the grating at 5220 Å. The model closest in shape is the triangular excess model. For the calibration of the I-band filter the models were able to predict the direction and the amplitude of the jump properly (when out-of-band emission is weak). However in case of the U-band filter the model fails to describe the proper shape (when out-of-band emission is strong, weak lamp spectrum). We therefore conclude that our model is able to describe the out-of-band emission properly, when the out-of-band contribution to the photodiode signal is low (at longer wavelength). In the following we will use the deviations between the predictions of the different obtained models as uncertainty estimate.

We now use all models to estimate the fraction of signal in the photodiode caused by out-of-band emission. The result of this estimate is shown in fig. 6.35. The upper panel shows the fractions based on the individual models, the ones colored in red have a high $\tau_{\mathrm{OOB}} = 4 \cdot 10^{-5}$ and those colored gray have a low $\tau_{\mathrm{OOB}} = 2 \cdot 10^{-5}$. The lower panel of the figure shows the fraction of generated signal averaged over all models. The green band is giving the maximum deviation between the estimates.

Common to all models is the same shape. The maximum signal is caused by out-of-band emission at wavelengths, where the lamp spectrum is low in amplitude. The flux from the target passband is low as the amplitude of the lamp spectrum is low. The out-of-band emission is caused by light from spectral regions with high amplitude (red to infrared wavelengths)

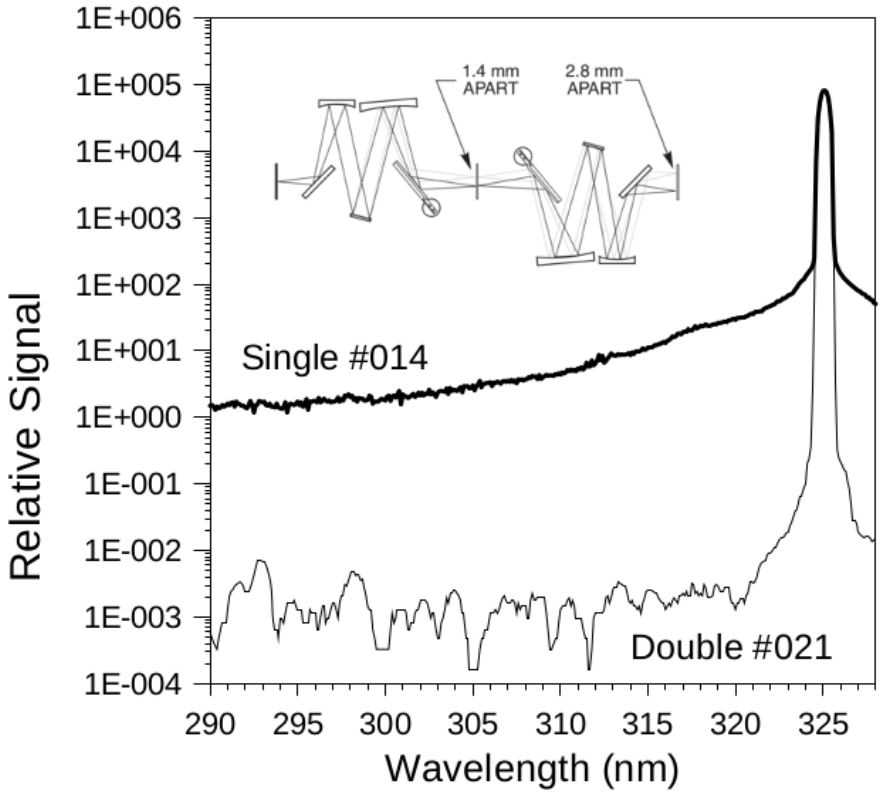

Figure 6.36: Bandpass of a single and a double monochromator measured by illumination with monochromatic light from a HeCd laser at 3250 Å. From [Fioletov et al., 2000], fig. 3. The optical configuration of a additive double monochromator is shown as an insert, the graphic is taken from the manual of the MS257 Newport monochromator http://assets.newport.com/pdfs/e5478.pdf, last checked 31.05.2018.

undesirably passing the monochromator, due to the finite value of τ_{OOB}. On the other hand, if the monochromator target wavelength is set to a value, where the amplitude of the lamp spectrum is strong the out-of-band emission causes offsets of $< 2.5\,\%$ between the through instrumental throughput and the measured throughput. For wavelength shorter than 4500 Å the corrections due to the out-of-band emission are larger than 2.5 %, we therefore restrict our final results to wavelength longer than 4500 Å.

From the models we have obtained the fraction of light detected by the photodiode but generated by out-of-band emission from the monochromator, see fig. 6.35. In the following section we will use this estimate to correct the photodiode current. We will now describe a possible improvement to the setup which allows a significant reduction of out-of-band emission.

We learned that out-of-band emission is a known problem for a single monochromator. An example of this can be found in [Fioletov et al., 2000] and fig. 6.36 shows the bandpass of a single monochromator. The figure also shows the solution to the problem. We should use a double

monochromator. A quick lab test showed that it would be possible to use two Cornerstone 260 monochromators after each other and to suppress the out-of-band emission.

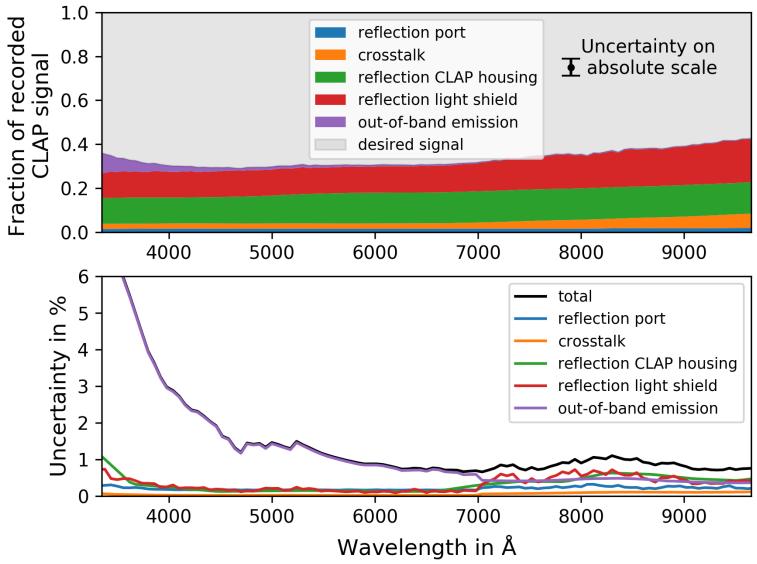

Figure 6.37: Composition of the photodiode signal, including the signal due to out-of-band emission from the monochromator.

6.5 Correcting for Backgrounds, combining Uncertainties

We are interested in the flux emitted by SCALA in the target passband (diffraction core), therefore we use eq. 4.3 and correct for the internal and external backgrounds of SCALA like in eq. 6.10. Therefore we obtain:

$$F_{\mathrm{SCALA}} = (I_{\mathrm{PD}} - B_{\mathrm{Ext.}}) \cdot (1 - CT - R_{\mathrm{LS.}} - R_{\mathrm{Port}} - R_{\mathrm{PDH.}} - F_{\mathrm{oobe}}) \frac{1}{g \cdot R} \cdot \frac{A_{\mathrm{Beam}}}{A_{\mathrm{PD}}} \cdot N_{\mathrm{eff.}} \quad (6.31)$$

Where compared to eq. 6.10 a term for the out-of-band emission F_{oobe} from the monochromator was added. The effect is the same as shown in fig. 6.35. Fig. 6.37 shows the updated composition of the signal incident on the photodiode. The out-of-band emission affects only the wavelengths shorter than 5000 Å.

The uncertainties (lower part fig. 6.37) are now limited by the uncertainties on the out-of-band emission for wavelengths shorter than 7000 Å, afterwards the limitation is still given by the uncertainties on the amount of light reflected off the IS light shield.

As the signal composition changed (we now also account for out-of-band emission), we need to recalculate the effective number of beams. The result is shown in fig. 6.38. As in fig. 6.16 we show the preliminary value of $N_{\mathrm{eff.}}$ provided by Simona Lombardo. After correction for internal backgrounds and out-of-band emission we obtain the value of $N_{\mathrm{eff.}}$ shown with blue errorbars. When including the uncertainties introduced by the reflection off the photodiode housing we obtain an uncertainty in the absolute value of the curve. This uncertainty is shown with the

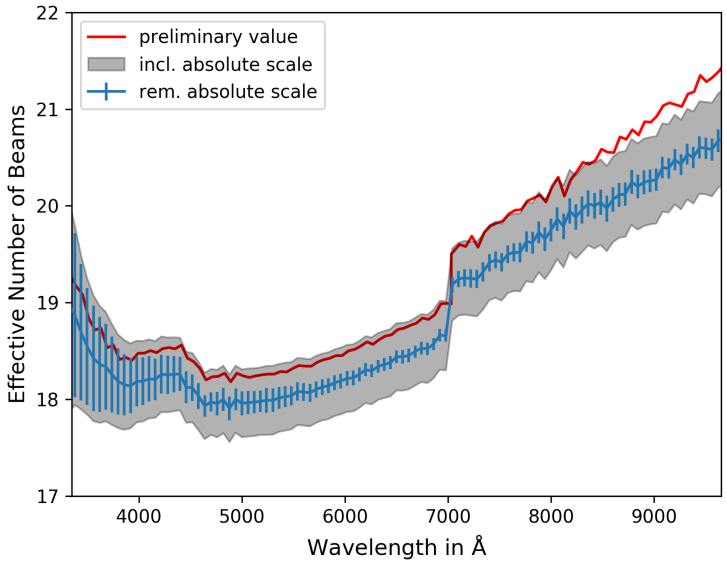

Figure 6.38: Effective number of beams corrected for out-of-band emission

gray band. The value of $N_{\text{eff.}}$ is compared to fig. 6.16 slightly reduced for short wavelengths and the uncertainty is increased due to the uncertainty of the out-of-band emission models.

After correcting the flux detected by the photodiode for background signals, we can compare the flux emitted by SCALA to the one observed by SNIFS using a flux calibration based on standard stars, like in eq. 4.7:

$$\text{RoC} = \frac{E_{\text{SNIFS}}}{E_{\text{Pd}}} \cdot \frac{\Omega_{\text{SCALA}}}{\Omega_{\text{spaxel}}} \tag{6.32}$$

where E_{SNIFS} and E_{Pd} are the energies detected by SNIFS and emitted by SCALA, respectively. Ω_{SCALA} is the solid angle corresponding to one spaxel and Ω_{spaxel} is the solid angle illuminated by SCALA (1° planet). The RoC is shown in fig. 6.39. As shown in fig. 6.39 upper panel we started from as significant wavelength trend. This trend was completely caused by internal backgrounds. These reflections off the SCALA structure can be suppressed by baffling the beam emitted from the IS and by baffling the photodiodes. After correction for the internal backgrounds (middle panel) the calibration by SCALA and CALSPEC is consistent in a broad wavelength range. However, we found a further systematic of the SCALA setup, the out-of-band emission. Taking into account the probable effect on the calibration of the spectroscopic channel we end up with the ratio of calibrations shown in the lower panel. The calibrations by SCALA and CALSPEC agree in the wavelength range from 4500 Å to 9000 Å within our uncertainties. The uncertainties are driven by the modeling of the out-of-band emission and are shown in fig. 6.40. The uncertainty given by the amount of light reflected off the photodiode housing

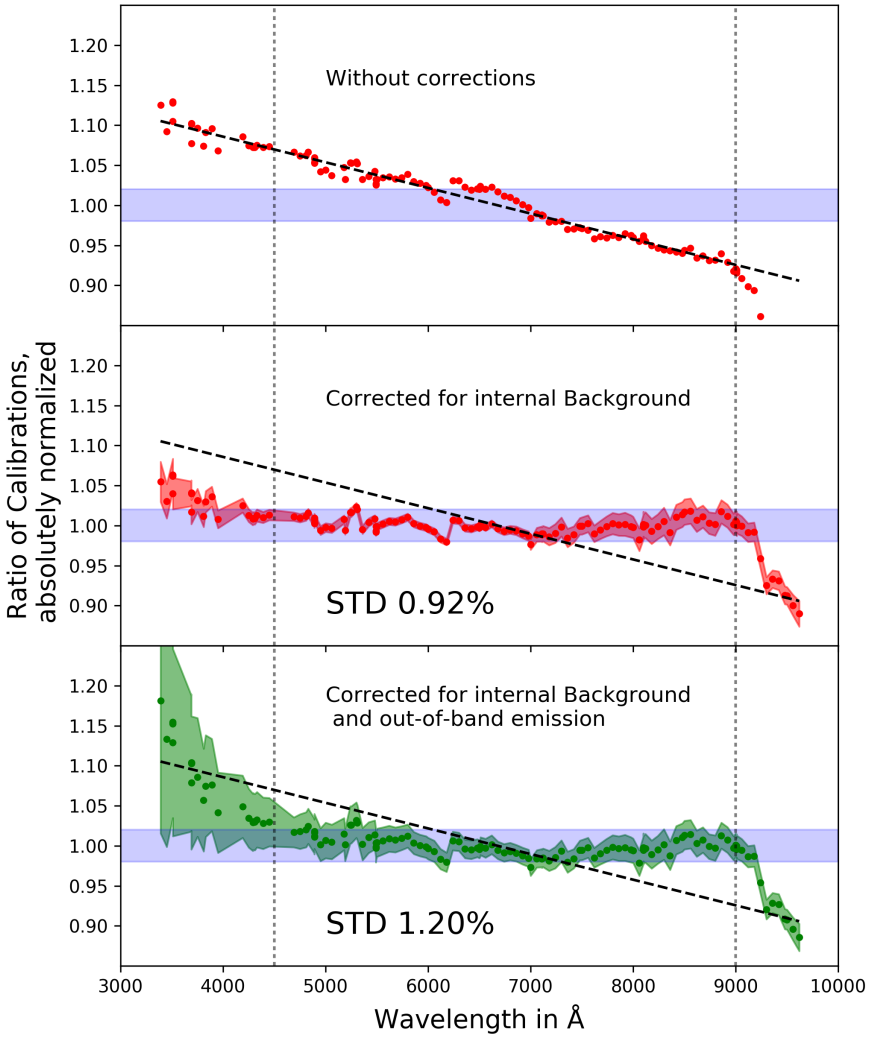

Figure 6.39: Ratio of calibration by SCALA and CALSPEC. The upper panel indicates the initial situation, as in sec. 4.4. The middle panel takes into account the corrections for internal backgrounds. The ratio of calibration in the lower panel is also corrected for out-of-band emission from the monochromator. The trend visible in the initial results is indicated in the middle and lower panel by a black dashed line. Also shown is the wavelength limitation at 4500 Å due to out-of-band emission. The increased deviation at 9000 Åis given by the calibration of SNIFS relative to standard stars. An agreement between the calibrations is indicated in all panels by a blue band of 2 % width. All calibration ratios have been normalized to one in the wavelength range 4500 Å to 9000 Å, and the STD in this range is given in the panels.

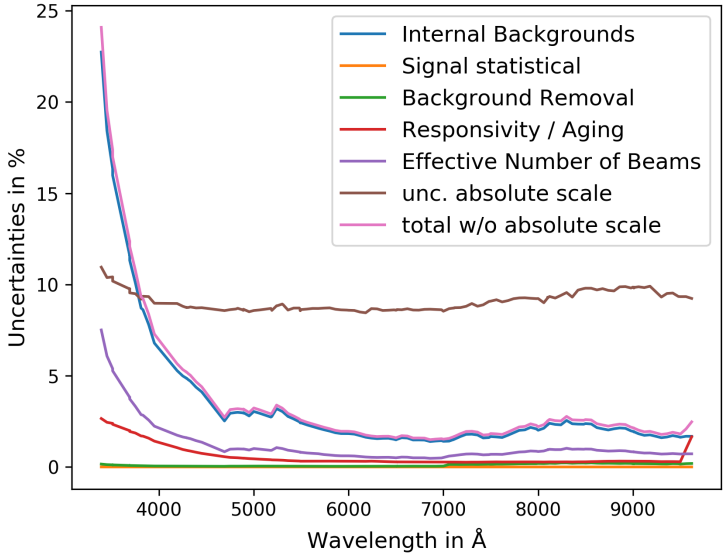

Figure 6.40: Uncertainties accounted for in the error bands of fig. 6.39. The uncertainty on the absolute scale is $\approx 10\,\%$ and is driven by the uncertainty on the aperture area in the measurement of the amount of light reflected off the photodiode housing. The uncertainty on the wavelength dependence of the calibration by SCALA is dominated by the variations between the models for the out of-band emission, followed by the uncertainty on the effective number of beams and the uncertainty on the responsivity / aging of the photodiode.

provides an large uncertainty on the absolute scale but only a weak wavelength dependence. The wavelength dependence is limited by the out-of-band emission correction. In case of an improved measurement for the photodiode housing reflection and the out-of-band emission we would be limited by the uncertainties incorporated in the responsivity of the photodiode, resulting from their aging.

SCALA was built to provide a measurement of the wavelength dependent throughput of SNIFS, and therefore should enable a calibration of standard stars. As shown in sec. D.1 the RoC can also be obtained from the comparison of the throughput measured with SCALA and CALSPEC. Deviations between the two systems at a scale $> 5\,\%$ are excluded by the consistency of the CALSPEC system with previous measurements using a laboratory standard ([Oke and Schild, 1970], [Hayes, 1970] and others. An overview can be found in [Hayes, 1985]). The preliminary results of SCALA (upper panel fig. 6.39) were therefore excluded and the SCALA setup useless without corrections. Including the corrections found in this thesis allows us to correct for the found systematics and makes SCALA a useful device. To reduce the uncertainties improvements to the setup are still needed.

However, so far only uncertainties due to SCALA have been incorporated, but the RoC is also incorporating the flux calibration of SNIFS based on CALSPEC standard stars. In the following chapter we will compare the spectra of the standard stars after application of the flux calibration with the tabulated CALSPEC spectra to obtain possible systematic differences.

Chapter 7

CALSPEC Flux Calibration for *our* Night

We have two independent calibrations of the SNIFS system, one obtained from observations of SCALA and the other one based on the observation of CALSPEC standard stars. In the comparisons shown so far (e.g. fig. 6.39) only uncertainties affecting SCALA have been accounted. In this section we focus on the calibration of SNIFS using CALSPEC standard stars. To quantify possible systematics, we compare the standard star calibrated spectra of the observed standard stars to their tabulated spectra. In case of a perfect calibration (using standard stars) we should find an agreement.

As described in sec. 4.2, we can use the observation of stars with known spectra to calculate the atmospheric and instrumental transmission using eq. C.6. The throughputs of atmosphere and instrument were evaluated for our night (159 of 2015). The spectra corrected for the instrumental and atmospheric transmission are shown in fig. 7.1. The SNIFS throughput evaluated from the observations has been shown in fig 4.5.

We will use the same parameterization for the atmospheric and instrumental throughput, as in the data-reduction pipeline, but we do not use the wavelength dependence of the scattering processes (sec. C.2.2) to further constrain the fit. We will calculate the atmospheric and instrumental throughput for each wavelength within the data-cube and apply a wavelength binning afterwards. The results will therefore not be limited by the statistical uncertainties on the individual observation, but by the systematics introduced in the data-reduction pipeline

We have to stress that our night is different from usual nights as the entrance pupil mask is mounted to the telescope, and the flux is therefore reduced by a factor ten. We did not increase the exposure time by a factor ten to collect the same signal, as this would result in a reduced number of observed objects. Due to the lower signal in the spectrograph the flux solution of our night might be different from usual nights, and might have other uncertainties.

To evaluate the systematic uncertainty on the instrumental transmission, we compare the observed, calibrated spectrum $S_{\mathrm{obs,cal}}$ to the tabulated spectrum S_{tab} via the functional dependence of the atmospheric transmission on the airmass (similar eq. C.5):

$$S_{\mathrm{obs,cal}} = S_{\mathrm{tab}} \tau_{\mathrm{inst.}} 10^{-kz} \tag{7.1}$$

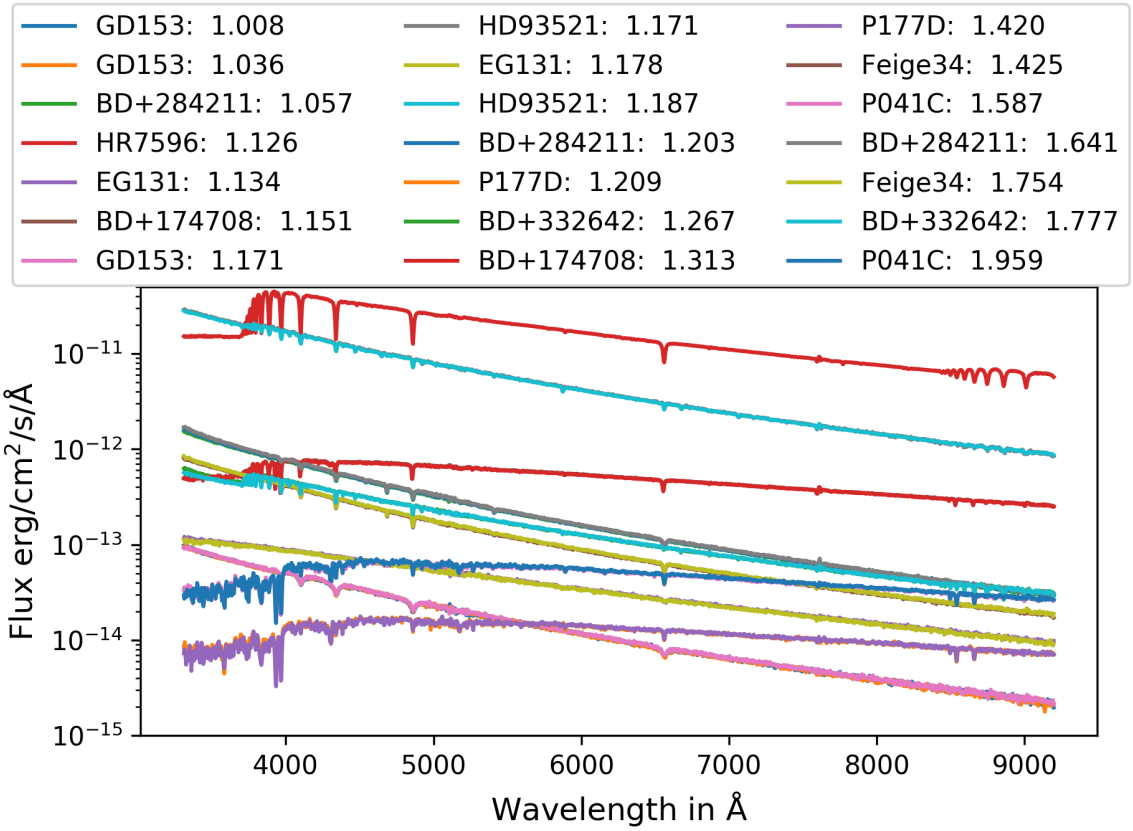

Figure 7.1: Flux calibrated spectra of the stars, which have been used for the fit of atmospheric and instrumental throughput, in log scale. The mean airmass of the observations is presented in the legend together with the object name.

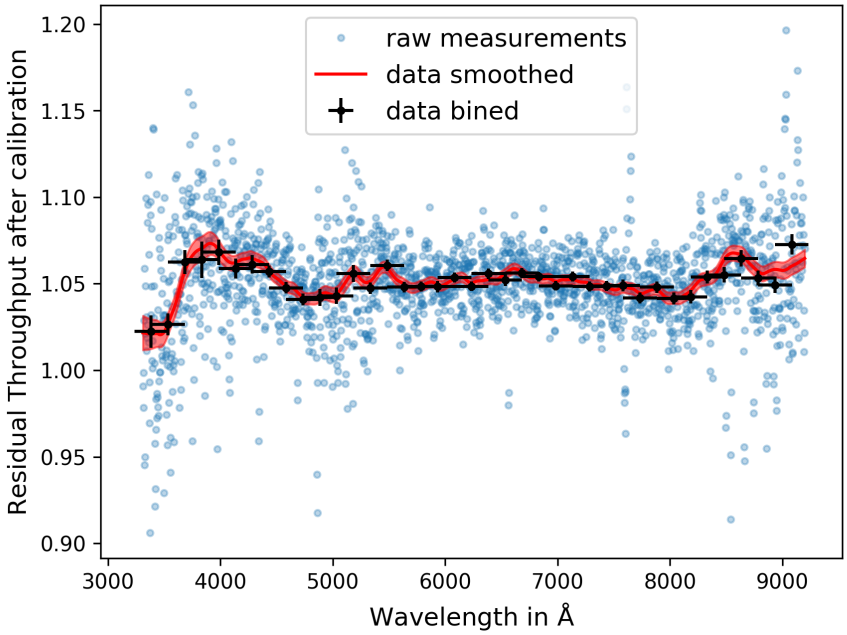

Figure 7.2: Residual throughput obtained from the flux calibrated standard star spectra, with its uncertainty.

With $\tau_{\text{inst.}}$ the instrumental throughput, k the wavelength dependent scattering constant and z the airmass. Rearranging the terms of eq. 7.1 gives:

$$\log\left(\frac{S_{\text{obs,cal}}}{S_{\text{tab}}}\right) = log\left(\tau_{\text{inst.}}\right) - kz = c + m(z - \langle z \rangle) \tag{7.2}$$

We see that the instrumental throughput $\lg(\tau_{\text{inst.}})$ and the atmospheric extinction k can be obtained from eq. 7.2 via linear fits at each wavelength in the SNIFS spectrum (each resolution element). This fit delivers residual instrumental throughputs $\tau_{\text{inst.}}$ around 1.0 and residual extinctions around ≈ 0.017. This residual extinction means that the flux calibration using CALSPEC standard stars is miss-estimating the atmospheric extinction, which means that the instrumental throughput, which we have used in the previous comparisons between SCALA and CALSPEC is off by 6 % with the weak wavelength dependence visible in fig. 7.2. The individual measurements (blue dots) show a large spread and spikes in the distribution, caused by the difference in spectral resolution between SNIFS and CALSPEC spectra. The CALSPEC spectra have not been smoothed to match their resolution to the one of SNIFS. The residual throughput at zero airmass is obtained via binning with 300 Å and is shown with black errorbars.

The residual throughput indicates a difference between tabulated spectrum and flux calibrated observations. This difference is of the order 5 % in amplitude and nearly wavelength

independent. The 5 % offset is caused by an overestimate of the atmospheric extinction. For the RoC (sec. 4.4) we therefore have to reduce the flux obtained by SNIFS for the SCALA observations by $\approx 5\,\%$, with the wavelength dependence shown in fig. 7.2.

For stars, measured in an airmass range of 1 to 2, the offset in flux is smaller, but SCALA measures the throughput of the system without the atmosphere (zero airmass). We therefore need to interpolate down to zero airmass and are more sensitive to the atmospheric extinction, due to the longer lever arm.

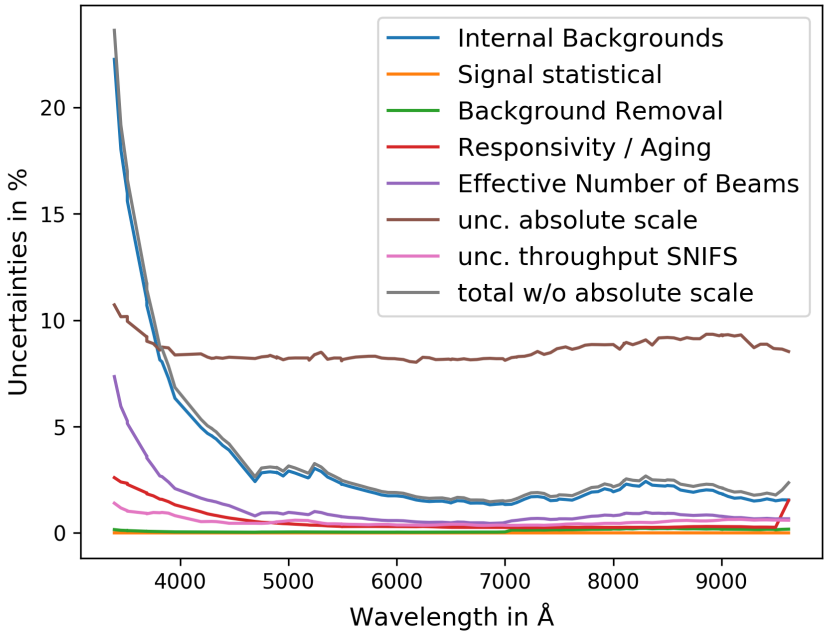

Figure 7.3: Uncertainties accounted for in the error bands of fig. 7.4. The uncertainty on the absolute scale is driven by the reflection off the photodiode housing (sec. D.7). The wavelength dependence of the calibration by SCALA is limited by the uncertainty on the out-of-band emission and the uncertainties in the measurement of the effective number of beams. The next smaller uncertainty is given by the aging of the photodiode and the uncertainty on the SNIFS throughput for our special night.

Applying Correction for SNIFS Throughput

Correcting the RoC from fig. 6.39 for the systematic found above, we obtain the results shown in fig. 7.4. As we normalize the RoC in the wavelength range 4500 Å to 9000 Å, the effect on the figure is minor. We see that the measurements in this wavelength range are consistent with a constant with a standard deviations (STD) of 1.0 %, when correcting for internal backgrounds only, and 1.3 %, when also correcting for the out-of-band emission. We see residual structures in the RoC, which are consistent with the wavelengths indicated by gray dashed lines (fig. 7.4). These wavelengths are special and caused by the SCALA working principle. SCALA is made to transfers the calibration from the calibrated photodiode to SNIFS, by stepping through wavelength using the discrete wavelength bands provided by the monochromator. As we step through wavelength we optimize the configuration of SCALA by switching filters, gratings and lamps. The dashed vertical gray lines indicate wavelengths where the SCALA setup is changed (switch of gratings, filters and lamps). Residual structures (jumps) in the RoC are expected e.g. due to change of out-of-band emission. The uncertainties contributing to the error bands in fig. 7.4 are shown in fig. 7.3. The only difference to fig. 6.40 is the uncertainty from the calibration of SNIFS relative to CALSPEC, which compared to other uncertainties is small.

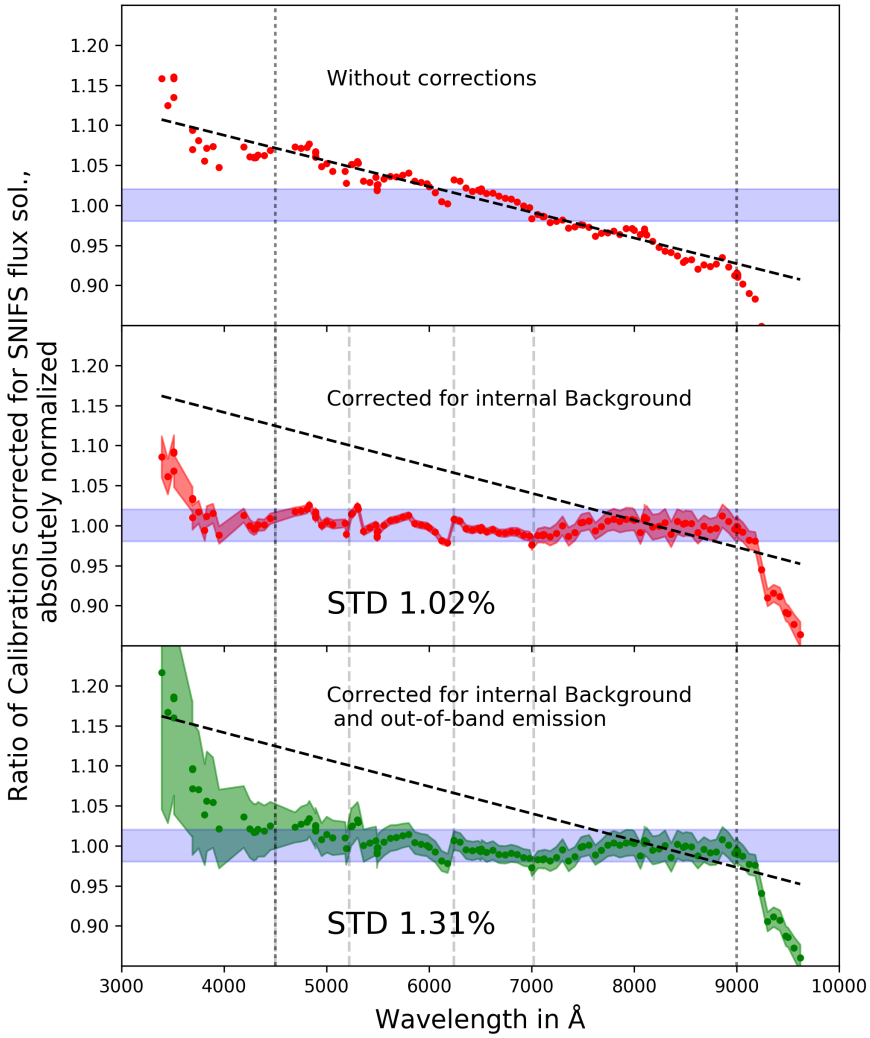

Figure 7.4: Ratio of calibration by SCALA and CALSPEC. The upper panel indicates the initial situation, the same as in sec. 4.4. The middle panel takes into account the corrections for internal backgrounds. The ratio of calibration in the lower panel is also corrected for out-of-band emission from the monochromator. Compared to fig. 6.39 all curves have been corrected for the residual throughput found in the previous paragraph. The vertical dashed lines indicate wavelength where the SCALA configuration is changed (use of different: gratings, order-sorting filters, lamps).

Chapter 8

Time Evolution of Corrections

So far we have assumed, that the corrections for the reflections within SCALA are constant in time, we used eq. 6.31, which is reproduced here:

$$F_{\mathrm{SCALA}} = (I_{\mathrm{PD}} - B_{\mathrm{Ext.}}) \cdot (1 - CT - R_{\mathrm{LS.}} - R_{\mathrm{Port}} - R_{\mathrm{PDH.}} - F_{\mathrm{oobe}}) \frac{1}{g \cdot R} \cdot \frac{A_{\mathrm{Beam}}}{A_{\mathrm{PD}}} \cdot N_{\mathrm{eff.}} \quad (8.1)$$

With I_{PD}, the photodiode current, $B_{\mathrm{Ext.}}$ the external background (e.g. daylight leaking into dome), CT accounting for the optical crosstalk between the SCALA beams, $R_{\mathrm{LS.}}$ the correction for light reflected off the light shields in front of the integrating spheres, R_{Port} accounting for the reflection of light at the IS ports, $R_{\mathrm{PDH.}}$ accounting for reflections off the photodiode housing and F_{oobe} accounting for out-of-band emission from the monochromator. For the crosstalk and the reflection off the integrating sphere light shield we know, that their amplitudes change in time. To account for this uncertainty, we will recalculate the ratio of calibration with varying amplitudes for crosstalk and light shield reflection.

In sec. 6.2.1 we have seen that the amplitude of the crosstalk (CT) decreased from Dec. 2015 to Aug. 2017 by 50 %. The calibration had been performed before in June 2015, therefore the amplitude of the crosstalk might have been larger than in Dec. 2015. Using a linear extrapolation, the crosstalk in June 2015 is expected to be 15 % larger than in Dec. 2015. We thus scale the correction for the crosstalk by $f_{CT} = 1.15$. To evaluate the influence of this scaling factor, we will vary it in the range $0 \leq f_{CT} \leq 2$, so between no crosstalk correction and a crosstalk twice as strong as measured.

In sec. 6.2.2 we have seen that the amplitude of the amount of light reflected off the light shield (R_{LS}) depends on the amount of dust on its surface. We know that heavy dust like in fig. D.2 & D.3 can reduce the amount of light detected on the photodiode (R_{Dust}) by up to 8 % (see. fig. 6.13). To account for this dust dependence we scale R_{Dust} in amplitude and subtract it from the correction for the light reflected on the IS light shield R_{LS}, we obtain $R_{\mathrm{LS}} - R_{\mathrm{Dust}} f_D$. Different amounts of dust are realized by the scaling factor f_D. To estimate the value of f_D for our measurement in May 2015, we take into account that our light shield was clean in May 2014 (when SCALA was mounted), we thus obtain $f_D = 0$. We can be sure, that the amount of dust on the light shield was never more than in fig. D.3 (Jan. 2018), as the light shields have never be cleaned before Jan. 2018. As the measurements for R_{Dust} have been obtained in Jan.

2018 we obtain $f_D = 1$. Based on a linear interpolation we obtain $f_D = 0.27$ for May 2015. To evaluate the influence of the dust we vary the scaling of the dust correction in the range $0 \leq f_D \leq 2$, so between no dust (clean light shield) and a dust correction twice as strong as measured.

We also apply a absolute scaling on the correction for light reflected of the photodiode housing. The scaling factor is f_{PDH}. To show its influence we vary the factor in the range $0 \leq f_{\mathrm{PDH}} \leq 2$, so between no correction for light reflected of the photodiode housing and a reflection twice as strong as measured.

Based on the above considerations we obtain the following parameterization for the correction of the photodiode signal:

$$S_{\mathrm{Corr.}} = (S_{\mathrm{PD}} - B_{\mathrm{Ext.}}) \cdot (1 - CT f_{CT} - (R_{\mathrm{LS}} - R_{\mathrm{Dust}} f_D) - R_{\mathrm{Port}} - R_{\mathrm{PDH.}} f_{\mathrm{PDH}}) \tag{8.2}$$

For each set of f_{CT}, f_D and f_{PDH} we evaluate the effective number of beams and afterwards the RoC. In sec. 7 we have seen that the RoC is nearly flat in the range from 4500 Å to 9000 Å. For each aging model we evaluate RoC, its mean $\overline{\mathrm{RoC}}$ and its STD in this wavelength range. We use the ratio of STD and $\overline{\mathrm{RoC}}$ to quantify the flatness of the RoC. Some example curves of the RoC for different combinations of f_{CT} and f_D are shown in sec. D.6. We decided to use the STD to evaluate the flatness of the RoCs, instead of performing a linear fit as the shape of the RoCs is deviating from a linear relation, and might therefore be unstable.

Fig. 8.1 shows the influence of the modeled aging on the corrections on the reflections within SCALA. In the upper left we see different combinations of f_{CT} and f_D. We see that the RoC is closest to a constant, when the scaling factor for the amplitude of the crosstalk f_{CT} is related linearly to the scaling factor for the dust f_D (upper left), when $f_{CT} \approx 1 + f_D/2$. This dependence is caused by the similar shape of the amplitude of crosstalk and light shield reflection. The cause of the similar shape is that both internal reflections occur off a black anodized surface.

A few points in the plain of f_{CT} and f_D have been picked. If we assume, that the corrections are stable in time, we obtain the red point. In case we assume a linear change in time, we obtain the red triangle. The orange dot is showing the minimum in the f_{CT} and f_D plane. The gray diamonds are showing extreme cases of possible aging. The RoC belonging to each of these points is shown in the lower panel of the figure. For $\lambda < 8000$ Å all curves practically overlap.

The STD of the RoC is only weakly depending on the amplitude of the reflection off the photodiode housing, which can be seen in the upper right panel, here we pick two different points in the f_{CT} - f_D plain (corresponding color) and vary the scaling factor to the photodiode housing reflection f_{PHD}.

The most probable case for our measurement in night 159 of 2015 is, that the crosstalk is slightly stronger in amplitude $f_{CT} = 1.15$ than its value in Dec. 2015. The amount of light reflected off the light shield is lower than that reflected off a clean light shield with $f_D = 0.27$. However, as can be seen from the lower panel of fig. 8.1 the curves with and without aging practically overlap, and their STD / $\overline{\mathrm{RoC}}$ is 1.28 % and 1.31 % respectively. Even extreme cases, shown in gray, are practically identical for wavelength < 8000 Å. Based on these findings we conclude that aging of the corrections is not limiting our results, even if the corrections have been measured up to three years after the calibration of SNIFS by SCALA.

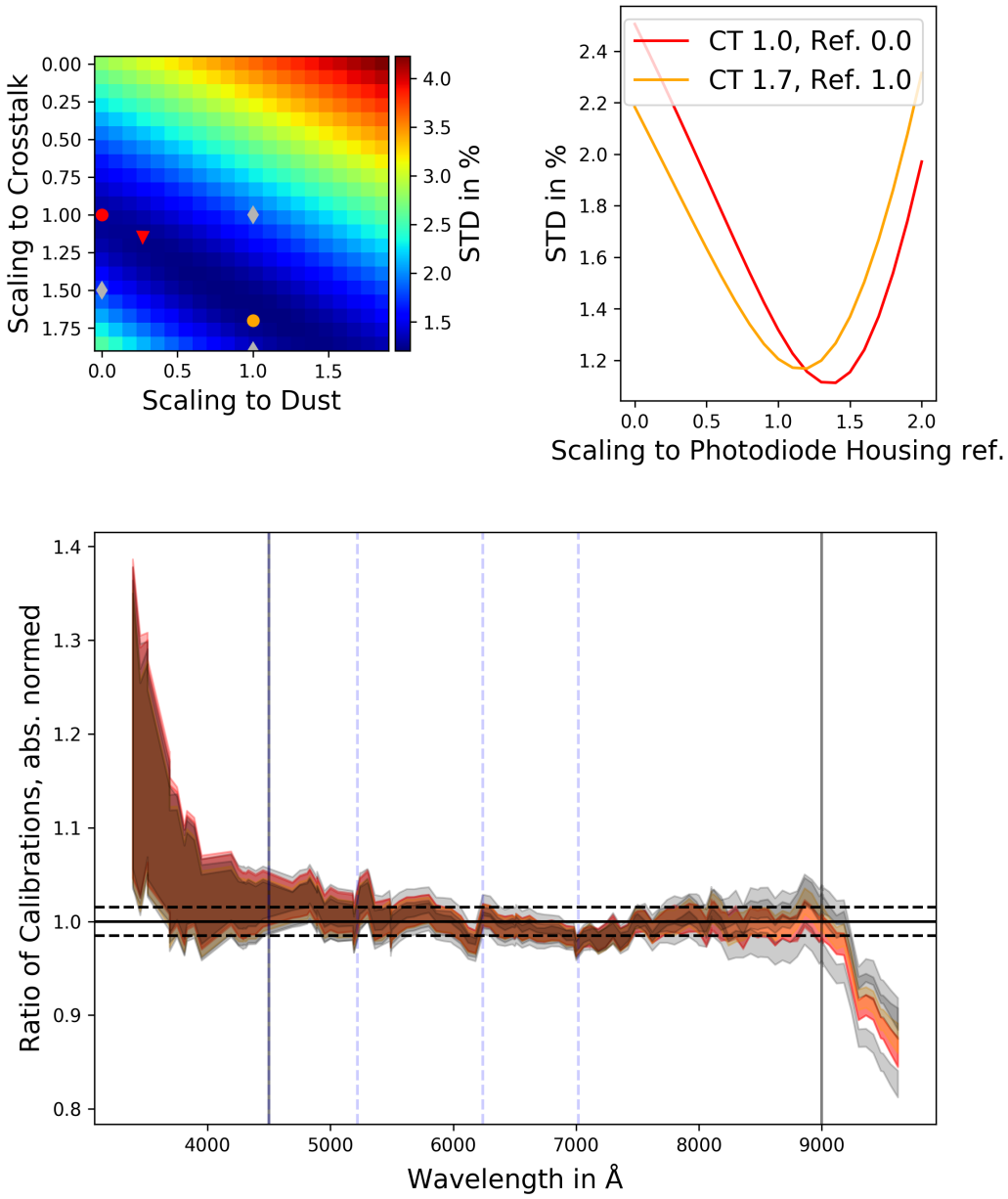

Figure 8.1: Upper left: deviation from a flat RoC in % while varying the amount of crosstalk and dust on the IS light shield. The red point indicates the value of the corrections without aging. The red triangle indicates the point, which is reached in case of a linear extrapolation of the corrections (expected aging). The deviation from a flat RoC is minimal for the combination of f_{CT} and f_D represented by the orange dot. The gray diamonds represent extreme cases resulting in the gray bands shown in the lower panel. Upper right: deviation from a flat ratio of calibrations in %, for the two points of corresponding color in the upper left (no aging, maximal flatness), by varying the amount of light reflected off the photodiode housing. Lower panel: Ratio of calibrations for the points and diamonds indicated in the upper left. The curves are normalized for the mean in the wavelength range 4500 Å and 9000 Å. The dashed black lines indicate a range of ±1.3 %. Up to 8000 Å the curves practically overlap.

Chapter 9

Results & Outlook

Results

In sec. 2.3 we have motivated the need for a physical calibration device which enables calibration of an astronomical source relative to a testable laboratory standard. SCALA was built for this goal. In the calibration measurements we transfers the calibration from the calibrated photodiode to SNIFS, by stepping through wavelength using the discrete wavelength bands provided by the monochromator. As we step through wavelength we optimize the configuration of SCALA by switching filters, gratings and lamps.

There were measurements in which Vega was measured relative to laboratory standards. These measurements are summarized in [Hayes, 1985]. The main figure is reproduced here, see fig. 9.1. The comparison of measurements of the Vega spectrum performed by six groups is shown. They agree to a scale of 1 % (indicated by red lines). As these measurements were obtained relative to standards provided by different institutes (From Washington, St. Petersburg (Leningrad) and Heidelberg) and with different devices, they can be regarded reliable.

We further know that the CALSPEC system is consistent in its wavelength dependence with the measurements by D. S. Hayes and D. W. Latham [Hayes and Latham, 1975], as shown in fig. 9.2. The upper panel shows a comparison between the spectra of Vega measured by Hayes (blue datapoints) and the spectra of Vega from CALSPEC. The Hayes measurements (2 % systematic uncertainties) deviate at absorption lines in the Vega spectrum, especially for wavelengths longer than 8500 Å, which is visible in the lower panel. This deviation is caused by the different spectral resolutions of Hayes and CALSPEC spectra.

The consistency of the measurements (fig. 9.1) and the consistency of them with the CALSPEC system (fig. 9.2) excluded the preliminary SCALA results shown in fig. 9.4. This thesis has shown that the systematic difference between the preliminary SCALA result and the CALSPEC system was caused by effects internal to SCALA, see fig. 9.4 middle panel. After correction for these effects (reflections, out-of-band emission, aging) our measurements are consistent with the above results (see green band[1] in fig. 9.2).

All remaining deviations between SCALA and CALSPEC can be explained by the uncertainties incorporated in the corrections for systematic biases (like internal reflections) and by

[1] the uncertainty band here is the reciprocal of the band in fig. 8.1, as we here compare fluxes and not throughputs

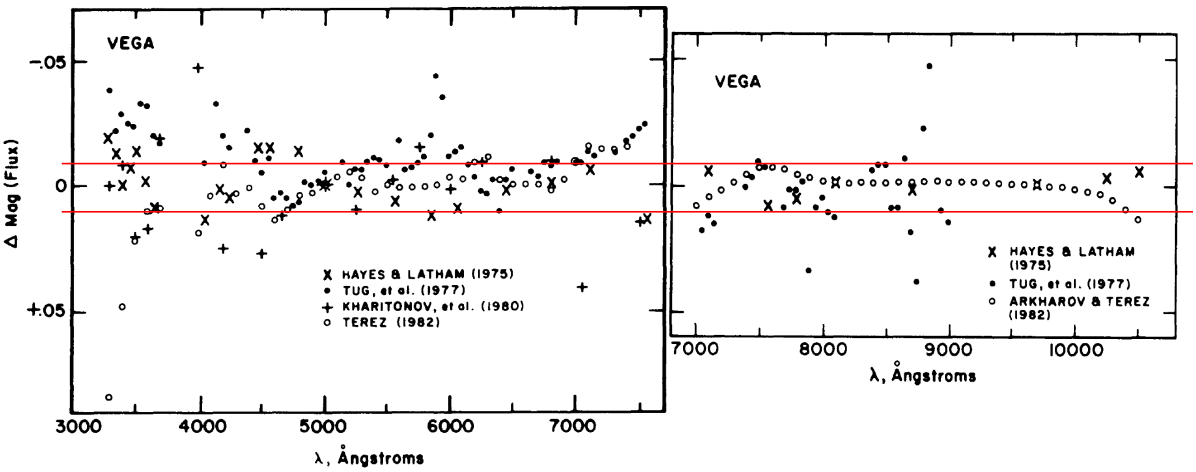

Figure 9.1: Deviation in magnitudes between measurements of the Vega spectrum performed by several groups worldwide. The two red lines indicate a band of ± 0.01 mag, which corresponds to a flux uncertainty of $\pm 1\,\%$.

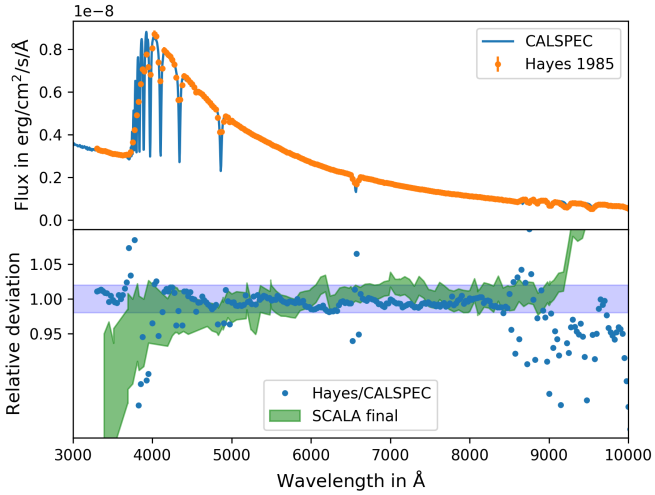

Figure 9.2: Upper panel: comparison of the Vega spectrum measured by Hayes and the CALSPEC reference spectrum of Vega. The lower panel shows the relative deviation between the two spectra. The spectra are consistent in regions without absorption lines. The blue band indicates the systematic uncertainties of the Hayes results. The green band shows the SCALA final result and is consistent with the previous results in the wavelength range from 4500 Å to 9000 Å.

changes in the SCALA system (like automated switch of filters, gratings, lamps). We conclude that the wavelength dependencies of the calibration by SCALA and CALSPEC agree at a scale of 1.3 % (within our uncertainties). As we do not find a systematic difference between the calibrations, there is also no influence on the cosmological parameters Ω_Λ, ω_0 and ω_a (equation of stat parameters).

We have shown that the results obtained so far are limited by the precision of our corrections and not by a fundamental limit like the precision of our photodiode. Improvements to our setup would allow for further reductions of the backgrounds (external, internal and out-of-band) and would therefore allow tests at the sub-percent scale.

The absolute scale of the calibration by SCALA deviates from the calibration by CALSPEC standard stars by 36 ± 15 %. The uncertainty on the absolute scale is mainly given by two effects. We found a reflection off the photodiode housing, allowing light which would usually miss the sensitive area of the photodiode to be detected, see sec. D.7. The second contribution is from possible stray light in the UH88 telescope and SNIFS. This light could also contribute a background of up to 7 %, see sec. F.4. We performed further tests, focused on the difference between the illumination of SNIFS by stars and SCALA. These tests did not reveal further systematics and are shown in sec. F. For cosmological measurements, the absolute scale is extracted from local measurements. The large uncertainty on the absolute scale in the SCALA measurements is therefore corrected and the scientific results are unaffected.

In the following I will summarize the results of the individual chapters. In sec. 2.3 we showed that improved constraints on time-varying dark energy require a sub-percent calibration of astronomical observations. Our calibration device SCALA was built for this purpose. We use a photodiode as a sub-percent flux standard, its properties are described in sec. 5.2. Based on the publication [Larason and Houston, 2008] we obtained an uncertainty for the aging of photodiodes. However, in the range 5500 Å to 9500 Å, we are limited by the transfer of calibration by the Paris supernova cosmology group and not by aging.

Afterwards, we investigated several backgrounds contributing to the measured photodiode signal. The external background (see sec. 6.1) is caused by light reaching the photodiode. For daytime measurements, sunlight leaking into the dome is the most important source. We found that the data reduction is able to remove this external background without introducing biases on average. Uncertainties for night time are limited by the data collection scheme. For long exposure times, we are limited by two effects. First, we do not know how the background is changing during the signal measurement. Second, the exposure time for background measurements is too short to collect enough statistics (see fig. 6.6). At the current stage we are not limited by the background removal and adapting the measurement procedure (e.g. by introduction of a chopper) will improve the background removal.

We found internal backgrounds, caused by reflections within the SCALA structure, which allow light, that would usually miss the photodiode to produce a signal. As the light source for these backgrounds is SCALA, these backgrounds are proportional to our desired photodiode signal. We differentiate these effects for the different surfaces where the reflections occur. As these internal reflections have been identified and quantified, we can correct the photodiode signal for these backgrounds. The effects are:

- **Crosstalk between SCALA beams:**

Light leaving one of the integrating spheres ports misses the collimating mirror belonging to it and illuminates the SCALA structure. There, the light is scattered, and reaches the photodiode via a reflection off the collimating mirror. The amplitude of crosstalk is constant up to 7000 Å and increases for longer wavelengths, like the reflection coefficient of black anodized aluminum. Its amplitude decreases with time due to dust accumulation on the involved surfaces (sec. 6.2.1).

- **Reflection off IS light shield:**
  Light can be reflected off the light shield mounted on the integrating sphere (sec. 6.2.2). As the surface of the light shield is anodized in black, the wavelength dependence is similar to the one of the crosstalk. Its amplitude shows a dependence on the amount of dust accumulated on the light shield.
- **Reflection off IS port and photodiode housing:**
  The surrounding of the integrating sphere port (sec. D.8) and the metal housing of the photodiode (sec. D.7) can also serve as surfaces for reflections, generating a background.

Our current result is not limited by these backgrounds and now that these biases are identified they could be suppressed by an upgrade of SCALA. The bandpass of the monochromator used in SCALA shows finite throughput outside of the desired passband. By the use of SNIFS we obtained models for the emission outside the desired passband. These models allowed us to estimate the contribution of out-of-band emission to our photodiode measurements.

Fig. 9.3 shows the composition of the photodiode signal. We find that $27\text{-}42 \pm 4\,\%$ of the signal observed by the photodiode is caused by the discussed backgrounds. Based on this calculation we estimated the effective number of SCALA beams which allows us to measure the total flux emitted by SCALA.

As we are comparing the flux calibration performed with SCALA to the one with standard stars, we need to take into account systematic uncertainties within this calibration. These differences might be caused by the introduction of an entrance pupil mask to the telescope via diffraction (change of PSF, see F.3) or the smaller collecting area (lower signal-to-noise). To test for these possibilities we compare the flux of the observed CALSPEC standard stars, after their calibration with themselves, to their known spectrum. Found deviations are thus based on biases introduced in the data reduction. We find a systematic deviation of up to 5 % with a weak wavelength dependence (see sec. 7).

In sec. 8 we investigated the aging of the background corrections. This step is necessary as some of the internal backgrounds (crosstalk, light shield reflection) have been measured up to three years after the calibration of SNIFS by SCALA. Our results are only weakly depending on the aging of the background corrections. We find that the wavelength dependence of a calibration performed with SCALA agrees to the one obtained with CALSPEC in the wavelength range from 4500 Å to 9000 Å within 1.3 %. The remaining structure visible in fig. 9.4 can be explained by changes in the SCALA setup (automated switch of filters, gratings and lamps). We therefore do not find a significant systematic difference ($> 1.3\,\%$) between the wavelength dependence of the calibration by SCALA and CALSPEC, cosmological parameters are therefore unaffected.

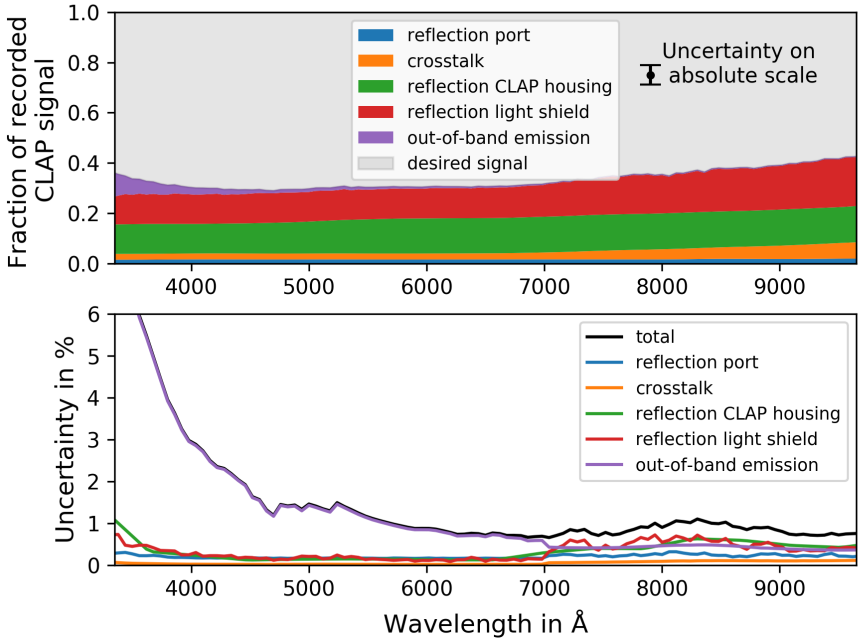

Figure 9.3: Composition of the signal detected by the photodiode after removal of the external background. The different backgrounds are discussed in sec. 6, up to 50 % of the measured signal can be caused by these effects.

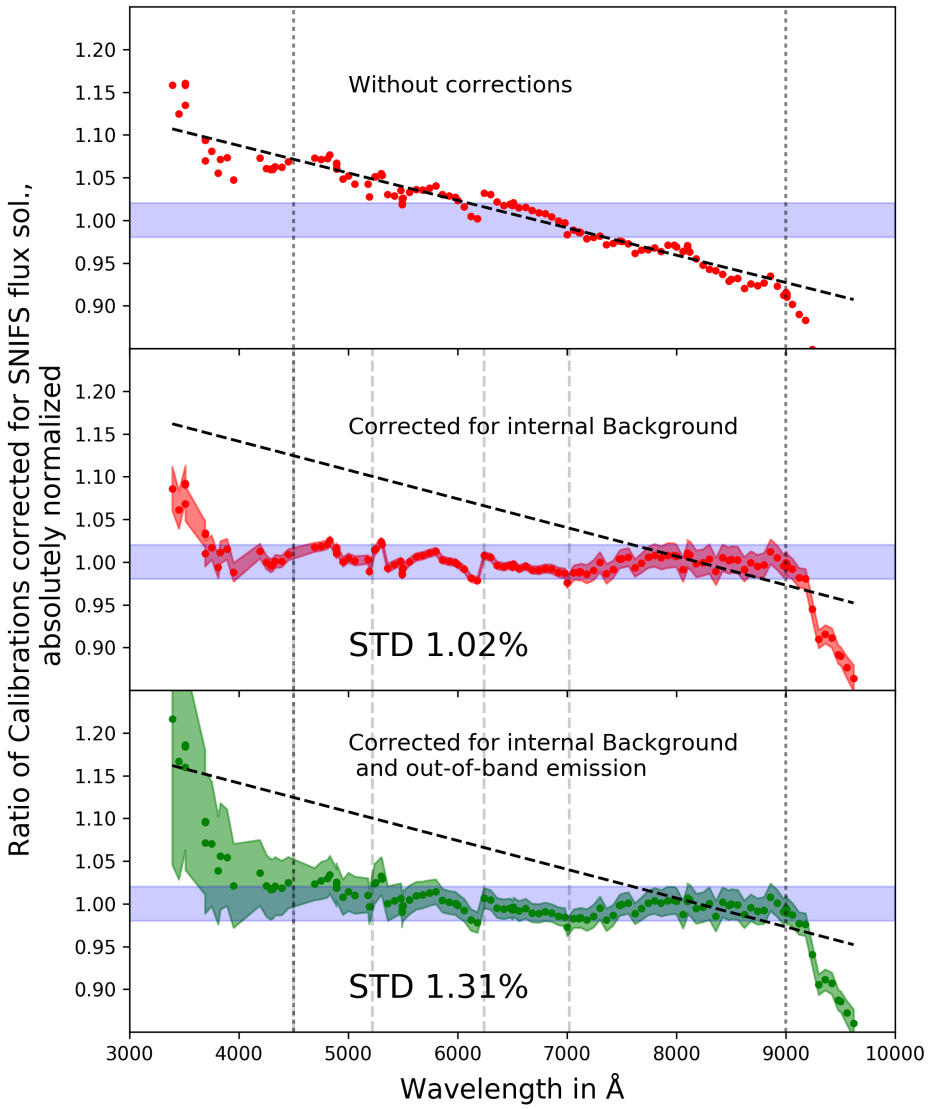

Figure 9.4: Ratio of the calibration performed with SCALA and with CALSPEC standard stars. The upper panel shows the preliminary result from [Lombardo, 2017]. The middle panel is obtained after correction for internal reflections. The lower panel shows the final result after taking into account out-of-band emission from our monochromator. In the range from 4500 Å to 9000 Å we find an agreement of SCALA and standard stars at a 1.3 % level. The grating, filter and lamp combination used by SCALA are optimized differently for different wavelength regions. Boundaries between these are indicated by vertical lines. Discontinuities at these wavelength are expected, e.g. due to changes in the out-of-band emission.

Outlook
Several suggestions for improvements to the SCALA setup have been made in this thesis and are summarized in the following.

- **SCALA shutter:**
  For long exposure times the photodiode measurements are limited by the statistical uncertainty of the external background measurement. We could replace the monochromator shutter by a chopper with a chopping frequency in the range of 1-3 Hz. We could then perform alternated measurements of the background and the signal, and would obtain the same amount of measurements on signal and background, see sec. 6.1.2
- **Internal reflection:**
  To suppress the internal reflections each integrating sphere port can be equipped with a baffle system, which reduces the angular extent of the emitted beam and therefore also reduce the light available for reflections, see sec. 6.2.1 and 6.2.2.
- **Dust protection:**
  A further improvement could be achieved in case all SCALA beams are separated from each other by light shields. This idea could be combined with the baffles and also could be made like a housing around the optical components to protect them from dust. The beam shutters could be used to close the housing in case SCALA is not used. In this way SCALA would be completely protected from dust.
- **Flux calibration of CLAP:**
  The photodiodes at Hawaii could be re-calibrated to investigate their aging and reduce the uncertainties on their calibration, see sec. 5.2.
- **Alternative flux reference:**
  In sec. 5.2 we investigated the possibility to use astronomical CMOS cameras as flux reference for the SCALA system. With them it is possible to equip all beams and therefore remove the need for a measurement of the effective number of beams, see sec. 5.2.
- **Out-of-band emission:**
  To suppress the out-of-band emission of the monochromator we could blacken the holder of the fiber bundle in the exit slit of the monochromator. To further reduce the out-of-band emission a second monochromator should be used. The first monochromator is then used to select the wavelength range and the second one to suppress the out-of-band emission, see end of sec. 6.4.2.1.

Such an improved setup would be of interest for several upcoming projects. One of them is the Large Synoptic Survey Telescope (LSST), an 8 m class telescope planned for surveying the night sky. In May 2018, the groups providing the calibration met in Paris to discuss the progress of their experiments. The presentations can be found at: https://indico.in2p3.fr/event/17361/overview (last checked 13.07.2018). A second project is the planned space mission WFIRST. This space telescope could include an Integral Field Channel (IFC), which would be used to observe thousands of SNe Ia in a redshift range of $0.3 < z < 1.7$. This project requires a nearby anchoring sample, firstly for the absolute magnitude of the used standard candle, but more importantly for the standardization of the supernovae. And here a sub-percent knowledge on the wavelength dependence of the flux calibration of the used instruments is required. A last example for the increased interest in calibration can be found here: https://astronomy2018.

univie.ac.at/abstractsFM12/ (last checked 13.07.2018). The International Astronomical Union (IAU) is organizing the "Focus Meeting 12: Calibration and Standardization Issues in UV-VIS-IR Astronomy" in parallel to their General Assembly (IAU 30) in Vienna in Aug. 2018.

Acknowledgement
I would like to thank Prof. Dr. Marek Kowalski, for enabling this thesis. I would especially like to thank the Supernova Factory group for critical discussions and help in understanding the SNIFS instrument. Specially I have to thank Greg Aldering for providing plenty of observing time at the UH telescope, and many hours of instructions and assistance in the observations. I would like to thank Luke McKay for being our hand on Hawaii and enabling the sometimes strange tests on SCALA. I have to thank many people enabling the SCALA device, including the staff of the mechanical workshop of the University of Bonn, Dr. Akos Hoffmann and Dr. Klaus Reif, for their support throughout the different stages of the SCALA project. I would like to thank Heike Prokoph, Maria Krause and Matteo Giomi, students at DESY Zeuthen for the Latex thesis template and Moritz Hütten for the citation style sheet. I would like to thank my colleagues Simona Lombardo, Robert Stein, Jakob Nordin and Matteo Giomi for the corrections to the thesis. The work was enabled through the projects Transregio 33: "The Dark Universe" and the joint graduate school "Mass, Spectrum, Symmetry" of Humboldt Universität zu Berlin, DESY Zeuthen and Technische Universität Dresden.

Finally thanks to my parents, who always support me.

Appendix A

Supernovae and Measures on Sky

A.1 Supernovae

Supernovae are explosions of stars. Depending on their observed spectrum and their lightcurve[1] one observationally differentiates them into two main types, I & II, based on the presence of hydrogen absorption lines. If these lines are visible it is a type II supernova, otherwise type I.

Type I supernovae are further subdivided for the presence of Silicon absorption lines. In case silicon absorption is visible, it is a Supernova type Ia, otherwise it is classified as a Supernova of type Ib or Ic. The further division is based on the presence of Helium absorption lines.

Supernovae type Ia are found by observation to be standardizable candles. Their brightness is, without any correction, the same within 40 % [Fakhouri et al., 2015] and using the ligthcurve width and supernova color, the variations in flux can be reduced to 15 % [Fakhouri et al., 2015].

The explosion itself is believed to be the thermonuclear runaway of a white dwarf, when the mass overcomes the stability limit - the Chandrasekhar mass limit ([Chandrasekhar, 1931])- it explodes.

There are two main models for how to pass the limit, both use a binary star system. In the first the star to explode accretes matter from a companion star in a late stage of its evolution, and therefore slowly gains mass. The second uses two white dwarfs which merge and therefore overcome the limit and ignite.

None of the models is ideal, in the first the accretion rate needs to be fine tuned, otherwise the material is lost due to novae[2]. For the second, the remnants of SNIa explosions are symmetric, while double degenerate scenarios result in asymmetric explosions. A review can be found in e.g. [Maoz et al., 2014], [Maeda and Terada, 2016] or [Goobar and Leibundgut, 2011].

A.2 Coordinate System

At every observing site we have a local spherical coordinate system with the two angles Altitude and Azimuth. The Altitude is measured as the angular elevation of an object above the horizon. An object at an Altitude of 90° is placed at the Zenith so directly above the observer. The Azimuth is the angle of rotation around the vertical axis pointing at the zenith. Zero Azimuth is obtained in south direction. These coordinates are useful for the calculation of the local time

[1] Evolution of brightness with time

[2] Small thermonuclear explosions not big enough to ignite the hole star, but able to remove mass from it

of rising, or falling of an object above the horizon or to calculate the relative amount of air along a given direction relative to the zenith, the so called airmass A.3.

For comparisons of observations taken at different locations on the earth a different coordinate system is needed. The system can be imagined by projecting the earth coordinate system to the sky. Instead of longitudes and latitudes one obtains hour angles and declination, where the declination of an astronomical object is fixed and the hour angle is changing as the earth rotates. By correction of the hour angle for the rotation of the earth one obtains the right ascension, which is constant, like the declination[1]. The declination is measured from the celestial equator and the right ascension is measured eastwards from the location of the sun at March equinox (crossing point of celestial equator and ecliptic). The right ascension is measured in hours, minutes and seconds, while the declination is measured in degrees [°], arc-minutes [′] and arc-seconds ["]. Important in the conversion is to note that the earth has moved on the orbit around the sun within a day, the mean sidereal day is therefore only 99.726958 % of the mean solar day (24h).

A.3 Air Mass

The optical path length through the atmosphere relative to the path length to an object at zenith is defined as airmass. There are various functional dependencies describing the airmass (X) to elevation (h) relation.

Assuming a plane earth one obtains:

$$X = \sin(h)^{-1} \tag{A.1}$$

An approximation not assuming a plane earth and working for smaller elevations h is:

$$X = (\sin(h) + 0.025 \exp(-11 \sin(h)))^{-1} \tag{A.2}$$

[Schaefer, 1993] & [Rozenberg, 1966]. More advanced description can be found in[2], which cites [Kasten and Young, 1989]:

$$X = \left(\sin(h) + 0.50572(6.07995° + h)^{-1.6364}\right)^{-1} \tag{A.3}$$

A further alternative can be found in [Chromey, 2016]:

$$X = \sec(h') \left(1 - 0.0012(\sec(h')^2 - 1)\right) \tag{A.4}$$

where h' means the true angle between horizon and object and not the observed one which is modified by ADR (see. sec. C.2.3). Airmass $X = 2$ corresponds to an elevation of 30°. At this angle the deviation between the flat atmosphere approximation and the other models is less then 0.4 %. Therefore we use eq. A.1.

[1] If we neglect the possible motion of objects which is usually $<< 1$ "/yr

[2] https://www2.pvlighthouse.com.au/resources/courses/altermatt/The%20Solar%20Spectrum/PDFs/Air%20mass%20calculations.pdf, last checked 02.03.2018

Appendix B

Photometry

Photometry measures brightness on the sky. The magnitude definition is given in sec. 3 and repeated here.

$$m_1 - m_2 = -\chi \log\left(\frac{f_1}{f_2}\right) \tag{B.1}$$

where m_1 and m_2 are the magnitudes of the observed objects and f_1 and f_2 the corresponding fluxes. In the following I will describe how Norman Pogson obtained the value of the proportionality constant χ. Afterwards I will give a summary of the history of photometry.

B.1 Pogson Magnitude Scale

In 1856 Norman Pogson selected the proportionality constant χ to be 2.5, resulting in a flux ratio of 2.512 for a magnitude difference of one. This estimate was based on the comparison of catalogs created by different people and instruments. He obtained from this catalogs a relation between the magnitude of the dimmest visible star and the collecting area of the used telescope. By this comparison he finds the flux ratio for a magnitude difference of one, to be 2.4. Based on the instrument used for the Bonnerdurchmusterung (described later) we can ourselves estimate the proportionality factor. The naked eye limiting magnitude is $m_{\text{eye}} \approx 6$ while the diameter of the eye pupil is $\approx 5\,\text{mm}$. The limiting magnitude of Argelanders Bonnerdurchmusterung using a telescope of 78 mm diameter was $m_{\text{BD}} > 10.5\,\text{mag}$. The collecting area is enhanced by a factor 244. With $\log(244) = 2.39$ and a magnitude difference of $m_{\text{BD}} - m_{\text{eye}} > 5$ we obtain a proportionality constant of > 2.09. In 1836 Carl von Steinheil [Steinheil, 1837] introduced a device to support the eye in measuring magnitudes, a so called photometer. He obtained a value of 2.853 ([Steinheil, 1837] P. 27), his instrument will be explained later. As Pogson notes there are other measurements obtaining a value of 2.519. For convenience he decided to take 2.512 for the flux ratio corresponding to a magnitude difference of one. This results in the known magnitude definition:

$$m_1 - m_2 = -2.5 \log\left(\frac{f_1}{f_2}\right) \tag{B.2}$$

B.2 History of Photometry

For this historic overview I will follow the papers of [Weaver, 1946] and [Miles, 2007]. The oldest catalog is attributed to Hipparchus of Nicaea (≈ 190-120 BC.). The first still in copies existing catalog is Ptolemy's Almagest (137 AD) listing already 1028 stars. Ptolemy used the term magnitude for the brightnesses and introduced six magnitudes for the visible stars, where the brightest are of magnitude 1 and the dimmest of magnitude 6 [Miles, 2007]. Zinner [Zinner, 1926] and also Lundmark [Lundmark, 1926] have estimated the random errors of this catalog relative to modern ones to be ±0.4 mag.

To improve the precision of magnitudes obtained by the unsupported eye, William Herschel introduced a method, in which the star to measure is compared to a set of reference stars within the same field of view. F. W. A. Argelander improved Herschels method and obtained with it the Bonner Durchmusterungen (1859-1862), containing positions and brightnesses of 458,000 stars brighter than 10.5 mag [Argelander, 1903]. The observations for these catalog were performed with a telescope of 78 mm diameter, allowing the dim objects to be seen. [Weaver, 1946] estimates the internal precision to 0.27 mag. A description of Argelanders method can be found in e.g. [Yendell, 1905] p. 455.

Visual Photometer

The catalogs mentioned above are limited by the precision of the eye to judge the absolute brightness of an object. However, the observers knew that the eye is good in judging whether two objects are of same brightness. To support the eye so called photometers have been build. These devices are able to show the two objects to measure next to each other and to attenuate the brighter one to match the brightness of the dimmer one.

Three of them are described here, as they are either already mentioned, or show new ideas or are important for the later history.

The photometer of Steinheil [Steinheil, 1837] was taken into account by Pogson in the definition of the magnitude system. The main element of his photometer is a refracting telescope with an objective that is divided in two half's along its diameter. Each half can be moved along the optical axis relative to the other half. Therefore there are essentially two telescopes next to each other and in each one, the focus can be adjusted differently. By splitting the objective, each half will produce an off focus image with the shape of a half moon, where the size of the half moon depends on the amount of off focus. To compare two objects in different directions from the telescope, Steinheil added prisms in front of each half objective, to redirect the light. By adjusting the prisms each half of the telescope could look in different directions, while the off focus star images could be placed next to each other with the secants of the half moon touching each other. Now the off focus was adjusted to make the surfaces next to each other of same brightness. The difference of defocus, needed to make the surface brightness of the two object the same is related to their flux ratios. Therefore the magnitude differences taken from a catalog can be related to flux ratios. The measured flux ratio of a science object relative to a known reference object can be used to determine the magnitude of the science object.

This device has the disadvantage, that at least two measurements are required to account for the different throughputs of the two halves of the instrument. Also measurements of dim

objects are difficult as the light of the object needs to be spread over a big area (half moon shape) and is not anymore visible. Additionally the off focus star image is seen superimposed on the night sky background around the star, which can vary in different direction. In case the star to measure is in a dense star field, its off focus image could overlap with other sources in the field and the measurement is therefore biased. According to [Miles, 2007] the instrument achieved a precision of ± 0.05 mag which corresponds to a flux uncertainty of 5 % (eq. 2.36).

Friedrich Zöllner built a photometer, which solves most of these issues [Zöllner, 1861]. He used a reference light source to create an artificial star, which is placed next to the star to measure. The light source for his artificial star was a standard candle driven by gas, supplied from a gas storage to stabilize its pressure. Also the air for the lamp was taken from another room to ensure its stability. The light from the gas lamp illuminated a small aperture. The light passing through this aperture was collimated and sent through a first Nicol prism to polarize it. The light then passed through a Quartz crystal plate and a second Nicol prism as analyzer. Due to circular birefringence in the Quartz one can select the wavelength of the light passing through, by turning the analyzer. By rotating this hole setup (2 Nicol Prisms + Quartz plate, angle of rotation θ) against a third Nicol prism, fixed to the telescope observing the stars, one can attenuate (throughput τ) the light from the gas lamp by Mallus law ($\tau \propto \sin(\theta)$). The now attenuated and colored light passes through a lens. Via a glass plate, which is mounted under an angle of 45° to the optical axis of the telescope, the light from the gas lamp is superimposed to the light from the star field. The light not being reflected off the glass plate is removed by a light trap.

As there is only one telescope which observes the stars, there are no different light paths which need to be measured against each other. Second, also dim stars can be observed as the stars do not need to be attenuated, it is the reference that is adjusted. Also the artificial star is placed on the same sky background as the star to measure. As the star image is not off focus there is no overlap of sources as long as a single star is observed (no unresolvable binaries).

However one could think that the second artificial star produced by the reflection on the back side of the glass plate is reducing the performance, but as Zöllner describes it is helpful, as it is dimmer than the front side reflection. Therefore the star to measure can be placed in between the two artificial stars and the method of Argelander can be used for brightness comparisons. In [Weaver, 1946] we find an estimate of its precision of ± 0.04 mag.

The main issue might be the gas lamp itself. Zöllner had taken this into account and controlled the flame size. He did various measures against a second artificial star illuminated by a second gas lamp. He investigated the brightness of the first artificial star against the second, while changing the flame size of the first. He found that the variations are small if the aperture creating the artificial star is small. Here we can see the advantages of a reference on the ground: it can be tested and controlled.

The last device I will describe was used by Edward Charles Pickering and lead to the Revised Harvard Photometry [Pickering, 1908], which contains 9110 stars brighter than 6.5 mag, with measurements performed between 1879 and 1906. Pickering knew of the instruments of Steinheil and Zöllner. He was not satisfied with the artificial star as it is absolutely stable, while the star to measure is experiencing seeing (see AC.2.3) and therefore changing its shape during observation. The instrument used by Pickering ([Pickering, 1908] p.1) therefore consisted of a

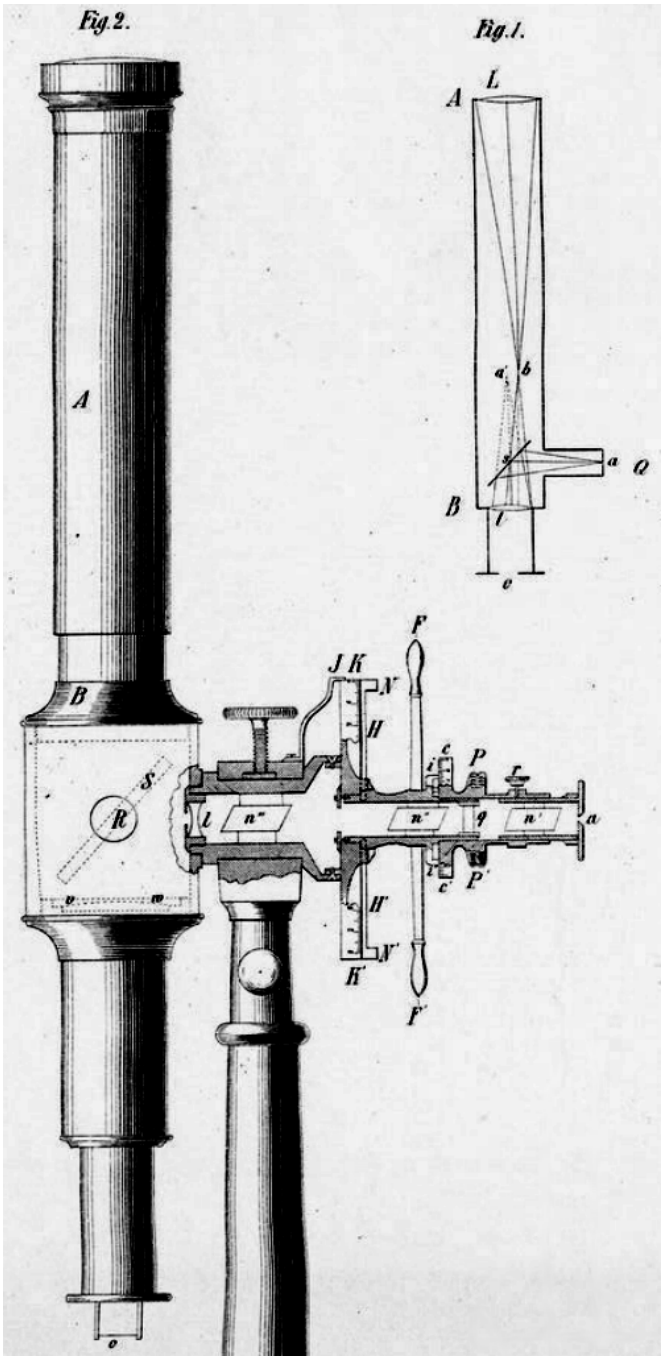

Figure B.1: Graphic illustrating the Zöllner photometer from [Zöllner, 1861]. In the upper right there is a schematic drawing of the optical path showing how the artificial star is superimposed to the image. The left shows the optics crating and attenuating the artificial star. From right to left we see the aperture (a) illuminated by the gas lamp (not show) the first Nicol Prism (n') the Quartz plate (q). These elements can be rotated against the Nicol Prism (n") and all of them can be rotated against the Nicol Prism (n"'). The orientation of this Prism is fixed relative to the tube of the telescope. The light is passing through lens (l) and is reflected off the front and back surface of the glass plate (s) towards the ocular (o) at the lower end of the tube. The whole book can be found at http://nbn-resolving.de/urn:nbn:de:bvb:210-09-010366100-7

TABLE 2

NORTH POLAR SEQUENCE

NPS	P_{gp}	$P_{g_{int}}$	$P_{gp}-P_{g_{int}}$	C_p	C_{int}	C_p-C_{int}	Class*
6.....	7.15	7.12	+0.03	+0.06	+0.06	0.00	1
2r.....	7.90	7.91	− .01	+1.56	+1.57	− .01	1
10.....	9.17	9.15	+ .02	+0.12	+0.12	.00	1
4r.....	9.24	9.23	+ .01	+1.02	+1.02	.00	1
13.....	10.51	10.55	− .04	+0.24	+0.22	+ .02	2
8r.....	11.43	11.43	.00	+1.02	+0.96	+ .06	2
16.....	11.56	11.57	− .01	+0.32	+0.34	− .02	1
19.....	12.66	12.68	− .02	+0.41	+0.44	− .03	1
12r.....	13.80	13.78	+ .02	+1.27	+1.30	− .03	2
426.....	13.87	13.89	− .02	+0.51	+0.51	.00	3
25.....	14.16	14.12	+ .04	+0.57	+0.56	+ .01	3
26.....	14.67	14.65	+ .02	+1.01	+1.00	+ .01	3
277.....	15.35	15.32	+0.03	+0.68	+0.74	−0.06	3

* Class 1, well observed in all three seasons; class 2, observed in two seasons; class 3, only one observation or discordant.

Figure B.2: Table from [Stebbins et al., 1950] used as absolute reference for the Johnson system

telescope pointed in east or west direction with two similar objectives. Via a system of reflectors (like by C. Steinheil), one of the telescope objectives was directed towards stars around the celestial pole, while the other was directed at the object to measure. The collected light of both objects was then polarized and one of them could be attenuated with the help of a second polarizer, again the magnitude difference was inferred from the attenuation calculated using Mallus law.

The flux reference for this system is the mean flux of a set of 100 stars around the celestial north pole, where each of them has been observed on 200-300 nights ([Pickering, 1908] p.2). The stars around the pole have several advantages. They are always visible and do not move quickly relative to the telescope. Weaver estimate the precision of the revised Harvard Photometry to ± 0.08 mag, while Pickering quotes residuals on average of ± 0.07 mag ([Pickering, 1908] p.3).

The Harvard Photometry was then used for the definition of the North Polar Sequence by Henrietta Leavitt and Edward Charles Pickering [Leavitt and Pickering, 1917], which was the basis for the photographic photometric system. As there are many difficulties with this system, I will leave this out and proceed to the Johnson Photometric System.

Photomultiplier Photometer

Johnson and Morgan observed stars with a photomultiplier at McDonald Observatory, Texas [Johnson and Morgan, 1951]. The light collected by the telescope creates an image of the sky in the focal plane. Diaphragms of different aperture sizes are used to select the light of one star and reject that of others. A Fabry lens is used to image the light passing through the diaphragm onto the 1P21 photomultiplier (PMT). For the observations at the 82-inch telescope, diaphragms of

15" and 21" have been used while a 1' diaphragm has been used on the 13-inch telescope. The current provided by the photomultiplier was amplified and recorded. The observations were performed through yellow (V), blue (B) and ultraviolet (U) filter. The filters used are colored glass filters manufactured by Schott. The blue filter is a Schott BG12 of 1 mm thickness and the yellow a Schott GG7 of 2 mm thickness (manufacturer naming convention). The thickness and sort of filter matters as the photometric system depends on these parameters. Using these bandpass filters a wavelength range within the sensitivity range of the PMT is selected, see also sec. C.4. The observations are taken alternated on and off the star to perform sky background removal. The recorded currents (b,y,u for the corresponding filter) are recorded on paper tapes. The current provided by the PMT is proportional to the number of photons, that created a signal per unit time. The current I corrected for the sky background can be converted to a "raw" magnitude as $m = 2.5\log(I)$, using the Pogson magnitude definition B.1. Also two raw colors can be defined:

$$\begin{aligned} C_{y_0} &= 2.5\log\left(\frac{y}{b}\right) \\ C_{u_0} &= 2.5\log\left(\frac{b}{u}\right) \end{aligned} \tag{B.3}$$

Colors in Astronomy mean magnitude differences obtained for the same object in different filters, as shown in eq. B.3 this corresponds to ratios of physical fluxes in different filters. The color is proportional to the slope of the spectrum of the source, which is as shown in sec. C.1 a measure of the stellar temperature. In the magnitude system provided by [Johnson and Morgan, 1953] the color is defined by a set of stars with a spectral type A0 V. Stars of this spectral class have magnitude differences between any filter combination of zero:

$$U - B = B - V = 0 \tag{B.4}$$

The set of reference stars for color consists of six stars, which are α Lyrae / Vega[1], γ UMa, 109 Vir, α CrB, γ Oph and HR 3314.

The magnitude of the stars is normalized to a subset of the north polar sequence stars, this subset is given in tab. B.2, for details and the correction of the atmospheric extinction see [Stebbins et al., 1950].

Arlo U. Landolt [Landolt, 1973] also performed observations with a photomultiplier but introduced more filters (U,B,V,R,I) spanning a wider range in wavelength and extended the system to fainter objects. The results are published in [Landolt, 1992]. It contains the stars in a band around the celestial equator in a V-band magnitude range from 11.5 to 16.0 in magnitude.

The Photomultiplier used was an RCA 31034A, thus different from the one used in [Johnson and Morgan, 1953]. [Landolt, 1983] shows the transformation from a system observing with an RCA 1P21 to one observing with an RCA 31034A photomultiplier. The important result is

[1]Vega Brightness: In the Bonnerdurchmusterung it is object # 3238 with a magnitude of 1, in the Revised Harvard Photometry it is # 7001 with 0.14 mag, in Johnson it is # 198 and 0.03 mag. Following Johnsons measurements its color in (B-V) is 0.00 mag and its (U-B) color is -0.01 mag.

that the transformation is non-linear. This effect will be explained in sec. 3, together with the modern photometric systems.

Appendix C

Propagation of Light from the Source to the Detector

We would like to measure the flux emitted by a cosmological source, but we only know the number of counts detected. To recover the flux emitted we have to correct for the absorption of light in the vicinity of the source, the host galaxy, and during the propagation to and through our own galaxy. Our atmosphere will also attenuate and redistribute the light before it is collected by the telescope and analyzed by the instrument. We determine the strength of these effects through the use of standard stars.

For photometry - measuring the apparent brightness of a celestial source - we compare the object of interest (our cosmological source) with stars (close within our own galaxy). As these are close to us we can neglect absorption in foreign and our own galaxy.

The Spectral Energy Density (SED) of calibrated stars will be described in sec. C.1. Section C.2 details how light is attenuated in the atmosphere. Section C.3 describes the properties of the telescope, collecting the light from a distant source for us. Section C.4 finally describes the analysis and detection of the collected light.

C.1 Stellar Spectra

Stars are objects, which produce energy by fusion or gravitational contraction. The produced energy is partially radiated away by electromagnetic waves. In first approximation a star can be described as a body formed from plasma and surrounded by an atmosphere. The plasma forming the stellar body is optically thick, the atoms will interact with each other and radiate a continuous spectrum, which can be described by a Planck blackbody spectrum. The light from this stellar body will propagate through the stellar atmosphere (which is optically thin) and will therefore be partially absorbed by the atoms / ions within it. The reemission of the atoms / ions will be isotropic, therefore even if the emission occurs at the absorption wavelength we see a reduction of the flux. As the interaction is only possible in a narrow wavelength range we will see small regions in the spectrum, where the flux is reduced compared to the continuum. These regions are called absorption lines. The discrete wavelength at which the absorption by ions / atoms / molecules (depending on temperature) will occur is characteristic

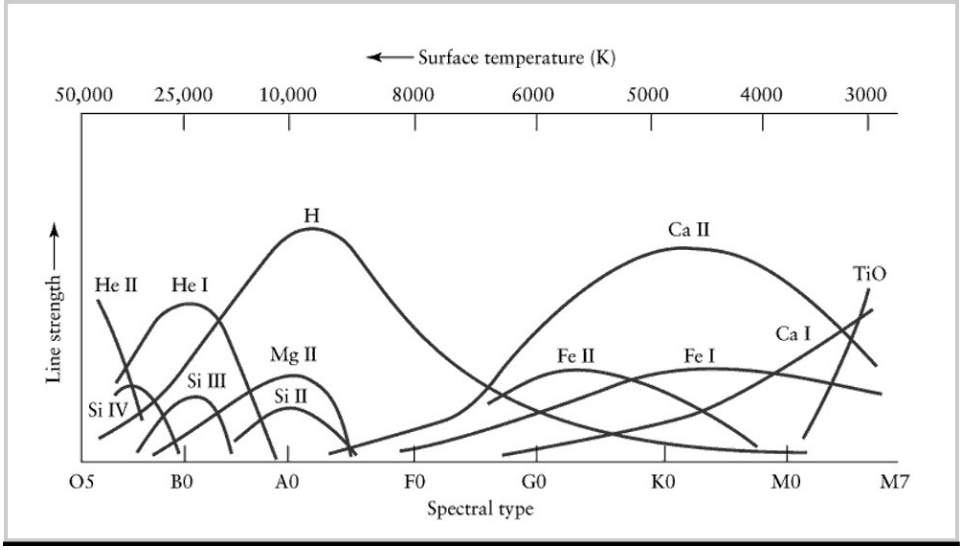

Figure C.1: Line strength of the absorption lines in the stellar spectra depending on the physical properties of the star atmosphere, from https://sites.ualberta.ca/~pogosyan/teaching/ASTRO_122/lect12/lecture12.html, last checked 09.02.2018

for the absorber. A star spectrum is thus a continuous blackbody spectrum superimposed with absorption lines from the stellar atmosphere. Depending on the mass / size of the star the conditions in the atmosphere of the star will change and therefore the visible absorption lines. Stars can be subdivided into the spectral classes (O, B, A, F, G, K, M). This classification was originally purely descriptive for the presence and strength of the different lines. Fig. C.1 shows the strength of the absorption lines depending on the physical properties in the stellar atmosphere, especially temperature. Sample spectra sorted for temperature are shown in fig. C.2.

Fig. C.3 shows the spectra of two white dwarfs and of α Lyrae (or Vega). White dwarfs are remnants of stars after a process of expelling the stellar atmosphere, therefore one observes immediately the plasma body, and none or very weak absorption lines are visible. As these objects are small and dense their surface temperature is high. As a first approximation to their spectrum, a blackbody spectrum can be used. Blackbody spectra with the temperatures given in [Bohlin, 2014] are shown for comparison. The lower panel of fig. C.3 shows the deviation of the observed spectra from the model blackbody curve.

As pointed out in the introduction and in more detailed in sec. 3,Vega has a traditional importance for photometry. Its spectrum and a blackbody approximation to it are also shown in fig. C.3.

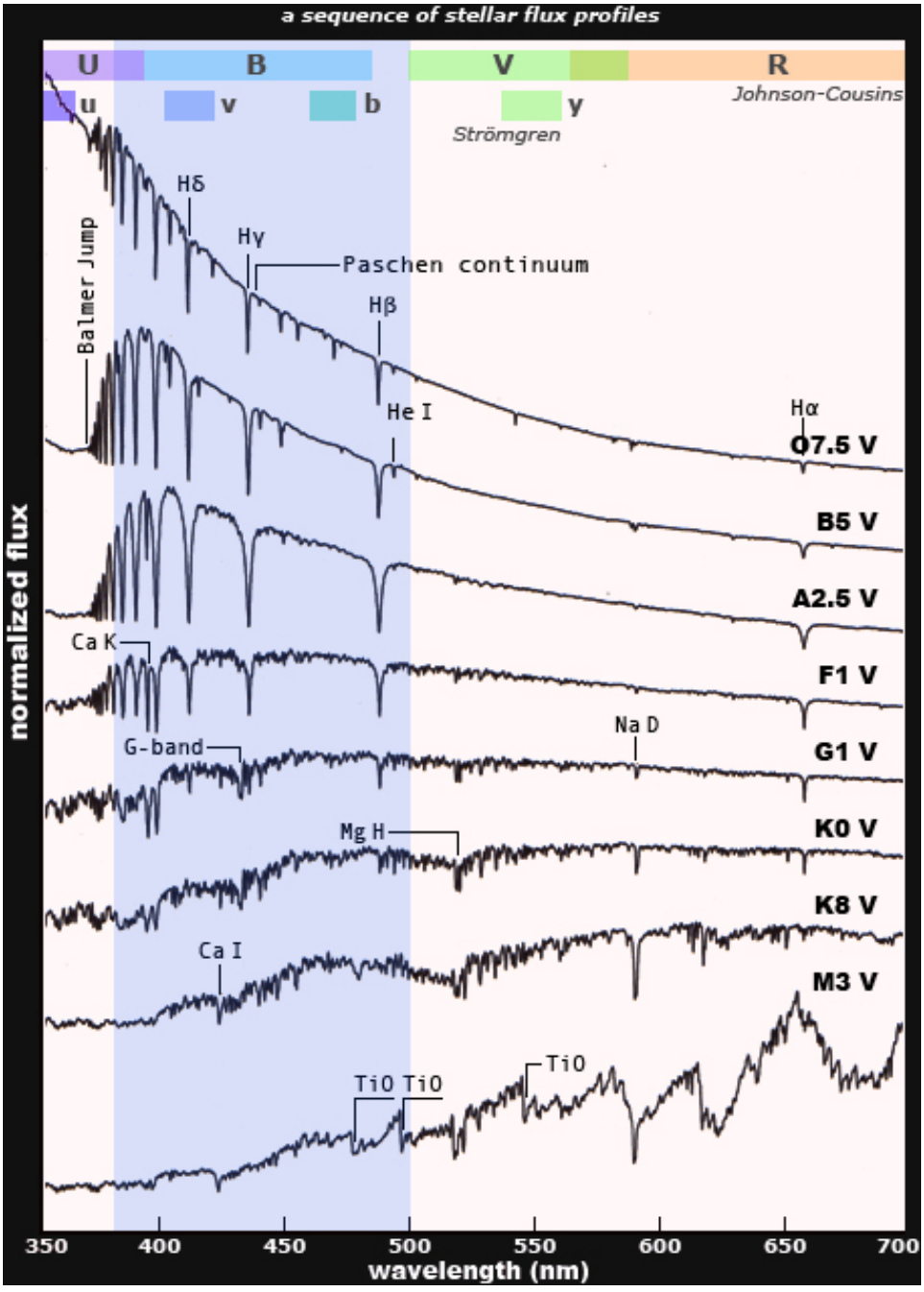

Figure C.2: Observed spectra of stars ordered for the spectral classes from O to M together with the wavelength range of different filters (upper part of figure see also sec. 3) and the nomenclature of the lines, from https://www.handprint.com/ASTRO/specclass.html, last checked 09.02.2018

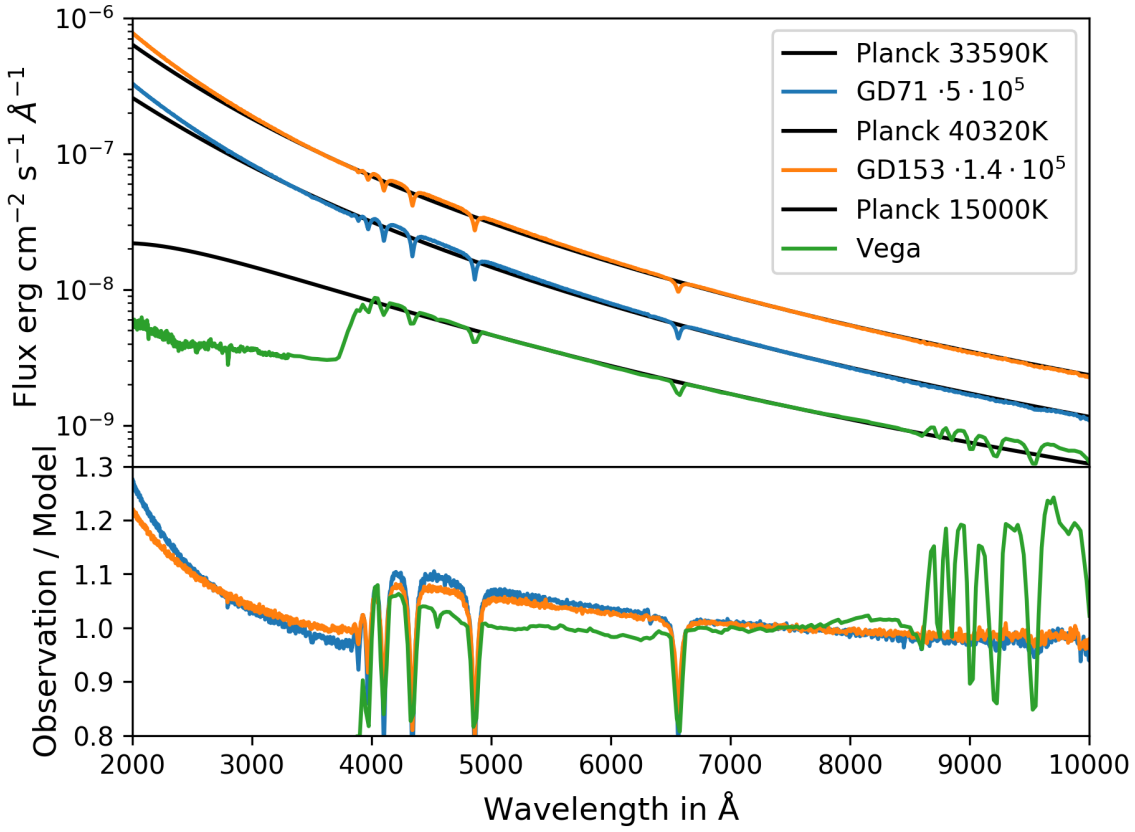

Figure C.3: Spectra of Vega and two white dwarfs, GD71 and GD153, shown in log scale. The spectra of the white dwarfs have been scaled in flux for better comparison. All three spectra show Balmer / Hydrogen absorption lines. The spectra of the white dwarfs do not show a strong Balmer break below 3870 Å which is visible in the Vega spectrum. They also do not show lines above 8600 Å. Scaled Black Body spectra are shown for comparison, the temperatures of the white dwarfs are taken from [Bohlin, 2014]. The lower figure shows the ratio of observed spectrum to a blackbody model.

C.2 Atmosphere

We need to account for several effects within the earth atmosphere affecting the observed flux. Light can be absorbed by the molecules in the atmosphere. Emission by the excited atoms can instead add light to the beam. Scattering processes can also remove light. All these effects modify the amplitude of the light, but there are also effects, which redirect (bend) the light rays in the atmosphere.

C.2.1 Absorption and Emission

The light propagation through the atmosphere is affected by absorption of molecules. As Kirchhoff and Bunsen ([Kirchhoff and Bunsen, 1860]) have shown, molecules leave a specific fingerprint in the spectrum of a source (absorption lines). As described in section C.1 also the star atmosphere produces absorption lines, therefore the question arises how to identify the absorption lines caused by the earth atmosphere.

There are several approaches to identify lines caused by the earth atmosphere. One could observe moving objects like double stars or rotating planets. Due to the Doppler effect the wavelength of absorption lines will move relative to the laboratory wavelength, while the wavelengths of the absorption lines created in the earth atmosphere are stable.

Other distinct properties of stellar absorption lines is the line broadening due to high gravity, pressure and temperature, while the ones from the atmosphere are narrow.

Finally the molecules in the earth atmosphere causing the absorption can be identified, these are O_2, O_3, H_2O and N_2. The wavelength of the absorption lines of these molecules are known and the absorption strength can be measured by the observation of sources with known spectra.

As these molecules were excited by absorption they will deexcite by emission of characteristic emission lines. These emission lines will be superimposed to the original spectrum and add flux to the light beam. Fig. C.4 shows a spectrum of the night sky at La Palma Observatory taken with the faint-object spectrograph of the William Herschel Telescope in March 1991. The different molecules causing the emission are labeled.

C.2.2 Scattering of Light

Scattering of the light in the atmosphere happens a few kilometer in front of the telescope, so small deflections will remove the light from the beam reaching the telescope. Therefore the amplitude of the incoming light is decreased. The scattering amplitude is given by:

$$I(z) = I_0 \cdot 10^{-0.4 \cdot \sum_i K_i z^j} \tag{C.1}$$

With I_0 the incoming light intensity, K_i the wavelength dependent scattering constants for each scattering process i and z the path length through the medium. According to the Beer Lambert law:

$$\log\left(\frac{I_0}{I(z)}\right) \propto z \tag{C.2}$$

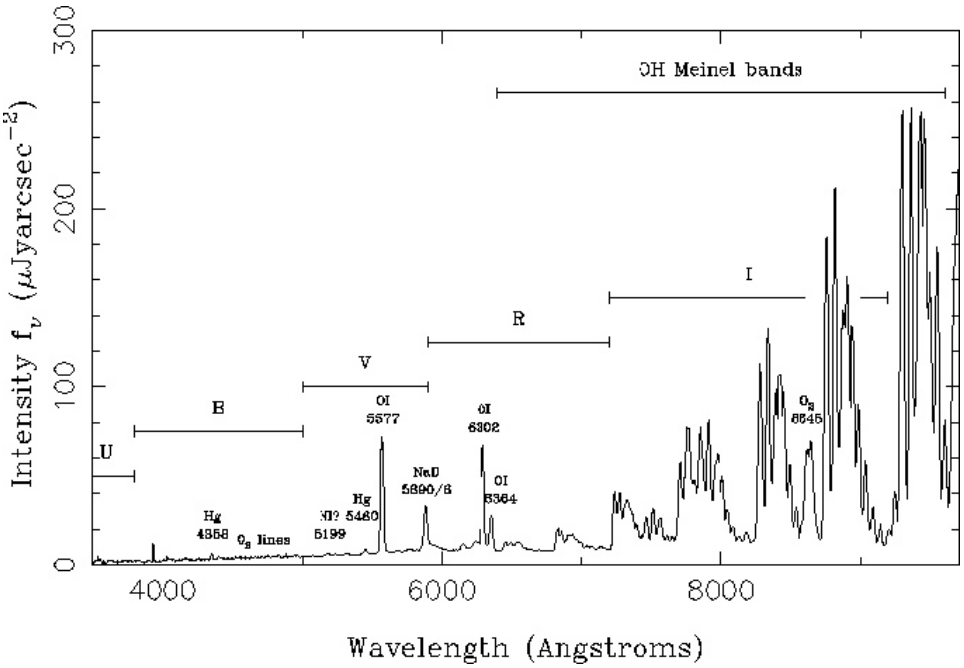

Figure C.4: Spectrum of the night sky at La Palma Observatory taken with the faint-object spectrograph of the William Herschel Telescope in March 1991, from http://www.ing.iac.es/Astronomy/observing/conditions/skybr/skybr.html#intr, last checked 01.01.2018

the attenuation is linear in the optical path length z and $j = 1$. For astronomical purposes the path length z is proportional to the airmass of the object, see sec. A.3. The light can be scattered out of the observing beam by molecules, aerosols or other particles within the atmosphere. Depending on the size of the particles there are different wavelength dependencies of the scattering constant K_i:

Rayleigh Scattering:
The molecules are small compared to the scattered wavelength ($d << \lambda$). The scattering constant $K_{\text{ray.}}$ is proportional to $\approx 1/\lambda^4$. As shown in [Buton et al., 2013] the Rayleigh scattering at Mauna Kea is better described by:

$$K_{\text{ray.}} = \frac{2.5A}{\ln(10)g(h)M}\lambda^{-4.15}P \tag{C.3}$$

with A a numerical parameter for the amplitude, $g(h)$ the gravitational acceleration at altitude h, P the atmospheric pressure and M the molecular mass of dry air [Bucholtz, 1995], [Bréon, 1998].

Aerosols Scattering:
The aerosol scattering ($d \approx \lambda$) is described by:

$$K_{\text{aero.}} = \tau\left(\frac{\lambda}{1\mu\text{m}}\right)^{-a} \tag{C.4}$$

where τ is the aerosol optical depth at $1\,\mu$m and a is the Ångström exponent, which is constrained to: $-2 < a < 4$.

Ozone Absorption:
The wavelength dependence of Ozone can not be described with simple relations and is therefore accounted for by a template. Ozone shows absorption below 3500 Å and in between 5000 Å and 7000 Å. The template is shown in fig. C.5.

Water Droplet, Ice Crystals:
In this case, the particles are large compared to the wavelength ($d >> \lambda$), the scattering does not show a wavelength dependency $K = \text{const.}$.

C.2.2.1 Measuring the attenuation of atmosphere and instrument

Observing a object of known brightness (above the atmosphere) or an object of stable flux at different airmasses / times one can measure the atmospheric and instrumental attenuation. With the observed flux S_{obs} and the tabulated / known flux S_{tab} we have:

$$S_{\text{obs}} = S_{\text{tab}} \cdot \tau_{\text{instr.}} \cdot 10^{-0.4 \cdot \sum_i K_i z} \tag{C.5}$$

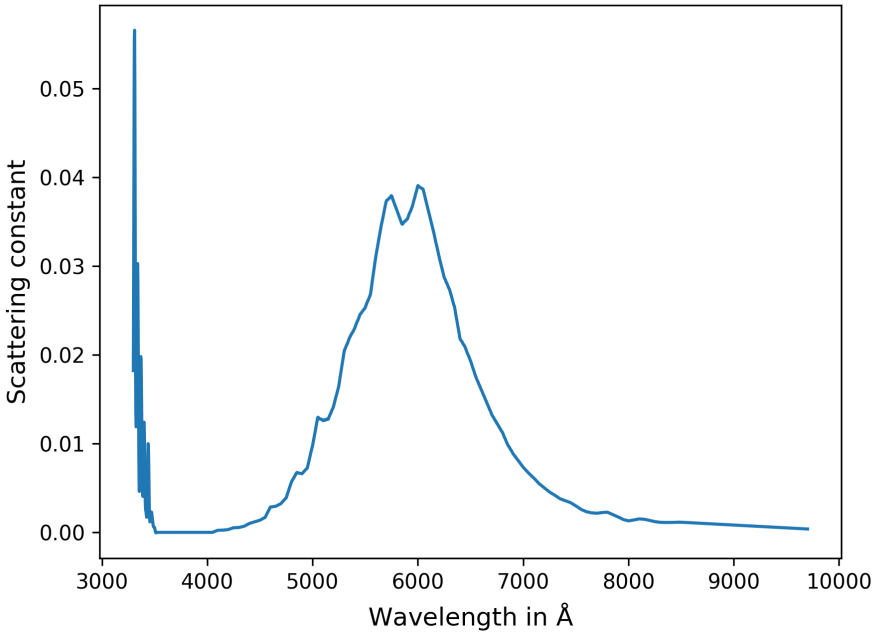

Figure C.5: Wavelength dependence of the scattering constant of Ozone.

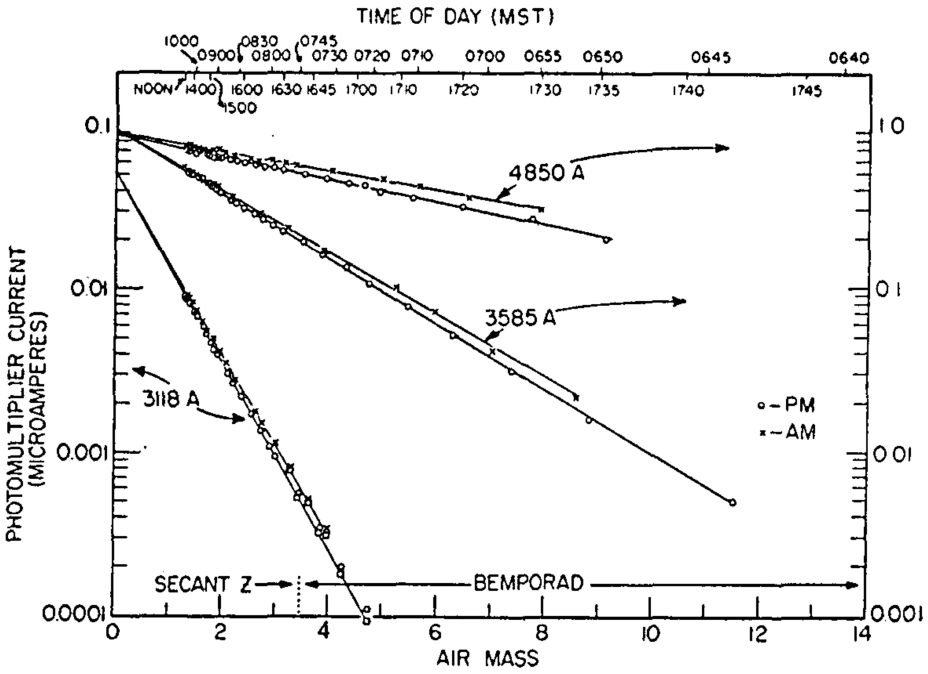

Figure C.6: Log plot of the photocurrent produced by the sunlight, depending on airmass and measured at different wavelength, from in [Dunkelman and Scolnik, 1959]. They observed the sun from sunrise to sunset (times are indicated at the top of the figure) with a double monochromator and a photomultiplier. The measurements are performed in an airmass range from of 1 to 11 at 100 wavelengths between 3030 Å and 6900 Å (due to the monochromator the measurement needs to be performed wavelength by wavelength). Fig. C.6 shows three representative wavelength (3118 Å, 3585 Å, 4850 Å). We see that for airmasses up to 11 the attenuation is linear in airmass. As the device was absolutely calibrated they were able to measure the sun flux above the earth atmosphere.

where $\tau_{\text{instr.}}$ is the instrumental throughput. After dividing for the tabulated spectrum and taking the logarithm we obtain:

$$\log\left(\frac{S_{\text{obs}}}{S_{\text{tab}}}\right) = \log\left(\tau_{\text{instr.}}\right) - 0.4 \cdot \sum_i K_i z \tag{C.6}$$

We see that by obtaining monochromatic measurements of different objects at different airmasses, one can measure the extinction coefficient and the instrumental throughput from a linear fit to the performed measurements.

If $\tau_{\text{instr.}}$ is known a sequence of observations of a stable object at difference airmasses can be used to measure both the flux outside the earth atmosphere and the atmospheric throughput. Fig. C.6 shows such a ground based measurement of the spectrum of the sun above the earth atmosphere, see. [Dunkelman and Scolnik, 1959].

C.2.3 Deflection

The effects described above modify the amplitude of the light, but do not change the angular distribution: the rays reaching the telescope remain parallel or plane waves. However the refractive index of air is wavelength, pressure and temperature dependent. There are several parameterizations for the refractive index of air, e.g. form [Zago, 1995]:

$$n - 1 = \frac{77.6 \cdot 10^{-6}}{T} \left(1 + 7.52 \cdot 10^{-3} \lambda^{-2}\right) \left(P + 4810 \frac{\nu}{T}\right) \tag{C.7}$$

with λ the wavelength of the observed light, P(mb) pressure of the gas, T the absolute temperature and v the water vapor pressure measured in milli-bars.

The temperature and pressure dependence of the refractive index of air leads to a bending of the optical path. The effects can be split into two pieces, a slowly varying and a fast one:

Atmospheric Differential Refraction

Atmospheric Differential Refraction (ADR) displaces the visible star position on the sky from its position without an atmosphere. The effect is similar to looking through a prism. As the refractive index is also wavelength dependent the displacement depends on the observed wavelength range. As the object is rising or falling due to the rotation of the earth the strength of the effect is varying. As shown in [Filippenko, 1982] the effect can be described by:

$$\Delta R = R(\lambda) - R(5000) \approx 206265 \left(n(\lambda) - n(5000)\right) \tan(z) \tag{C.8}$$

with ΔR the displacement relative to 5000Å in arc seconds and z the zenith angle. As shown in table I of [Filippenko, 1982] the deflection at airmass 2.0 for 300 nm is 3.67" and -1.4" for 1 μm, both compared to the position at 500 nm.

ADR primarily affects slit spectroscopy as the fraction of light observed will vary with wavelength. A key advantage of Integral Field Units (IFU's) like SNIFS is, that the whole extend of the star distribution (PSF) can be observed.

Seeing

As shown above, the refractive index of air depends on the temperature of the air. A bubble of air at a different temperature than the surrounding atmosphere deflects the light beam and moves within the atmosphere. The deflection is therefore changing on sub-seconds time scales, as the bubble moves in and out of the beam.

As typical exposure times are longer than the times scale of this process one observes a superposition of different small-angle deflections. To first approximation the angular distribution of the deflection angles can be described by a Gaussian distribution centered at zero with a Full Width at Half Maximum (FWHM) of α_{seeing}. Following a turbulence analysis [Quirrenbach, 2006] one finds the following wavelength dependence for the FWHM:

$$\alpha_{\text{seeing}} \approx \lambda^{-1/5} \tag{C.9}$$

The amplitude of the deflection is wavelength dependent, at smaller wavelength the deflection is

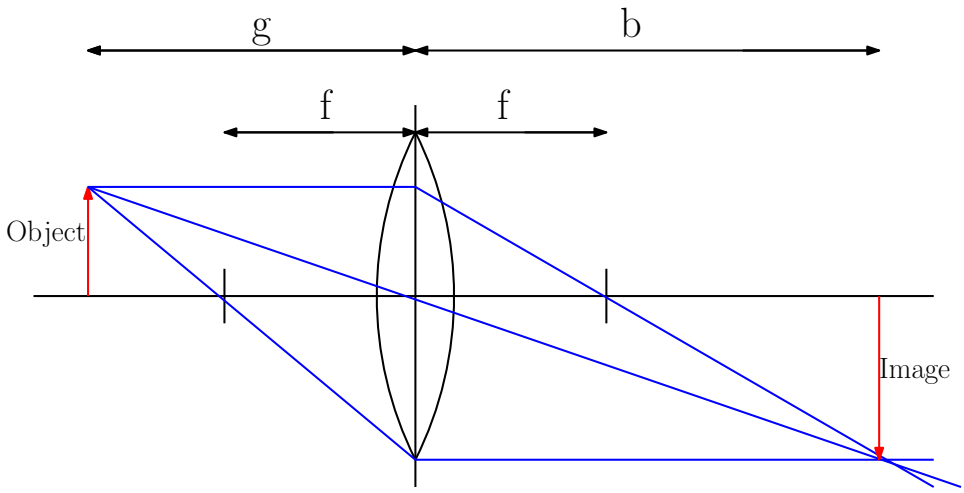

Figure C.7: Image formation with a lens. For an astronomical telescope the object is placed at large distances $g \gg f$, the light reaches the lense as plane waves (same as parallel rays) and therefore the image is placed at $b = f$.

larger than at longer wavelength. The important parameter for observations is the characteristic size scale of these bubbles: For Mauna Kea Observatory the average seeing is 0.72" and the median is 0.65"[1], this corresponds to a bubble diameter of roughly 16.7-18.5 cm. As long as one observes an astronomical source with optics with a diameter smaller than the characteristic size, like with the naked eye, one will see the source twinkle as the deflection changes and displaces the source slightly but quickly. With an optic larger in diameter than the characteristic size, seeing will cause a blur of the image. The star images will be a superposition of multiple displaced star images, each one seen through a different bubble.

C.3 Telescope

A telescope collects the light of an object and provides a map of the angular light distribution entering it. In the following I will describe what this means. Due to the two fold ray and wave nature of light, a geometric description is followed by a description using the wave nature of light. From this we will obtain constrains on the resolution of the telescope.

C.3.1 Geometrical Optics

With astronomical telescopes we observe objects at large distances g ($g \gg f$) from the telescope, where f is the focal length and will be defined later (see fig. C.7). It consists of one optical element represented by the lens plane. The lens placed in this plane has a diameter (D) and defines the entrance pupil of our idealized telescope and is called objective. Light rays from

[1] http://mkwc.ifa.hawaii.edu/current/seeing/analysis/climate.cgi, last checked 01.01.2018

the object reach the entrance pupil of the telescope as parallel rays. The optical axis of the telescope is orthogonal to the lens plane and goes through its symmetry center.

Rays incident parallel to the optical axis through the entrance pupil will be bent in such a way that they all meet in one point on the optical axis. The distance between lens plane and this point is the focal length (f) of the telescope. Rays incident under an angle (α) with the optical axis will be focused into a point on a plane parallel to the lens plane, in a distance f from the lens plane. This point is displaced from the optical axis in the plane by $x = f \cdot \tan(\alpha)$. For small incidence angles this can be simplified to $x = f \cdot \alpha$. The telescope creates an image in the focal plane also called image plane. One can describe the telescope as a device collecting the light within the entrance pupil and performing a mapping from angular distances to spacial distances in the image plane. For completeness we define the focal ratio of a telescope to the ratio of focal length to diameter of the entrance pupil.

Aberrations

Aberrations are causing deviations from the above idealized telescope. According to [Seidel, 1856] there are five first order aberrations: Spherical aberration, Astigmatism, Coma, image distortion and field curvature. The perfect telescope is realized by a parabolic mirror (rotationally symmetric: $h(r) = r^2/4f$) in case the light is incident along the optical axis. Parallel rays, will be focused in a point placed on the optical axis at a height f above the minimum of the parabolic mirror. To explain the aberrations we divide the entrance pupil, in rotational symmetric zones. Each of the so defined annuli has a different focal ratio.

- **Field Curvature** means that the image is formed on a curved surface, instead of a plane, as described above.
- **Image distortion** means, the mapping from angles to space is non-linear and not rotationally symmetric.
- **Spherical Aberration** in the simplest case can be found when replacing the lens by a spherical mirror. Each of the above defined annuli will have a different focal length, with larger focal lengths for smaller annuli. The image of a point source will therefore be a superposition of images for each zone, which all have slightly different focus, see fig.C.8. The image is therefore blurred compared to using a parabolic mirror which does not show aberrations on the optical axis. An example of this effect can be observed as caustic on the bottom of an empty coffee cup, reflecting the light from a distant source.
- **Astigmatism** can be imagined if one deforms the parabolic mirror elliptically. We will therefore have different focal length f_1, f_2 with respect to the semi major axes of the ellipse. Therefore a point source is focused to two orthogonal lines, placed in two planes at distances f_1 and f_2 from the minimum of the paraboloid. The best concentration of the light is reached in the point of least confusion, which is placed at $(f_1 + f_2)/2$ in our example, see fig. C.9.
  Astigmatism occurs also for a perfect parabolic mirror in case the parallel rays are incident on it under an angle to the optical axis. The mirror seen under an angle is asymmetric due to the projection and therefore behave like elliptically distorted. Astigmatism is therefore also called a asymmetry aberration.
- **Coma** is the second asymmetry aberration. As in the case of spherical aberration the

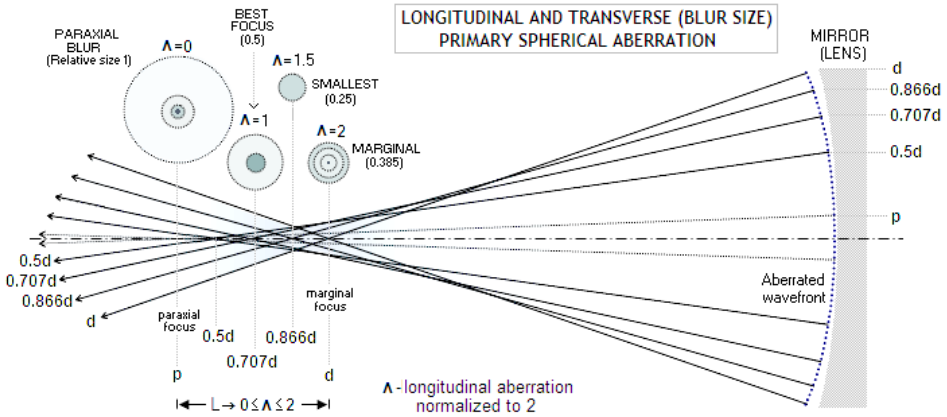

Figure C.8: From http://www.telescope-optics.net/spherical1.htm, last checked 01.01.2018

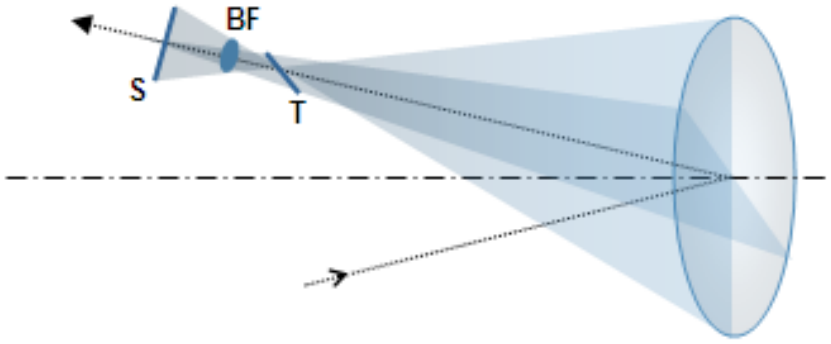

Figure C.9: From http://www.telescope-optics.net/astigmatism1.htm, last checked 01.01.2018

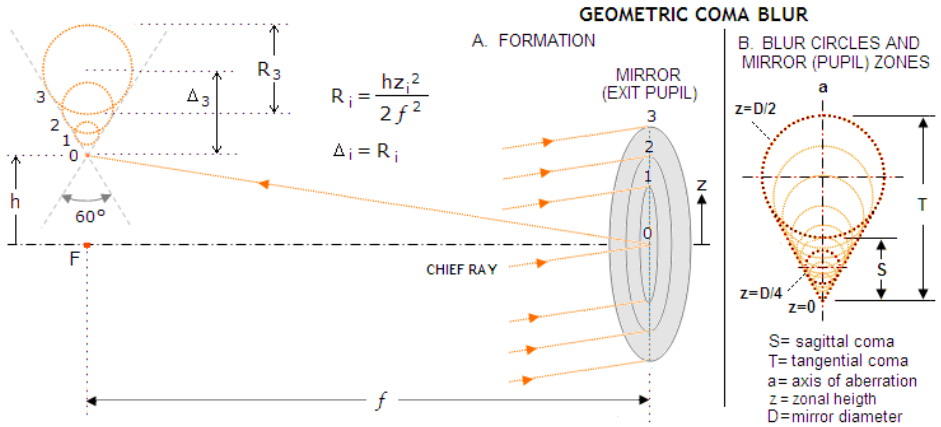

Figure C.10: From http://www.telescope-optics.net/coma.htm, last checked 01.01.2018

different zones (annuli defined above) will have different focal length. Different to the spherical aberration the centers of the images are shifted relative to each other. Therefore the resulting image is a superposition of off-focus images, which are slightly shifted relative to each other, and form a cone like image, see fig. C.10.

In case transmitting optical elements like lenses or windows are used within the telescope, there are two further effects to consider, chromatic aberration and ghosts:

- **Chromatic Aberration:** The refractive index of the medium is wavelength dependent, resulting in the focal length being wavelength dependent. Therefore the image formed is the superposition of off-focus images, where the amount of off-focus is wavelength dependent. This effect can be minimized by combining different material to build the optical element.
- **Ghosts:** Because there is a difference in the refractive index between air/vacuum and the optical element, there is a finite reflection coefficient $r = (n_1 - n_2)^2/(n_1 + n_2)^2$ (Fresnel equation). This means that some rays will be reflected inside the telescope. In case the optics is using multiple optical elements - e.g. to correct for chromatic aberration - the reflected light can reach the focal plane again and form ghost images. The effect can be *reduced* by anti-reflection coatings on the surfaces of the optical elements.

C.3.2 Wave optics

So far the telescope will have infinitely high resolving power, as long as the surface of the optical elements follows exactly the shape given by the geometry and the possible aberrations being small, which could be achieved by a large focal ratio. In case of a large focal ratio the diameter of the used optics is small compared to the focal length, therefore the difference between a spherical mirror and a parabolic mirror is small, which reduces spherical aberrations. As the mirror is close to a sphere the asymmetry aberrations are also suppressed. We know that the resolving power of a telescope is limited. To also obtain this in our description we use wave optics. This will also show that the surfaces of the optical elements need to follow the

geometrical shape within fractions of the wavelength.

The wavefront produced by a source far away from the telescope is a plane wave. To understand the response of the telescope to a plane wave we look at the response of a rotationally symmetric parabolic mirror to a plane wave propagating along the rotation axis, optical axis of the telescope. A parabolic mirror focuses all beams propagating parallel to the optical axis into one point, at a distance f from the minimum of the parabola. For the following calculation we use a parabola with the following functional behavior: $h(x) = ax^2$. For the focal length we find the point $(x_{m=1})$, in which the slope of the parabola is equal to unity, because at this point a ray propagating parallel to the y-axis will be reflected to a ray propagating parallel to the x-axis. This ray will intersect with the optical axis, which is the same as the y-axis at $h(x_{m=1})$, this height will then be the focal length.

$$\begin{aligned} h'(x) &= \frac{\partial h}{\partial x} = 2ax \stackrel{!}{=} 1 \\ x_{m=1} &= 1/2a \\ f = h(x_{m=1}) &= \frac{a}{4a^2} \\ a &= \frac{1}{4f} \end{aligned} \tag{C.10}$$

Fig. C.11 shows the effect of a parabolic mirror on a plane wave reaching it from a distant

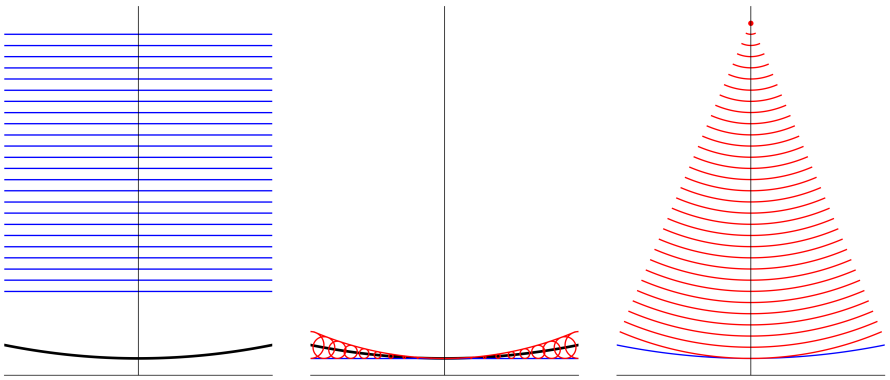

Figure C.11: The left figure shows the basic setup, parallel plane wavefronts are reaching the telescope from above. In the middle figure we look at one incoming wavefront, which has just be reflected at the minimum of the parabola. At each point of the parabola it has caused spherical waves which have different radii. The different radii are caused by the fact that the light reaching the parabola at larger distant from the y-axis/symmetry axis have been reflected earlier. The individual spherical waves form a new spherical wavefront centered around the focal point. In the right figure we see the reflected wavefronts reaching the focal point.

source. The plane waves propagating along the minus y direction, will be reflected by the mirror. The reflection occurs first further away from the optical axis. One can use the Huygens

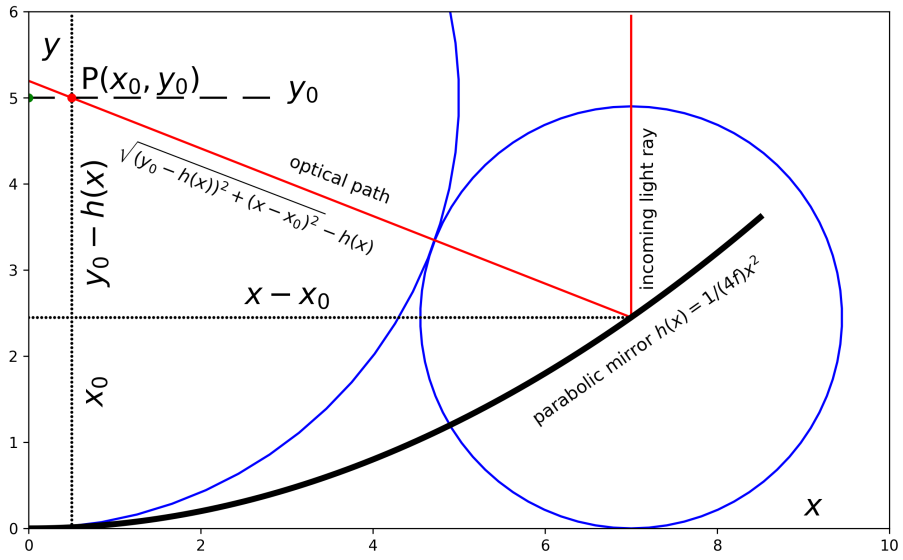

Figure C.12: Construction to determine the off-axis pattern of reflection from a parabolic mirror. The incoming red ray will be reflected into the the red point $\mathrm{P}(x_0, y_0)$. The path length for a ray incident on the parabola is measured from the point of incidence on the parabolic mirror to the point $\mathrm{P}(x_0, y_0)$, minus the path difference caused by the shape of the mirror. This path length difference then transforms the incoming plane wave into a spherical wave centered around the focal point ($x = 0, y = 5$, green).

principle and draw in each point on the parabola a spherical wave, to infer the wavefront after reflection. We now select the moment in time in which the wavefront has just been reflected at the minimum of the parabolic mirror. At the distance x from the optical axis the spherical wave has traveled the distance $h(x)$. The outgoing wavefront is determined by the tangential curve to all spherical waves after reflection. It is a spherical wave, but now centered on the focal point[1]. For all points within the entrance pupil[2] the incoming wavefront is interfering constructively in the focal point as for each point in the entrance pupil the path length differences are zero. The ideal telescope transforms the entering plane wave into spherical waves with the center being the focal point.

In order to achieve constructive interference the deviation of the optics of a real telescope from the ideal parabolic geometry have to be far smaller than the wavelength of the light.

On the optical axis we find perfect constructive interference but also at small distances away

[1]We have to evaluate the path length s from eq. C.11 at the point $\mathrm{P}(x_0 = 0, y_0 = f)$ and $h(x) = x^2/(4f)$. $s = \sqrt{(f - h(x))^2 + x^2} - h(x) = \sqrt{(f + h(x))^2} - h(x) = f = \text{const.}$. So the distance to all points is constant, we have a spherical wave centered around $\mathrm{P}(x_0 = 0, y_0 = f)$.

[2]Footprint of the mirror on the entering plane wave

from the axis we will find constructive interference, therefore the image of a point source is not a point but an extended disk, which limits the resolution of the telescope. To calculate the distribution pattern we use again the Huygens principle for a point in the focal plane with coordinates x_0, y_0, as shown in Fig.C.12. The mirror is placed with its height minimum at $(x, y) = (0, 0)$, we want to evaluate the intensity at the point $\mathrm{P}(x_0, y_0)$ (red in the figure). The distance between P and the incidence on the mirror is $\sqrt{(y_0 - h(x))^2 + (x - x_0)^2}$. Because of the phase shift introduced by the height of the mirror the optical distance will be reduced by $h(x)$. So the total distance to account for is:

$$s = \sqrt{(y_0 - h(x))^2 + (x - x_0)^2} - h(x) \tag{C.11}$$

The electric field strength in the point P is given by:

$$E(x_0, y_0) \approx \int E(x) \frac{\exp(-i\frac{2\pi}{\lambda}s)}{s} \,\mathrm{d}x \tag{C.12}$$

where $E(x)$ describes the electric field strength in the entrance pupil. The integration is reduced to the sensitive area of the telescope, the entrance pupil. To evaluate this equation we expand s in the two variables x/f and x_0/f:

$$s = f\left(1 + \frac{-1}{f^2}xx_0 + \frac{1}{2f^2}x_0^2 + O((x/f, x_0/f)^4))\right) - f \tag{C.13}$$

The whole calculation can be found in the sec. C.5.

While f and x are of the order of meters, $x_0 \approx 0.1\,\mathrm{mm}$. The term $\propto x_0^2$ can then be neglected in eq. C.13 (Fraunhofer condition). If x_0 is small and y_0 is close to f, we have a spherical wave and for each point in the focal plane $s = f$, we can thus rewrite eq. C.12.

$$E(x_0) = \frac{E_0}{f} \int E(x) \exp(-2\pi i \frac{x}{\lambda} x_0) \,\mathrm{d}x \tag{C.14}$$

we see that $E(x_0)$ is the Fourier transform of the entrance pupil illumination $E(x)$. The intensity pattern in the focal plane is given by $|E(x_0)|^2$. This pattern describes the response of the telescope to a plane wave such as those from a star like source and is called Point Spread Function (PSF). The PSF caused by a telescope with homogeneous illumination of the round entrance pupil is known as airy pattern. This PSF is by construction rotationally symmetric and has a central peak surrounded by rings (an example is shown in fig. F.6). The Full Width Half Maximum (FWHM) is proportional to λ/D, were D is the diameter of the telescope and λ the observing wavelength. For $D = 10\,\mathrm{cm}$ and $\lambda = 500\,\mathrm{nm}$ the width is of the order 1". The finite width of the central peak shows that the resolving power is limited. Unlimited resolution can only be achieved if the entrance pupil of the telescope is unlimited.

More complex entrance pupil illuminations can be described by decomposing the entrance pupil illumination into a sum of simple geometrical objects for which the Fourier transforms are known analytically, see sec. F.3 for an example.

Due to the telescope being operated from the ground the resolving power is further decreased

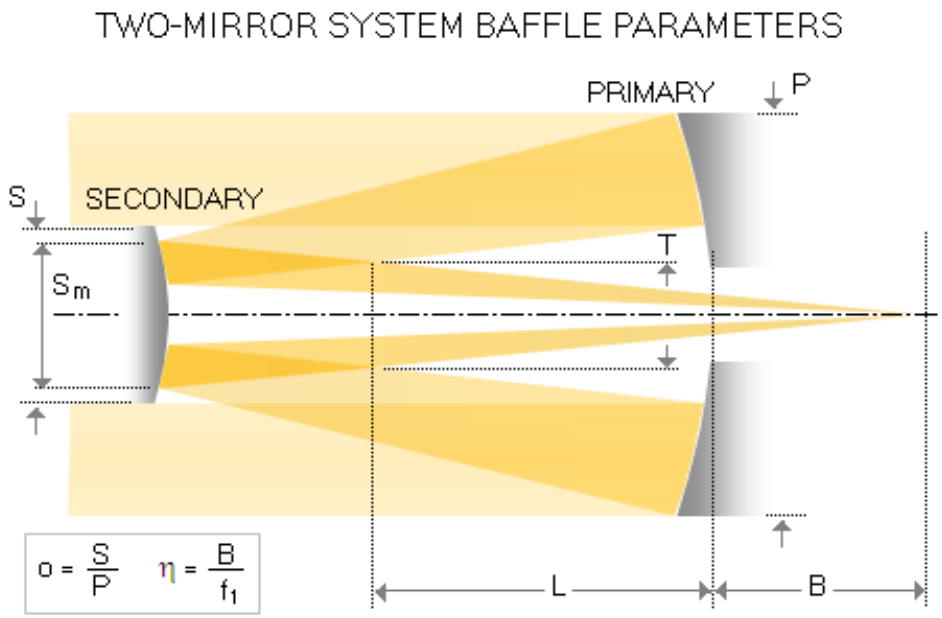

Figure C.13: From http://www.telescope-optics.net/two-mirror.htm, last checked 01.01.2018

by the atmosphere, due to the seeing effect. In case of a small telescope, with a diameter smaller than the turbulence cells, we see the PSF of the telescope moving quickly in the image plane. In long exposures, we see the convolution of the telescope PSF with the distribution of deflection angles as described in C.2.3. The convolution of the diffraction PSF ($p(x0-u)$) with the distribution ($d(u)$) of inclination angles (u) caused by the seeing is:

$$p = \int d(u) \cdot p(x0-u)\,\mathrm{d}u = d(x) * p(x) \tag{C.15}$$

Which can be rewritten using the Fourier transforms $\mathcal{F}(p(x)) = \mathcal{P}(u)$ and $\mathcal{F}(d(x)) = \mathcal{D}(u)$ to:

$$\mathcal{F}(d(x) * p(x)) = \mathcal{P}(u) \cdot \mathcal{D}(u) \tag{C.16}$$

In case of a larger telescope, big compared to the size of the turbulence cell, already the shortest possible exposures shows several superimposed PSFs, due to the telescope beam passing through multiple turbulence cells. The long time average can again be described by the convolution of the seeing with the PSF.

Casegrain Telescope

The University Hawaii 2.2 m telescope is a Cassegrain telescope. By the combination of mirrors the optical path within the telescope is folded, and a long effective focal length is created within a small physical length. The light is collected by a concave primary mirror with a short focal length, see fig. C.13. A second convex mirror placed just before the focal plane of the first

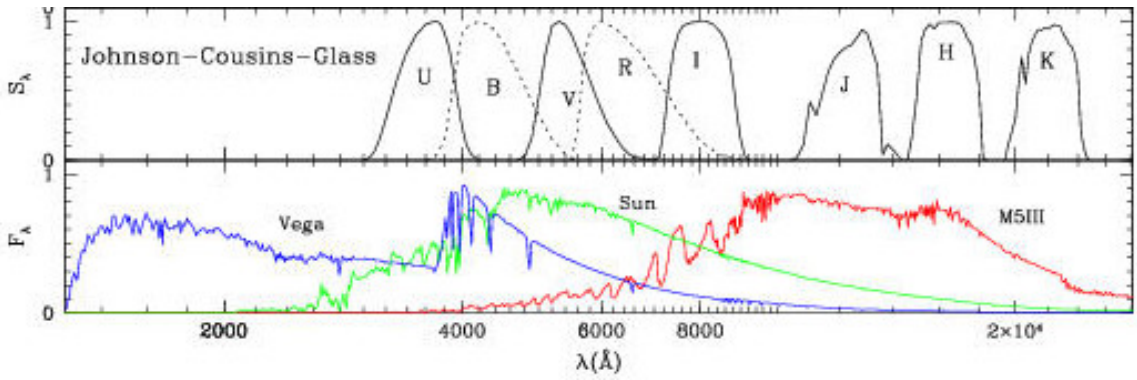

Figure C.14: The upper panel shows the transmission bands of the listed filters, while the lower panel shows some example spectra. The astronomical color gives the magnitude difference between two filter-bands and is therefore proportional to the logarithm of the flux ratio in these bands. The reference for color in the Johnson-Morgan system is given by the Vega spectrum, so all magnitude differences are defined to zero. A comparison of the colors of the different objects can then be related to the temperature of the stellar body. From http://pleiadi.pd.astro.it/isoc_photsys.00/filters1.jpg, last checked 02.01.2018

mirror, widens the beam and increases the focal length. The light is sent back to the primary mirror. In the classical Cassegrain design the light passes through a hole in the primary mirror. In the configuration on Hawaii a plane mirror is used to redirect the beam and send it radially outwards of the telescope tube. The resulting focal plane lies outside of the beam entering the telescope and illuminating the primary mirror.

C.4 Instruments & CCD

The image provided by the telescope can be analyzed in several different ways. The oldest form would be to view the image via an eyepiece and the eye. Later photographic films and photo-multipliers have been used. Nowadays Charge Coupled Devices (CCDs) are used. Using the CCD we obtain a two dimensional binned, time integrated measurement of the image provided by the telescope. To select a wavelength range within the sensitivity range of the CCD optical bandpass filters can be inserted between telescope and CCD. Using these filters one can obtain information about the SED of the emitting object. Fig.C.14 shows in the upper panel different filter bands. Shown are the transmission curves of Johnson-Cousins $(\mathrm{U, B, V, R, I, J, H, K})$[1] filters the lower part shows the absolutely normalized spectra of Vega, the Sun and a cold M star. The comparison of flux in the different filter bands can therefore be used to differentiate between the spectral classes.

There are two main types of optical filters, so called colored glass filters or interference filters. Colored glass filters use a pigment within the glass or on its surface, to absorb the light. The filter properties are therefore dependent on the pigment and can not freely be designed.

[1] U: ultraviolet, B: blue, V: visual, 'green', R: red, I: infrared, J,H,K: far infrared filters

Because of this the throughput of the filter is not dependent on the inclination to the light beam or humidity.

Interference filters use thin layers on one side to select the transmitted light via interference of the light with itself. Therefore the thickness of the layers need to be adjusted to the wavelength of transmission. Therefore the bandpass shape and wavelength can freely be designed. As the throughput depends on the layer thickness the properties will change, if the filter is inclined, and the layer is effectively thicker for the inclined ray. Also the layer thickness can change with humidity. For higher spectral resolution more and more narrow filters can be used but this would then cause a loss of sensitivity. Spectrograph's can provide high spectral resolution but have limitations in spatial/angular resolution, see sec. 4.1.

C.4.1 Charge Coupled Device: (CCD)

A Charge Coupled Device (CCD) is an electronic detector, with spatial resolution and a signal which is proportional to the number of photons illuminating each spatial element (pixel). The CCD was invented in 1969 at Bell laboratories by Willard Boyle and George Smith, as a digital storage device ([Boyle and Smith, 1974b], [Boyle and Smith, 1974a]). However, they noticed that the storage cells were sensitive to illumination. In 1976 the first astronomical image was taken at Mount Lemmon by Bradford Smith, James Janesick and others and is shown in fig. C.15 [Smith, 1976]. For the invention of the CCD Boyle and Smith were awarded one half of the Nobel prize in physics in 2009[1].

As a rough approximations a CCD is like a big photodiode, to which on one side an isolator and a grid of gates are applied. By the application of different voltages to the grid, potential wells are formed, which subdivide the big photodiode into an array of photodiodes, each one a pixel. Photons illuminating the photodiode create electron-hole pairs via the internal photoelectric effect [Howell, 2006]. The electrons are collected within the potential wells.

In commonly used CCDs the photodiode bulk is subdivided in columns by regions, which are highly doped between the columns, the so called channel stop. Electrons in their wells can only be moved along the columns, so called parallel registers (up and down). The last row of this shift register does not have channel stops. The electrons can then be shifted across columns, the so called serial or shift register (left or right). This last row is shielded against light, so photons can not produce a signal here.

To take an image the potential wells are first emptied. The mechanical shutter is then opened so that photons can illuminate the pixels and the created electrons are collected within the wells. At the end of the exposure the mechanical shutter is closed and no more electrons are collected. The potential wells with the collected electrons are all shifted down by one row. The last row of the sensitive area is shifted into the shift register. Now the wells of the shift register are moved to one side, e.g. to the right. Therefore the electrons collected in the right-most pixel of the last row are pushed into a so called readout pixel. This readout pixel acts like a capacitor to convert the amount of charge to a voltage, which is then amplified and digitized by an Analog to Digital Converter (ADC). Once all pixels in the shift register have been read out, another row is shifted. Repeating this process a digital representation of the image is formed and can

[1] http://www.nobelprize.org/nobel_prizes/physics/laureates/2009/press.html, last checked 17.01.2018

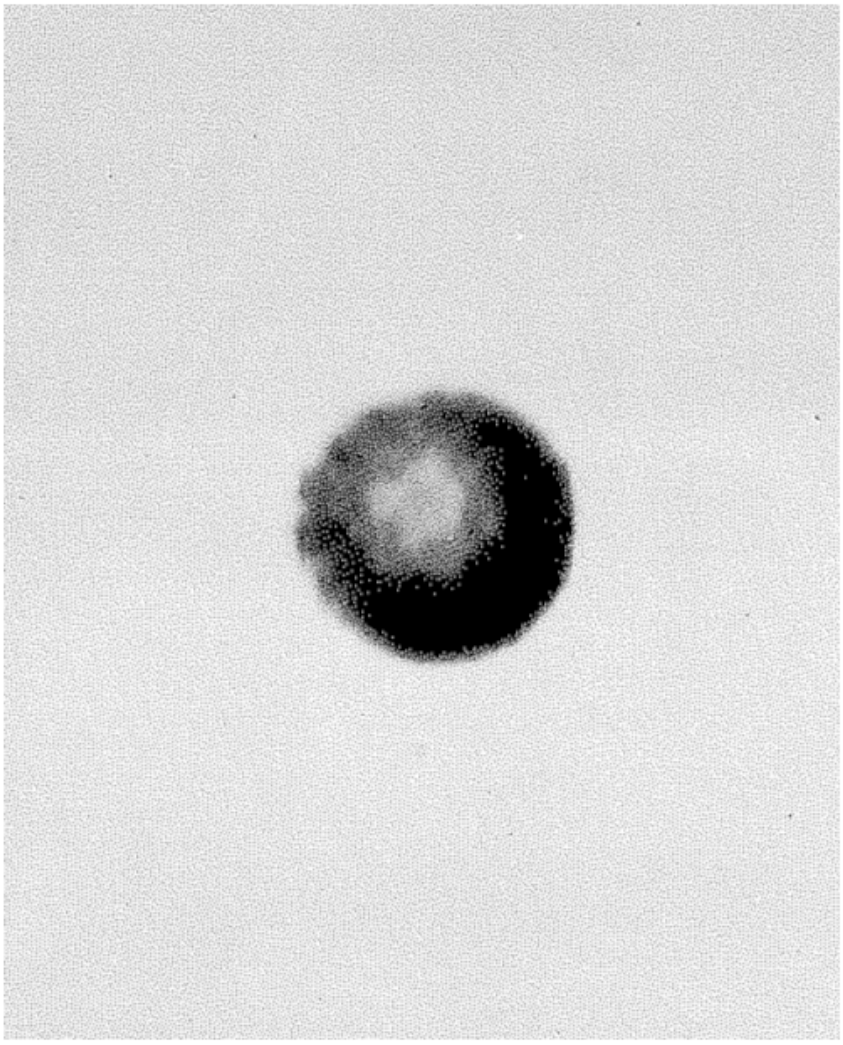

Fig. 1. Uranus in the 890-nm CH_4 absorption band.

Figure C.15: One of the first astronomical CCD images. The image was taken by Bradford Smith, James Janesick and others in 1976 at the University of Arizona 154 cm telescope at Mount Lemmon and shows Uranus at 890 nm [Smith, 1976]. The camera used was provided by the Jet Propulsion Laboratory to promote CCDs in astronomy.

be stored. The raw count from the ADC (represented in Analog-to-Digital Units (ADU)) can be converted to the number of photons which have been collected in each pixel, using the gain of the CCD.

The functioning of a CCD can be illustrated by buckets which are mounted to transport bands, fig. C.16 shows this analogy.

By shifting more than one row into the shift register, or by shifting more than one pixel into the readout pixel one can sum the electrons from multiple potential wells prior to the readout (binning). This operation saves time and in case of low illumination increases the sensitivity by effectively increasing the pixel size. Additionally it also reduces noise compared to first digitizing (including read noise to each pixel) and then summing the digital values, at the expense of lower spatial resolution.

A real CCD will deviate from this idealized description. Some of the pixels will not be able to collect electrons, so called dead pixels. Therefore also the charge shifted into them in the readout process is lost, which results in dark lines in the final digital image.

Departing from this extreme case, some of the pixels are more sensitive, while others are less sensitive than the mean pixel. These pixels are called hot or cold pixels, respectively.

In case the exposure takes too long or for very bright objects, the potential wells will fill up with electrons and the pixel gets saturated. At such locations the electrons will start flowing into neighboring pixels in the same column, as they can not cross the channel stops. This effect is known as blooming.

In case of a short exposures with no light illuminating the detector some of the pixels will result in a negative signal at the ADC. To prevent this, a stabilized offset voltage is added to the signal prior to the digitization, this voltage is called bias. In a real device this voltage is not perfectly stable, therefore dedicated exposures need to be taken to measure it. The amplitude of the bias can also be obtained from the so called overscan region, which can be obtained by shifting the shift register more often than there are pixels in it, therefore no real signal can be shifted into the readout pixel. The signal is only generated by the bias voltage.

Photons of longer wavelength can penetrate deeper into the Silicon bulk of the CCD. At infrared wavelengths and for a thin CCD the photons can be reflected on the back side and bounce back into the detector. The light will then undergo interference with itself and forms an interference pattern. In case of a broadband detector the light from sky emission (forbidden emission lines, long lived excitation states of the molecules) will produce a wave like pattern superimposed to the image, the so called fringe pattern.

In an ideal detector all electrons collected in a potential well are shifted to the output. In a real CCD not all electrons are shifted from one potential well to another. Imagine a sensor 4000 x 4000 pixels is read to one corner, then the electrons of the opposite corner had to be transfered through 8000 pixels. With an efficiency of 99.99 percent per shift one would still be left with only $\approx$45 % of the originally collected electrons.

Due to thermal excitation, free electrons can be created and collected within the potential wells, without the presence of light. Therefore, reading a CCD which was not exposed to light after some time, will result in a signal after the removal of the bias level. This signal grows linearly with the exposure time of the CCD and is called dark current. The dark current is effectively reduced by cooling the CCD. A reduction by 50 % is obtained for every decrease of

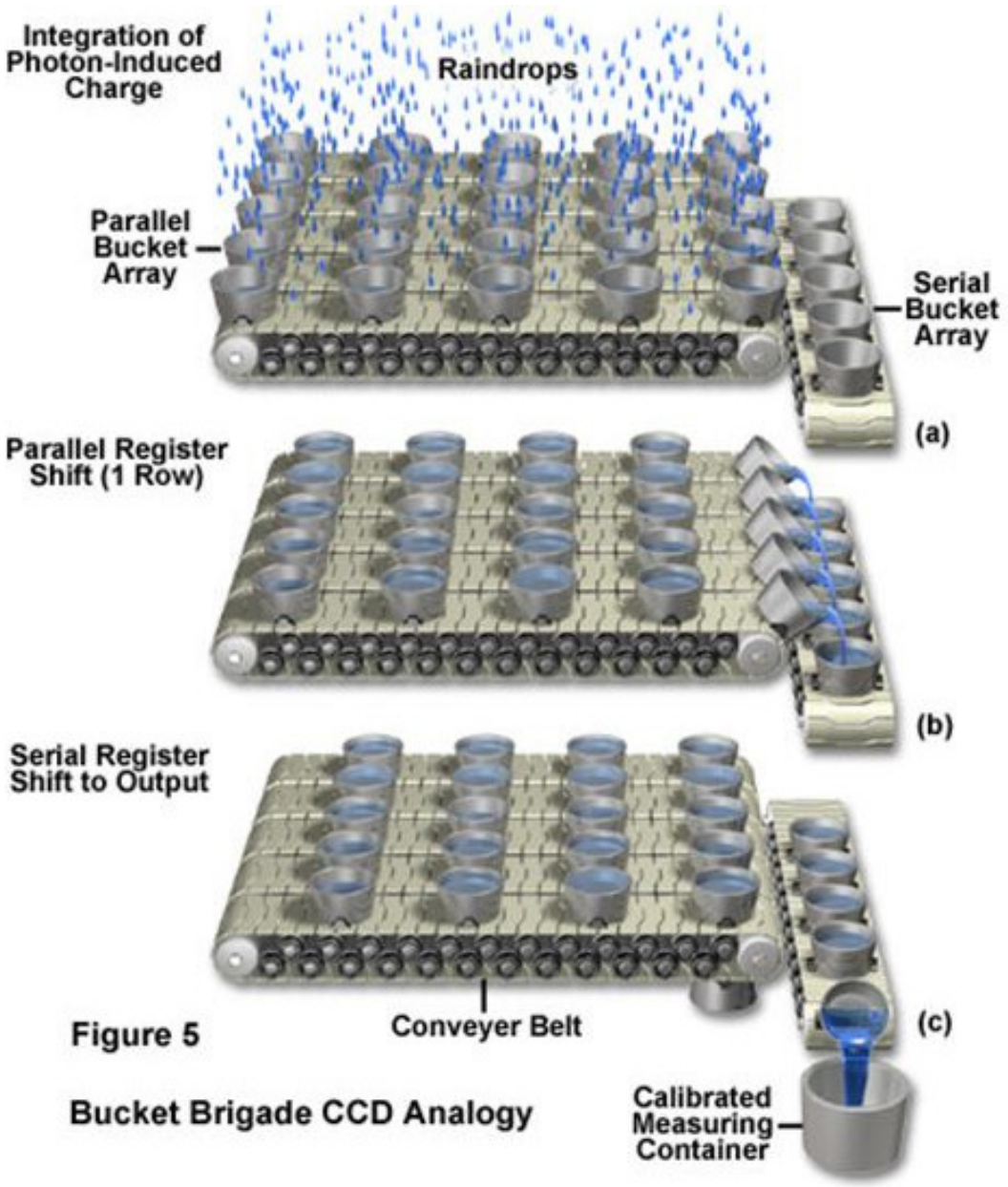

Figure C.16: Bucket analogy for CCD signal creation and readout form https://www.zeiss.com/microscopy/us/solutions/reference/basic-microscopy/understanding-the-digital-image.html#inpagetabs_ffc8-6, last checked 03.01.2018. The upper panel shows the creation of the image by the collection of the rain drops (photons) in the buckets. The second part shows the movement of a hole row to the right into the shift register and the last part shows the readout of the serial register in the readout pixel.

the device temperature by $\approx 7\,^{\circ}\mathrm{C}$. To prevent ambient humidity to condense and freeze on the CCD surface the CCD chip is placed in a vaccum chamber and the light is reaching the CCD through a window.

To define the properties of the CCD and to correct for the above mentioned properties one has to take measurements under special conditions. Observing a source of constant flux with different exposure times, one can check the linearity of the device and measure the saturation level. Additionally, one can use such measurements to measure the conversion factor from electrons to ADUs (the CCD gain). If N electrons are collected in the pixel, the statistical uncertainty will be $\sqrt{N}$. The signal S after conversion to ADU is obtained from the gain g by $S = g \cdot N$, while the uncertainty is $\sigma = g\sqrt{N}$. Therefore we can obtain the gain (slope) and the read-noise (intercept) of the comparison of the variance and the mean signal level.

The corrections that need to be applied to a raw CCD image are summarized in the following.

Cosmics: Cosmic Particles detected by the CCD
During the exposure the CCD will be hit by particles originating from cosmic rays, which will create a signal in the detector. By taking several exposures we can identify these cosmics as they are randomly distributed, therefore a pixel hit in one of the exposures will not be hit in the other exposures (rate of cosmics is low). Therefore we can remove it by calculating mean and standard deviation of the set of images pixel wise. Pixels deviating from the mean image by more than n times the standard deviation are rejected and will not be taken into account in the next calculation of the mean and standard deviation. This cleaning process is called sigma clipping and can be iterated.

Alternatively one can identify the cosmics from their shape. All signals on the CCD caused by light are convolved with the instrumental resolution of the telescope or spectrograph. The signals of cosmics are not following this distribution and can therefore be identified.

Bias Subtraction
Images with the shortest possible integration time, allow the measurement of the bias voltage and its pattern. Multiple measurements of the bias level are taken to remove the cosmics and improve the signal to noise ratio. This approach does not take into account possible variations of the bias level with time. To correct for this some CCD readout controllers read more pixels than physically existing on the CCD, the so called overscan region. One can use them to check for drifts in the bias voltage. To correct for possible drifts of the bias level one can resale the measured bias image by the mean within the overscan regions.

Dark Subtraction
To measure the dark current of the CCD one obtains several long[1] exposures with closed mechanical shutter. Again taking several exposures allows to reduce uncertainties and removal of cosmics. In this way one creates a mean dark frame, which needs to be bias subtracted prior to subtracting it from the science data.

In case the exposure time of the science image deviates from the exposure time of the dark frames one removes the bias level from the mean dark image. This corrected dark frame is then

[1] Same length as the data or the same length as the longest exposure time.

scaled for the ratio of exposure times of the science to the dark image. This scaling is possible as the temperature of the CCD is stabilized and the dark current therefore constant in time.

Fringe Correction
Through combining all science images of the night via sigma clipping one can remove cosmics and stars. As the stars have different positions in the individual exposures (assuming different pointings), they look randomly distributed. The residual image after bias and dark subtraction will show the fringe pattern (large scale variations) and pixel to pixel variations (small scale variations). To remove the small scale variations the image is smoothed on scales bigger than ≈ 50 pixels. This smoothed image is then subtracted from the science images like bias and dark.

Flatfielding
The pixels have different sensitivity. To correct for this one tries to observe a light source, which will illuminate all pixels in the same way. This image can then be used to scale the corrected image for the different pixel sensitivity. The measured flat field needs to be corrected for bias and dark signal prior to the application to the science image.

C.5 Taylor Series Expansion of the Optical Path

We start from the eq. C.11 as shown in fig. C.12. All points in the entrance pupil (footprint of telescope sensitivity on a plane wavefront) interfere constructively at the focal point. The following Taylor series expansion in $a = x/f$ & $b = x_0/f$ will be around this point P($x = 0, x_0 = 0, y_0 = f$).

$$s = \sqrt{(y_0 - h(x))^2 + (x - x_0)^2} - h(x) \tag{C.17}$$

$$s = f \cdot n = f \cdot \left(\sqrt{\left(1 - \frac{a^2}{4}\right)^2 + (a-b)^2} - \frac{a^2}{4} \right) = f \cdot \sqrt{p} - \frac{a^2}{4} \tag{C.18}$$

with:

$$\begin{aligned} p &= \left(1 - \frac{a^2}{4}\right)^2 + (a-b)^2 \\ &= 1 - \frac{a^2}{2} + \frac{a^4}{16} + a^2 - 2ab + b^2 \\ &= 1 + \underbrace{\frac{1}{2}a^2 + b^2 - 2ab + \frac{1}{16}a^4}_{\epsilon} \end{aligned} \tag{C.19}$$

up to 4.th order in a, b: $\sqrt{p} = \sqrt{(1+\epsilon)} = 1 + \frac{\epsilon}{2} - \frac{\epsilon}{8}$

$$\begin{aligned}
\epsilon^2 &= \frac{1}{4}a^4 + b^4 + 5a^2b^2 - 2a^3b - 4ab^3 \\
\sqrt{p} &= 1 + \frac{1}{4}a^2 + \frac{1}{2}b^2 - ab - \frac{1}{8}b^4 - \frac{5}{8}a^2b^2 + \frac{1}{4}a^3b + \frac{1}{2}ab^3 \\
n &= \sqrt{p} - \frac{a^2}{4} = 1 + \frac{1}{2}b^2 - ab - \frac{1}{8}b^4 - \frac{5}{8}a^2b^2 + \frac{1}{4}a^3b + \frac{1}{2}ab^3 \\
s &= f \cdot n \\
s &= f\left(1 - \frac{xx_0}{f^2} + \frac{x_0^2}{2f^2} + \frac{1}{f^4}\left(0x^4 + \frac{1}{4}x^3x_0 + \frac{5}{8}x^2x_0^2 + \frac{1}{2}xx_0^3 + \frac{1}{8}x_0^4\right)\right) \\
s &\approx f - \frac{xx_0}{f}
\end{aligned} \tag{C.20}$$

We had to perform the expansion up to 4th order as terms proportional to x, x^2, x^3, x^4 can be larger than the xx_0 term, as $\frac{x}{f} \leq \frac{1}{20}$ and $\frac{x_0}{f} \leq 2 \cdot 10^{-3}$. We see that all this terms cancel out due to the path length difference introduced by the mirror shape (converting plane wave to spherical wave). The leading term is proportional to xx_0, which is the Fraunhofer diffraction.

Appendix D

Additional Material

D.1 RoC obtained from Throughputs

We start from the definition of the ratio of calibrations RoC:

$$\mathrm{RoC} = \frac{(\mathrm{E}/\Omega)_{\mathrm{SNIFS}}}{(\mathrm{E}/\Omega)_{\mathrm{Pd}}} \tag{D.1}$$

Observing standard stars we obtain the atmospheric and instrumental throughput via:

$$S^{\mathrm{e}^-}_{obs} = S^{\mathrm{e}^-}_{\mathrm{tab}} \cdot A_{\mathrm{tel}} \cdot t_{\mathrm{exp}} \cdot \tau_{\mathrm{CALSPEC}} \cdot 10^{-kz} \tag{D.2}$$

with $S^{\mathrm{e}^-}_{\mathrm{tab}}$ the number of photons incident at the top of the atmosphere per unit area and time, A_{tel} the telescope collecting area and t_{exp} the exposure time. Both $S^{\mathrm{e}^-}_{obs}$ and $S^{\mathrm{e}^-}_{\mathrm{tab}}$ have the same spectral resolution, which will be assumed throughout the whole calculation. τ_{CALSPEC} is the instrumental throughput based on the CALSPEC system and 10^{-kz} gives the airmass dependence for the atmospheric transmission.

As SCALA is mounted in front of the telescope, the airmass z is zero and the airmass term vanishes. $S^{\mathrm{e}^-}_{\mathrm{tab}}$ is related to the physical flux F_{tab} by:

$$S^{\mathrm{e}^-}_{\mathrm{tab}} = F_{\mathrm{tab}} \cdot A_{\mathrm{tel.}} \cdot t_{\mathrm{exp}} \cdot \frac{1}{h\nu} \tag{D.3}$$

We now use definition of the flux solution F_{sol}:

$$F_{\mathrm{tab}} = F_{\mathrm{sol}} \cdot S^{\mathrm{e}^-}_{obs} \tag{D.4}$$

Substituting eq. D.4 & D.3 in eq. D.2 we obtain the instrumental throughput of SNIFS based on the CALSPEC system:

$$\tau_{\mathrm{CALSPEC}} = \frac{h\nu}{F_{\mathrm{sol}} A_{\mathrm{tel}} t_{\mathrm{exp}}} \tag{D.5}$$

We can now use the above equations and the equations from sec. 4.4 and obtain RoC:

$$\mathrm{RoC} = \frac{(\mathrm{E}/\Omega)_{\mathrm{SNIFS}}}{(\mathrm{E}/\Omega)_{\mathrm{Pd}}} = \frac{\frac{A_{\mathrm{tel}} t_{\mathrm{exp}}}{\Omega_{\mathrm{spaxel}}} \int_{\lambda_c-\Delta\lambda}^{\lambda_c+\Delta\lambda} F_{\mathrm{SNIFS}}\,\mathrm{d}\lambda}{\frac{1}{\Omega_{\mathrm{SCALA}}} \int_0^{t_{\mathrm{exp}}} F_{\mathrm{SCALA}}\,\mathrm{d}t} \tag{D.6}$$

with F_{SCALA} measured in [W] like in eq. 8.1:

$$\begin{aligned} F_{\mathrm{SCALA}} &= (I_{\mathrm{PD}} - B_{\mathrm{Ext.}}) \cdot (1 - CT - R_{\mathrm{LS.}} - R_{\mathrm{Port}} - R_{\mathrm{PDH.}} - F_{\mathrm{oobe}}) \frac{1}{g \cdot R} \cdot \frac{A_{\mathrm{Beam}}}{A_{\mathrm{PD}}} \cdot N_{\mathrm{eff.}} \\ &= I_{\mathrm{PD,corr}} \frac{1}{g \cdot R} \cdot \frac{A_{\mathrm{Beam}}}{A_{\mathrm{PD}}} \cdot N_{\mathrm{eff.}} \end{aligned} \tag{D.7}$$

and the flux observed by SNIFS F_{SNIFS} measured in [J/(s cm^2 Å)] via illumination by SCALA:

$$F_{\mathrm{SNIFS}} = F_{\mathrm{sol}} S^{\mathrm{e}^-}_{\mathrm{obs,SCALA}} \tag{D.8}$$

Inserting eq. D.7 and eq. D.8 in eq. D.6 we obtain:

$$\mathrm{RoC} = \frac{\Omega_{\mathrm{SCALA}} \int_{\lambda_c-\Delta\lambda}^{\lambda_c+\Delta\lambda} F_{\mathrm{sol}} S^{\mathrm{e}^-}_{\mathrm{obs,SCALA}}\,\mathrm{d}\lambda A_{\mathrm{tel}} t_{\mathrm{exp}}}{\Omega_{\mathrm{spaxel}} \int_0^{t_{\mathrm{exp}}} I_{\mathrm{PD,corr}} \frac{N_{\mathrm{eff.}}}{g \cdot R} \cdot \frac{A_{\mathrm{Beam}}}{A_{\mathrm{PD}}}\,\mathrm{d}t} \tag{D.9}$$

Comparing the number of photons emitted by SCALA $n_{\gamma,\mathrm{SCALA}}$ per solid angle Ω_{SCALA} to the number of electrons observed by SNIFS $S^{\mathrm{e}^-}_{\mathrm{obs,SCALA}}$ per solid angle Ω_{spaxel} we obtain the throughput of SNIFS as measured by SCALA to:

$$\begin{aligned} \tau_{\mathrm{SCALA}} &= \frac{S^{\mathrm{e}^-}_{\mathrm{obs,SCALA}}}{n_{\gamma,\mathrm{SCALA}}} \frac{\Omega_{\mathrm{SCALA}}}{\Omega_{\mathrm{spaxel}}} \\ &= \frac{\Omega_{\mathrm{SCALA}}}{\Omega_{\mathrm{spaxel}}} \frac{\int_{\lambda_c-\Delta\lambda}^{\lambda_c+\Delta\lambda} S^{\mathrm{e}^-}_{\mathrm{obs,SCALA}}\,\mathrm{d}\lambda}{\int_0^{t_{\mathrm{exp}}} \frac{F_{\mathrm{SCALA}}}{h\nu\,\mathrm{d}t}} \\ &= \frac{\Omega_{\mathrm{SCALA}}}{\Omega_{\mathrm{spaxel}}} \frac{\int_{\lambda_c-\Delta\lambda}^{\lambda_c+\Delta\lambda} S^{\mathrm{e}^-}_{\mathrm{obs,SCALA}}\,\mathrm{d}\lambda}{\int_0^{t_{\mathrm{exp}}} I_{\mathrm{PD,corr}} \frac{N_{\mathrm{eff.}}}{h \cdot \nu \cdot g \cdot R} \cdot \frac{A_{\mathrm{Beam}}}{A_{\mathrm{PD}}} \cdot \mathrm{d}t} \end{aligned} \tag{D.10}$$

Combining eq. D.5 with eq. D.10 we obtain:

$$\begin{aligned} \frac{\tau_{\mathrm{SCALA}}}{\tau_{\mathrm{CALSPEC}}} &= \frac{\Omega_{\mathrm{SCALA}}}{\Omega_{\mathrm{spaxel}}} \frac{\int_{\lambda_c-\Delta\lambda}^{\lambda_c+\Delta\lambda} S^{\mathrm{e}^-}_{\mathrm{obs,SCALA}}\,\mathrm{d}\lambda}{\int_0^{t_{\mathrm{exp}}} I_{\mathrm{PD,corr}} \frac{N_{\mathrm{eff.}}}{h \cdot \nu \cdot g \cdot R} \cdot \frac{A_{\mathrm{Beam}}}{A_{\mathrm{PD}}} \cdot \mathrm{d}t} \frac{F_{\mathrm{sol}} A_{\mathrm{tel}} t_{\mathrm{exp}}}{h\nu} \\ &= \mathrm{RoC} \end{aligned} \tag{D.11}$$

Comparing eq. D.6 with eq. D.11 there is only a small difference. In eq. D.6 the flux solution F_{sol} is included in the integral over wavelength, while in eq. D.11 it is not. As the light emitted by SCALA is nearly monochromatic and the change of the flux solution within the wavelength range is small, we can treat it like a constant and therefore take it out of the integral in eq. D.6.

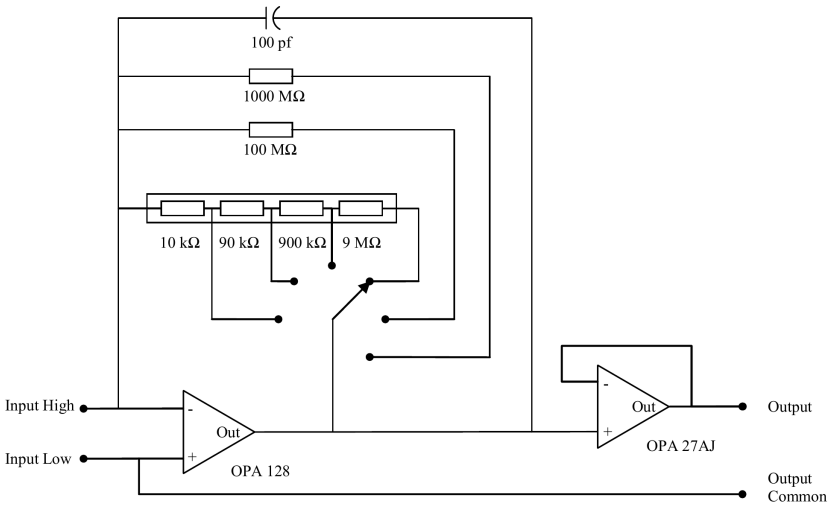

Figure D.1: Trans impedance amplifier for the readout of small photodiode currents as described in [Larason and Houston, 2008]

D.2 Transimpedance Amplifier

The transimpedance amplifier in this example (see. [Larason and Houston, 2008]) uses two operational amplifiers (OpAmps, see fig.D.1). To understand the circuit we will use the simplification of an ideal OpAmp: a device with no current flow into inputs + and −, the voltage difference between them is adjusted to zero in case of a feedback, the amplification of the difference applied between + and − is infinitely high and the operational amplifier output can provide unlimited current.

The photodiode is connected to both inputs of the OpAmp (see fig.D.1). The cathode is connected to the − input and the anode to + and to ground. The output photodiode current will flow from the cathode to the − input and through the feedback resistor to the output. As the + input is connected to ground, the difference of the inputs should be zero, the − input is at a virtual ground. The current through the resistor will result in a voltage of $R \cdot I_{\text{photo}}$ between − input (virtual ground) and the output. The input current has been converted into a proportional voltage. As the photodiode is connected to ground and virtual ground it is operated in shortcut mode, which results in good linearity between photon flux and electron current. The second OpAmp is operated without amplification and therefore provides a low impedance output. Shown in fig. D.1 is a capacitor in parallel to the resistor. Resistor and capacitor together define the time constant of the device, so the time over which the current is effectively averaged.

Due to the transimpedance amplifier we obtain a voltage proportional to the input current according to $U_{\text{meas}} = R \cdot I_{\text{photo}}$, without applying an ohmic load R to the photodiode.

D.3 Error Propagation

The error on the function e is given by $\Delta e = J^T C J$ with J the jacobian or the vector of the partial derivative of e and C the covariance matrix[1]:

$$C = \begin{pmatrix} \mathrm{cov}(x_i, x_i) & \mathrm{cov}(x_i, x_j) \\ \mathrm{cov}(x_j, x_i) & \mathrm{cov}(x_j, x_j) \end{pmatrix} \tag{D.15}$$

$$(\Delta e)^2 = \begin{pmatrix} \frac{\delta e}{\delta x_i} \\ \frac{\delta e}{\delta x_j} \end{pmatrix}^T \cdot \begin{pmatrix} \mathrm{cov}(x_i, x_i) & \mathrm{cov}(x_i, x_j) \\ \mathrm{cov}(x_j, x_i) & \mathrm{cov}(x_j, x_j) \end{pmatrix} \cdot \begin{pmatrix} \frac{\delta e}{\delta x_i} \\ \frac{\delta e}{\delta x_j} \end{pmatrix} \tag{D.16}$$

using $\mathrm{cor}(x_i, x_j) = \mathrm{cov}(x_i, x_j)/(\sigma_i \sigma_j)$ and $\mathrm{cov}(x_i, x_i) = \mathrm{var}(x_i) = \sigma_i^2$

$$(\Delta e)^2 = \begin{pmatrix} \frac{\delta e}{\delta x_i}\sigma_i \\ \frac{\delta e}{\delta x_j}\sigma_j \end{pmatrix}^T \cdot \begin{pmatrix} 1 & \mathrm{cor}(x_i, x_j) \\ \mathrm{cor}(x_j, x_i) & 1 \end{pmatrix} \cdot \begin{pmatrix} \frac{\delta e}{\delta x_i}\sigma_i \\ \frac{\delta e}{\delta x_j}\sigma_j \end{pmatrix} \tag{D.17}$$

For SCALA effective area we take ratios of photodiode measurements so the function we have to look on is like $e = x_i/x_j$:

$$(\Delta e)^2 = \left(\frac{\delta e}{\delta x_i}\sigma_i\right)^2 + 2\left(\frac{\delta e}{\delta x_i}\frac{\delta e}{\delta x_j}\sigma_i\sigma_j \mathrm{cor}(x_i, x_j)\right) + \left(\frac{\delta e}{\delta x_j}\sigma_j\right)^2 \tag{D.18}$$

with $\frac{\delta e}{\delta x_i} = \frac{1}{x_j}$ and $\frac{\delta e}{\delta x_j} = -\frac{x_i}{x_j^2}$. The above formula can be specialized to three limiting cases: *no* correlation $\mathrm{cor}(x_i, x_j) = 0$ with an uncertainty Δe_u and *perfect* correlation $\mathrm{cor}(x_i, x_j) = 1$ with an uncertainty e_c and *anti*-correlation $\mathrm{cor}(x_i, x_j) = -1$. I will skip the anti-correlation as this case was not observed in the measurements.

- **no Correlation** $\mathrm{cor}(x_i, x_j) = 0$

$$(\Delta e_u)^2 = \left(\frac{\sigma_i}{x_j}\right)^2 + \left(-\frac{x_i}{x_j}\frac{\sigma_j}{x_j}\right)^2 \tag{D.19}$$

[1] with the following definitions for mean, covariance, variance and standard deviation.
mean

$$\bar{x} = \frac{1}{n}\sum_{i=0}^{n}(x_i) \tag{D.12}$$

covariance

$$\mathrm{cov}(x, y) = \frac{1}{n}\sum_{i=0}^{n}(x_i - \bar{x})(y_i - \bar{y}) \tag{D.13}$$

variance (var) and standard deviation σ_x

$$\mathrm{var}(x) = \mathrm{cov}(x, x) = \sigma_x^2 \tag{D.14}$$

$$\frac{\Delta e_u}{e} = \sqrt{\left(\frac{\sigma_i}{x_i}\right)^2 + \left(\frac{\sigma_j}{x_j}\right)^2} \tag{D.20}$$

- **Correlation** $\mathrm{cor}(x_i, x_j) = 1$

$$(\Delta e_c)^2 = \left(\left(\frac{\sigma_i}{x_j}\right)^2 - 2\frac{x_i}{x_j^3}\sigma_i\sigma_j + \left(\frac{x_i}{x_j}\frac{\sigma_j}{x_j}\right)^2\right) = \left(\frac{\sigma_i}{x_i} - \frac{x_i}{x_j}\frac{\sigma_j}{x_j}\right)^2 \tag{D.21}$$

For the effective SCALA area we have 17 independent measurements so the total error in the uncorrelated case will be proportional to:

$$\frac{\Delta e_u}{e} = \sqrt{\frac{1}{17}}\sqrt{\left(\frac{\sigma_i}{x_i}\right)^2 + \left(\frac{\sigma_j}{x_j}\right)^2} \tag{D.22}$$

and for the correlated case it will be:

$$\frac{\Delta e_c}{e} = \sqrt{\frac{1}{17}}\left|\frac{\sigma_i}{x_i} - \frac{x_i}{x_j}\frac{\sigma_j}{x_j}\right| \tag{D.23}$$

D.4 Examples of Dust on SCALA

In 2017 the dome of the UH88 telescope was refurbished, in these processes the dome was "vapor blasted" with garnet particles prior to the new painting. The following two images show pieces of SCALA which are covered with dust.

Figure D.2: View on the black anodized housing of the tungsten lamp. The housing was wiped with a finger to show the change due to the dust.

Figure D.3: View on the unmounted light shield of the integrating sphere, the upper corner was wiped

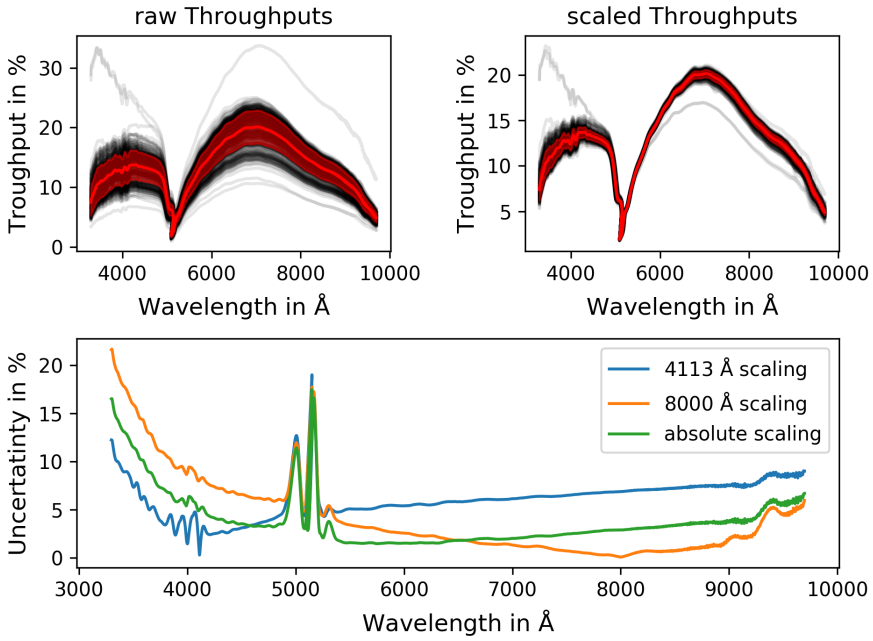

Figure D.4: The upper left figure shows the measured throughputs from SNIFS between 2004 and 2015 in gray. The red band indicates the mean value and its standard deviation. Upper right: The same data, but normalized by their all wavelength average. Lower plot: Relative uncertainty by the use of different normalizations. The green is the deviation between the throughputs while normalized in a band of 20 Åaround 4113 Å. The orange band results from a normalization in a 20 Åband at 8000 Å. For the blue curve the throughputs have been normalized by the all wavelength average.

D.5 Long-time average Throughput of SNIFS

The throughput of SNIFS has been obtained in photometric nights (nights without visual clouds) since 2004. For this average all throughputs till 2015 have been used.

The raw dataset is shown in fig. D.4, gray curves. Except from some clear outliers the shape of the throughputs seem to be the same. The difference between the measured throughputs is consistent with a wavelength independent gray scaling factor. The upper right figure shows the same curves, but with the mean throughput (average over all wavelength) normalized to the 11-year average. In this way the absolute scaling factors are removed. A drastic reduction of the spread is visible. The lower panel of the figure shows the relative uncertainty of the mean after correcting for gray scalings. We show the uncertainties for three different scalings. The green curve is obtained by using the all wavelength average for normalization, while the blue and orange curve are obtained by normalizations around 4113 Å and 8000 Å respectively. The long-time average throughput does not allow us to measure the absolute fluxes (uncertainty up to 40 %) but it allows us to perform comparisons between wavelengths with uncertainties smaller then 10 % over a wide wavelength range.

D.6 Details on the Aging of the Corrections

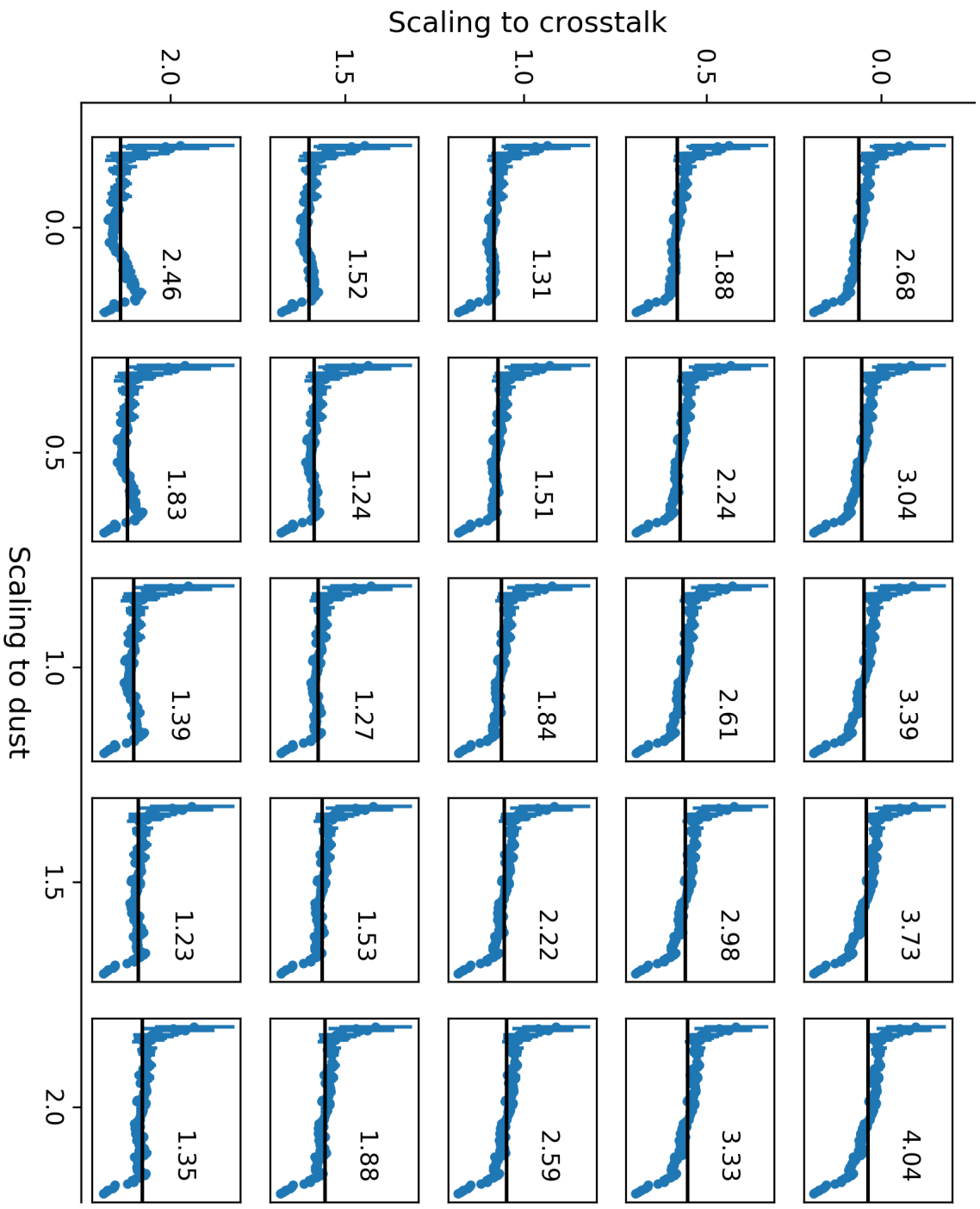

Shown are the RoC for different combinations of f_{CT} and f_D as used in capt. 8, the number given in each panel is the ratio of STD over mean RoC in the wavelength range 4500 Å to 9000 Å.

D.7 Reflection off the Photodiode Housing

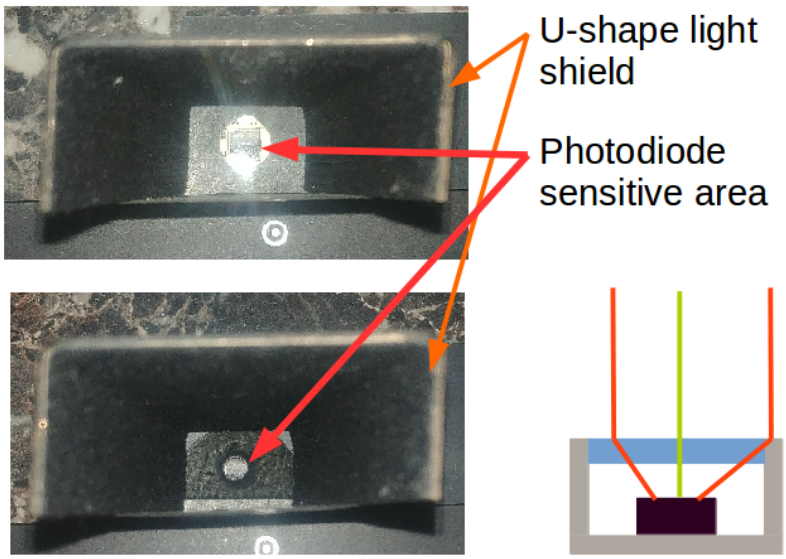

Figure D.5: Upper panel: Original setup of the CLAP front end. Lower panel: Aperture stop mounted by the telescope engineer in front of the photodiode. The flash light used to illuminate the object is reflected off the metal photodiode housing in the upper picture. Also visible is the U-shaped light shield. The small sketch on the lower right shows two possibilities for the generation of a background signal, via dust (left) and via reflection off the housing (right)

The upper panel of fig. D.5 shows an image taken by the telescope engineer of the original CLAP front-end. We see the metal packaging of the photodiode with the reflection of the flash light.

The beam provided by SCALA is far bigger than the sensitive area of the photodiode (small dark square in fig. D.5). The lower right of fig. D.5 is showing two possibilities in which non-direct light can produce a signal. Light can illuminate the metal housing and from there be reflected on the sensitive area (right), or it can be scattered off dust on the entrance window onto the photodiode sensitive area (left).

To evaluate the amount of light reaching the photodiode via non-direct path we compare measurements with and without an aperture stop see fig. D.5. Fig. D.5 lower part shows the CLAP device with the aperture mounted. Based on the above pictures we calculated that the flux level should be reduced by a geometric scaling factor of 1.6 ± 0.1.

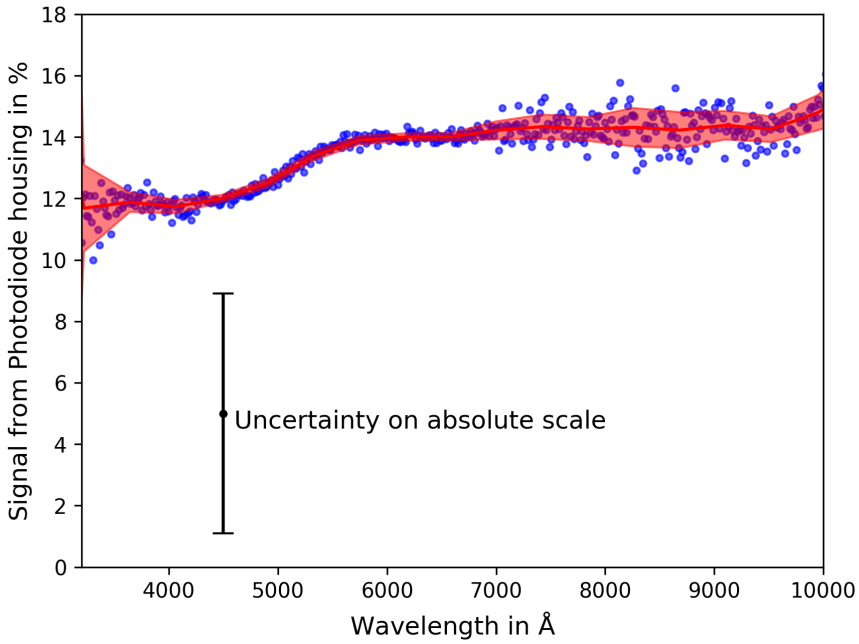

Figure D.6: Percentage of signal detected by photodiode but generated by a reflection of the metallic photodiode housing.

Be I_0 the photo current measured without aperture stop and I_{geom} the photo current geometrically expected, then they are related as $I_0 = I_{\text{geom}} \cdot f_{\text{geom}}$. For the observed photo current I_{meas} we find $I_0 = I_{\text{meas}} \cdot f_{\text{meas}}$. The photo-current resulting from the reflection off the photodiode housing is $I_{\text{refl}} = I_{\text{geom}} - I_{\text{meas}}$. The relative contribution is then $I_{\text{refl}}/I_0 = 1/f_{\text{geom}} - 1/f_{\text{meas}}$, we assume that all reflections from the photodiode housing to the sensitive area are removed by the aperture stop. We obtain that 12 % to 15 % (±4 % uncertainty) of our usual signal are caused by reflections off the photodiode housing see fig. D.6. The uncertainty is limited by the uncertainties of the geometric scaling, which was obtained from images.

The above calculation assumed a reflection off the housing as source of the difference, in case of scattering off dust on the photodiode window the result would be different. Before mounting the aperture stop, light from outside the beam was scattering into the beam. But also light within the beam was scattering outside by dust on the window. With the aperture stop the dust outside the beam is not anymore illuminated but the dust within it is still scattering light outside of the beam.

When this measurement was taken the whole setup was already covered with dust due to the dome refurbishment. At the point of the measurement we did not yet know that everything was covered with dust. It might therefore be possible that the measurement without aperture stop was taken with a dirty photodiode. When the telescope engineer unmounted the photodiode for

us and placed the aperture stop, he might have cleaned the device accidentally. Therefore the difference in signal might be caused by the change in the amount of dust, which would change the interpretation again.

As described in [Larason and Houston, 2008] NIST provides calibration of photodiodes of type S1337-1010BQ. These photodiodes are larger than the one used in CLAP and they are mounted in a ceramic package. They describe that the beam used for calibration is smaller than the sensitive area of the photodiode and that the sensitive area is rastered to obtain a homogeneity map.

According to the Paris Supernova Cosmology Group the photodiode is placed in the beam provided by a monochromator, which is illuminated with an LED (Light emitting Diode). It is mentioned that the position is optimized for high signal, therefore we conclude that the beam is bigger than the photodiode. Therefore reflections of the photodiode housing could already be included, if no additional aperture stop was used.

In fig. 5.3 we compared their calibration with the one from Hamamatsu. We also calculated the quantum efficiency of our photodiode based on the quantum efficiency of an S1337-1010BQ photodiode, using the throughputs of a UV fused silica and a sapphire window. All obtained values agree, indicating that the calibration is not contaminated by a reflection of the photodiode housing.

Based on these measurements we can not conclude whether the signal we see is caused by dust on the photodiode window or by reflections on the photodiode housing, more measurements on this would be required. For the following uncertainty calculation we proceed with the above values and uncertainties shown in fig. D.6. In sec. 8 we found that the deviation in the wavelength dependence of the SCALA and CALSPEC calibration is only weakly affected by the photodiode housing reflection, as its wavelength dependence is small.

D.8 Reflection off the IS Exit Port Walls

In fig. 6.10 we had seen that a reflection can occur on the walls of the IS port. To measure its amplitude we place an aperture stop at the IS exit port. The aperture stop is made of Acktar Metal Velvet. The hole was inserted via an office hole puncher, therefore the diameter of the hole is 6.2-6.25 mm (measured by the telescope engineer). The diameter of the IS port is 14 mm (technical drawing, uncertainty not known). Based on the measurements we expect a reduction of the light by a factor $f_{\text{geom.}} = 5.02 - 5.10$. Fig.D.7 shows the measured reduction $f_{\text{meas.}}$ We see that the measured reduction is larger than expected from the geometry. As the aperture stop is placed on the IS housing and its diameter is small, we assume that the photodiode is insensitive to light reflected off the photodiode housing. We thus attribute the difference between observation and measurement to this reflection. In the same way as in sec. D.7 we obtain the relative contribution of the light reflected off the port walls to: $I_{\text{refl.}}/I_0 = 1/f_{\text{geom.}} - 1/f_{\text{meas.}}$. The relative contribution to the photodiode signal is shown in fig. D.8.

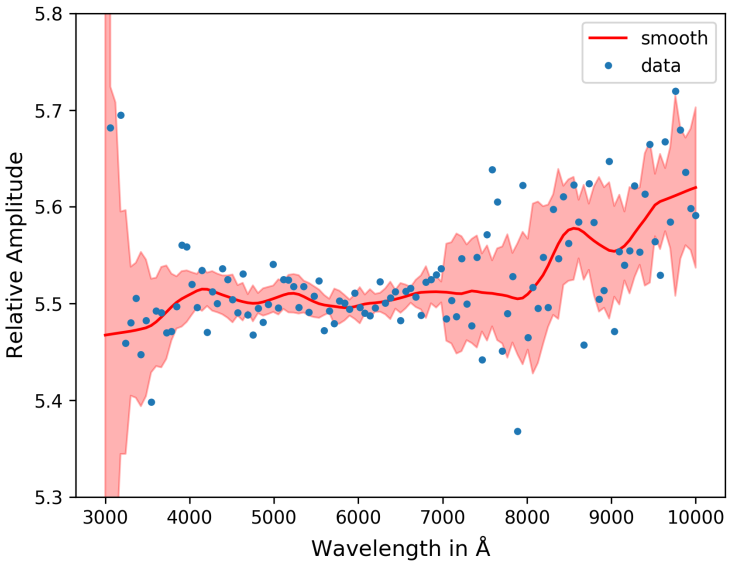

Figure D.7: Measured flux reduction factor using the reduced IS port.

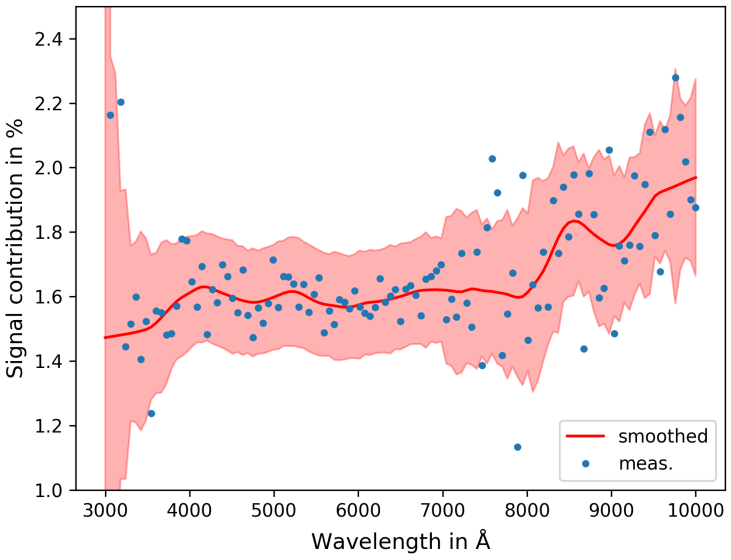

Figure D.8: Percentage of the usually measured signal originating from a reflection off the IS port walls.

Appendix E

Further tests

E.1 Signal Amplitude

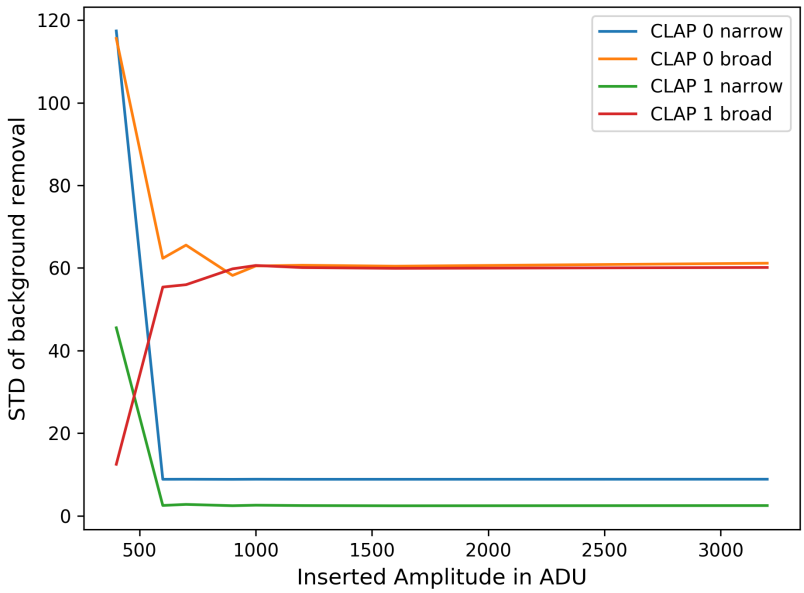

Figure E.1: Uncertainties of the background removal for daytime data for both CLAPs depending on the amplitude of the introduced artificial signal. We see that the code is working for amplitudes larger than 600 ADU .

All tests in sec. 6.1 use a signal amplitude of 3200 ADU. The data reduction code for the photodiodes uses a five sigma clipping technique on the signal level to remove the background. The typical signal standard deviation for CLAP1 is 65 ADUs, therefore a minimal signal of 325 ADU is needed. As visible in the average spectrum (fig.5.2) our minimum signal is 800 ADU. However, if the background level is changing between pre-signal and post-signal background,

like during daytime, the minimal signal needed to be detected by the code, increases.

In the daytime dataset the variations of the background are maximal. Therefore this code will sometimes fail to split the background from the signal region and the measurement will be flagged (nan) and not contribute to the measured uncertainties.

At the minimum tested amplitude of 400 ADU 4330 of 8640 measurements are rejected, at 600 ADU only 15 are rejected and at 800 ADU only 6.

We find that the results are consistent as long as the signal / hight of top hat is larger than 600 ADU (see fig.E.1). A comparison to fig. 5.2 shows that the smallest detected signal is larger than 800 ADU. Therefore the code described above can securely be used in usual operation.

E.2 Quantum Efficiency of Canon EOS 1000D

Besides the photodiodes a Canon EOS 1000D is used as a independent detector in the SCALA setup. The camera can be used without an objective as a big photodiode, or it can be operated as a pinhole camera, useful to detect the sources and directions of unknown backgrounds, like stray light. The setup was calibrated in the optical lab in Berlin relative to S1337-1010BQ photodiodes from Hamamatsu. In the following the calibration setup and data reduction is discussed.

Calibartion Setup The setup in the laboratory is close to the configuration of the SCALA device. The used light source is a 150 W Xenon lamp equipped with a filter wheel with order sorting filters (cut on wavelength 3090 Å & 4950 Å). A Cornerstone 260 monochromator is used as wavelength tunable bandpass (FWHM ≈35 Å). The grating can be of 3500 Å blaze wavelength or of 7500 Å, both with a grove density of 1200 l/mm. The exit slit of the monochromator is imaged via a UV-Fused Silica lense into the entrance port of an IS from Labsphere (3.3 inch diameter, coated with Spectralon[1]). Between lens and IS a UV-Fused Silica window is used as beam splitter illuminating a reference photodiode (PD.1). The light leaving the IS is illuminating a parabolic mirror of 200 mm diameter and 800 mm focal length, the mirror is acting as a collimator. Between IS and mirror reference photodiode (PD.2) is positioned. To provide an image of the IS port two different pinhole objectives can be mounted to the Canon EOS 1000d, which are:

- self made pinhole: using camera body cap with a 1 mm drilled hole, focal length in field center ≈60 mm, angular resolution 0.95°
- HOLGA DSLR Pinhole Objective: hole diameter 0.25 mm, focal length in field center ≈38 mm, angular resolution 0.38°

At the third port of the IS a photodiode is mounted to measure the exposure time of the monochromator shutter. The reference PD's are read via a Keithley 6482 Dual Channel Picoamperemeter, which is controlled via the serial port from a Raspberry Pi 2 (RPi2) computer. The monochromator, it's shutter and filter wheel are also controlled via the serial ports. The photodiode for the exposure time measurement is read via an impedance amplifier using two operational amplifiers of type OP27GP and an analog-to-digital converter of type MCP3208

[1] Barium sulfat within PTFE

communicating via SPI with the RPi2, enabling readouts at the 1.1 kHz rate. The Canon EOS 1000d is connected via USB and controlled via `gphoto2` from the RPi2.

All measurements are synchronized via a `Python` script. The measurement starts with setting the monochromator wavelength, filter and grating, while the shutter of the monochromator is closed. The readout of the timing PD is started for 41,000 samples, as a background process. The exposure of the camera is started as a second background process, and due to change of camera setting via the code the exposure is delayed by $\approx$5 s. The picoamperemeter is read 30 times, afterwards the shutter of the monochromator is opened. 90 further readings of the picoamperemeter are taken before closing the shutter. While the picoamperemeter is read for 30 further background measurements, the measurements of the timing photodiode and the camera end and are saved, before the measures of the picoamperemeter follow. We therefore obtain a measurement of the picoampermeter with 150 samples, a measurement of the timing PD and a exposure of the Canon camera.

For the absolute normalization of the quantum efficiency a measurement with the 1 mm pinhole has been obtained, in which the camera was replaced by a photodiode(PD.3, originally placed between IS and mirror).

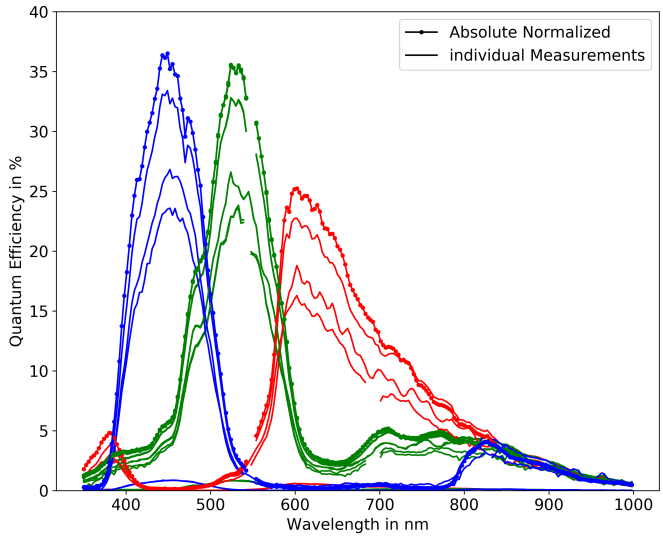

Figure E.2: Shown are the quantum efficiency curves measured with different configurations (with or without order sorting filters, different pinhole size and different alignment). The dotted dashed curve was measured with the 1 mm pinhole, for which the absolute normalization is possible.

Data Reduction

Exposure Time

The exposure time of the monochromator shutter is measured from the dataset obtained with the timing PD, which is read at a frequency of ≈1.1 kHz giving a time resolution of 0.9 ms. Given exposure times of the order of 30 s, the uncertainty on the timing is negligible.

The resistor of the transimpedance amplifier was selected such that the ADC was saturated whenever the shutter was opened. This corresponds to a signal level of 2.5 V, while the background signal is of the order 0.25 V. The first 5 s of the timing PD data is used to calculate an average background and its standard deviation. All data points which have a signal bigger than background plus three standard deviations are counted to be in the signal regions. The number of all signal data points times the mean time in between two measurements is the exposure time of the monochromator.

Flux Level

The flux level is measured with the picoamperemeter using the reference PDs 1 and 2. Based on the fixed number of pre-background, light and after-background measurements the data reduction calculates the mean values and standard error[1] within each of the three regions. The measured current is obtained by correcting the photo current for the background current, which

[1] standard deviation over square root of number of measurements

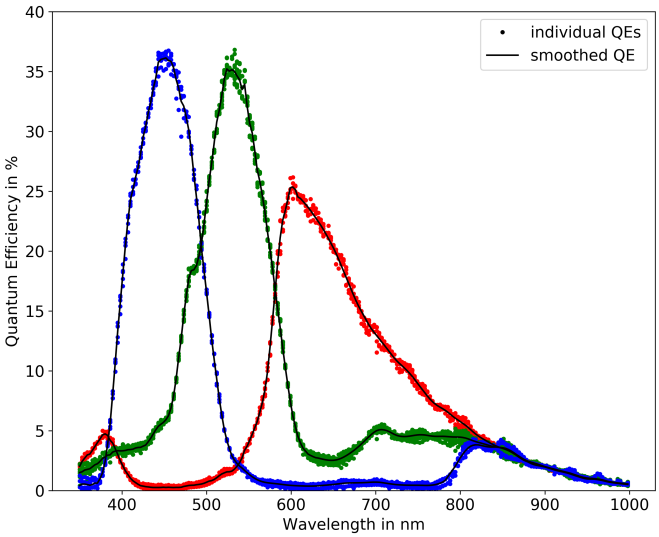

Figure E.3: Shown are the smoothed quantum efficiency curves for the EOS 1000D in each of the color filters (solid black). The measurements with different configurations are shown with dots after allowing for a absolute scaling factor.

is taken as the mean of the pre- and after-background. The number of registered electrons is obtained from the electron charge and the exposure time measured. Interesting for us is the number of photons which have illuminated the photodiode, therefore we need to divided the number of registered electrons by the quantum efficiency of the PD. We use the quantum efficiency of a PD different than the one used in the measurements but of the same type as the one used (S1337-1010BQ), which was calibrated by Hamamatsu, this introduces a relative error of less than 1.5 % as shown in section 5.2.

Number of detected Photons at the Canon EOS 1000D

The number of detected Photons is obtained from the raw images (`cr2-format`). For reading the images the `rawpy` module is used. The images are split into the over-scan region, from which the bias level can be measured, and the image area.

As we use a camera with micro color filters in front of the pixels we need to subdivide the image area for color. The micro filters are arranged in a Bayer pattern which is $\begin{bmatrix} r & g_0 \\ g_1 & b \end{bmatrix}$, therefore we obtain four images of 1301 x 1953 pixels in red (r), green0 g_0, green1 g_1 and blue b. Additional image information like date of exposure, exposure time and ISO are extracted from the `cr2-format` via `exifread`. As the pinhole camera does not move relative to the light source while changing wavelength, the region where we find the image of the IS opening in the data array will not move. Two different rectangular apertures have therefore been defined on the

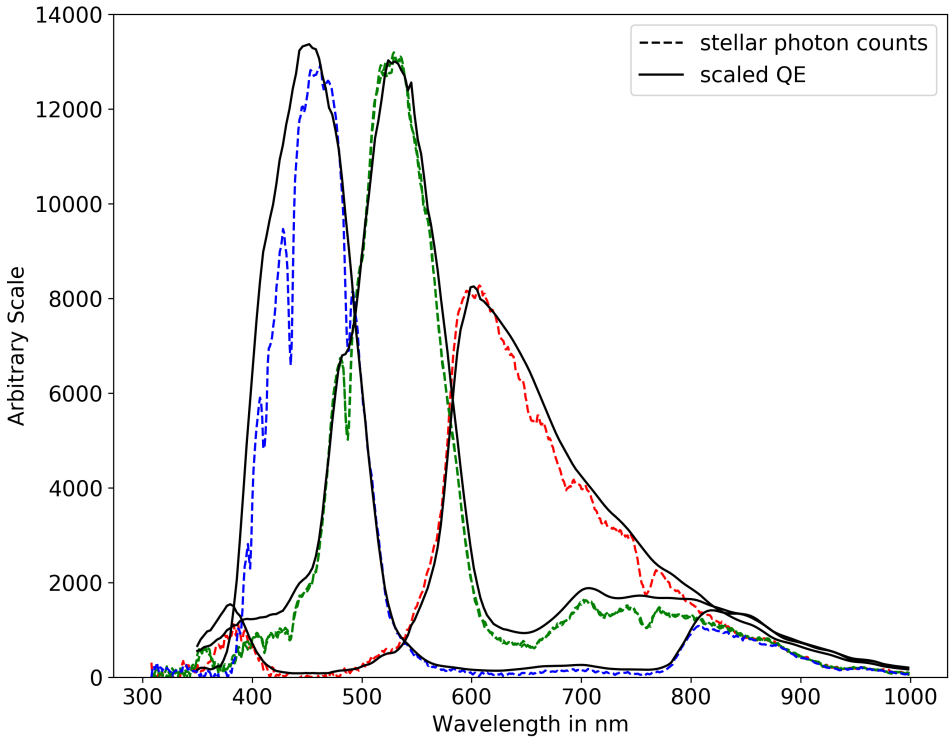

Figure E.4: Shown are the smoothed quantum efficiency curves for the EOS 1000D in each of the color filters in solid black with an arbitrary scaling. The dashed curves show the electron count level observed for a star of spectral type A2

dataset. In these regions we obtain the signal and the background with their standard errors.

The Quantum Efficiency of the EOS 1000D is given by:

$$QE = \frac{n_{\gamma,\mathrm{EOS}}}{n^0_{\mathrm{PD.2}}} \frac{n^1_{\mathrm{PD.2}}}{n_{\mathrm{PD.3}}} \tag{E.1}$$

with $n_{\gamma,\mathrm{EOS}}$ the number of photons detected / registered by the camera, $n^0_{\mathrm{PD.2}}$ the number of photons detected by the reference photodiode in the same time as the camera was illuminated, $n_{\mathrm{PD.3}}$ the number of photons illuminating the photodiode behind the pinhole, and $n^1_{\mathrm{PD.2}}$ the number of photons registered by the photodiode in the same time as the measurement behind the pinhole. The measurements of PD 2 are used for normalization, as the Xe-lamp light level is not stabilized in time. As we did not correct the camera data for hot or cold pixels nor flat fielded it, we use variations of the setup for consistency checks. These variations are:

- the diameter of the pinhole has been changed resulting in a change of count level by a factor ≈16 and a different distribution on the sensor - probe for a sensitivity on hot/cold pixels.
- Inclining the pinhole camera relative to the collimated beam, will move the image relative to the sensor - probe for sensitivity on flat fielding issues.
- not using the order sorting filters will result in second order light registered on PD and Canon EOS 1000D, as well as a change of possible out-of-band emission from the monochromator.

Fig. E.2 shows all obtained measurements. A difference in their overall normalization is visible but the QE-shape is the same. As the normalization is different between measurements and given the impossibility to repeat the absolute normalization measurement at the small pinhole (too low light level) as well as the usage of the QE of a different photodiode than the one used for the absolute normalization, the measured QE is precise to $\approx \pm 5\,\%$.

In red to IR wavelength range the QE measurement becomes bumpy, this is due to the emission lines in the Xenon spectrum and different detectors seeing slightly different wavelength bands. To correct for this one could use a tungsten lamp as light source, therefore avoid the Xe-emission lines or sample the measurements at a wavelength step much smaller than the FWHM of the monochromator. Afterwards one could adjust all measurements for a small wavelength shift before taking ratios. As no other lamp was available and the second approach is heavily time consuming, we decided to smooth the curves on scales of 33 nm, for wavelength longer than 540 nm in blue, for longer than 630 nm in green and longer then 610 nm in red. Smoothing the curves for shorter wavelength would have resulted in modifying the peaks of the throughput. The resulting curves are shown in fig. E.3 together with the raw measurements, where the uncertainty introduced by the Xe emission lines has been enhanced by introducing a wavelength shift to the linearly interpolated measurements prior to calculating the ratios.

Consistency

As the above calculation of the quantum efficiency depends on several assumptions and approximations (i.e. second order light, out-of-band emission of monochromator, normalization and

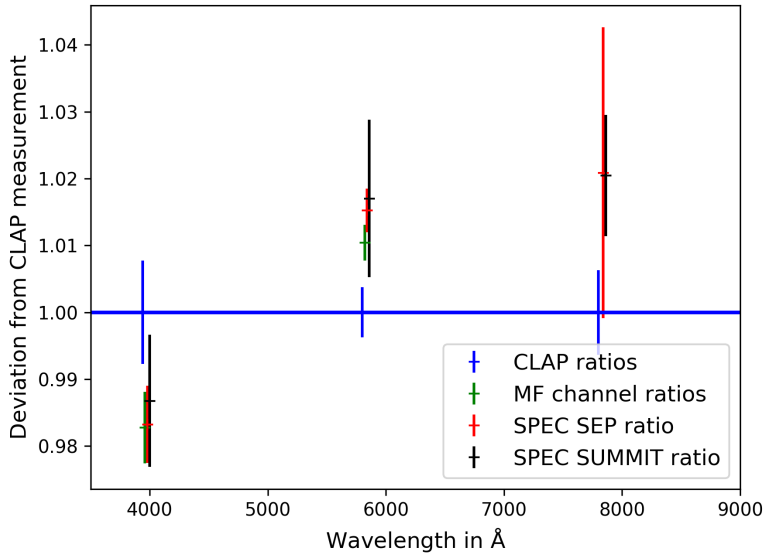

Figure E.5: relative difference between the attenuations for the different measurements referenced to the CLAP attenuation.

smoothing) we compare the measured QE with the spectra obtained at my Schmidt telescope equipped with an objective prism. Using this setup we have an independent measurement as the throughput of the telescope combined with a prism is smoothly varying in wavelength, therefore small scale structures in the observed spectrum need to be caused by the observed source or the color filters of the Canon camera.

A star of spectral class A2 was observed, such a spectral class was selected as the spectrum is smooth and the only absorption lines visible are from hydrogen. Therefore the observed spectrum has the same shape as the quantum efficiency of the used detector (except for narrow absorption lines and the absolute scale)

The measured QE was scaled to fit the measured spectrum in amplitude. The two curves are shown in fig. E.4. The spectrum of the star is not corrected for the earth atmosphere, therefore we expect the amplitude of the spectrum to be smaller than the QE curve for blue wavelength, as the throughput of the system is reduced due to Rayleigh scattering. For wavelength longer then 7000 Å, we see additional absorbing bands which are caused by O_2. Above 8000 Å we see the influence of water vapor on the spectrum. The throughput obtained in the laboratory is consistent with the shape of the observed spectrum as visible in fig. E.4. Deviations between the curves can be explained by absorption in the stellar and earth atmosphere.

Filter name	62073	62103	62120
Wavelength in Å	3940	5800	7800
Wavelength range Å	3850-4050	5700-5900	7680-7930
File names with Filter	17_101_010	17_101_012	17_101_014
Exposure time in s	180	45	180
File names without Filter	17_101_011	17_101_013	17_101_015
Exposure time in s	33	20	90
Throughput spec in %	30-40 %	57 %	55-60 %
Suppression factor	≈ 3	≈ 2	≈ 2
Measurements			
CLAP1	12.89±0.07	9.97±0.03	3.83±0.02
CLAP0	10.38±0.17	10.73±0.11	3.53±0.05
MF channel	12.7±0.2	10.0±1.3	1.2±0.3 not in filter band
SPEC SEP	12.67±0.03	10.12±0.02	3.91±0.08
SPEC SUMMIT	12.7±0.1	10.1±0.1	3.91±0.03

Table E.1: Summary of the bandpass filter test

E.3 Quantifying Out-of-Band Emission using Bandpass Filters

In the following a test on the amplitude of out-of-band emission is presented. Even if this test is inconclusive, it might serve as the basis for further tests and might help to improve them. An intuitive method to measure out-of-band emission from the monochromator is through the use of extra narrow band filters inserted into the beam (just in front of the fiber bundle). Three such filters, listed in tab. E.1, were send to UH88 for tests.

The SCALA monochromator wavelength was then set to the central wavelength of the bandpass filters. In this way the filters would suppress the out-of-band emission more, than the emission within the band, as the in-band throughput is between 30 % and 60 %, while the out-of-band suppression is greater than 10^3. As the throughput within the band of the filter is not 100 %, we observed simultaneously with SNIFS and the photodiode. In case there is no influence of out-of-band emission on the photodiode current, we should see the same suppression for SNIFS and the CLAP photodiode. On the other hand, if the filter is removing out-of-band emission, we should see a bigger suppression for CLAP than for SNIFS. Therefore the difference between the suppression factors is a measurement of the amount of out-of-band emission.

As the measurements require the presence of an engineer at the summit the measurements have to be performed during day time. The CLAP data are divided into signal and background (pre- and after signal) regions and σ-clipping is used to remove cosmics. The removed background is the mean of the pre- and after-background. To correct for the loss due to the finite throughput of the filters the exposure times are increased compared to normal operation. The results can be found in tab. E.1 (CLAP0/1) The setup was switched on well before the mea-

surements so that the lamp was stable and therefore no normalization based on CLAP0 was used.

The light emitted by SCALA was observed by SNIFS with the imaging channel using the multi filter array (MFA) and the spectroscopic channel. The SCALA light at 7800 Å can not be measured by the imaging channel, as its wavelength is in the rejection region of all filters of the multi filter array. The measurement at 3940 Å was taken first, the leakage of sunlight into the dome of the UH88 telescope is not detected. For the 5800 Å measurement we use the measurement performed at 7800 Å as a background model. We use one of the MFA filters to scale the signal amplitude in the 7800 Å background measurement to fit the background present in the 5800 Å measurement. As we did not obtain flat fields we take the ratio of the image (pixel-wise) without filter to with filter and then average over a region of 400x200 pixels. The ratios are listed as MF channel in the tab. E.1.

As the spectroscopic channel exposures do not contain multiple wavelengths, we have two possibilities to reduce the data. We can use the summit reduction and a manual reduction. Using the summit reduction we can correct for the sunlight leaking into the dome using the measurement at 7800 Å as a background model for the measurements at 3940 Å and 5800 Å. The measurement at 5800 Å is then used as background for the 7800 Å measurement. The background spectra are scaled to the measurements containing the SCALA bandpass in regions next to the bandpass and are subtracted from the measured spectrum. Afterwards we take the ratio of the spectra obtained without and with bandpass filter. The number listed as SPEC SUMMIT in the tab. E.1 is obtained as the mean of the spectral ratio in a region of 200 Å around the SCALA line.

We can also reduce the images without the summit data reduction pipeline. As the spectroscopic channel was illuminated by SCALA each spaxel trace on the CCD will look like an elliptical peak. Theses peaks can be localized by the SEP module in python. SEP[1] was also used to calculate a background which was subtracted from the image before summing the signal in rectangular apertures around the spaxel traces. The ratio is listed as SPEC SEP in the tab. E.1.

Fig. E.5 is showing the attenuations measured above relative to the attenuation measured by the CLAP photodiode. For the measurement at 3940 Å we see that the attenuation is larger for the CLAP than for the other detectors, while for the other measures it is the other way around. From this measurement we originally concluded that out-of-band emission is affecting our measurements at the percent level.

However, we figured out that this test is not representative. The filter will shadow the outer edges of the fiber bundle. Fig.4.8 is showing how the different arms of the fiber bundle are sampling the exit slit of the monochromator. Not illuminating the ends of the slit will result in changing the illumination strength of the arms relative to each other. As SNIFS is observing the light from all arms but CLAP is only observing one arm, the filters introduced to the system will change the scaling between the two kinds of detectors in a filter dependent way. This effect can be seen at two points in the table. First the reductions due to the filters are much higher than expected and additionally they are different from filter to filter. Second and more important the attenuations are different for the CLAPs.

[1] https://sep.readthedocs.io/en/v1.0.x/, last checked 04.07.2018

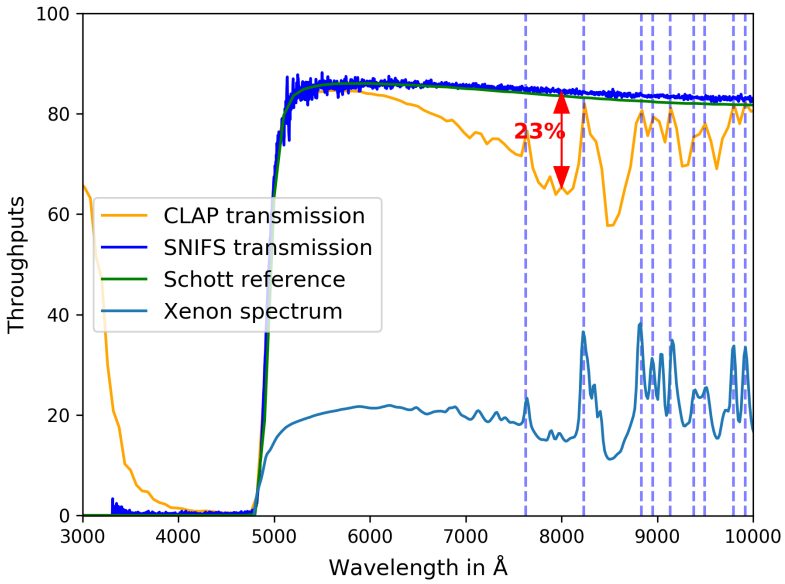

Figure E.6: Transmission of the GG495 order sorting filter as measured by SNIFS and CLAP, together with the normalized SCHOTT throughput. The blue dashed vertical lines indicate positions of the Xenon emission lines. For reference the scaled spectrum of the Xenon lamp is shown

For representative measurements, we should have switched off all modules of SCALA not equipped with a photodiode.

E.4 Measurement of the Out-of-Band Emission at 8000 Å

Our initial idea to measure the effect of out-of-band emission was to insert additional bandpass filters, and therefore increase the purity of the monochromatic light emitted from SCALA at the wavelength selected by the filters, see previous section. It took a while, till we realized that this measurement was inconclusive.

But we can use the second order sorting filter (GG495) to obtain a lower limit on the amount of out-of-band light[1]. When we insert the filter into the system, we remove light of wavelength shorter than the cut-on wavelength, therefore this light is not longer available for the production of out-of-band emission.

To obtain the amount of out-of-band emission we measure the throughput of this filter with SNIFS and the photodiode. Setting the monochromator to a wavelength of 0 Å, means that the not dispersed 0th order of diffraction is placed at the exit slit. In this way we can observe with SNIFS the full Xenon lamp spectrum, by placing a filter in the beam we can measure

[1]The order sorting filter is placed at the entrance of the monochromator and is offset of the slit. Compared to the filter close to the exit slit (made by fiber bundle) the order sorting filter does not change the throughput of the fiber bundle arms relative to each other.

the filter transmission curve through comparison with the original filter-less observation. The throughput of the monochromator and the other unchanged optical elements drops out.

We can also measure the spectrum of the lamp via the photodiode by stepping through the target wavelengths with the monochromator. Again we can calculate the transmission curve of the filter through repeating the measurement sequence with the filter in place.

In case the photodiode is seeing additional out-of-band light, the throughput measured by the photodiode will be smaller than the one measured with SNIFS. Introducing the filter does not only reduce the light level, due to the throughput of the filter, but also due to the removal of out-of-band emission from the monochromator visible for the photodiode. An obvious source of out-of-band light is second order throughput by the monochromator, as there is no way to remove this light without the order sorting filter.

Fig. E.6 shows the calculated throughput, measured with SNIFS and the photodiodes, also shown is the throughput as specified by the producer of the filter (SCHOTT). The reference transmission of the datasheet was scaled to fit the SNIFS measurement. This scaling accounts for dust accumulation and possible solarization (paper of SCHOTT, private communication) of the filter close to the Xenon lamp. We can see that the SNIFS measurement agrees with the filter curve from SCHOTT, which can be seen as a consistency check

The throughput measured with the photodiode differs from the SNIFS measurement. At the Xenon emission lines the contribution of second-order light is small, as the emission lines are stronger than the continuum at half the wavelength. The CLAP measurement thus approaches the SNIFS measurement. If we are now able to measure the contribution by second-order light the residual difference between SNIFS and CLAP throughput needs to be caused by out-of-band light. Unfortunately there are no emission lines in the Xenon spectrum at short wavelength, where the out-of-band emission is expected to be strong.

The filter throughput using CLAP is 65.3 % and using SNIFS 84.3 % at 8000 Å (see fig. E.6), so a difference of 23 %. We now use SNIFS to obtain a spectrum of the monochromator set to 8000 Å without the order sorting filter. We can then measure the amplitude of the first order light (8000 Å) and the second order light (4000 Å). Using the long time average throughput for SNIFS (see sec. D.5) and the quantum efficiency of the CLAP (see sec. 5.2), we can calculate the contribution by second order light to the signal. According to the measurement the second order is contributing 25.0 ± 2.0 % of the CLAP signal.Therefore the whole difference between the filter throughput measured by SNIFS and the photodiode can be explained by second order light. Out-of-band emission can not be detected within the uncertainties at 8000 Å.

E.5 Calibration of a Broadband Detector and Test using GD153

Calibration of the Detector

The imaging channel of SNIFS is equipped with a multi filter array: 6 optical bandpass filters placed next to each other. We obtain the throughput of the system from the comparison of the generated signal in SNIFS and the amount of light emitted from SCALA and measured with the CLAPs.

The calibration is performed in 50 Å steps between 3215 Å and 9907 Å. The exposure time used for each wavelength was the same as that used for the spectroscopic channel, as the spatial

elements of the two channels are of roughly of the same size.

The measurement was performed during night 145 in 2016, the effective number of beam is the same as shown in fig. 6.38. To use this N_{eff} we need to assume that SCALA is stable in throughput as this measurement was performed in night 159 of 2015, so roughly a year before. The number of photons emitted towards the telescope into a unit solid angle is:

$$N_{\gamma,\Omega} = \frac{I_{\text{corr}} N_{\text{eff}} A_{\text{beam}}}{A_{\text{PD}} \cdot g \cdot R \cdot \Omega_{\text{SCALA}} h\nu} \tag{E.2}$$

With I_{corr} the time integrated, background corrected signal of the CLAP1 photodiode, N_{eff} the effective number of beams (sec. 6.3), A_{beam} the area of one of the SCALA beams, A_{PD} the area of the photodiode sensitive surface, R the responsivity (sec. 5.2) of the photodiode, Ω_{SCALA} the solid angle illuminated by SCALA and $h\nu$ the energy of a photon.

The exposures of the imaging channel have been binned in cells of 80 x 80 pixels. The throughput of the filter is measured by extracting the mean pixel value in one of these cells close to the center of the filter. The edges have been avoided to reduce backgrounds from reflections between filter and CCD[1]. The mean number of electrons per pixel C_{Pixel} is scaled by the solid angle of the pixel $\Omega_{\text{Pixel}} = 4.65 \cdot 10^{-13}$ sr. The throughput τ_{MF} is therefore:

$$\tau_{\text{MF}} = \frac{C_{\text{Pixel}}}{N_{\gamma,\Omega} \Omega_{\text{Pixel}}} \tag{E.3}$$

and shown in fig. E.7. The uncertainties[2] on τ_{MF} are small and are shown in fig. E.8. We have here assumed that the artificial planet is homogeneously illuminated (we scale for the ratios of the solid angles) and that the mirror is homogeneously illuminated (scale for the area ratio). Both assumptions have been tested ([Lombardo, 2017], [Küsters, 2014]). The transmission curves of the filters have been measured by the manufacturer. Multiplying these curves with the reflectivity of the mirror to the power of three (three mirror telescope), the quantum efficiency of the CCD and the transmission of the window of SNIFS, we obtain the theoretical throughput for the imaging channel which is shown for each filter in fig. 4.3.

As shown in sec. 6.4, SCALA is only able to measure the throughput within the passband, but not the out-of-band rejection, due to out-of-band emission from the monochromator. The measured throughputs within the passband are smaller than the theoretical expectation, except for the F3 filter. An explanation for lower throughput of the filters could be aging or dust accumulated in the optical system. Looking at fig. E.8 we see that the limiting uncertainty is given by the reflections within SCALA, so the internal backgrounds, followed by the uncertainty on the effective number of beams and the uncertainties in our flux reference (response of

[1] The filters used in the multi filter array are interference filters, therefore they are reflective at all wavelengths outside of their transmission band. When light passes through one of the filters it will be partially reflected off the CCD (reflectivity ≈ 1 - quantum efficiency), and propagate towards the filter array again. At the edges of the filters reflected light reaches the neighboring filters, which are reflectors for the light, which passed through another filter. The light will then propagate back to the CCD and bounces between filter and CCD. By the selection close to the center of the filter this disturbance will be reduced as multiple reflections are needed.

[2] Uncertainty from SCALA including internal backgrounds, the uncertainty on N_{eff}, the photodiode response, the external backgrounds and the statistical uncertainties on C_{Pixel}

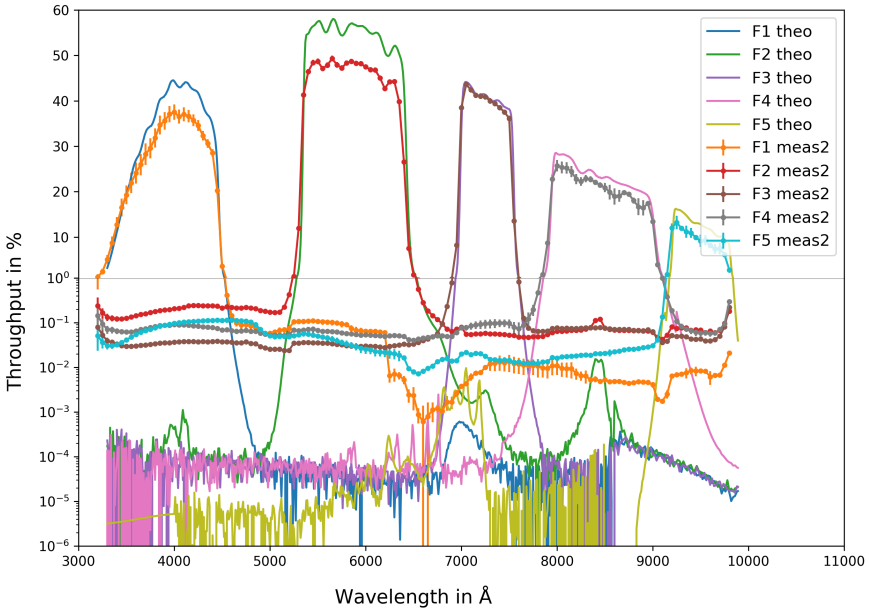

Figure E.7: Throughput of the system UH88 + multifilter array + imaging channel as measured by SCALA. To show the features of the transmission band together with the rejection, the figure is split at 1 % throughput. For throughputs larger then 1 % the y-scale is linear, while for lower values it is logarithmic. Shown are the theoretical expectations together with the measured throughputs.

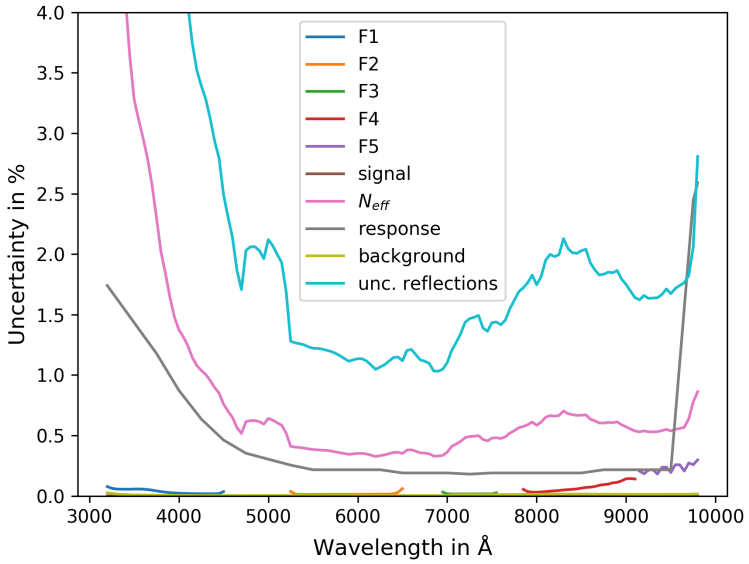

Figure E.8: Uncertainties for the calculated throughput in fig. E.7

photodiode and its aging).

Test of the obtained Calibration

We selected GD71, a white dwarf standard star and a primary standard of the CALSPEC system, for observation. The spectrum of the star is known and we have measured the throughput of the observing system. We can therefore calculate the amount of photons we should see at the detector, after correcting for the atmospheric throughput.

From sec. 6.4 we know that the out-of-band rejection of the filters in the multi-filter array is higher than measured due to out-of-band emission from the monochromator. We use two different approaches to correct our measured system throughput. In the first we use the theoretical curve and scale it to fit the measured passband throughput (scaling factors are listed in tab. E.2). In the second approach we set all measured throughputs smaller then 0.5 % to a value of 10^{-4}. We use this approach as the width of the measured passband is in some cases different from the manufacturer value (see e.g. fig. 6.20).

The last component that needs to be included is the atmospheric attenuation.

Atmospheric Throughput

The dominant contribution of the atmospheric absorption is Rayleigh scattering. As shown in sec. C.2.2 the strength can be determined from the measured / monitored local pressure. For the other components we took average values. The atmospheric throughput used is shown in fig. E.9 with the following parameters:

- atmosphere pressure 616.75 mbar

Name	λ_c	λ_{low}	λ_{high}	s_{λ_c}
F1	4070	3530	4470	0.858
F2	5910	5330	6420	0.854
F3	7270	6990	7540	1.0
F4	8500	7920	9050	0.874
F5	9510	9190	9800	0.743

Table E.2: Scaling factors between theoretical and measured throughput.

- Ozone intensity 273.6 DU[1]
- Aerosol wavelength $\lambda_A = 1\,\mu$m
- Aerosol optical thickness at λ_A: $9.1 \cdot 10^{-3}$
- Angström index: 1.125

To measure water vapor absorption we use the SNIFS spectroscopic channels and observations before and after the broadband observations. Both spectra after summit flux calibration are shown in fig. E.10 together with the CALSPEC spectrum of GD71. The observations have been performed in 2017, therefore no final calibration of the files is available. The summit reduction pipeline is an old version of the final reduction pipeline, and applies a average flux solution including Rayleigh & aerosol scattering as well as Ozone absorption. It will therefore not correct for water vapor or line absorption by oxygen or nitrogen. The deviation of summit flux calibrated spectra to the CALSPEC one at small wavelength scales can be used to measure the water vapor absorption. However, as visible from fig. E.10 the summit reduced spectrum deviates in a broad wavelength range. The deviation in fig. E.11 can be approximated by a power law. After application of this power law correction, the relative difference to the CALSPEC spectrum was taken as a measure of the atmospheric throughput. The result shown in fig. E.12 indicates that this approach removes more than the water vapor absorption band, as the narrow absorption at 7600 Å is not caused by water but by O_2.

The python module `Py6S`[2], a wrapper to the Second Simulation of the Satellite Signal in the Solar Spectrum (6S), is atmospheric Radiative Transfer Model. We used it to calculate the extinction of a model earth atmosphere. The configuration is a Mid Latitude Summer atmosphere with a sensor altitude of 0.267 km and a water concentration of $3\,\text{g/cm}^2$. The resolution is set to 20 Å. The model is able to describe the measured attenuation due to water. At the O_2 bands the amplitude of the attenuation obtained by the model is too small compared to the observation and is therefore scaled to match the observation. By the usage of the model we suppress the noise in the dataset and reduce therefore the overall attenuation. In the comparison of the expected to observed number of electrons on the CCD we will take into account three different corrections for the water vapor, namely: no correction, raw attenuation, modeled attenuation. The difference between the results might then be seen as an approximation to the uncertainties of the atmosphere.

[1] 300 DU corresponds to a pure Ozone layer of 3 mm thickness, under standard temperature and pressure, 300 DU is a typical value for the earth atmosphere

[2] https://py6s.readthedocs.io/en/latest/, last checked 11.07.2018

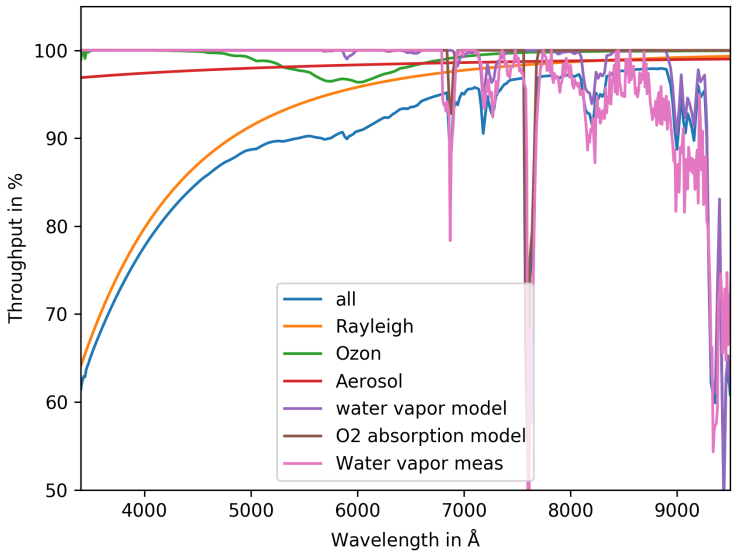

Figure E.9: Transmission of the atmosphere and its contributing components, Rayleigh Scattering, Ozone absorption bands and aerosol scattering.

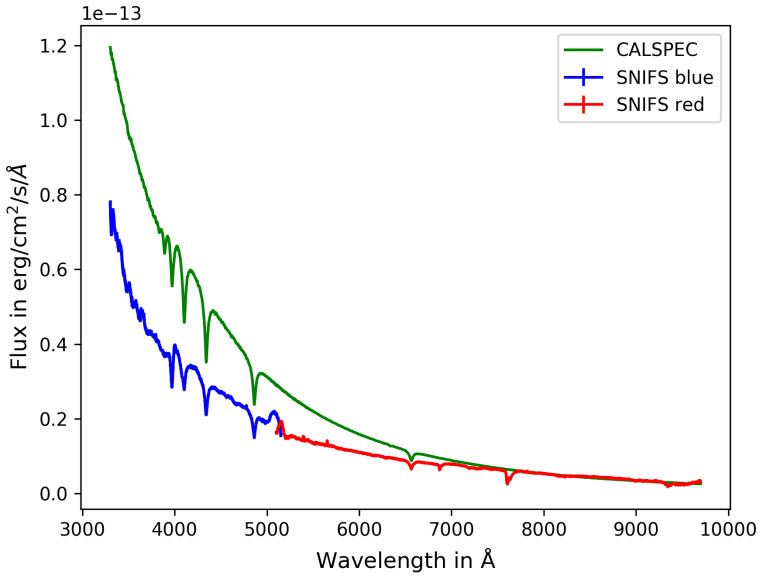

Figure E.10: Spectrum of GD71 obtained with SNIFS in blue and red channel (colors blue and red respectively) after summit flux calibration, together with the reference spectrum for GD71 from CALSPEC http://www.stsci.edu/hst/observatory/crds/calspec.html, last checked 14.09.2017.

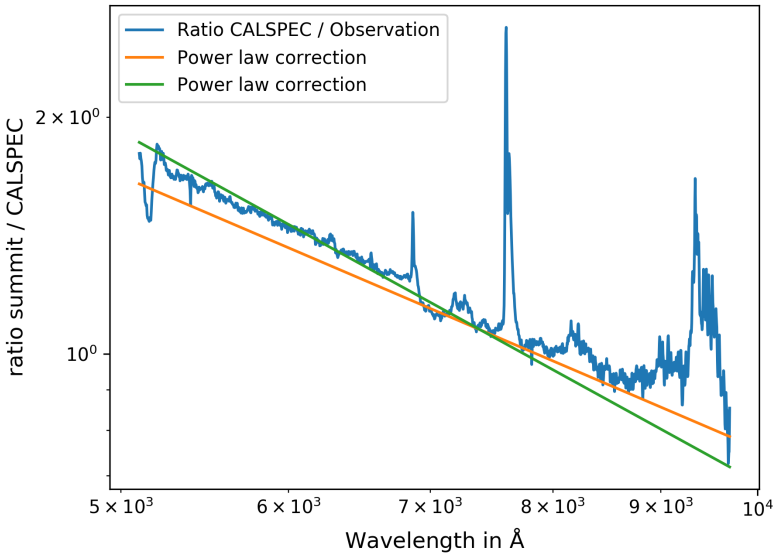

Figure E.11: Log-log plot of ratio of observed flux to CALSPEC flux against wavelength for the red channel of SNIFS, together with a power law long-wavelength-scale correction.

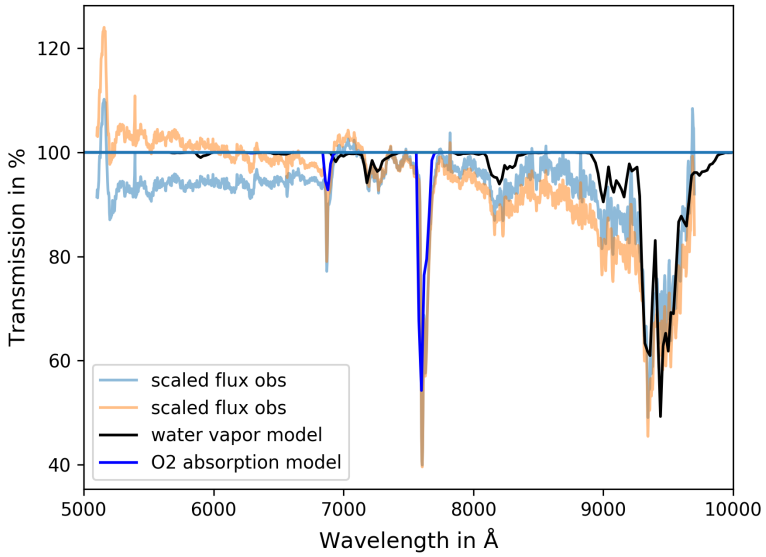

Figure E.12: Absorption estimate based on the relative difference between corrected summit flux calibration and CALSPEC flux. Also shown is the calculation using the `Py6S` radiative transfer model.

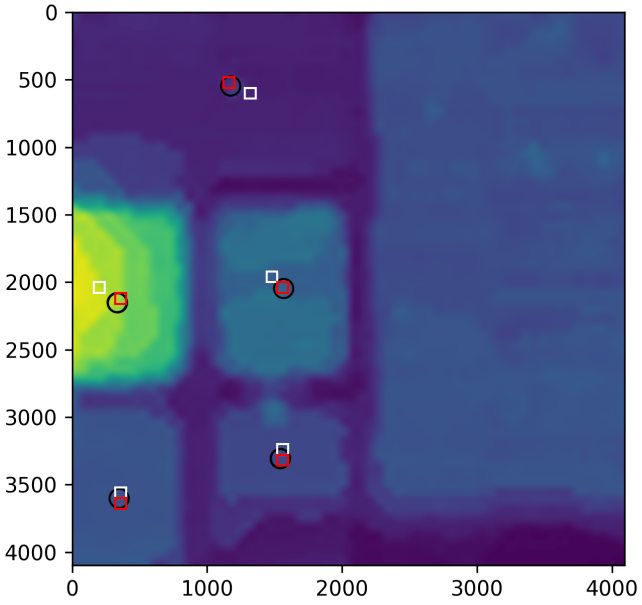

Figure E.13: Sky background of one of the star measurements with the positions of the stars (circles) and squares where the filter throughput has been measured.

Comparison of the Calibrations

We can now use the spectrum of GD71, the throughput of the atmosphere, the modeled throughput of the imaging channel, and the collecting area of the telescope to estimate the number of electrons detected on the CCD per unit time.

Using aperture photometry at a radius of 20" we obtain the observed signal currents. Figure E.13 shows the sky background as estimated by Source Extractor for Python (SEP)[1] together with circles indicating the positions were GD71 has been measured. The squares (80 x 80 pixels) show the regions where the filter throughput has been measured. The difference between throughputs measured at two different regions in the same filter are used as error estimate in fig. E.7.

Fig. E.14 shows the ratio of estimated to measured signal current in the imaging channel, which is the same as the ratio of CALSPEC flux calibration to the flux calibration of SCALA. The results for the imaging channel are shown with dots and triangles and the result for the spectroscopic channel is shown with the red band. The triangles result from the estimates based on the measured throughput, which was set to 0.02 % outside the filter passband. The dots are resulting from the estimate based on the scaled theoretical curves. The difference between the two is a representation of systematic uncertainties. For the filters F4 and F5 two observations

[1] https://sep.readthedocs.io/en/v1.0.x/, last checked 11.07.2018

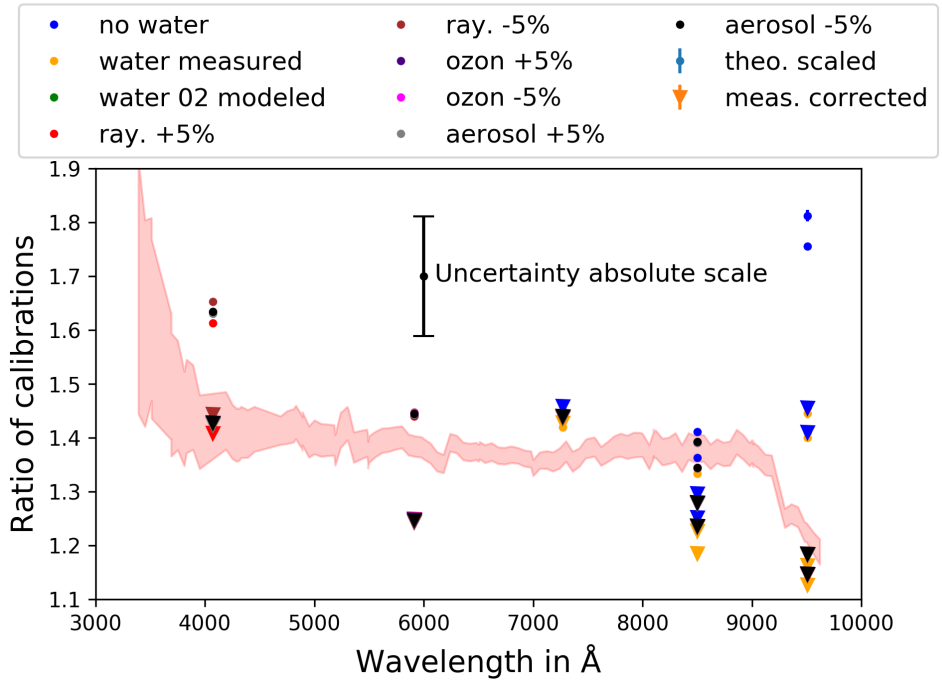

Figure E.14: Comparison of the ratio of calibrations using CALSPEC and SCALA. Shown are the spectroscopic channels as a band and the imaging channel values at the center wavelength of the used filter band.

have been performed. The results from these two measurements (at ≈8500 Åand at ≈9500 Å) do not agree within the error bars. The change in airmass during the observation is from 1.007 to 1.025 and was taken into account in the atmospheric throughput. The exposures show that fringing in the F4 and F5 filter is affecting the measurements. Unfortunately not enough pointings are available to calculate a correction. Therefore we expect a difference between the repeated exposures.

To estimate the uncertainty introduced by the model of the atmosphere we calculated the estimated signal current with scattering coefficients varied by 5 %. We see that the first measurement at 4070 Å is only sensitive to Rayleigh scattering. Changing the ozone or aerosol strength is not able to to affect the results in noticeable way. The measurements at 7270 Å, 8500 Å and 9510 Å are only sensitive to the used water and oxygen model.

For the imaging channel we also have to account for the fact that the filter throughputs have been measured in night 145 of 2016, while the observation of GD71 took place in night 23 of 2017. Additionally we know that SCALA is not able to calibrate the whole entrance pupil. The observation of GD71 was performed without entrance pupil mask. In my master thesis a measurement with an array of pinholes was used to estimate the difference in average throughput on the whole pupil relative to the area calibrated by SCALA. This study showed that the difference can be up to 8 % in the blue (≈ 4000 Å to ≈ 5000 Å). An extension to longer wavelength was not possible as the pinhole grid used for the pupil measurements is mounted to a blue filter.

Taking into account all the above issues (reflections between CCD and Filter, fringing, scale factors, aging, sampling of pupil) we see the same ratio of calibration as in the spectroscopic channel. The absolute scale difference between SCALA and CALSPEC seems to be in a range from 1.3 to 1.6, with large uncertainties on this test.

To address these issues, more measurements are needed to improve the constraints on the calibration of broadband photometry. It is necessary to reduce the out-of-band emission, which made the modeling of the filter throughput necessary. It would also be useful to perform the test with filters covering the whole CCD. A combination of spectroscopic and broadband photometric observations could allow a better modeling of the absorption due to water vapor and oxygen. Repeated observations would allow a better estimate on the uncertainties as well as a removal of the fringing in IR filters. Obviously the time delay between calibration and observation should be reduced and the entrance pupil mask should be used.

The study presented in this chapter shows that it is possible to use SCALA for the calibration of a broadband photometer. More precise results can be obtained, once the above mentioned issues are addressed.

Appendix F

Differences between SCALA and Stars

Illuminating just a fraction of the telescope entrance pupil will introduce systematic differences to the usual operation. This section will describe these systematics and will motivate the use of an entrance pupil mask to reduce or remove possible biases, which are otherwise hard to evaluate.

On the other hand, the entrance pupil mask will cause new systematics, which are also discussed. An essential ingredient for the following section are the geometrical properties of the telescope listed in tab. F.1.

d_{tel}	Telescope entrance pupil diameter = Outer diameter of primary mirror: 2.2 m
d_{sec}	Diameter of secondary mirror: 65 cm
d_{obs}	Diameter of baffle around secondary: 86 cm
w_{vane}	Width of the sider vane: 8 mm Support structure for secondary mirror
f_{tel}	Focal length of telescope: 22.5 m
l_{baf}	Primary mirror light baffle, length: 245 cm
l_{baf}	Primary mirror light baffle, diameter: 52 cm
s_{pix}	Pixel size: 15 μm
$d_{\text{SCALA Beam}}$	Diameter of the SCALA mirrors = Diameter of the SCALA beams: 20 cm
$d_{\text{mask beam}}$	Diameter of the apertures in the entrance pupil mask: 16 cm
$d_{\text{FoV @ } f_{\text{tel}}}$	Size of the field of View of SNIFS in the focal plane of the UH88: 0.7 mm

Table F.1: Geometrical properties of the UH88, SNIFS and SCALA

F.1 Cross Dispersion Profile

The cross dispersion profile is the profile of the spectral traces on the CCD detectors of the spectroscopic channel. The image provided by the telescope is enlarged (by a factor $e_{\text{f}} = 32$)

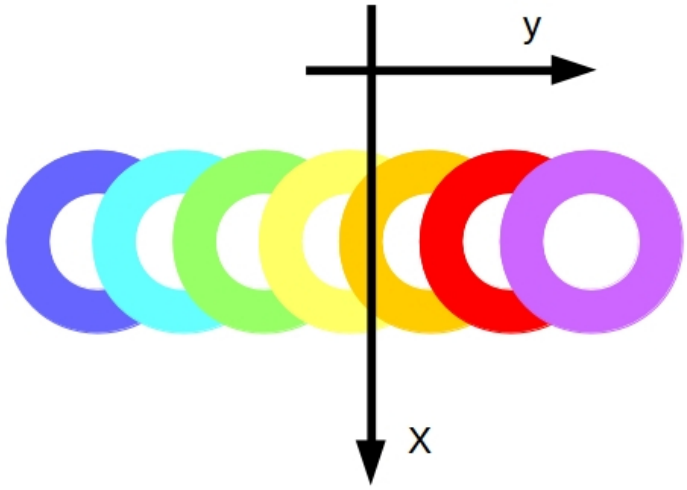

Figure F.1: Each color represents a monochromatic image of the entrance pupil provided by one of the microlenses. Due to the spectrograph, the monochromatic images are shifted relative to each other. The spectral dispersion is therefore parallel to y while a cut in x direction represents the cross dispersion profile.

and projected onto the MicroLens Array (MLA) with 15 x 15 lenses on an area of 21 x 21 mm (lens pitch 1.4 mm). Each of the lenses of the MLA acts as a field lens, creating an image of the entrance pupil of the telescope. To estimate the size of the image produced by the field lens, we use geometric optics. The entrance pupil (our object) is placed at the effective focal length of the telescope and the enlarger: $f_{\mathrm{eff}} = f_{\mathrm{tel}} \cdot e_{\mathrm{f}} = 720\,\mathrm{m}$. The focal length of the individual micro lens is $f_{\mathrm{MLA}} = 6.67\,\mathrm{mm}$. We can therefore assume the object is infinitely far away ($10^5 \cdot f_{\mathrm{MLA}}$), forming the image at a distance equal to f_{MLA}. An object of size $d_{\mathrm{tel}} = 2.2\,\mathrm{m}$ will produce an image of size 20.3μm. All light illuminating a microlens will be directed into one image of the entrance pupil of 20.3 μm size. Therefore the image provided by the telescope will be split by the MLA into 15 x 15 images of the entrance pupil, each with a diameter of 20.3μm, while spaced by 1.4 mm

These images are now used as entrance slits for the spectrograph. This spectrograph is separating the individual pupil images by wavelength, as shown in fig. F.1. Each spectral trace on the CCD detector can be understood as a superposition of entrance pupil images (produced by the same micro lens), shifted relative to each other due to the wavelength dependent composition of the light. The cross dispersion profile is the cut profile orthogonal to the dispersion direction, x-axis in fig. F.1. In case of a wavelength independent spectrum this profile can then be described by the summation of the entrance pupil illumination in one direction (see fig. F.2).

This means that SCALA, which is illuminating only a small fraction (10 %) of the entrance pupil, should produce a different cross-dispersion profile than a star illuminating the whole telescope pupil homogeneously, see fig. F.2. As the same data reduction pipeline is used both,

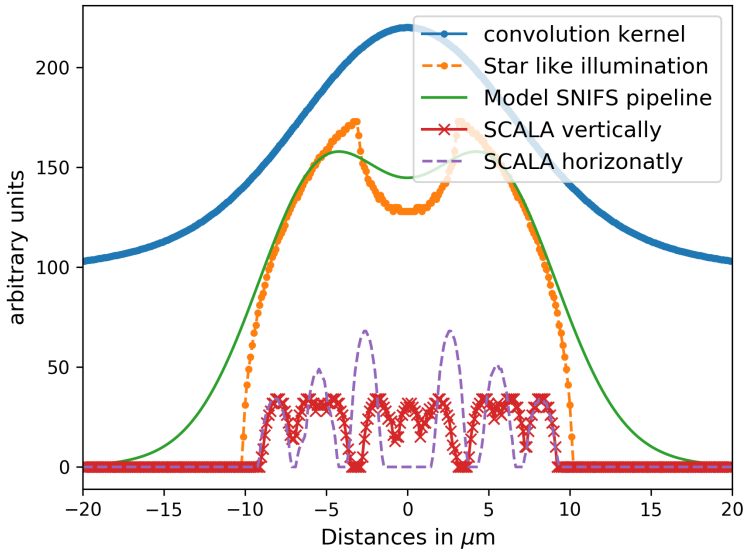

Figure F.2: Cross-dispersion profiles for different entrance pupil illuminations, prior to convolution by the microlense resolution. The orange curve shows the summation over an annulus, which represents the homogeneous illumination of the entrance pupil by a star. In green we see the model of the orange curve used in the SNIFS data reduction pipeline. Red and purple curves show the summed illumination caused by SCALA. The profiles are different as SCALA has a hexagonal structure. The blue curve represents the resolution of the microlenses and is scaled by x110 for better visibility. This curve will be convolved with the others to describe the signal on the detector.

for SCALA and for stars, a wavelength dependent difference in the cross dispersion profile would result in a systematic bias of the extracted flux.

Fortunately there are physical limitations which reduce this difference. First, the resolution of the microlenses is finite. The resolution kernel can be described by two concentric Gaussians, one with a width of 70 cm and a second with a width of 5.6 m and 1.4 % of the amplitude of the first. Second, we are usually observing star-like objects, which are always infinitely far away (compared to the telescope focal length). Such sources illuminate the entrance pupil homogeneously and no information can be obtained by sampling the cross dispersion profile on many pixels. The core (20μm) of the cross dispersion profile is sampled by only 3 pixels. Small scale differences are therefore washed away.

Based on these limitations we can calculate the shape of the SCALA and star cross dispersion profiles. The results are shown in fig. F.2.

For a star-like source, the illumination of the pupil can be described by an annulus with a outer diameter of 2.2 m and a inner diameter of 65.8 cm. As described before the cross-dispersion profile is the cut profile of a continuous source, and can thus be obtained by summing the two dimensional pupil image in one direction. The result is shown in the orange dotted curve in figure F.2. In case of SCALA we have to take into account the hexagonal pattern of the 18 SCALA beams (see fig. 6.15 for reference). We calculate the pattern for two different orientations of SCALA, equivalent to summing in the vertical and in the horizontal direction (see red-cross and purple-dashed curves in fig. F.2, respectively). Shown as green curve is the model used in the data reduction pipeline to describe the summed annulus[1]. This model consists of three Gaussians: a central with a width of 70 cm and two ones shifted by 63 cm from the center with a width of 30 cm and a ampitude of 119.1 % of the first component. All spatial dimensions are given in the dimensions, they would have, if they would be placed in the entrance pupil. The absolute height of the curves is arbitrary as we are only interested in a bias introduced by a change of the shape.

While these profiles are quite different, the low resolution of the microlenses (shown by the blue curve in fig. F.2) makes the profiles more similar, as shown in figure F.3. All curves do overlap and are not differentiable by eye.

To enhance the differences between them we binned them to a scale of 6.6μm per bin (3 pixels per 20μm), and we calculated the relative difference[2] of the SCALA to a star profile. The result is shown in fig. F.3. We find that the core of the SCALA cross dispersion profile is dimmer than the one of a star, while it is brighter for larger diameters compared to a star[3].

Shown in green in fig. F.3 is the deviation between the model used by the pipeline (sum of three Gaussians) and the one assuming a homogeneously illuminated pupil (summed annulus). No differences are visible as the model is adjusted to describe the profile.

Based on these calculations we do not expect systematic biases introduced by the different illumination of SCALA compared to a star at the percent level. A wavelength dependence is not expected as the optics of SCALA uses integrating spheres and mirrors and therefore the

[1] From a discussion with Yannick Copin.

[2] Difference between SCALA and star profile divided by star profile

[3] In fig.F.2 we see that the SCALA profiles are flatter / less peaked than the model or the summed annulus representing a star. The SCALA curves will therefore lack intensity in the center, but being brighter in the wings.

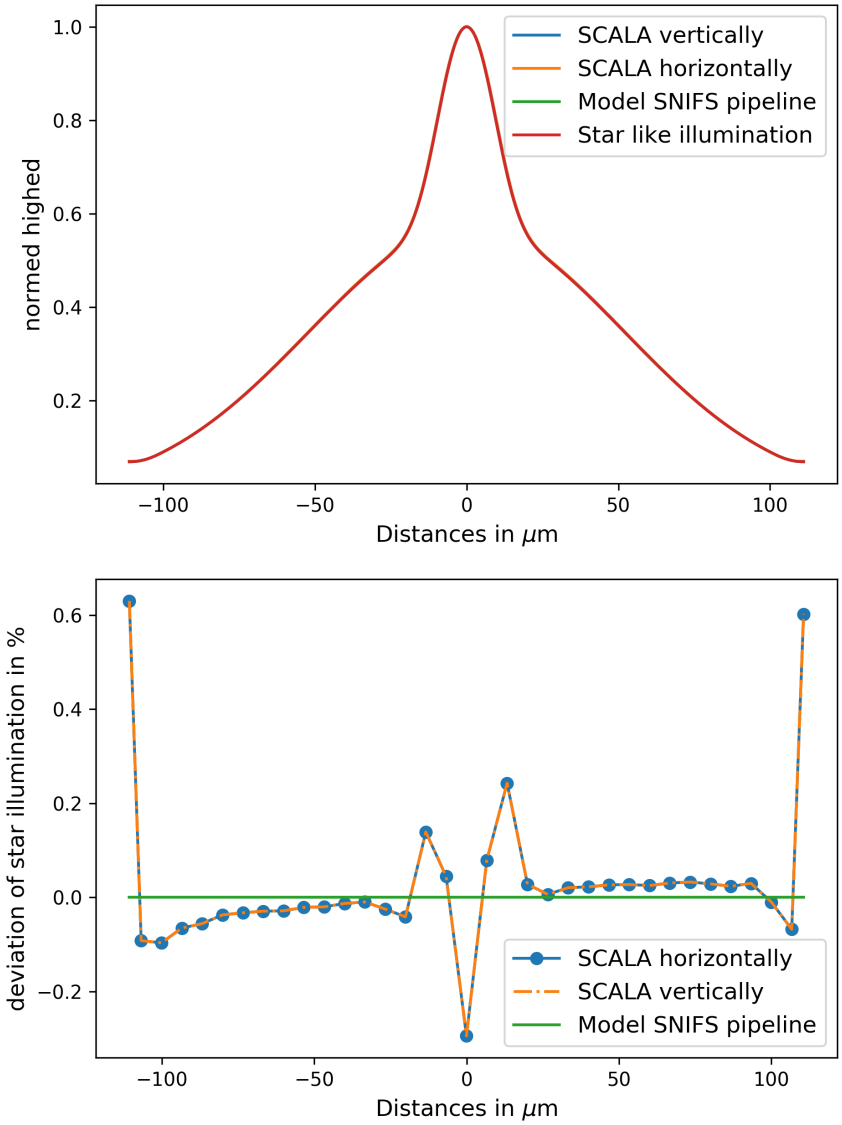

Figure F.3: The upper panel shows the convolution of the curves of fig. F.2 with the resolution of the microlenses. The curves of fig. F.2 differentiate at scales smaller than the convolution kernel. Therefore they are nearly identical after convolution and normalization. The lower panel therefore shows the relative difference between the binned cross dispersion profile of SCALA and the binned profile of a star. The ratio shows that the width of the two profiles is slightly different and there is a small offset between the curves introducing the slope from left to right in the wings of the profile.

sampling of the entrance pupil will not change with wavelength. After our observations in 2015, we had the data to check for biases introduced by the change of the cross dispersion profile. Results are shown in ([Lombardo, 2017] fig 10.3.1: Extraction window for SNIFS data), no difference between star like and SCALA source was detected at the 1 % level.

Using the entrance pupil mask, like in night 159 of 2015, will result in a occultation of all area not illuminated / calibrated by SCALA. Therefore the mask will introduce the same systematics to a star, as we experience in SCALA. As the systematics is the same, it will cancel in the comparison of our calibration to the one with standard stars.

F.2 Flat-Field Imprint from Dust

A isotropic emitter, a source shining in all directions, will homogeneously illuminate the focal plane of the telescope (neglecting stray light and ghosts in the telescope), as it provides a mapping from angular distribution to a spatial distribution. If dust is placed in the optical chain, e.g. on optical bandpass filters, it will result in imprints in the throughput. The telescope will be less transmitting to special directions, determined by the position of the dust relative to the optical axis and the distance to the focal plane.

The creation of the dust imprint on the throughput of a telescope can be visualized with the following example. Imagine we are observing a point source and have a dust grain which can be moved in a plane, orthogonal to the optical axis, across the beam[1], see fig. F.4. The dust grain moving into the beam will start to shadow parts of the beam and reduce the sensitivity of the detector. If the dust grain is fully within the beam, the amount of shadowing depends only on the grain size. Moving the grain further, the signal at the detector will increase again as the grain is entering the shadow of the central obscuration.

We see that the throughput of the telescope to a selected direction depends on the dust size and position in the beam. Now we apply the result of fig. F.4 to a fixed grain and an isotropic source. The source can be decomposed into point sources with different directions to the optical axis of the telescope. We see that the dust grain has different positions with respect to the individual entering beam, while moving from one to the next pixel on the detector (moving form one point source to the neighbor in the entrance illumination). We therefore observe the above pattern in dependence of the pixel position and not anymore in dependence of the grain position. The result on the CCD is a negative image (removal of light from the beam due to the dust) of the entrance pupil illumination added to the homogeneous illumination caused by the isotropic emitter. The size of the pattern in the negative image just depends on the distance of the dust grain from the detector, while the intensity / depth of the negative image is dependent on the grain size.

We have to take this fact into account when working with SCALA, as it illuminates only parts of the entrance pupil and therefore the negative image imprinted on the sensitivity will change compared to a star.

Fig.F.5 shows a flat field (sensitivity map) obtained looking at SCALA. We see the hexagonal arrangement of the 18 beams of SCALA for each dust grain in the beam. If the entrance pupil

[1] We assume a Cassegrain like telescope, a telescope with a central obscuration in the entrance pupil

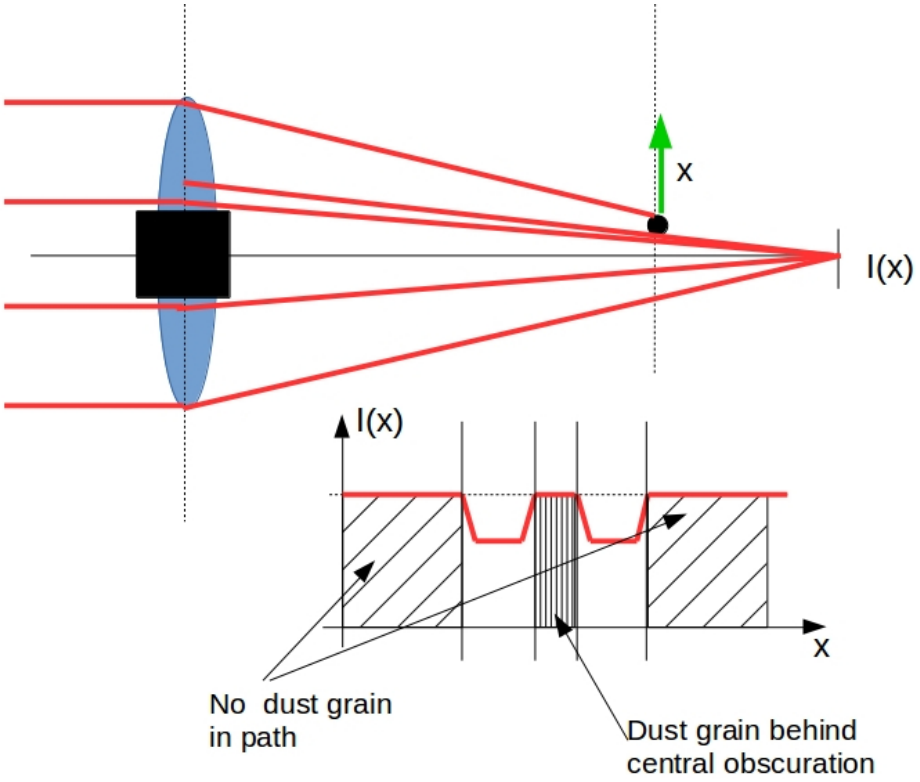

Figure F.4: To visualize the effect of a dust grain in the optics on the telescope directional sensitivity one can imagine a telescope looking at a star-like source. The dust grain is placed in the optical chain on a surface in front of the detector. The dust grain can be moved in x direction. Depending on its x position it blocks more or less light, resulting in the curve sketched in the bottom panel. The depth of the shadow introduced by the dust grain depends on its size, while the size of the imprint in the throughput depends on the distance of the dust grain from the detector.

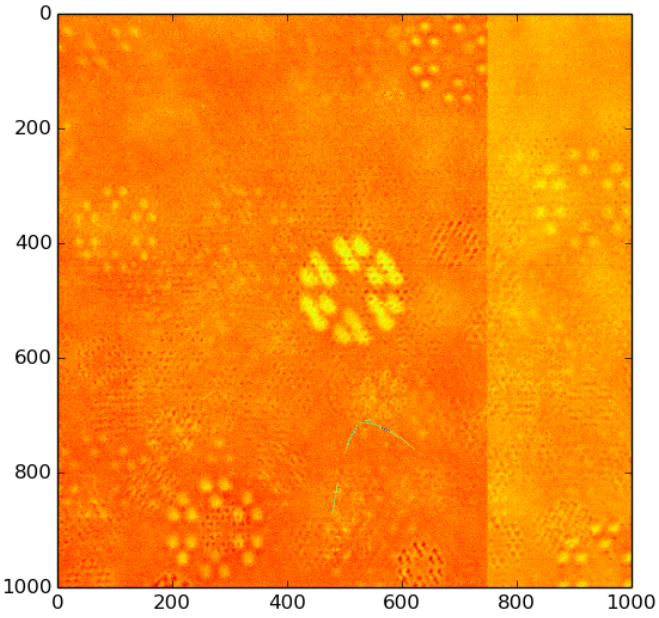

Figure F.5: We see a flat field obtained by illuminating the UH88 via SCALA and white light. As the entrance pupil is only illuminated by the beams we see the hexagonal pattern of the 18 SCALA beams, see fig. 6.15 for reference.

were illuminated homogeneously we would not see a group of 18 beams, but an annulus like shape. In case we do not use the entrance pupil mask our SCALA calibration would measure the directional sensitivity as shown in fig. F.5, while the calibration using standard stars would measure a directional sensitivity containing annuli. As the field of view of the spectrograph is tiny we are not able to distinguish, where in the pattern our source is placed. The observed star might be in the annulus, while in the calibration with SCALA we do not have an annulus. By the introduction of an entrance pupil mask, we introduce the same systematic differences to star like illumination as if we are observing with SCALA. To ensure that the SCALA beams are also cut, the holes (16 cm diameter) in the mask are smaller than the SCALA beams (20 cm diameter).

F.3 Point Spread Function of UH88 with Mask

The previous sections have motivated the use of an entrance pupil mask, as it will result in the same systematics for SCALA and regular observations of stars. As described in sec. C.3.2 and calculated in sec. C.5, a change of the entrance pupil illumination will result in a change of the point spread function (PSF) in the focal plane. As a model is fitted to the data to extract the signal of the star from the SNIFS datacube, we have to check that the extraction code can handle the introduced systematic effects. Therefore we will obtain the PSF of the UH88 with and without the mask, based on diffraction. Afterwards we apply wavelength-dependent seeing to our model. To check the data extraction from the data cubes we compare instrumental throughputs obtained with and without mask.

Sec. C.3.2 showed that the PSF of the telescope can be written as the modulus value squared of the Fourier transform of the entrance pupil illumination. In case of a Cassegrain telescope the entrance pupil can be described by an annulus, with the outer diameter being the outer dimension of the primary mirror (2.2 m) and the inner diameter being the housing / baffle around the secondary mirror (65.8 / 85.6 cm). This annulus is then split by the construction supporting the secondary mirror, which can be represented by rectangles of 8 mm width. The whole illumination pattern can be described by the superposition of two disks (D_1, D_2) for the annulus and four rectangles (R_{1-4}) for the support structure. Using the linearity of the Fourier transform and the fact that the Fourier transform of a disk and a rectangle are analytically known, we can evaluate the PSF analytically[1]. We calculate the PSF analytically for a set of wavelengths in the range from 3200 Å to 9500 Å. The result of the calculation is shown in fig. F.6, the left side shows the two dimensional distribution, while the right side shows a cut to visualize the amplitudes.

For SCALA we apply an entrance pupil mask to the telescope. The entrance pupil illumination can be described as the superposition of 18 disks of 16 cm diameter arranged in the grid, as shown in figure 6.15. A translation in the space domain is equivalent to a phase-shift in the Fourier space. Using this property of the Fourier transform to calculate the interference pattern caused by the entrance pupil mask, results in the summation over phase shifted Fourier Transforms of a disk with 16 cm diameter. The result is shown in fig. F.7. The two dimensional

[1] An approximation to the pattern can be obtained by calculating the Fast Fourier Transform (FFT) of an image of the entrance pupil illumination.

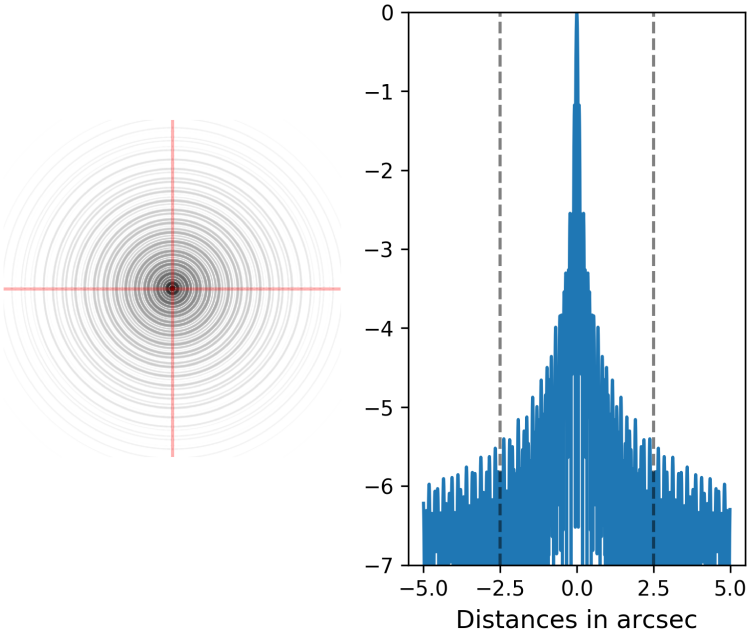

Figure F.6: The left panel shows the core of the two dimensional monochromatic PSF pattern of the UH88 telescope without mask. The side lobes are rotationally symmetric, as the entrance pupil is. The right panel shows the profile at the directions indicated on the left with red lines. The vertical dashed lines indicate the region shown in the left.

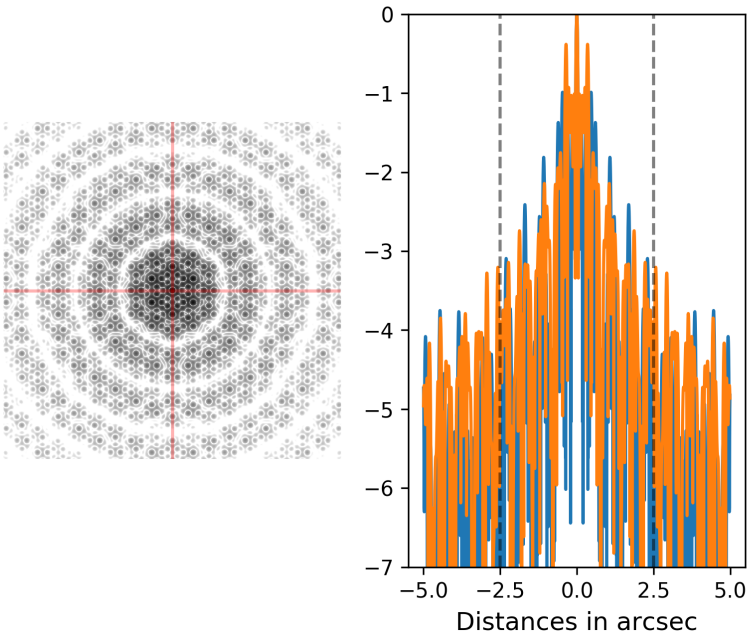

Figure F.7: The left panel shows the core of the two dimensional monochromatic PSF pattern of the UH88 telescope with mask. We see a hexagonal pattern in the PSF side lobes, as the entrance pupil is illuminated in the hexagonal setup of SCALA. The rotationally symmetric rings in the PSF are determined by the diameter of the apertures in the mask. The right panel shows the profile at the directions indicated on the left with red lines. The vertical dashed lines indicate the region shown in the left. Comparing to Fig. F.6 we see that the side lobes are of larger amplitude and are located further away from the core.

pattern shows the hexagonal structure of the entrance pupil illumination superimposed to the rotationally symmetric interference pattern caused by the apertures in the mask. As the diameter of the apertures (16 cm) is smaller than the diameter of the full entrance pupil of the UH88 telescope the side lobes are found at larger radii. Due to the separation into 18 apertures the amplitude of the side lobes is increased, see the right panel of fig. F.6 and fig. F.7.

The calculation describes the response of the telescope to a plane wave. However, the light arriving at the telescope has passed through a turbulent atmosphere, therefore the wavefronts entering the telescope are distorted. As described in sec. C.2.3 this distortion can be approximated by the superposition of plane waves with small inclinations relative to each other. The number density of inclination angles follows a Gaussian distribution centered around zero (deflection taken out) with a wavelength dependent width $\approx \lambda^{-1/5}$, according to [Quirrenbach, 2006].

To describe the observed light distribution on the detector, we have to convolve the calculated monochromatic intensity pattern with Gaussians of wavelength dependent width to account for

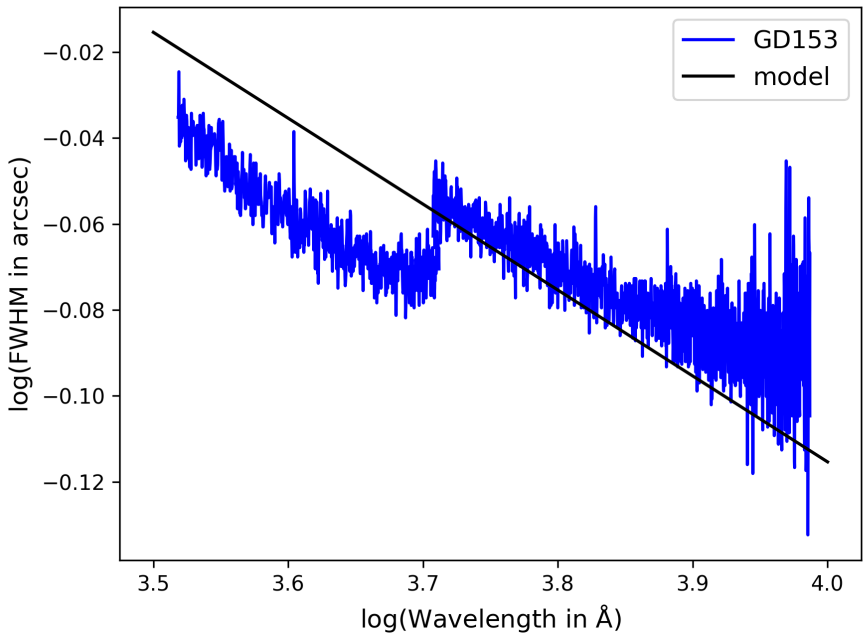

Figure F.8: Log-log plot of PSF diameter against wavelength with the model power law $\approx \lambda^{-1/5}$. For long wavelength the diameter increases due to low signal to noise. The jump at ≈ 3.7 is caused by the switch between the SNIFS channels.

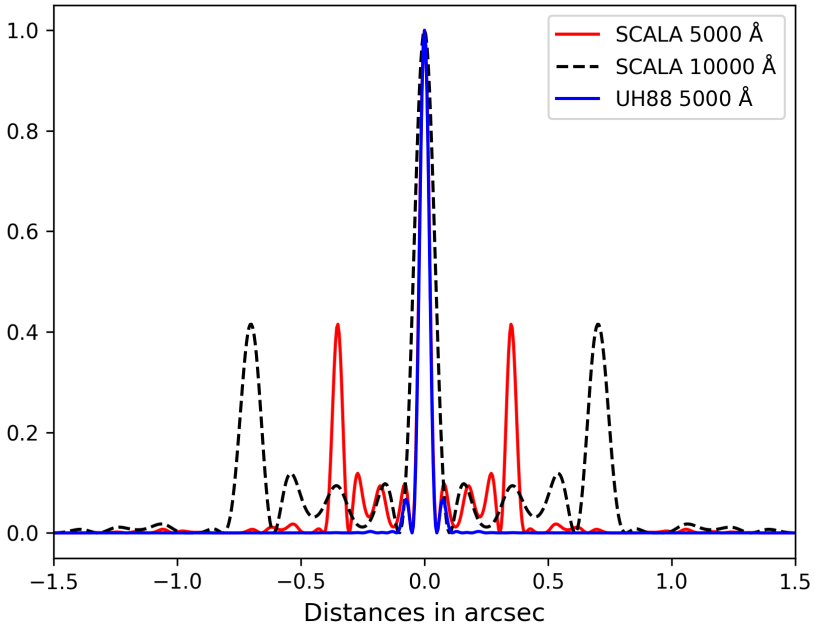

Figure F.9: Shown are the profiles of the PSF of the UH88 with mask (SCALA in the legend) at 500 nm and 1000 nm and of the UH88 telescope without mask, linear scale. One can see the strong side lobes of the PSF with mask, in comparison to the UH88 PSF without mask.

the seeing. In case there is no mask mounted to the telescope we should observe the PSF diameter to fall off like $\lambda^{-1/5}$, as the resolution of the telescope is always limited by the seeing.

We can use observations to test this prediction. For each wavelength in the datacube we subsample each spaxel with 10 x 10 sub-spaxels and measure the maximum brightness. We then count the number of sub-spaxels brighter than half the maximum brightness. The FWHM of the PSF in spaxels is then proportional to the square root of the sub-spaxel count.

Fig.F.8 shows the logarithmic diameter of the PSF as function of the logarithmic wavelength for one observed star. Indeed we find a power law dependence for each of the SNIFS channels. The jump at ≈ 3.7 corresponds to the intercept between the SNIFS blue and red channel at 5100 Å and is not surprising. At long wavelengths we see an increase in the measured width compared to the $\lambda^{-1/5}$ power law. This increase is the result of the SNIFS throughput being low, and therefore the amplitude of the PSF being low. With the amplitude being small, background spaxels will be included in the number of pixels being brighter than half the amplitude, therefore the width increases.

Fig. F.9 shows a comparison between the PSF of the telescope with mask and without mask. We see that the PSF with mask shows stronger side lobes than the telescope PSF without mask. The position of the side lobes is wavelength dependent, for longer wavelength the side lobes can dominate the PSF after convolving for the seeing. We should therefore see the PSF-width

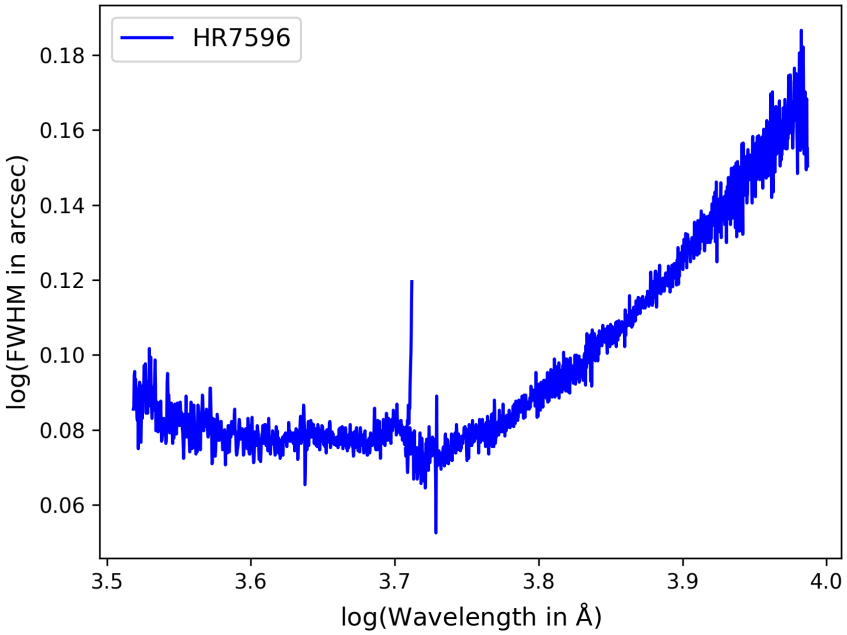

Figure F.10: Observed PSF diameter when using the mask. The previous decline of the PSF diameter with wavelength is not anymore visible as the distance of the side lobes from the core grows and broadens the PSF after convolution with Gaussian seeing.

decreasing with seeing for blue wavelength (following the seeing) and increasing in the red as the side-lobes move outwards.

Fig. F.10 shows the diameter of the observed PSF as function of wavelength for a star observed with entrance pupil mask. This wavelength dependence is in good agreement with the expectations.

The data reduction pipeline calculates the PSF width in 12 bins for the blue and red channel (bin width 150 Å in blue and 400 Å in red [Copin, 2013]). A polynomial of second order is used to interpolate between the bins and provide a stable PSF diameter, where the count rates in the detector are low (beginning and end of channel in wavelength). Afterwards the PSF model is fit to the data cube, where the width of the PSF is fixed by the second order polynomial and the PSF amplitude is variable. The wavelength-dependent amplitude of the PSF is the source spectrum we want to extract.

To check for wavelength-dependent calibration errors, possibly introduced by inaccuracies in the PSF model, we observed several standard stars in night 159 of 2015 with mask. This makes it possible to calculate the throughput of SNIFS based on the observed and known spectra. By comparison of SNIFS throughputs (based on standard stars) with and without mask, we can check whether the extraction of the spectra introduced a bias, as the mask should introduce a constant, wavelength-independent attenuation. The ratio of throughput with and without mask

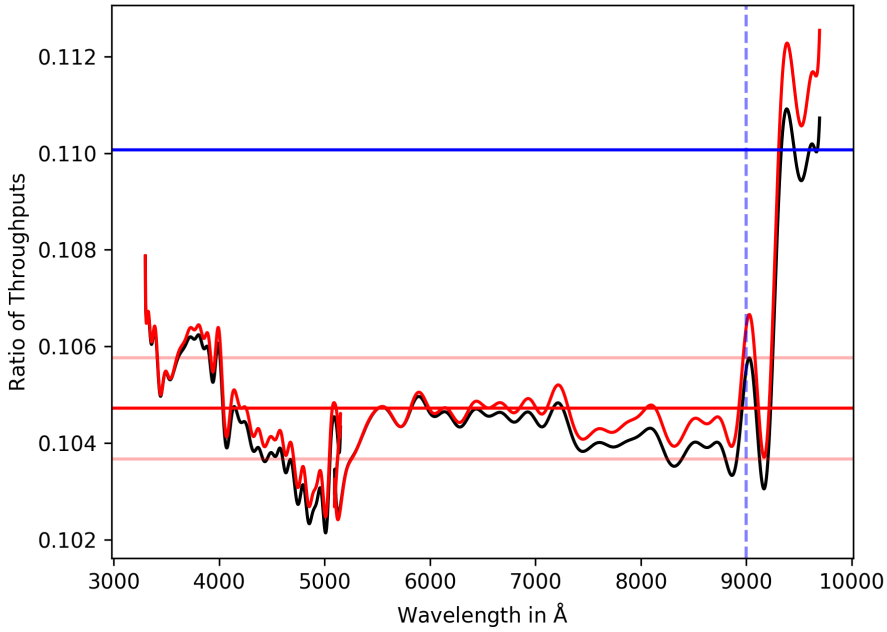

Figure F.11: Ratio of SNIFS throughput obtained with and without the entrance pupil mask. We expect the ratio to to be comparable to the blue horizontal line based on the geometric properties of the telescope. The red line shows the mean value of the ratio in the wavelength range up to 9000 Å indicated by vertical dashed line. The light red lines indicate a 1 % uncertainty range.

should be flat. Fig. F.11 shows the ratio of the SNIFS throughput with and without mask. We compare the throughput with mask once to the closest night without mask and in the second curve to the averaged throughput without mask. The ratio is 0.1047 ± 0.0008 in the wavelength range up to 9000 Å. For the blue channel a wavelength-dependent trend of $\approx$1.5 % amplitude is visible. For wavelength longer then 9000 Å there is a strong deviation from a gray attenuation. As shown previously, the mask is modifying the PSF at long wavelength, therefore it can not introduce the trend in the blue channel. For wavelength longer then 9000 Å the deviation might be caused by the calibration of SNIFS[1].

The blue horizontal line indicates the geometric expectation for the attenuation of the mask. The collecting area of the telescope is determined by the size of the entrance pupil area. The pupil is limited at the outside by the primary mirror diameter d_{tel} and at the inside by the outer diameter of the secondary mirror baffle d_{obs}. Additionally we have to take into account the area obscured by the support structure of the secondary mirror, the spider vanes w_{vane}.

[1]There are several effects for longer wavelengths. There is second order light contributing signal for long wavelengths and also water vapor absorption, which might be strong and variable. Therefore the wavelengths longer than 9000 Å are less often used and the calibration less tested.

Taking these factors into account, we obtain:

$$A_{\text{no mask}} = \left(d_{\text{tel}}^2 - d_{\text{obs}}^2\right)\frac{\pi}{4} - 2\left(d_{\text{tel}} - d_{\text{obs}}\right)w_{\text{vane}} = 32680 \pm 95\text{cm}^2 \tag{F.1}$$

In case of the mask applied to the telescope the entrance pupil area is given by 18 apertures of 16 cm diameter where two of them are split by a spider vane:

$$A_{\text{mask}} = d_{\text{SCALA Beam}}^2\frac{18\pi}{4} - 2d_{\text{SCALA Beam}}w_{\text{vane}} = 3590 \pm 32\text{cm}^2 \tag{F.2}$$

The ratio of throughput with to without mask is therefore expected to be 0.110 ± 0.001 as shown by the blue line. In sec. 7 we found that the throughput of the system had been underestimated by 5 %. Taking that into account we should find a ratio of throughputs of $0.110/1.05 = 0.1047 \pm 0.001$ which fits to the observed value of 0.1047 ± 0.0008.

As visible in fig. F.11, the wavelength dependent trend in the blue channel is small, of the order ≈1.5 %. The throughput ratio can thus be considered wavelength-independent to a good approximation. We conclude that the PSF model can handle the changes introduced by diffraction on the entrance pupil mask. Further comparisons between throughputs with and without mask would be helpful to understand the origin of the small scale trends visible in fig. F.11, blue channel. The agreement of expected and measured attenuation indicates that the throughput within the entrance pupil of the telescope is homogeneous. Therefore the calibration obtained on the area calibrated by SCALA might also be valid on the whole entrance pupil (with the limitations discussed in sec. F.2).

F.4 Stray Light within UH88 and SNIFS

SCALA is designed to illuminate a FoV of 60 arcmin in diameter. This corresponds to an illuminated circle of 400 mm[1] in the focal plane of the telescope. According to the UH88 user manual [2] the unvignetized FoV has a diameter of 46 arcmin. That means that an object which appears under a smaller diameter will not be shadowed by the internal light baffling system of the UH88 telescope. For our setup this means that up to 41 % of the light provided by SCALA could be interacting with the baffling system.

The baffle system is not able to absorb all the light shining on it and part of this light will be scattered onto the focal plane, where it can be detected. The baffle system is conical: narrow at the beginning and getting larger in diameter closer to the focal plane. Because of this geometry we can expect that possible scattering onto the detectors happens at the beginning of the baffle system. The surface is covered with a black matt finish. Light which is not absorbed but reflected of the matt surface will be redistributed into a solid angle of 2π. The length of the baffle system is more than 1 m. For the following calculation we assume that all the light hitting the baffle will be diffusely scattered (no absorption). Additionally we know that the FoV of SNIFS (6.4 arcsec) corresponds to a length of 0.7 mm in the focal plane of the telescope. This

[1] $(\tan(1°) \cdot f_{\text{tel}} = \tan(1°) \cdot 22500\,\text{mm} = 400\,\text{mm})$

[2] University of Hawaii Telescopes at Mauna Kea Observatory, User Manual, http://www.ifa.hawaii.edu/88inch/manuals/user.pdf, last checked 05.07.2018

FoV captures $4 \cdot 10^{-4}$ % of the light provided by SCALA. From these numbers one can compare the signal (S) sent to the detector with the parasitic signal (P) provided by the stray light.

$$\frac{P}{S} = \frac{0.41}{4 \cdot 10^{-6}} \cdot \frac{0.7^2}{2\pi 1000^2} \leq 0.8\,\% \tag{F.3}$$

The less equal accounts for the fact that we have made a conservative approximation, that no light will be absorbed by the black matt finish. The effect is therefore small and can be neglected. Optical path with more scattering surfaces will be further suppressed, and are therefore neglected.

Scattering surfaces closer to the focal plane can have a larger contribution to stray light. Figure F.12 shows the SNIFS instrument in the assembly phase. Two optically important pieces are marked with red ellipses in fig. F.12. First the pick-off prism, which directs the light coming from the telescope (in fig. F.12 the light comes from below) towards the enlarging doublet. Both the holder of the pick-off prism and the housing / holder of the enlarging doublet can serve as a source of scattered light. As they are close to the beam, also small reflection coefficients are enough to provide disturbing stray light.

In regular observation SNIFS is pointed to stars or supernovae superimposed to a faint background, which is caused by the sky emission and the host galaxy. In these observations the housings and holders will not be illuminated, as the point source normally does not illuminate these. In case a star is misaligned, only a small area on the housing of the enlarger or the pick off prism will be illuminated. For the case of SCALA however, the light source is extended (1° diameter) and homogeneous in brightness and can therefore produce a large amount of stray light.

To test the above case we would like to illuminate holders and housings without illuminating the FoV. We therefore pointed the telescope onto a star and defocused it. As a Cassegrain telescope provides a central obscuration the off focus star image will look like an annulus. In case the mentioned elements do not serve as source of stray light, the detector FoV would stay empty / dark. We can therefore use the signal on the detector to estimate the amount of stray light.

Based on geometric optics, there are two configurations which can be used: an intra-focal and an extra-focal position. Figure F.13 shows both of them.

Using an ideal detector (detection = absorption = 100 %) both configurations would be equal, but a CCD has a finite detection efficiency and also needs to be placed in a vacuum chamber to prevent humidity from freezing on the cooled CCD. Light, which will not be detected, will be reflected off the CCD back towards the telescope. On its way it will be partial reflected off the dewar window[1]. This reflected light will again hit the CCD and produce a second image which corresponds to an off focus star image twice the distance CCD - dewar window behind the CCD.

In case the CCD is placed intrafocal the second image can be more focused than the first and in this way fill up the central hole of the annulus and would provide a background for our measurement.

Figure F.14 is showing the intrafocal image of a star. The outer diameter of the disk is

[1] Sealing for the vacuum chamber

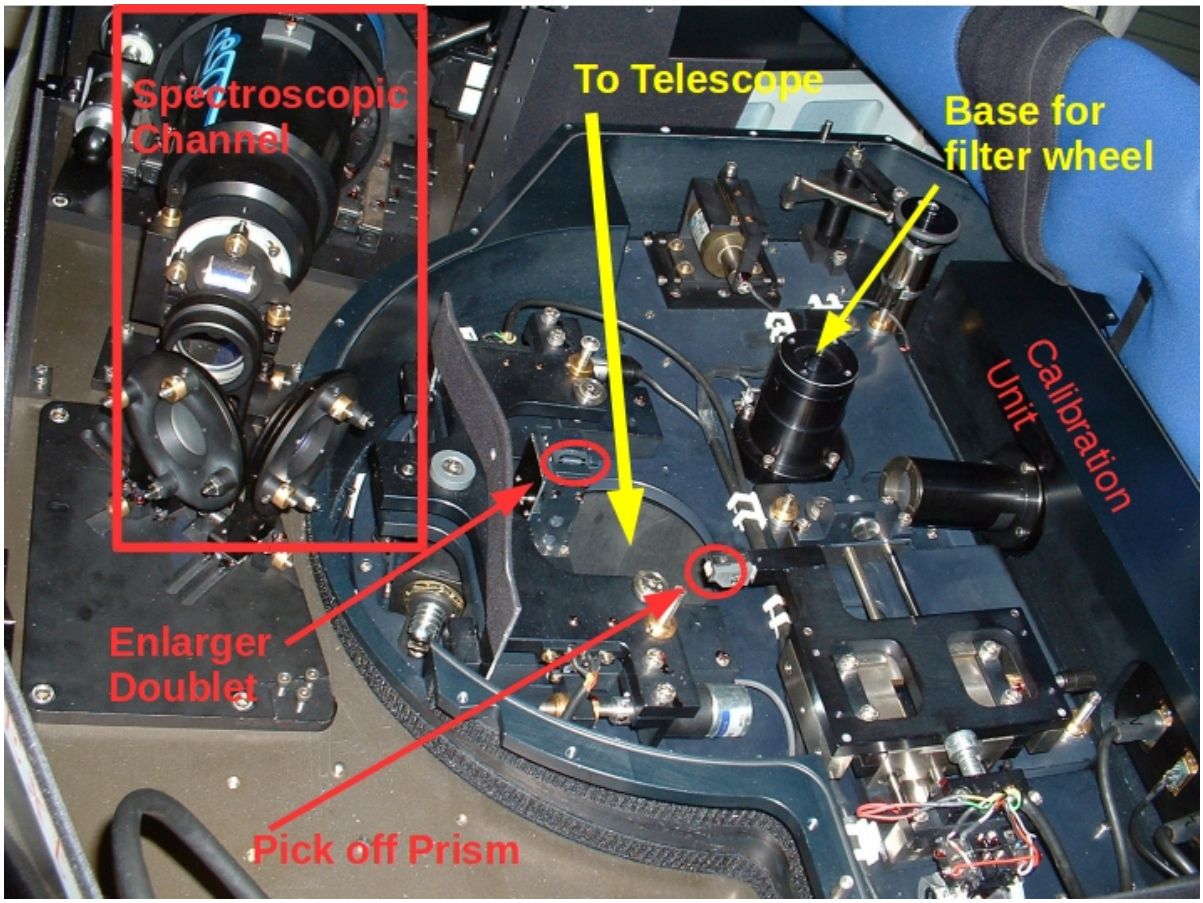

Figure F.12: Shown is an image of SNIFS in the assembly phase. The instrument will be mounted with its lower side towards the telescope. That means the light is coming through the central hole from below. Towards the right side there is the internal calibration unit, on the left there are the two spectroscopic channels, of which one is mounted. The filter wheel of the imaging channel is not yet mounted as it would cover the view on the pick off prism and the enlarger. The detector of the imaging channel will be mounted on top of the instrument as it is oriented down. Two elements are marked with ellipses: the pick-off prism and the enlarging doublet.

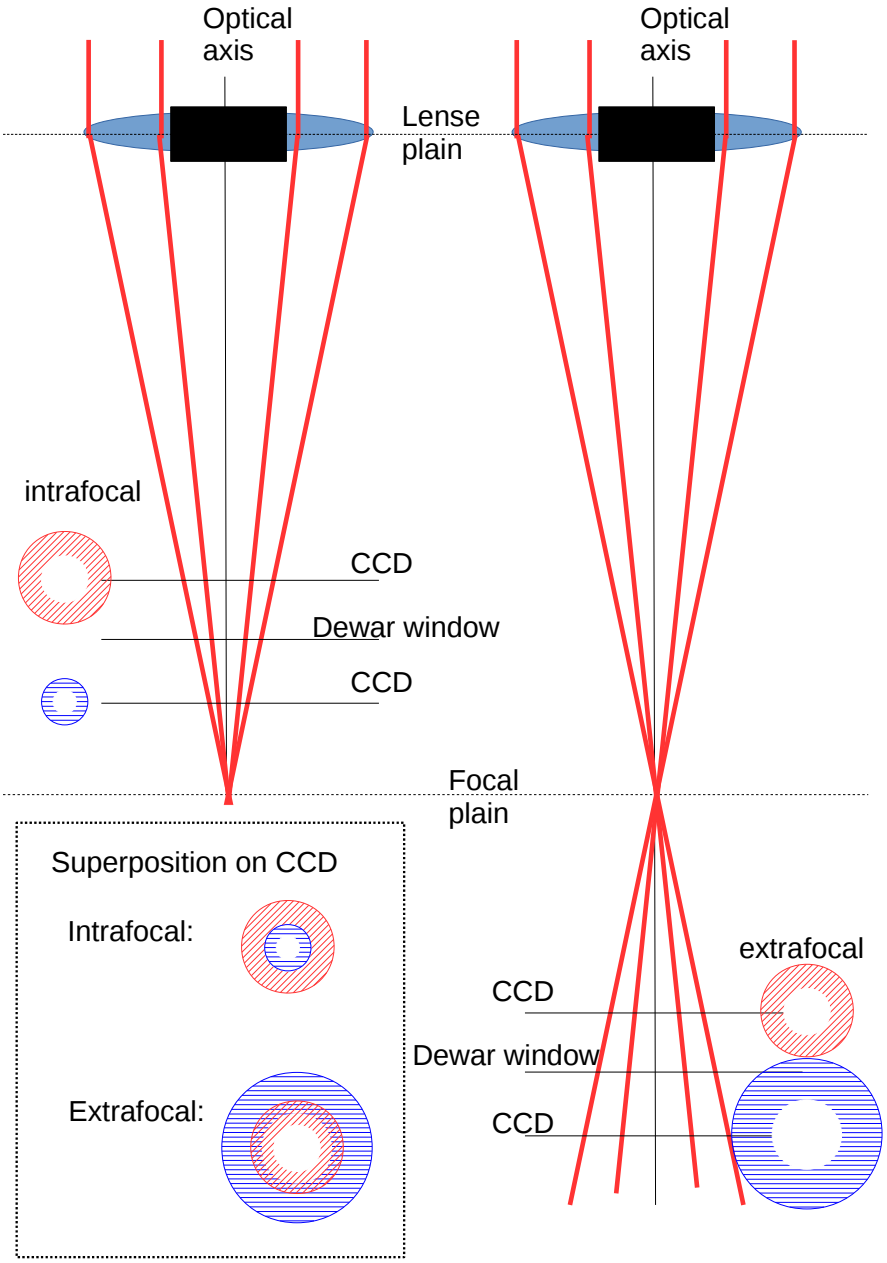

Figure F.13: Shown is a simplified sketch of the intra- and extrafocal geometry together with the imprints on the CCD. The red annulus represents the signal produced by the light which is directly detected on the CCD, while the green annulus represents the signal produced by the light reflected off the CCD and the dewar window.

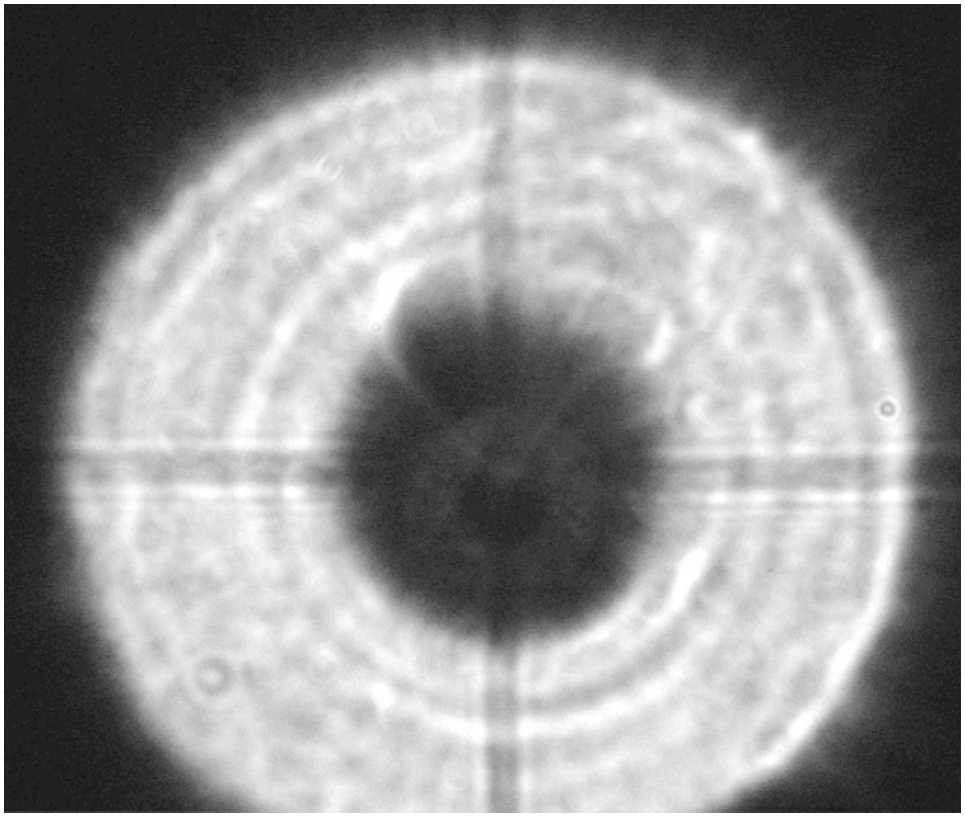

Figure F.14: Shown is an intrafocal image of a star. One can see in the central region the described reflection. In the annulus there is more structure than expected from the geometrical optics.

$\approx 442 \pm 5\text{pixel} = 6.63 \pm 0.08\mu\text{m}$, while the inner diameter is $\approx 180 \pm 5\text{pixel} = 2.7 \pm 0.08\mu\text{m}$. The ratio (0.39 ± 0.08) of inner to outer diameter fits to the ratio (0.40) of the diameters of the central obscuration and the primary mirror. Based on the focal length and the dimensions of the mirror, the off focus image is placed $67.8 \pm 0.8\,\text{mm}$ in front of the focal plane. In the central hole of the entrance pupil image a second disk is visible with an outer diameter of $104 \pm 5\text{pixel} = 1.59 \pm 0.08\,\text{mm}$ and a inner of $42 \pm 5\text{pixel} = 0.63 \pm 0.08\,\text{mm}$. This second off focus image is caused by the reflections off the CCD and the dewar window. Based on the outer diameter we can calculate its distance to the focal plane to be $16.26 \pm 0.08\,\text{mm}$. The distance of CCD to dewar window is then either $((67.8 - 16.26)/2. = 25.8 \pm 0.1)\,\text{mm}$ or $((67.8 + 16.26)/2. = 42.0 \pm 0.1)\,\text{mm}$ depending on the second image being intra or extrafocal. Additionally, the disk is not homogeneous in brightness, but shows five concentric modulations, which are caused by the wave properties of the light. This also causes a local maximum of brightness in the center of the disk, known under several names like Arago , Fresnel or Poisson spot [Fresnel, 1868](better visible on the right panel of fig. F.17).

To properly describe the interference pattern we have to evaluate equation C.12 for every pixel on the detector. For a detector in the focal plain it has been possible to approximate the intensity pattern by the modulus value squared of the Fourier transform of the entrance pupil illumination. This approximation is no longer applicable and one has to evaluate the integral numerically. In the following we will calculate the diffraction pattern of the off focus star image. This model should then be subtracted from the observation to obtain the residual signal caused by stray light. To scale the model properly we will use the amplitude of the Poisson spot.

The numerical implementation[1]: the entrance pupil is sampled with a resolution of 1 mm, while the detector is sampled with a resolution of 15 μm resolution (pixel size). As the observation was obtained through a Bessel V filter the pattern was evaluated in the wavelength range from 470 nm to 690 nm in 2 nm steps. The monochromatic patterns are then averaged using the throughput curve of the Bessel V filter as weighting function. The influence of the atmospheric and telescope transmission and of the CCD quantum efficiency was neglected in the weighting, as well as the spectrum of the observed star. As the observation is performed through the V-band filter, the wavelength range of interest is reduced and so the change in width of the seeing. Therefore we first average the diffraction pattern in wavelength and afterwards apply the smoothing, instead of smoothing the individual interference pattern for wavelength dependent seeing. Fig. F.15 shows a comparison of the observation with the wavelength averaged model and the result after Gaussian smoothing for the seeing. The wavelength averaged model shows concentric modulations in the disk. However, the width of the modulations is smaller than the seeing width, therefore smoothing will remove them. The model is able to describe the overall shape of the off focus star image, but fails to describe the structure of the off focus star light disk. We find from the model that the width of the Poisson spot based on diffraction is growing with wavelength. However the width of it is far smaller than the seeing therefore we should find that the observed width is decreasing as the seeing is. This behavior is also found in the

[1] A implementation via `Python` takes roughly one day per wavelength. As the calculation has to be performed for a set of wavelength, the calculation of the optical path length and the integral has been implemented in C-code. The code was compiled, vectorized and parallelized using Intel ICC software. In this way a calculation at a single wavelength is performed in 30 min.

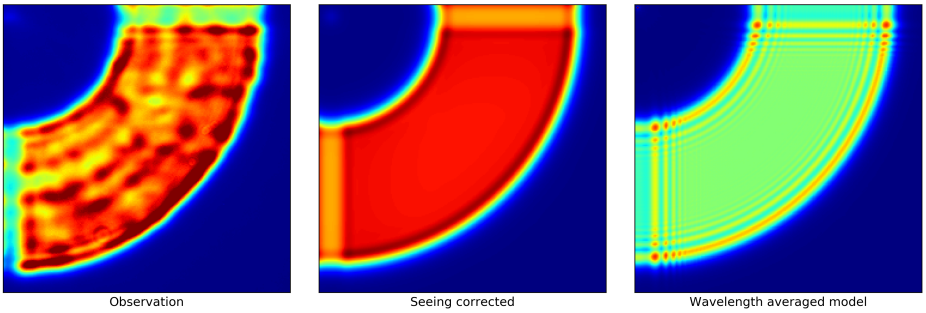

Figure F.15: The left figure shows the intensity pattern observed by the telescope in a distance of 67.8 mm from the focal plane. The right side shows the wavelength averaged model based on equation C.14. The middle should reproduce the observation therefore the model on the right was convolved with Gaussian seeing. The model however lacks the intensity modulations in the disk.

observation of the Poisson spot with the spectroscopic channels of SNIFS. We also find that the shape of the Poisson spot is slightly triangular, as visible in the upper panel of fig. F.16. Both the triangular shape and the missing interference pattern in the off focus star disk indicate that the aberration properties of the UH88 telescope would need to be included.

We have introduced small asymmetries to the calculation to estimate the influence of aberrations on the off focus diffraction pattern. These calculations did not show significant changes. We therefore think that a detailed model of the aberrations would be required. We know of measurements presented in [Roddier et al., 1990], which could provide us with the necessary information. We decided to not proceed with the modeling approach (time consumption) but to obtain a first approximation by application of masks to the data cubes. Fig. F.16 shows these preliminary results. In the upper panel we show the sum over all wavelengths for the blue and red data-cube. Slightly off centered we see the triangular Poisson spot. The middle panel shows the masks obtained from the blue and red channel images by requesting the spaxel value to be smaller then 40 % of the Poisson spot amplitude. The lower panel finally shows the mean flux per spaxel relative to the star flux, scaled for the surface of the off focus star disk. The diameter of the off focus star was measured from observations with the imaging channel of SNIFS. The fraction of scattered light to star light is nearly constant 7.5 %. The narrow lines visible in the infrared are caused by sky emission, see fig. C.4 for comparison. To suppress the sky emission we should have taken additional observations of the clear night sky.

From this measurement we can not yet conclude about the amplitude of the stray light within SNIFS, as aberrations can also cause the signal. Fig. F.17 shows the intensity distribution visible in the imaging channel of SNIFS. The left shows the intra-focal image with the more focused ghost image. The right image shows the extra-focal image with the triangular Poisson spot. Additionally rays reaching outward from the Poisson spot are visible. These rays also contribute to the signal but are caused by interference and are a background to our measurement. The measured fraction of 7 % can therefore only be an upper limit to the amount of possible stray

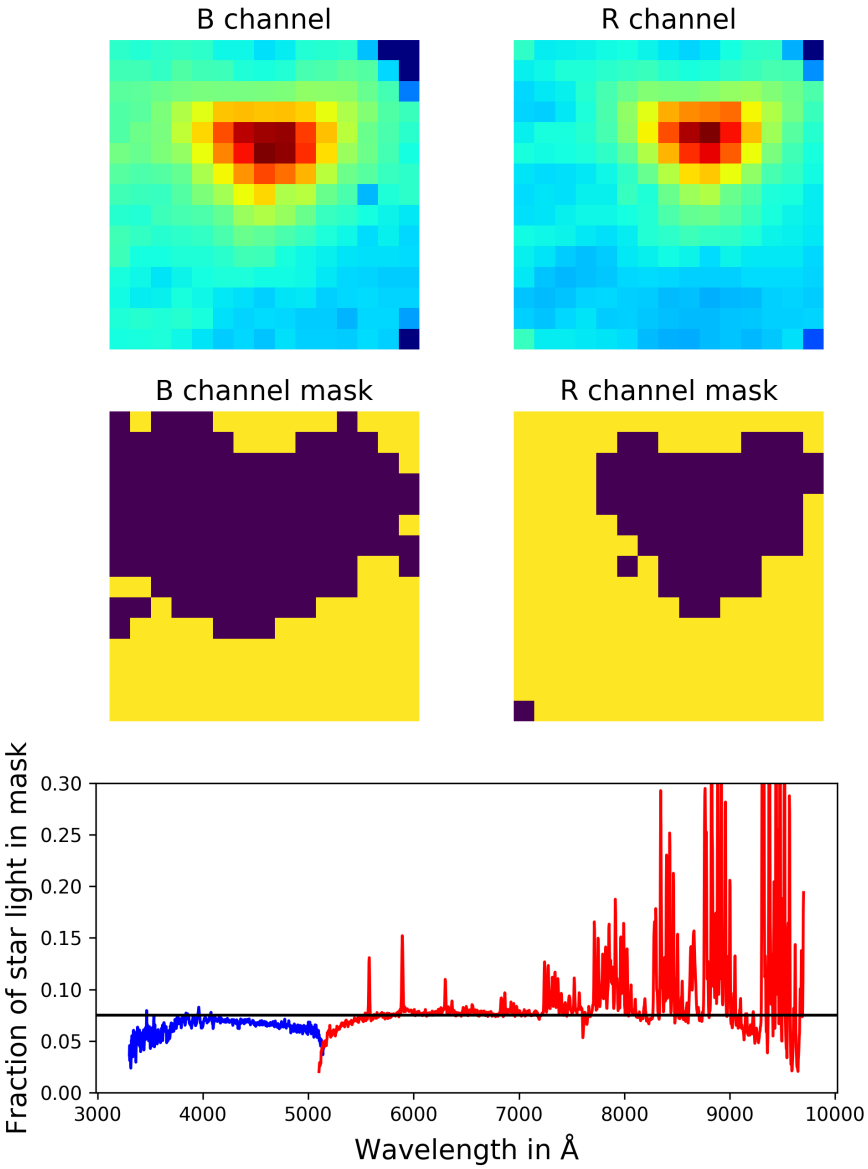

Figure F.16: The upper panel shows the sum over all wavelengths for a blue and red channel observation of an off focus star. The Poisson spot is slightly triangular and smaller in the red channel due to its width being defined by seeing. The middle panel shows masks obtained for both channels by requesting the flux per pixel to be lower than 40 % of the peak brightness of the Poisson spot. The lower panel shows the flux per spaxel relative to the star spectrum and scaled by the extent of the off focus star disk. The black solid line is indicating a level of 7 % which can be seen as a upper limit.

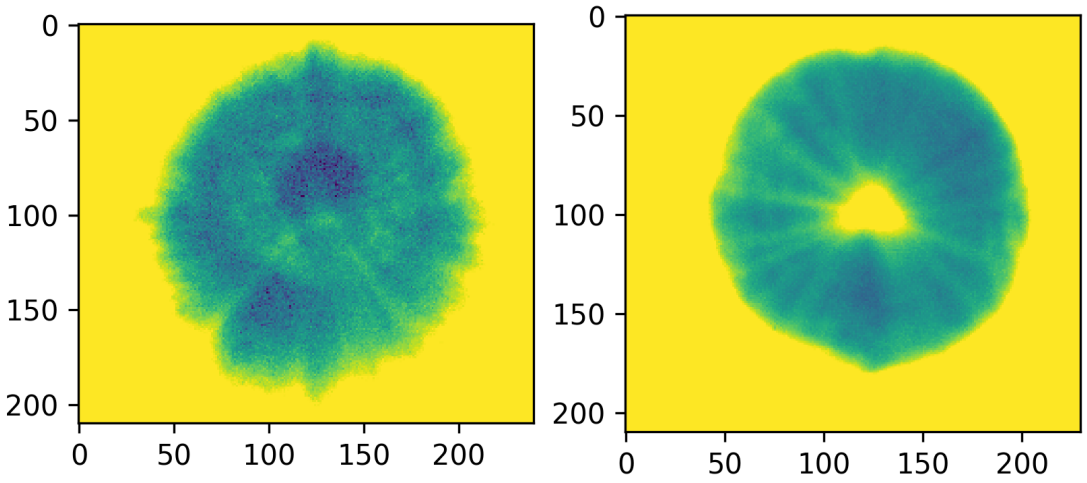

Figure F.17: Log plot of the intensity distribution of the off focus star image, obtained with the imaging channel. The left panel shows the intra-focal image with the ghost caused by reflections off the CCD and the dewar window. The right panel shows the extra focal image, in which we can clearly see the triangular shape of the Poisson spot and the diffraction spikes around it.

light. A further systematic to this analysis is given by the usage of wavelength independent masks for the blue and red channel, as the width of the Poisson spot is wavelength dependent due to diffraction and seeing. Based on these observations we increase the uncertainty on the absolute scale of the calibration performed by SCALA by 7 %. A more refined model of the diffraction including the telescope aberrations would be required to constrain the amount of scattered light within the optics of SNIFS.

Bibliography

[Ade et al., 2016] Ade, P. A., Aghanim, N., Arnaud, M., et al. (2016). Planck 2015 results-XIII. Cosmological parameters. *Astronomy & Astrophysics*, 594:A13.

[Albert, 2011] Albert, J. (2011). Satellite-mounted light sources as photometric calibration standards for ground-based telescopes. *The Astronomical Journal*, 143(1):8.

[Argelander, 1903] Argelander, F. W. A. (1903). Bonner Durchmusterung des nordlichen Himmels. In *Eds Marcus and Weber's Verlag, Bonn (1903)*.

[Bergström and Goobar, 2006] Bergström, L. and Goobar, A. (2006). *Cosmology and particle astrophysics*. Springer Science & Business Media.

[Bessell, 1990] Bessell, M. S. (1990). UBVRI PASSBANDS. *Publications of the Astronomical Society of the Pacific*, 102(656):1181.

[Betoule et al., 2014] Betoule, M. e. a., Kessler, R., Guy, J., et al. (2014). Improved cosmological constraints from a joint analysis of the SDSS-II and SNLS supernova samples. *Astronomy & Astrophysics*, 568:A22.

[Bohlin, 2014] Bohlin, R. (2014). Hubble space telescope calspec flux standards: Sirius (and Vega). *The Astronomical Journal*, 147(6):127.

[Bohlin and Gilliland, 2004] Bohlin, R. and Gilliland, R. (2004). Hubble Space Telescope absolute spectrophotometry of Vega from the far-ultraviolet to the infrared. *The Astronomical Journal*, 127(6):3508.

[Bohlin, 2000] Bohlin, R. C. (2000). Comparison of White Dwarf Models with STIS Spectrophotometry. *The Astronomical Journal*, 120(1):437.

[Botner et al., 2011] Botner, O., Bergstrom, L., et al. (2011). Nobel Prize in Physics-2011.

[Boyle and Smith, 1974a] Boyle, W. and Smith, G. (1974a). Buried channel charge coupled devices. US Patent 3,792,322.

[Boyle and Smith, 1974b] Boyle, W. and Smith, G. (1974b). Three dimensional charge coupled devices. US Patent 3,796,927.

[Bréon, 1998] Bréon, F.-M. (1998). Comment on Rayleigh-scattering calculations for the terrestrial atmosphere. *Applied optics*, 37(3):428–429.

[Brown et al., 2006] Brown, S. W., Eppeldauer, G. P., and Lykke, K. R. (2006). Facility for spectral irradiance and radiance responsivity calibrations using uniform sources. *Applied Optics*, 45(32):8218–8237.

[Brown et al., 2004] Brown, S. W., Eppeldauer, G. P., Rice, J. P., et al. (2004). Spectral irradiance and radiance responsivity calibrations using uniform sources (SIRCUS) facility at NIST. In *Earth Observing Systems IX*, volume 5542, pages 363–375. International Society for Optics and Photonics.

[Bucholtz, 1995] Bucholtz, A. (1995). Rayleigh-scattering calculations for the terrestrial atmosphere. *Applied Optics*, 34(15):2765–2773.

[Buton et al., 2013] Buton, C., Copin, Y., Aldering, G., et al. (2013). Atmospheric extinction properties above Mauna Kea from the Nearby SuperNova Factory spectro-photometric data set. *Astronomy & Astrophysics*, 549:A8.

[Chandrasekhar, 1931] Chandrasekhar, S. (1931). The maximum mass of ideal white dwarfs. *The Astrophysical Journal*, 74:81.

[Chromey, 2016] Chromey, F. R. (2016). *To measure the sky: an introduction to observational astronomy*. Cambridge University Press.

[Colina and Bohlin, 1994] Colina, L. and Bohlin, R. C. (1994). Absolute flux calibration of optical spectrophotometric standard stars. *The Astronomical Journal*, 108:1931–1935.

[Copin, 2013] Copin, Y. (2013). *Spectro-photométrie à champ intégral dans le cadre du projet" The Nearby Supernova Factory"*. Habilitation, Université Claude Bernard-Lyon I.

[Dunkelman and Scolnik, 1959] Dunkelman, L. and Scolnik, R. (1959). Solar spectral irradiance and vertical atmospheric attenuation in the visible and ultraviolet. *JOSA*, 49(4):356–367.

[Einstein, 1917] Einstein, A. (1917). *Kosmologische Betrachtungen zur allgemeinen Relativitätstheorie*, pages 142–152. Sitzungsberichte. Königlich Preußischen Akademie der Wissenschaften zu Berlin. Feb. 2nd 1917.

[Fakhouri et al., 2015] Fakhouri, H., Boone, K., Aldering, G., et al. (2015). Improving cosmological distance measurements using twin Type Ia supernovae. *The Astrophysical Journal*, 815(1):58.

[Filippenko, 1982] Filippenko, A. V. (1982). THE IMPORTANCE OF ATMOSPHERIC DIFFERENTIAL REFRACTION IN SPECTROPHOTOMETRY. *Publications of the Astronomical Society of the Pacific*, 94(560):715.

[Finley et al., 1990] Finley, D. S., Basri, G., and Bowyer, S. (1990). The temperature scale of hot DA white dwarfs-Temperatures from far-ultraviolet continuum fluxes. *The Astrophysical Journal*, 359:483–498.

[Fioletov et al., 2000] Fioletov, V., Kerr, J., Wardle, D., et al. (2000). Correction of stray light for the Brewer single monochromator. In *Proc. Quadrennial Ozone Symp*, pages 369–370.

[Fox et al., 1986] Fox, N., Key, P., Riehle, F., et al. (1986). Intercomparison between two independent primary radiometric standards in the visible and near infrared: a cryogenic radiometer and the electron storage ring BESSY. *Applied optics*, 25(14):2409–2420.

[Fresnel, 1868] Fresnel, A. J. (1868). *Œuvres complètes d'Augustin Fresnel: Théorie de la lumière*, volume 2. Imprimerie impériale.

[Goobar and Leibundgut, 2011] Goobar, A. and Leibundgut, B. (2011). Supernova cosmology: legacy and future. *Annual Review of Nuclear and Particle Science*, 61:251–279.

[Hayes, 1970] Hayes, D. (1970). An absolute spectrophotometric calibration of the energy distribution of twelve standard stars. *The Astrophysical Journal*, 159:165.

[Hayes, 1985] Hayes, D. (1985). Stellar absolute fluxes and energy distributions from 0.32 to 4.0 μm. In *Symposium-International Astronomical Union*, volume 111, pages 225–252. Cambridge University Press.

[Hayes et al., 1970] Hayes, D., Oke, J., and Schild, R. (1970). A Comparison of the Heidelberg and Nbs-Palomar Spectrophotometric Calibrations. *The Astrophysical Journal*, 162:361.

[Hayes and Latham, 1975] Hayes, D. S. and Latham, D. (1975). A rediscussion of the atmospheric extinction and the absolute spectral-energy distribution of VEGA. *The Astrophysical Journal*, 197:593–601.

[Howell, 2006] Howell, S. B. (2006). *Handbook of CCD astronomy*, volume 5. Cambridge University Press.

[Johnson and Morgan, 1951] Johnson, H. and Morgan, W. (1951). On the Color-Magnitude Diagram of the Pleiades. *The Astrophysical Journal*, 114:522.

[Johnson and Morgan, 1953] Johnson, H. and Morgan, W. (1953). Fundamental stellar photometry for standards of spectral type on the revised system of the Yerkes spectral atlas. *The Astrophysical Journal*, 117:313.

[Juramy et al., 2008] Juramy, C., Barrelet, E., Schahmaneche, K., et al. (2008). SNDICE: a direct illumination calibration experiment at CFHT. In *Ground-based and Airborne Instrumentation for Astronomy II*, volume 7014, page 701451. International Society for Optics and Photonics.

[Kaiser et al., 2010] Kaiser, M. E., Kruk, J. W., McCandliss, S. R., et al. (2010). ACCESS: enabling an improved flux scale for astrophysics. *arXiv preprint arXiv:1001.3925*.

[Kasten and Young, 1989] Kasten, F. and Young, A. T. (1989). Revised optical air mass tables and approximation formula. *Applied optics*, 28(22):4735–4738.

[Kirchhoff and Bunsen, 1860] Kirchhoff, G. and Bunsen, R. (1860). Chemische Analyse durch Spectralbeobachtungen. *Annalen der Physik*, 186(6):161–189.

[Küsters, 2014] Küsters, D. (2014). Development of a calibration unit for the SuperNova Integral Field Spectrograph (SNIFS). Master's thesis, Rheinische Friedrich Wilhelms Universität Bonn.

[Küsters et al., 2016] Küsters, D., Lombardo, S., Kowalski, M., et al. (2016). Calibrating the SNfactory Integral Field Spectrograph (SNIFS) with SCALA. In *Ground-based and Airborne Instrumentation for Astronomy VI*, volume 9908, page 99084V. International Society for Optics and Photonics.

[Landolt, 1983] Landolt, A. (1983). UBVRI photometry of stars useful for checking equipment orientation stability. *The Astronomical Journal*, 88:853–866.

[Landolt, 1973] Landolt, A. U. (1973). UBV photoelectric sequences in the celestial equatorial Selected Areas 92-115. *The Astronomical Journal*, 78:959.

[Landolt, 1992] Landolt, A. U. (1992). UBVRI photometric standard stars in the magnitude range 11.5-16.0 around the celestial equator. *The Astronomical Journal*, 104:340–371.

[Lantz et al., 2003] Lantz, B., Aldering, G., Antilogus, P., et al. (2003). SNIFS: a wideband integral field spectrograph with microlens arrays. In *SPIE Proceedings Series*, volume 5249, pages 146–155.

[Larason and Houston, 2008] Larason, T. C. and Houston, J. M. (2008). Spectroradiometric Detector Measurements: Ultraviolet, Visible, and Near-Infrared Detectors for Spectral Power. Nist special publication 250-41, National Institute of Standards and Technology.

[Leavitt and Pickering, 1917] Leavitt, H. S. and Pickering, E. C. (1917). The north polar sequence. *Annals of Harvard College Observatory*, 71:47–232.

[Linder, 2003] Linder, E. V. (2003). Exploring the expansion history of the universe. *Physical Review Letters*, 90(9):091301.

[Lombardo, 2017] Lombardo, S. (2017). *Flux calibration device for Integral Field Spectrographs*. PhD thesis, Humboldt Universität zu Berlin.

[Lombardo et al., 2014] Lombardo, S., Aldering, G., Hoffmann, A., et al. (2014). A flux calibration device for the SuperNova Integral Field Spectrograph (SNIFS). *arXiv preprint arXiv:1412.1109*.

[Lundmark, 1926] Lundmark, K. (1926). The estimates of stellar magnitudes by Ptolemaios, al-Sufi and Tycho Brahe. *Vierteljahresschrift der Astronomischen Gesellschaft*, 61:230–236.

[Maeda and Terada, 2016] Maeda, K. and Terada, Y. (2016). Progenitors of type Ia supernovae. *International Journal of Modern Physics D*, 25(10):1630024.

[Maoz et al., 2014] Maoz, D., Mannucci, F., and Nelemans, G. (2014). Observational clues to the progenitors of type Ia supernovae. *Annual Review of Astronomy and Astrophysics*, 52:107–170.

[Marshall and et al., 2014] Marshall, J. L. and et al. (2014). Characterization of the Reflectivity of Various Black Materials. Technical report, Department of Physics and Astronomy, Texas A&M University, 4242 TAMU,College Station, TX 77843-4242 USA. http://instrumentation.tamu.edu/publications/reflectance_marshall_spie2014, 16.04.2017.

[Mégessier, 1995] Mégessier, C. (1995). Accuracy of the astrophysical absolute flux calibrations: visible and near-infrared. *Astronomy and Astrophysics*, 296:771.

[Miles, 2007] Miles, R. (2007). A light history of photometry: from Hipparchus to the Hubble Space Telescope. *Journal of the British Astronomical Association*, 117:172–186.

[Oke, 1990] Oke, J. (1990). Faint spectrophotometric standard stars. *The Astronomical Journal*, 99:1621–1631.

[Oke and Gunn, 1983] Oke, J. and Gunn, J. (1983). Secondary standard stars for absolute spectrophotometry. *The Astrophysical Journal*, 266:713–717.

[Oke and Schild, 1970] Oke, J. and Schild, R. (1970). The absolute spectral energy distribution of Alpha Lyrae. *The Astrophysical Journal*, 161:1015.

[Paus, 2002] Paus, H. J. (2002). *Physik in Experimenten und Beispielen.* Hanser München.

[Pereira et al., 2013] Pereira, R., Thomas, R., Aldering, G., et al. (2013). Spectrophotometric time series of SN 2011fe from the Nearby Supernova Factory. *Astronomy & Astrophysics*, 554:A27.

[Pereira, 2008] Pereira, R. D. S. (2008). *Nearby Supernova Factory: Calibration of SNIFS data and spectrophotometric Type Ia supernovae light curves.* PhD thesis, Université Paris-Diderot-Paris VII. https://tel.archives-ouvertes.fr/tel-00372504v2.

[Perlmutter et al., 1999] Perlmutter, S., Aldering, G., Goldhaber, G., et al. (1999). Measurements of Ω and Λ from 42 high-redshift supernovae. *The Astrophysical Journal*, 517(2):565.

[Pickering, 1908] Pickering, E. C. (1908). Revised Harvard Photometry. *Harvard Annals*, 50(1).

[Pogson, 1856] Pogson, N. (1856). Magnitudes of Thirty-six of the Minor Planets for the first day of each month of the year 1857. *Monthly Notices of the Royal Astronomical Society*, 17:12–15.

[Quirrenbach, 2006] Quirrenbach, A. (2006). The effects of atmospheric turbulence on astronomical observations. *A. Extrasolar planets. Saas-Fee Advanced Course 31*, 137:137.

[Rauch et al., 2013] Rauch, T., Werner, K., Bohlin, R., et al. (2013). The virtual observatory service TheoSSA: Establishing a database of synthetic stellar flux standards-I. NLTE spectral analysis of the DA-type white dwarf G191- B2B. *Astronomy & Astrophysics*, 560:A106.

[Reichel et al., 2015] Reichel, S., Biertuempfel, R., and Engel, A. (2015). Characterization and measurement results of fluorescence in absorption optical filter glass. In *Optical Systems Design 2015: Optical Design and Engineering VI*, volume 9626, page 96260S. International Society for Optics and Photonics.

[Riess et al., 1998] Riess, A. G., Filippenko, A. V., Challis, P., et al. (1998). Observational evidence from supernovae for an accelerating universe and a cosmological constant. *The Astronomical Journal*, 116(3):1009.

[Roddier et al., 1990] Roddier, C. A., Roddier, F. J., Stockton, A. N., et al. (1990). Testing of telescope optics: a new approach. In *Advanced Technology Optical Telescopes IV*, volume 1236, pages 756–767. International Society for Optics and Photonics.

[Rozenberg, 1966] Rozenberg, G. V. (1966). *Twilight*. Springer.

[Schaefer, 1993] Schaefer, B. E. (1993). Astronomy and the limits of vision. *Vistas in astronomy*, 36:311–361.

[Seidel, 1856] Seidel, L. (1856). Zur Dioptrik. Über die Entwicklung der Glieder 3ter Ordnung, welche den Weg eines ausserhalb der Ebene der Axe gelegenen Lichtstrahles durch ein System brechender Medien bestimmen, von Herrn Dr. L. Seidel. *Astronomische Nachrichten*, 43(19):289–304.

[Smith, 1976] Smith, B. A. (1976). Astronomical imaging applications for CCDs. In *Charge-Coupled Device Technology and Applications*.

[Stebbins et al., 1950] Stebbins, J., Whitford, A., and Johnson, H. (1950). Photoelectric Magnitudes and Colors of Stars in Selected Areas 57, 61, and 68. *The Astrophysical Journal*, 112:469.

[Steinheil, 1837] Steinheil, C. A. (1837). *Elemente der Helligkeits-Messungen am Sternenhimmel*. Denkschriften der k. b. Akad. d. Wiss., Bd. 13. http://opacplus.bsb-muenchen.de/title/BV001650961/ft/bsb10053142?page=1.

[Stubbs and Tonry, 2006] Stubbs, C. W. and Tonry, J. L. (2006). Toward 1% photometry: end-to-end calibration of astronomical telescopes and detectors. *The Astrophysical Journal*, 646(2):1436.

[Vaz, 2011] Vaz, A. L. (2011). *Building a better flat-field: an instrumental calibration projector for the Large Synoptic Survey Telescope*. PhD thesis, Massachusetts Institute of Technology. http://hdl.handle.net/1721.1/65435.

[Weaver, 1946] Weaver, H. F. (1946). The development of astronomical photometry. *Popular Astronomy*, 54:504.

[Yendell, 1905] Yendell, P. S. (1905). On the Observation of Variable Stars. I. The Argelander Method. *Popular Astronomy*, 13:453–460.

[Zago, 1995] Zago, L. (1995). *The effect of the local atmospheric enviroment on astronomical observations*. PhD thesis, départment de génie civil École Polytechnique Fédérale de Lausanne pour l'obtention du grade de docteur ès science techniques par Lorenzo ZAGO Lauréat en génie aéronautique, Ecole Polytechnique.

[Zinner, 1926] Zinner, E. (1926). Helligkeitsverzeichnis von 2373 Sternen bis zur Größe 5.50. *Veroeffentlichungen der Remeis-Sternwarte zu Bamberg*, 2.

[Zöllner, 1861] Zöllner, J. K. F. (1861). *Grundzüge einer allgemeinen Photometrie des Himmels*. Mitscher & Röstell.

[Zong and et al., 2006] Zong, Y. and et al. (2006). Simple spectral stray light correction methode for array spectrometers. *Apl. Opt.*, 45(6).